SV2A - JUST A SYNAPTIC VESICLE PROTEIN? UNRAVELLING THE INTERACTION OF SV2A AND MITOCHONDRIA IN THE PATHOGENESIS AND THERAPY OF MORBUS ALZHEIMER

Dissertation
zur Erlangung des Grades
„Doktor der Naturwissenschaften“
im Promotionsfach Pharmakologie und Toxikologie

am Fachbereich Chemie, Pharmazie, Geographie und Geowissenschaften
der Johannes Gutenberg-Universität Mainz

vorgelegt von

Jonas Sebastian Reichert
geboren in Berlin-Wilmersdorf

Mainz, März 2022

D77

Dekan:

Erstgutachter:
Zweitgutachter:

Tag der Einreichung: 15.03.2022
Datum der mündlichen Prüfung: 27.04.2022

EIDESSTATTLICHE ERKLÄRUNG

Die vorgelegte Dissertation wurde am Institut für Pharmazeutische und Biomedizinische Wissenschaften (IPBW) der Johannes Gutenberg-Universität in Mainz zur Erlangung des Grades „Doktor der Naturwissenschaften“ angefertigt.

Hiermit erkläre ich an Eides statt, dass ich die vorliegende Dissertation selbstständig und nur mit den angegebenen Hilfsmitteln angefertigt habe. Diese Dissertation wurde noch nicht als Prüfungsarbeit für eine andere Prüfung eingereicht. Zudem wurden bisher weder die gleiche noch Teile der Abhandlung als Dissertation bei einer anderen Fakultät oder einem anderen Fachbereich eingereicht.

_____

Ort, Datum Jonas Sebastian Reichert

Nothing in life is to be feared, it is only to be understood.
Now is the time to understand more, so that we may fear less.
-Marie Curie

ZUSAMMENFASSUNG

Dank der Fortschritte in Medizin und Gesundheitswesen altert die Weltbevölkerung jährlich. Mit dem Alter nimmt auch die Prävalenz altersbedingter Erkrankungen wie Demenz zu. Derzeit leiden weltweit mehr als 55 Millionen Menschen an Demenz, wobei die Alzheimer Krankheit mit 60-70 % die häufigste Form darstellt. In Anbetracht der unbekannten Ursache und des Mangels an wirksamen Diagnose- und Behandlungsmöglichkeiten der Alzheimer Krankheit ist es von entscheidender Bedeutung, den Auslöser sowie neue Behandlungsmöglichkeiten zu erforschen und zu entwickeln.

In dieser Dissertation wurde die Wirkweise des Antiepileptikums Levetiracetam (LEV) im Hinblick auf dessen nachgewiesene protektive Wirkung auf die Mitochondrien und die Verbesserung der Kognition beim Morbus Alzheimer untersucht. LEV könnte aufgrund seiner Mitochondrien protektiven Wirkung einen neuen therapeutischen Ansatz für die Behandlung der Alzheimer Krankheit im Rahmen der "Mitochondrial Cascade Hypothesis" darstellen. Als Ligand des synaptischen Vesikelproteins 2 A (SV2A) wurde angenommen, dass dieses Vesikelprotein in den Mitochondrien vorhanden und für die mitochondrialen Effekte von LEV verantwortlich ist. Ziel dieser Arbeit war es daher, SV2A in Mitochondrien nachzuweisen und zu untersuchen, wie sich die Lokalisation von SV2A bei mitochondrialem Stress verändert. Darüber hinaus sollten die Effekte von SV2A und LEV auf Mitochondrien und zelluläre Prozesse untersucht werden.

Zum ersten Mal wurde die Lokalisierung von SV2A an der äußeren Mitochondrienmembran nachgewiesen, die durch mitochondrialen Stress gesteigert wird. Daneben wurde untersucht, wie sich verringerte SV2A Proteinspiegel auf die Morphologie der Mitochondrien auswirken. Sowohl in Zelllinien als auch in Neuronen von SV2A Knockout Mäusen führte der Verlust von SV2A zu einer ausgeprägten mitochondrialen Fragmentierung, die im Mausmodell sogar geschlechtsspezifisch auftrat. Auch konnte gezeigt werden, dass der Verlust von SV2A zu einer allgemeinen Verringerung der Teilung und Fusion beeinträchtigter Mitochondrien führt. Vermutlich wirkt SV2A als Fusionsfaktor auf die mitochondriale Dynamik ein. In Übereinstimmung mit diesen Daten wurde gezeigt, dass LEV zu einer Verlängerung der Mitochondrien in Abhängigkeit von SV2A führt. Schließlich konnte noch nachgewiesen werden, dass SV2A und LEV eine Rolle bei der Regulierung der Autophagie, insbesondere der Mitophagie, spielen. So führte der Verlust von SV2A zu einem Rückgang der Autophagierate, nicht weil SV2A ein Bestandteil der Autophagosomen oder Lysosomen ist, sondern wahrscheinlich den Angriff beider Organellen auf Mitochondrien fördert.

ABSTRACT

Thanks to advances in medicine and healthcare, the world's population ages every year. As we age, the prevalence of age related diseases such as dementia increases. Currently, more than 55 million people worldwide suffer from dementia, with Alzheimer's disease being the most common form (60-70 %). Given the unknown cause and lack of effective diagnostics as well as therapies for Alzheimer's disease, it is vital to research the causative agent for the onset of Alzheimer’s disease and develop new therapeutic approaches.

In this dissertation, the mode of action of the antiepileptic drug levetiracetam (LEV) was investigated in relation to its demonstrated mitochondrial protective effects and improvement on cognition in Alzheimer's disease. LEV, due to its mitochondria protective effects, may represent a new therapeutic approach for the treatment of Morbus Alzheimer in context of the "Mitochondrial Cascade Hypothesis". Being a synaptic vesicle glycoprotein 2 A (SV2A) ligand, the synaptic vesicle protein SV2A was hypothesized to be abundant among mitochondria and responsible for the mitochondrial effects of LEV. Therefore, the aim of this scientific work was to detect SV2A in mitochondria and to investigate how the mitochondrial localization of SV2A alters upon mitochondrial stress. In addition, the impact of SV2A and LEV on mitochondria and cellular processes was to be investigated.

Mitochondrial localization of SV2A was detected, with SV2A located at the outer mitochondrial membrane and mitochondrial stress enhancing mitochondrial localization of SV2A. Furthermore, the influence of reduced SV2A protein levels on mitochondrial morphology were investigated. In cell lines and neurons from SV2A knockout mice, depletion of SV2A caused pronounced mitochondrial fragmentation, which in mice even was sex specific. In addition, loss of SV2A caused an overall decline in fission and fusion events of impaired mitochondria. Presumably, SV2A acts as a fusion factor on mitochondrial dynamics. In accordance with these data, LEV triggered mitochondrial elongation relying on SV2A. Finally, SV2A and LEV were found to regulate autophagy, in particular mitophagy. Consequently, depletion of SV2A led to a decrease in autophagic flux, not as SV2A is a constituent of autophagosomes or lysosomes, but likely as SV2A promotes the targeting of mitochondria by both organelles.

TABLE OF CONTENT

1 ABBREVATIONS

Table 1 Abbrevations

Aβ	Amyloid beta
AD	Alzheimer's disease
ADP	Adenosine diphosphate
ATP	Adenosine triphosphate
AICD	APP intracellular domain
AMBRA1	Activating molecule in BECN1 regulated autophagy protein1
APAF1	Apoptotic protease-activating factor 1
APOE4	Apolipoprotein E4
APP	Amyloid precursor protein
APS	Ammonium persulfate
ATG	Autophagy related protein
ATP	Adenosine triphosphate
BACE1	β-site cleaving enzyme 1
Bafi	Bafilomycin A1
BAK1	BCL-2 homologous antagonist/killer
BAX	BCL-2 associated X, apoptosis regulator
BCA	Bicinchoninic acid
BNIP3	BCL2-interacting protein 3
Bradford reagent	Acidic Coomassie Brilliant Blue G-250 solution
BRV	Brivaracetam
BSA	Bovine serum albumin
BTX	Botulinum neurotoxin
CA	Cornu Ammonis
CBC	Coordinate-based colocalization
CCCP	Carbonyl cyanide m-chlorophenylhydrazone
CFU	Colony forming unit
CNS	Central nervous system
COX	Cytochrome c oxidase
CTF	Carboxy-terminal fragment

DG	Dentate gyrus
DRP1	Dynamin-related protein 1
DYN2	Dynamin 2
e. coli	Escherichia coli
EDTA	Ethylenediaminetetraacetic acid
EGTA	Ethylene glycol bis (β-aminoethylether) tetraacetic acid
ER	Endoplasmic reticulum
ESR	Estrogen receptors
E-SYT	Extended synaptotagmin
ETC	Electron transport chain
FAD	Familial Alzheimer's disease
$FADH_2$	Flavin adenine dinucleotide
FBS	Fetal bovine serum
FDA	U.S. Food and Drug Administration
FIP200	FAK family kinase-interacting protein of 200 kDa
FIS1	Mitochondrial fission 1 protein
FKBP8	FK506-binding protein 8
FUNDC1	FUN14 domain-containing protein 1
GABA	γ-aminobutyric acid
GAPDH	Glyceraldehyde 3-phosphate dehydrogenase
GRIK4	Glutamate receptor, ionotropic, kainate 4
GSDIM	Ground state depletion microscopy followed by individual molecule return
HEK-293	Human embryo kidney-293 cells
HRP	Horseradish peroxidase
HSC70	Cochaperone heat shock cognate 71 kDa protein
ICC	Immunocytochemistry
ICD	International Statistical Classification of Diseases and Related Health Problems
IHC	Immunohistochemistry
IMM	Inner mitochondrial membrane
IMS	Intermembrane space
IQWiG	Institut für Qualität und Wirtschaftlichkeit im

	Gesundheitswesen (Institute for Quality and Efficiency in Health Care)
KD	Knockdown
KO	Knockout
LAMP2A	Lysosome associated membrane glycoprotein 2A
LB medium	Lysogeny broth medium
LC3	Microtubule associated protein 1 light chain 3
LC-MS/MS	Liquid chromatography-tandem mass spectrometry
LEV	Levetiracetam
LIR	LC3 interacting region
LOAD	Late onset Alzheimer's disease
LTD	Long term depression
LTP	Long term potentiation
MCI	Mild cognitive impairment
Mdivi-1	Mitochondrial division inhibitor-1
MDV	Mitochondria derived vesicles
MEA	β-Mercaptoethylamine
MFF	Mitochondrial fission factor
MFN	Mitofusin
MIB	Mitochondrial Isolation Buffer
MiD	Mitochondrial dynamics protein MiD
MIRO1/2	Mitochondrial Rho GTPase 1 and 2
MMP	Mitochondrial membrane potential
MOMP	Outer mitochondrial membrane permeabilization
mPTP	Mitochondrial permeability transition pore
MRI	Magnetic resonance imaging
mRNA	Messenger ribonucleic acid
mtDNA	Mitochondrial deoxyribonucleic acid
mTOR	Mammalian target of rapamycin
mTORC1	mTOR complex 1
MTP18	Mitochondrial protein, 18 kDa
NADH	Nicotinamide adenine dinucleotide
NDP52	Calcium binding and coiled-coil domain containing protein 2

Neg. ctl	Negative control
NFT	Neurofibrillary tangles
NIX	NIP3-like protein X
NMDA	N-methyl-D-aspartate
OGT	O-linked N-acetylglucosamine transferase
OMM	Outer mitochondrial membrane
OPA1	Optic atrophy protein 1
Opti-MEM	Opti-MEM Reduced Serum Medium
OPTN	Optineurin
OXPHOS	Oxidative phosphorylation
PBS	Phosphate Buffered Saline
PBS CMF	Phosphate Buffered Saline without CA^{2+} and Mg^{2+}
PBST	Phosphate Buffered Saline + Tween® 20
PCR	Polymerase chain reaction
PD	Postnatal day
Pearson's r	Pearson's correlation coefficient
PET	Positron emission tomography
PFA	Paraformaldehyde
PGC-1α	Peroxisome proliferator activated receptor gamma coactivator-1alpha
PHB2	Proinhibitin 2
PI3KC3	Class III phosphatidylinositol 3 kinases
PINK1	Phosphatase and tensin homologs (PTEN) induced putative kinase 1
PIP_3	Phosphatidyl inositol triphosphate
PSN	Presenilin
qPCR	Real time quantitative polymerase chain reaction
RAB7	Ras related protein Rab 7
RIPA buffer	Radioimmunoprecipitation Assay buffer
ROS	Reactive oxygen species
ROT	Rotenone
rpm	Rounds per minute
RT	Room temperature

sAPP	Soluble APP
SEM	Standard error of the mean
SMAC	Second mitochondria derived activator of caspase
SNAP25	Synaptosomal associated protein of 25 kDa
SNARE	Soluble N-ethylmaleimide-sensitive-factor attachment receptor
SRM	Super-resolution microscopy
STX17	Syntaxin 17
SV2A	Synaptic vesicle glycoprotein 2A
SVOP	Synaptic vesicle 2 related protein
SYT1	Synaptotagmin 1
TBS	Tris Buffered Saline
TBST	Tris Buffered Saline + Tween® 20
TCA	Trichloroacetic acid
TIM	Translocase of the inner membrane
TIM23	Mitochondrial import inner membrane translocase subunit Tim23
TMR	Transmembrane regions
TOM	Translocase of the outer membrane
TOM20	Mitochondrial import receptor subunit TOM20 homolog
TRAK1/2	Trafficking kinesin binding protein 1 and 2
ULK1	Unc51 like kinase 1
ut	Untransfected
VAMP	Vesicle associated membrane protein
V-ATPase	Vacuolar-type H^+-ATPase
VDAC	Voltage dependent anion channel
VGlut1	Vesicular glutamate transporter 1
VPS34	Phosphatidylinositol 3 kinase VPS34
WB	Western blot

2 INTRODUCTION

2.1 Synaptic vesicle glycoprotein 2A (SV2A)

SV2A belongs to the synaptic vesicle glycoprotein 2 (SV2) family and is an integral constituent of vertebrate synaptic vesicle membranes[1–5]. The SV2 family also comprises the SV2A paralogs SV2B and SV2C, which, unlike SV2A, are not ubiquitously expressed in the brain[2,6]. Although it is known that SV2A is involved in normal synaptic vesicle function and neurotransmission, its exact role is still not fully understood. SV2A is considered to play a role in calcium dependent exocytosis, endocytosis, neurotransmitter loading/retention in synaptic vesicles, synaptic vesicle priming as well as transport of vesicle constituents[2,7–11]. The importance of SV2A for proper central nervous system (CNS) functioning is demonstrated in SV2A knockout (KO) mice. Knockout of SV2A leads to severe CNS defects in these mice, as 50 % of them die during their first postnatal days (PD) and the remaining pups die within three weeks expressing severe seizures[1,9].

2.1.1 SV2A structure

SV2A is a hydrophobic transmembrane protein with a molecular weight of 82.6 kDa. It consists of 742 amino acids forming 12 transmembrane regions (TMR), loops connecting those TMR and extravesicular N- and C-terminal sequences (Figure 1)[1,2,4]. The TMR and extravesicular loops are highly conserved among the three SV2 homologs, whereas the intravesicular loops and N-terminal sequence are not[1]. Since the SV2 protein sequence is similar to proteins of the Major Facilitator Superfamily, a family of membrane transporters transporting sugars, citrate, and transmitters in eukaryotes and bacteria, SV2A is discussed to function as a transporter. In detail, the first six transmembrane domains of SV2A are highly homologous to sugar transporters, including the human glucose transporter, whereas the other transmembrane domains are homologous to neurotransmitter transporters[2].

Besides SV2A, SV2B and SV2C synaptic vesicles contain a distantly related protein called synaptic vesicle 2 related protein (SVOP)[12]. SVOP shares only 20−22 % sequence homology with SV2s, but a similar transmembrane structure with 12 putative TMR and cytoplasmic N- and C-termini. However, SVOP lacks the loops between TMR 6-7 and TMR 7-8 which are conserved among all SV2s. Interestingly, no SV2

homologs have been identified in invertebrates, whereas SVOP is conserved in vertebrates and invertebrates, suggesting that SVOP may be the evolutionary precursor of SV2s.

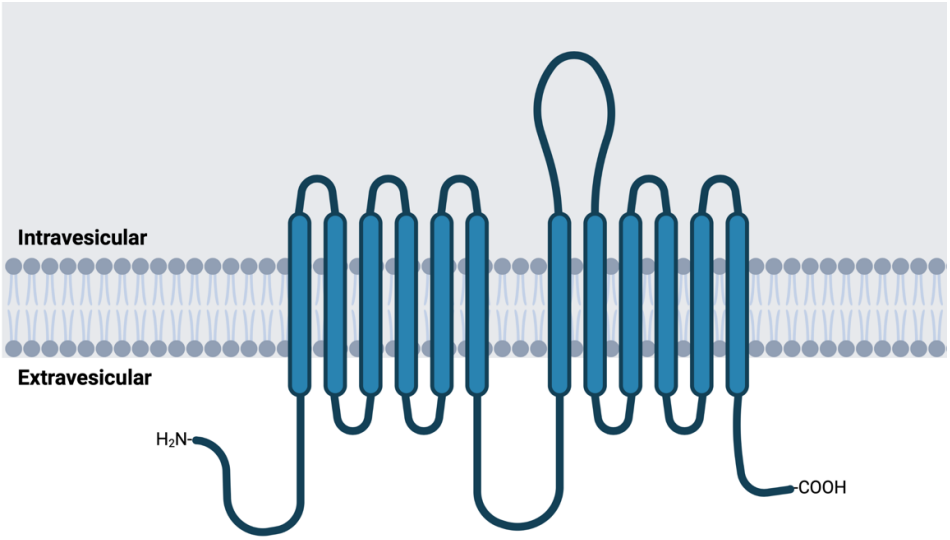

Figure 1 Simplified structure of SV2A

2.1.2 SV2A functions

Being a vesicle protein, almost entirely vesicle related functions have been reported for SV2A, including vesicular transport, vesicular loading of neurotransmitters, anchoring of vesicular proteins, support in vesicular transport, regulation of calcium dependent exocytosis and interaction with the extracellular matrix[2,4]. Although SV2A is known to be involved in normal functioning of synaptic vesicles, its exact role remains elusive. Recent data from Stockburger et al. (2016) suggest a novel mode of action for SV2A, involving mitochondria[13]. That SV2A is critical for proper CNS functioning and survival has been demonstrated in SV2A (-/-) KO mice which die either immediately after birth or within three weeks expressing severe seizures[1,9].

2.1.2.1 Calcium dependent exocytosis

Calcium dependent exocytosis of neurotransmitters is essential for proper CNS functioning. To release neurotransmitters into the synaptic cleft, synaptic vesicles must fuse with the presynaptic membrane of the synapse. This calcium dependent fusion is regulated by soluble N-ethylmaleimide-sensitive-factor attachment receptor (SNARE) proteins residing on synaptic vesicles and plasma membranes[11].

Neuronal SNAREs mediating synaptic exocytosis at the vesicle site (v-SNAREs) are vesicle associated membrane proteins (VAMP) and at the target membrane (t-SNAREs) synaptosomal associated protein of 25 kDa (SNAP25) and syntaxin 1[14,15]. Each of the aforementioned SNARE proteins feature SNARE motifs, with VAMP and syntaxin 1 bearing one and SNAP25 bearing two. Prior to fusion, SNAREs join to form a tight SNARE complex consisting of a parallel four helix bundle derived from the SNARE motifs of the three individual SNAREs (Figure 2). The energy released during assembly of the SNARE complex is then used to initiate membrane zipping and fusion. Once the vesicle is fused to the presynaptic plasma membrane, transmitters are released into the synaptic cleft.

Like any physiological process in vertebrates, the fusion of vesicles and plasma membranes is tightly regulated by several proteins. In regard to SV2A, we will focus on synaptotagmin 1 (SYT1), which is known to interact with SV2A. SYT1 acts as the Ca^{2+} sensor on synaptic vesicles during synaptic exocytosis, explaining the calcium dependence of transmitter release. With its C2A and C2B domains sharing similar β-sandwich structures, SYT1 binds five Ca^{2+} ions via five aspartate residues on loops at the top of the sandwiches[15]. These loops mediate Ca^{2+} dependent binding of now positively charged C2 domains to negatively charged phospholipids through hydrophobic residues, phospholipid headgroups and electrostatics. These findings led to a model according to which SYT1 cooperates with SNAREs in membrane fusion by simultaneously binding to membranes and SNARE complexes, thereby helping to bring membranes together in a Ca^{2+} dependent manner (Figure 2). In this model, repulsion between the membranes and negatively charged C2 domains prevents fusion before Ca^{2+} influx. While SYT1 promotes the release of transmitters, complexin represents its counterpart preventing synapses from continuously discharging in an uncontrolled manner. Complexin acts as a fusion clamp and inhibits SNARE induced membrane fusion by binding VAMP and syntaxin1 at their SNARE motifs[14,15]. This interaction is abolished by SYT1 once Ca^{2+} is bound.

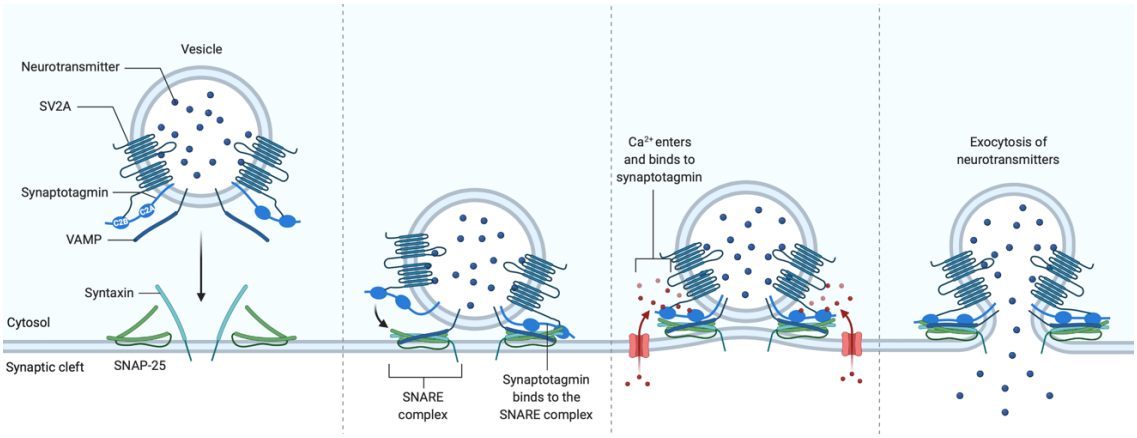

Figure 2 SV2A regulated vesicle fusion and exocytosis of neurotransmitters

During membrane fusion and vesicle release, SV2A was found to regulate the fusion of synaptic vesicles with the presynaptic membrane and thus the release of neurotransmitters by interacting with vesicle proteins, in particular SYT1. All three SV2 isoforms bind SYT1, but only SV2A and SV2C contain the SYT1 C2B domain binding motif in their N-terminal domains[7,8] (Figure 2). However, how SV2A regulates the release of neurotransmitters has not yet been elucidated. Proposed is that SV2A may prime SYT1 for interactions with other molecules or prevents it from forming inappropriate interactions until suitable calcium concentrations are reached. Another explanation is that by binding to SYT1 once calcium influx rises during an action potential, SV2A blocks the ability of SYT1 to interact with other effectors. SV2A was also found to affect the internalization of SYT1, supporting the idea that SV2A plays an important role in regulating the amount of SYT1 in synaptic vesicles and thereby transmitter release[16].

2.1.2.2 Transporter

Being a member of the Major Facilitator Superfamily of transporters, SV2A was initially thought to function as either a neurotransmitter or carbohydrate transporter. However, despite intensive efforts, there is little to no evidence for SV2A mediated neurotransmitter transport.

Concerning the transport of carbohydrates Madeo et al. (2014) were the first to identify a sugar transporting function of SV2A when they expressed recombinant human SV2A in a hexose transporter deficient *Saccharomyces cerevisiae* strain[17]. This yeast strain survived exclusively on medium containing galactose implying that SV2A transports

galactose. Radioactive galactose transport sensitive to levetiracetam further evidenced that human SV2A functions as a galactose transporter when expressed in yeast. This novel role of SV2A may be responsible for its neuronal effects, as carbohydrates, including glucose and galactose, contribute to the development and proper function of the CNS. In this regard, SV2A may play a crucial role in the CNS as a hexose transporter. Nevertheless, the sugar transport of SV2A remains to be verified in models of higher order than yeast.

Another transporter like feature of SV2A and SV2 paralogs in general is their involvement in the entry of botulinum neurotoxins (BTX)A and BTXE into the neuron[2,4]. They are not the only synaptic protein involved in BTX entry, since SYT1 and SYT2 are also receptors for BTXB and BTXG. BTX enter the cell taking advantage of luminal proteins becoming extracellular proteins during exocytosis which completely changes their potential binding partners. After exocytosis BTX bind to the N-glycosylated luminal domain 4 of SV2A and hijack an endocytic ride into the presynaptic neuron. Inside the neuron, BTX interfere with the SNARE complex and inhibit the release of neurotransmitters by cleaving SNAP25, VAMP or syntaxin 1, depending on the toxin subtype. The tetanus toxin also enters neurons via SV2 mediated endocytosis.

2.1.2.3 Proteoglycan gel matrix – Neurotransmitter loading

Although SV2A may not be a neurotransmitter transporter, it may play a role in neurotransmitter concentration and release forming an intravesicular gel matrix of proteoglycans[2,4]. Since SV2A is the major integral keratan sulfate membrane proteoglycan of synaptic vesicles with the glycans located in the lumen, SV2A is a likely candidate for matrix assembly. Proteoglycans are negatively charged, so they can adsorb positively charged or zwitterionic neurotransmitters such as monoamines, glycine and GABA. This proteoglycan matrix would bind neurotransmitters and adenosine triphosphate (ATP) within the vesicle, requiring ion exchange for their release, thereby regulating neurotransmission. The importance of an intravesicular proteoglycan matrix in vesicular uptake, storage and release of neurotransmitter has not yet been investigated in higher order organisms. Nevertheless, changes in vesicle size in response to neurotransmitter loading have been demonstrated in mice.

2.1.2.4 Mitochondria

Concerning mitochondria, Stockburger et al. (2016) demonstrated that knockdown (KD) of SV2A has severe impact on mitochondrial health and fitness[13]. Reduction of SV2A protein levels impairs mitochondrial dynamics associated with mitochondrial shortening and decreased MMP as well as ATP levels. On the other hand, SV2A ligand levetiracetam (LEV) enhances mitochondrial morphology, inducing mitochondrial elongation and increased MMP and ATP levels. LEV consequently provides protection to mitochondria while improving mitochondrial health and functionality likely via SV2A, given that LEVs effects on mitochondria vanish upon the onset of SV2A KD[13].

2.1.3 SV2A ligands

Currently, two SV2A ligands are registered for the treatment of epilepsy. The first levetiracetam (Keppra®), was approved and introduced to the market by UCB Pharma in 2000. More than a decade later, in 2016, brivaracetam (Briviact®), a derivative of LEV, was approved. Both drugs share a similar structure, binding site (SV2A) and are registered for the treatment of epilepsy. However, it remains unknown whether they act as SV2A agonists or antagonists.

Levetiracetam, the (*S*)-enantiomer of the ethyl analogue of piracetam, is a prescription drug for the treatment of epilepsy that differs from classic anticonvulsants in its target and mode of action. In preclinical studies, LEV showed strong anticonvulsant effects in epilepsy mouse models and patients, but failed conventional tests for antiepileptic drugs, revealing its unique mode of action[18]. Years after LEV was introduced to the market, SV2A was identified its molecular target[19]. Besides epilepsy, the pharmacological use of LEV is also discussed in neurodegenerative diseases such as Alzheimer's disease (AD). In an AD animal model, levetiracetam improved molecular abnormalities and reversed cognitive decline[20]. Clinical data supported these findings demonstrating positive effects of LEV in patients suffering from mild cognitive impairment (MCI) or late onset AD[21,22]. Currently, several clinical trials investigating the clinical outcome of LEV treatment in AD patients are still ongoing[23]. In addition, several articles have associated the use of levetiracetam with memory and executive function enhancement suggesting a role of SV2A in cognition[24]. Beyond the effects associated with vesicle and transmitter release, LEV exhibits protective effects on mitochondria by increasing ATP levels and mitochondrial size in healthy cells, AD model cells and cells

treated with mitochondrial stressors[13,25]. These may contribute to LEVs effects in epilepsy and AD.

Brivaracetam (BRV) is a 2-pyrrolidone derivative related to LEV approved for the treatment of focal epilepsy. In trials, BRV showed potent pharmacological activity suppressing epileptiform activity in three rodent models of epilepsy and in humans. In these trials, BRV proved to be highly effective, probably due to its 15- to 30-fold higher binding affinity for SV2A compared to LEV and the resulting greater effect on SV2A[26,27]. LEV is less selective for SV2A with multiple different modes of action, involving inhibition of N-type calcium channels and acting as an AMPA receptor antagonist[28,29]. This explains why LEV and BRV bind to SV2A at closely related sites but interact with these sites differently. In this context, mutations of SV2A identified three amino acids with different effects on LEV or BRV binding. Regarding cognition, brivaracetam also improves cognition in epilepsy patients and rodents similarly to LEV compared to control[30]. Presumably, BRV improves cognition in AD as well, as Nygaard et al. (2015) showed that BRV reverses memory impairment in APP/PS1 mice, a transgenic AD mouse model[31]. No data on the effect of BRV on mitochondria exist.

2.2 Mitochondria

According to the endosymbiotic theory, mitochondria originat from archaebacteria, which were incorporated by progenitors of prokaryotic cells about 2 billion years ago. In school, we were taught that mitochondria are the bean shaped power plants of our cells. However, in reality mitochondria are more complex than just ATP producing power plants and not bean shaped. Instead, they form highly dynamic interconnected networks composed of mitochondria with different shapes and sizes. Besides the generation of ATP by the Krebs cycle and subsequent oxidative phosphorylation (OXPHOS), other crucial mitochondrial functions include Ca^{2+} homeostasis and the initiation of apoptosis.

2.2.1 Structure

Mitochondria are double membrane organelles consisting of an outer mitochondrial membrane (OMM) separated from the inner mitochondrial membrane (IMM) by the intermembrane space (IMS)[32]. The IMM surrounds the mitochondrial matrix and forms invaginations, called cristae, in which the OXPHOS system is located (Figure 3). The

phospholipid composition and protein to lipid ratio of the OMM differs markedly from those of the IMM. Within the OMM, the protein to lipid ratio is about 50:50[33]. The OMM is mainly composed of phosphatidylcholine, phosphatidylethanolamine and pore forming membrane proteins (porins) such as the voltage dependent anion channel (VDAC), making the OMM porous and freely permeable to ions and small molecules.

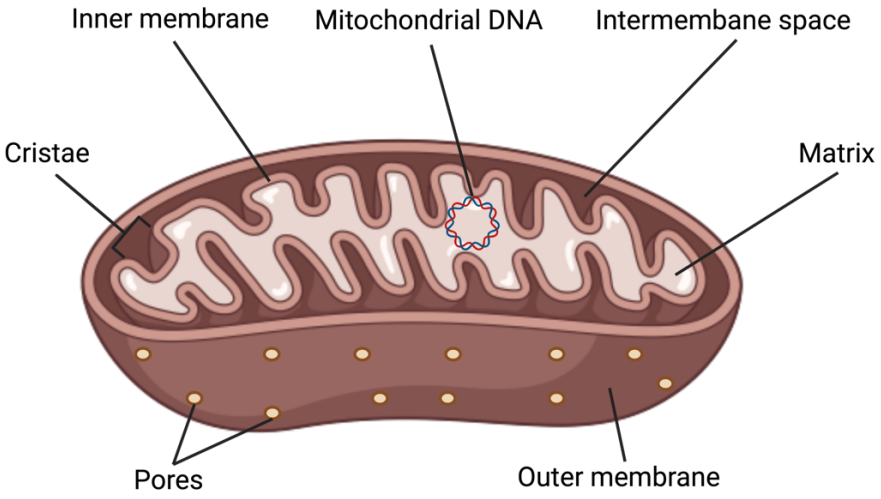

Figure 3 Structure of a mitochondrion

Larger molecules, especially nuclear encoded proteins, must be imported by the translocase of the outer membrane (TOM) complex. Because of its porosity, no membrane potential is formed at the OMM. In contrast, the IMM is a tight diffusion barrier for all ions and molecules with a protein to lipid ratio of ~75:25[33]. Ions and molecules can only pass the IMM with the help of specific membrane transport proteins, each of which is selective for a particular ion or molecule. As a result of the ion selectivity, an electrochemical membrane potential builds up at the IMM, referred to as the mitochondrial membrane potential (MMP)[34]. The IMM forms invaginations called cristae where oxidative phosphorylation is performed by a series of membrane protein complexes generating a proton gradient across the IMM used for ATP synthesis. In addition, the IMM is the only membrane of eukaryotic cells containing cardiolipin, a phospholipid synthesized in mitochondria[35]. Besides maintaining the MMP and architecture of the inner mitochondrial membrane, cardiolipin contributes to the structure and function of several proteins involved in mitochondrial respiration.

Mitochondria possess their own double stranded circular DNA (mtDNA) consisting of 16,569 base pairs, which, unlike nuclear DNA, are not wrapped around histones[36,37]. mtDNA is maternally inherited only. Although mitochondria contain their own mtDNA and ribosomes, they produce only a fraction of the required proteins and are therefore reliant on nuclear encoded proteins as well. Nuclear encoded mitochondrial proteins or subunits are transported into mitochondria by TOM and translocase of the inner membrane (TIM) complexes. Proteins carrying a mitochondrial target sequence are recognized by the TOM complex and transported into the IMS. In the IMS, proteins can either be incorporated into the IMM or transported across the IMM by the TIM complex.

2.2.2 Functions

Mitochondria play a crucial role in cellular energy metabolism, as they are responsible for fatty acid oxidation, the Krebs cycle and oxidative phosphorylation. In addition to the generation of ATP, mitochondria induce apoptosis, among other functions.

2.2.2.1 Oxidative phosphorylation

The OXPHOS system is unique owing to its dual genetic control, which involves an interplay between mitochondrial and nuclear genome. Only a small fraction of electron transport chain (ETC) polypeptides are encoded by mtDNA, whereas the majority of ETC subunits are encoded by the nuclear genome[38]. The ETC consists of transmembrane protein complexes (I-IV) and the freely mobile electron transport carriers ubiquinone and cytochrome c (Figure 4). According to recent studies, ETC complexes must assemble into distinct configured supercomplexes for proper function[39,40]. During aerobic ATP synthesis by OXPHOS, energy derived from glycolysis, fatty acid oxidation and the Krebs cycle is stored in form of nicotinamide adenine dinucleotide (NADH) and flavin adenine dinucleotide ($FADH_2$). Complexes of the respiratory chain later utilize the energy stored in NADH and $FADH_2$ to pump protons across the IMM, creating a proton gradient fueling the synthesis of ATP[41].

Complex I, known as NADH ubiquinone oxidoreductase, is the largest complex of the ETC. Its main function is to transfer two electrons derived during the oxidation of NADH to ubiquinone (also known as coenzyme Q), as the name suggests. The energy derived by the transfer of electrons from NADH to coenzyme Q triggers the pumping of four protons from the matrix into the IMS. Complex II, also referred to as succinate dehydrogenase, is part of both the Krebs cycle and the ETC. It serves as a link

between metabolism and OXPHOS. As part of the Krebs cycle, complex II catalyzes the oxidation of succinate to fumarate. In the ETC, it functions as another entry point for electrons by oxidizing $FADH_2$ and transferring the two resulting electrons to coenzyme Q, similar to complex I. Unlike complex I, complex II does not contribute to the formation of the proton gradient, as the generated energy is not used to pump protons. Once coenzyme Q receives electrons derived from the oxidation of NADH and $FADH_2$, it transfers them to complex III, coenzyme Q cytochrome c oxidoreductase. Complex III transfers these electrons to electron carrier cytochrome c and the derived energy is used to pump four protons across the IMM, contributing to the formation of the proton gradient. During the final step of the respiratory chain, complex IV, known as cytochrome c oxidase (COX), accepts four electrons from cytochrome c and donates them to elemental oxygen in the matrix, reducing it to water. The energy released is used to boost the proton gradient further by transferring two more protons into the IMS.

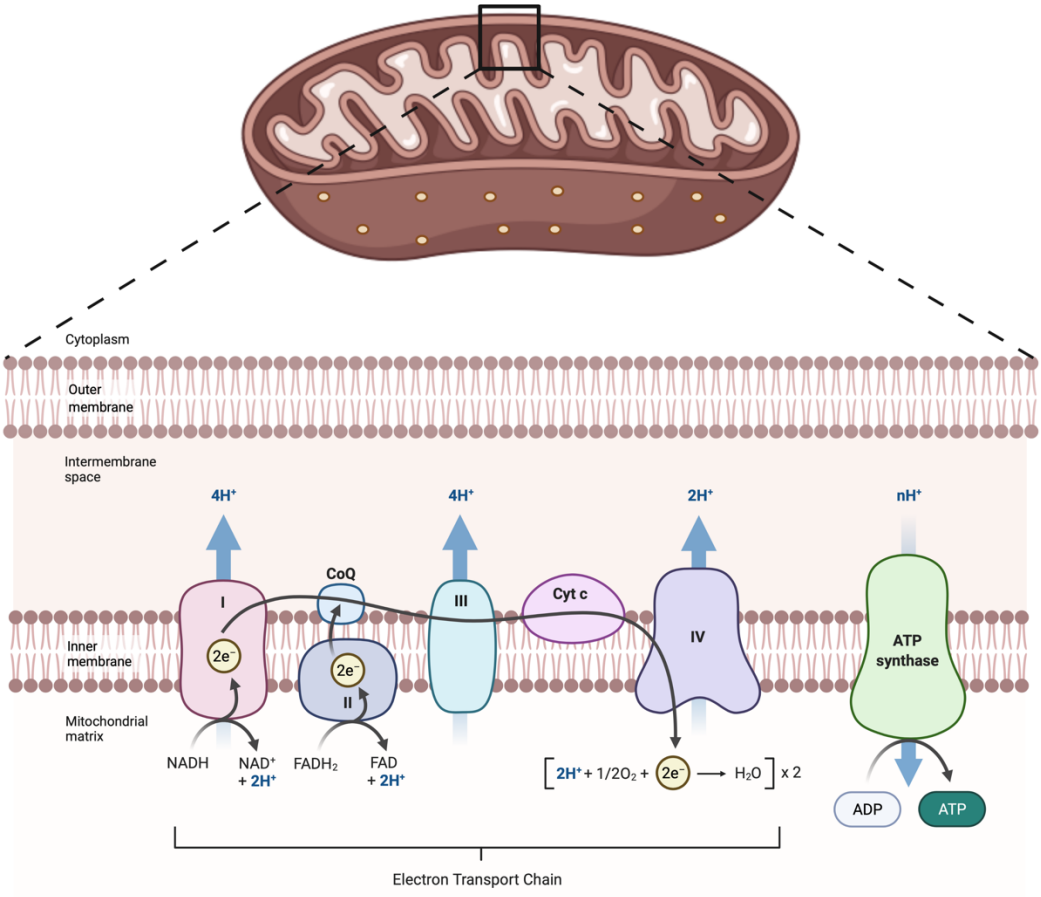

Figure 4 Electron transport chain

After numerous biochemical processes, the resulting electrochemical gradient is used to generate ATP via Complex V, the F_0F_1 ATP synthase. Protons travel from the IMS into the matrix via the F_0 subunit, which transfers the energy stored in the electrochemical proton gradient to the F_1 subunit, inducing a conformational change allowing the phosphorylation of adenosine diphosphate (ADP) to form ATP. The entire process is illustrated in Figure 4.

Owing to oxidative phosphorylation, mitochondria are the major source of cellular reactive oxygen species (ROS). Under physiological conditions, 0.2-2 % of the electrons in the ETC fail to obey the regular transfer order, exiting the ETC early interacting with oxygen to generate superoxide (O_2^-) or hydrogen peroxide (H_2O_2)[42]. Superoxides and hydrogen peroxides may then cause oxidative damage to mitochondria. Hydrogen peroxide even causes oxidative damage throughout the cell as it passes through mitochondrial membranes being uncharged and stable. To avoid oxidative damage to mitochondrial and cellular proteins, ROS scavengers scavenge ROS in both mitochondria and the cell. Superoxide dismutases are ROS scavengers converting highly reactive superoxide to hydrogen peroxide. Since hydrogen peroxides still oxidize proteins, the glutathione and thioredoxin/peroxiredoxin systems scavenge hydrogen peroxide[43].

2.2.2.2 Induction of apoptosis – Intrinsic pathway

Apoptosis, programmed cell death, is a physiological feature of non degenerate cells which occurs naturally during development, aging and as a defense mechanism. Apoptosis is stimulated by various intracellular and extracellular stimuli as well as effectors. Apoptosis can be initiated via two pathways. The extrinsic pathway, where external stimuli activate the so called death receptor and the intrinsic pathway, involving cellular stimuli and mitochondria.

The intrinsic pathway of apoptosis is controlled by the BCL-2 protein family and later release of mitochondrial proteins[44,45]. In response to intrinsic apoptotic stimuli (ROS, DNA damage, growth factor withdrawal and many more), BCL-2 associated X, apoptosis regulator (BAX) and BCL-2 homologous antagonist/killer (BAK1) are activated by pro-apoptotic BH3 only proteins. Upon their activation, BAX and BAK1 oligomerize, inducing outer mitochondrial membrane permeabilization (MOMP). MOMP is the crucial event of intrinsic apoptosis and is considered the point of no return.

MOMP allows cytosolic release of IMS proteins cytochrome c and second mitochondria derived activator of caspase (SMAC or DIABLO). Upon release of cytochrome c, the apoptosome is formed from cytochrome c, apoptotic protease-activating factor 1 (APAF1), ATP and procaspase-9. Within the apoptosome, procaspase-9 is converted to caspase-9, which activates executioner caspases-3 and -7. The executioner caspases rapidly begin to break down proteins, leading to cell death. The intrinsic apoptosis pathway is illustrated in Figure 5.

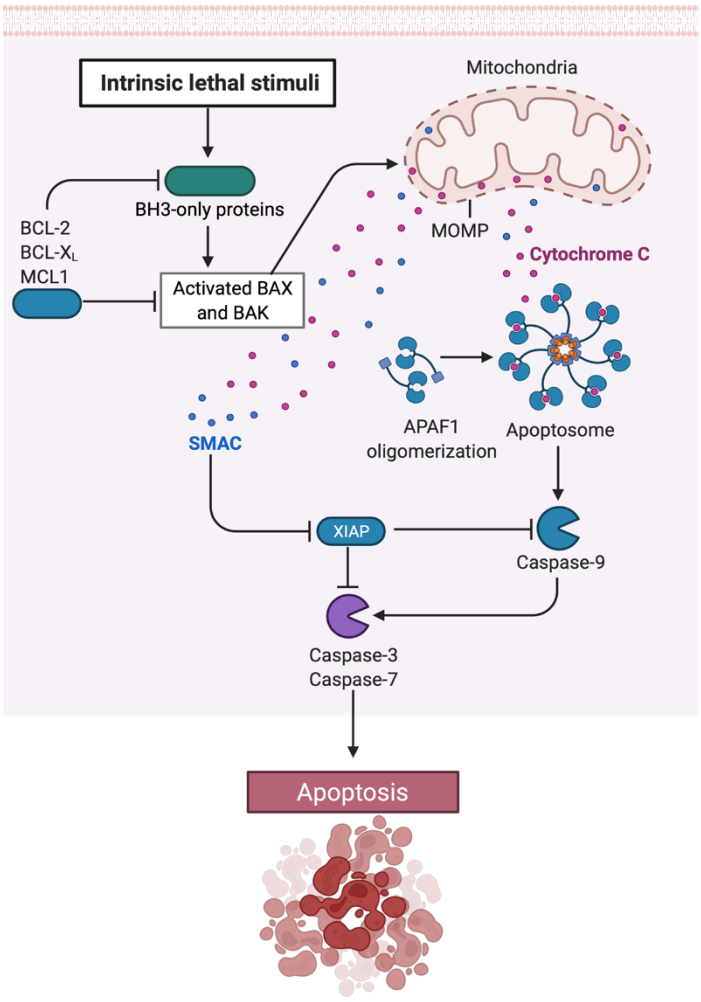

Figure 5 Apoptosis - Intrinsic pathway

2.2.3 Mitochondrial dynamics

The functional plasticity of mitochondria is linked to their morphology. Whereas mitochondria used to be viewed as small individual organelles, nowadays they are considered highly dynamic organelles forming networks throughout the cell. The

integrity and functionality of these networks is secured by continuous fission and fusion of mitochondria. Fission of mitochondria causes mitochondrial fragmentation, which is often associated with mitochondrial dysfunction, but important for maintenance of mtDNA integrity, mitochondrial transport and degradation of impaired mitochondria. Mitochondrial fusion, on the other hand, generally associated with intact mitochondrial networks, leads to elongated mitochondria associated with distribution of matrix components and stimulation of OXPHOS activity, resulting in higher ATP levels. Consequently, the balance of mitochondrial fission and fusion is essential for mitochondrial health. A shift in any direction will eventually cause mitochondrial impairment and apoptosis. Mitochondrial fission and fusion are regulated and mediated by specific proteins. Fusion of two mitochondria is mediated by the dynamin-like GTPases mitofusin 1 and 2 (MFN1 + MFN2) anchored inside the OMM and optic atrophy protein 1 (OPA1) of the IMM. Their counterparts responsible for mitochondrial fission are dynamin-related protein 1 (DRP1), dynamin 2 (DYN2) and DRP1 receptor proteins mitochondrial fission 1 protein (FIS1), mitochondrial fission factor (MFF) and mitochondrial dynamics proteins (MiD) 49 and MiD51. Besides the mentioned proteins, other proteins are also involved in mitochondrial fission and fusion but will not be discussed in detail.

2.2.3.1 Mitochondrial fusion

Given the amount of information regarding mitochondrial dynamics, it is remarkable that so little is known about the actual mechanistic mediating mitochondrial fusion. Accepted concepts assume that mitochondrial fusion is a two step process starting with OMM fusion, followed by IMM fusion. The mitochondrial fusion mechanism is illustrated in Figure 6.

OMM fusion requires MFN1 and MFN2 and is characterized by three distinct, consecutive steps. First, mitochondrial tethering by the formation of MFN homodimeric (MFN1-MFN1; MFN2-MFN2) or heterodimeric (MFN1-MFN2) complexes; second, docking of the two membranes which increases the contact area while decreasing the distance between the two membranes; and finally, fusion of the two OMMs owing to conformational changes induced by GTP hydrolysis[46,47]. Following fusion of the OMM by MFN1+2, fusion of the IMM is performed by OPA1. OPA1 is a dynamin related GTPase responsible for IMM fusion as well as maintaining normal architecture of mitochondrial cristae and thus proper functioning of the ETC[46]. To drive IMM fusion in

mammals, OPA1 must be localized in at least one of the two opposing mitochondrial membranes. Alternative splicing of OPA1 results in IMM anchored long forms (L-OPA1) which can be proteolytically cleaved into soluble short forms (S-OPA1)[46]. L-OPA1 alone is capable of fusing IMMs, whereas S-OPA1 not and rather seems to play a role in IMM fission.

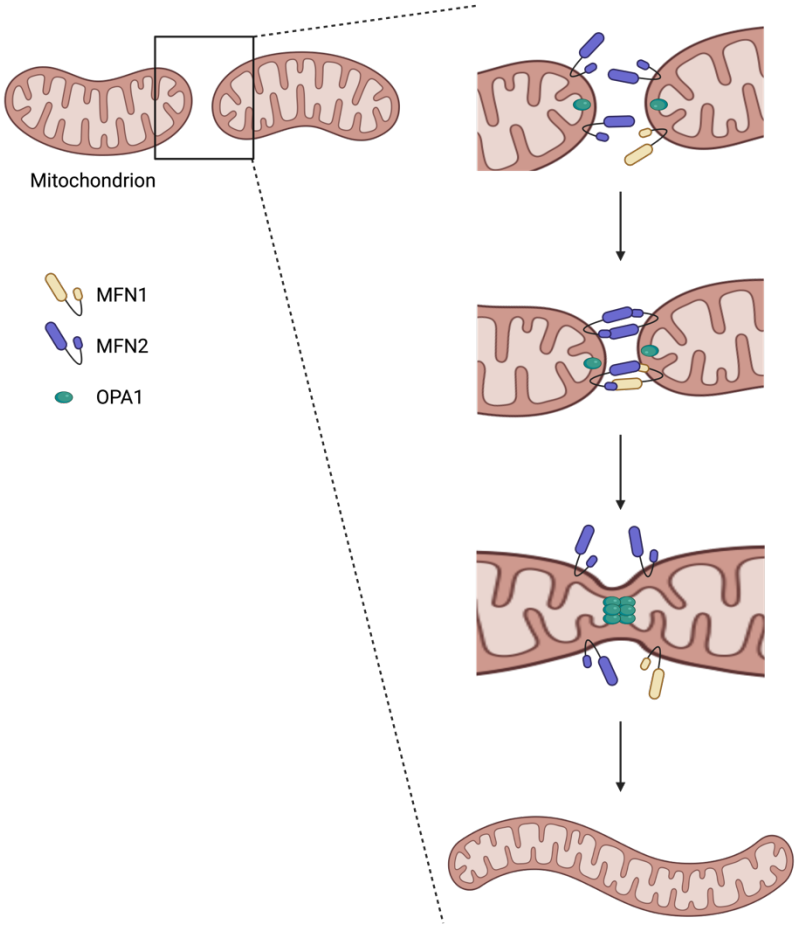

Figure 6 Mitochondrial fusion

2.2.3.2 Mitochondrial fission

Mitochondrial fission in mammals is mediated by DRP1, a large cytosolic GTPase which translocates from the cytosol to the OMM in response to specific cellular stimuli. At the OMM DRP1 oligomerizes into ring like structures. Since DRP1 lacks a pleckstrin homology domain to directly bind membrane phospholipids, its recruitment to the OMM relies on specific adaptor proteins: FIS1, MFF, MiD49 and MiD51. Upon recruitment to the OMM, GTP binding and hydrolysis induce a conformational change of DRP1,

resulting in membrane constriction and cleavage[48]. Although the role of DRP1 in membrane constriction is well described, its ability to drive fission has always been questioned. Recently, Lee et al. (2016) suggested that DYN2 may perform membrane division at constriction sites[49]. Similar to DRP1, DYN2 is a GTPase that assembles in a collar like structure around the constriction sites of the cleavage membrane. Furthermore, besides DRP1, the endoplasmic reticulum (ER) is involved in the constriction of mitochondrial membranes prior to their division. The ER wraps around mitochondria to create constriction upstream of DRP1, which is necessary given that the diameter of mitochondria is ~300 nm and the polymeric rings assembled by either DYN2 or DRP1 are too small to wrap around unconstricted mitochondria. The entire mechanism is illustrated in Figure 7.

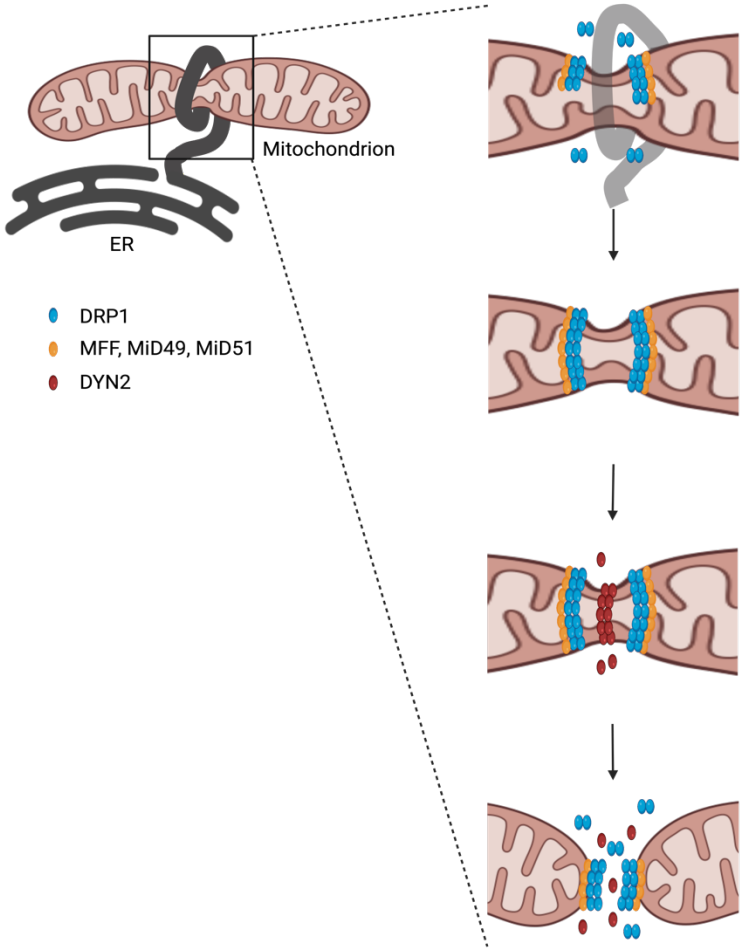

Figure 7 Mitochondrial fission

Another organelle that appears to be involved in mitochondrial fission is the lysosome. Lysosomes potentially influence mitochondrial dynamics beyond mitophagy as Wong et al. (2018) recently demonstrated the presence of lysosomes at pre mitochondrial fission sites[50].

While our understanding of OMM fission has advanced since the discovery of DRP1 and its receptors, still little is known about how the IMM divides. It remains uncertain whether the constriction of the OMM by DRP1 is sufficient to cleave the IMM or whether an additional protein or mechanism is required. In this context, mitochondrial proteins S-OPA1 and mitochondrial protein, 18 kDa (MTP18) are currently being discussed as potential IMM fission proteins[47].

2.2.4 Mitochondrial motility

Mitochondrial motility is one of the key features of mitochondria. It ensures that mitochondria meet to fuse and are transported to sites of high energy demand. Consequently, mitochondrial locomotion is critical for mitochondrial quality control. In this section, the focus will be on mitochondrial motility in neurons since most research on mitochondrial motility has been conducted in neurons.

Regarding the life cycle of mitochondria in neurons, the accepted concept states that mitochondria are assembled in the soma and transported to neurites to meet high energy demands of, for example, firing synapses. Once these mitochondria "aged", they are transported back to the soma for degradation as the soma is enriched with ribosomes, lysosomes and other organelles. However, it remains controversial whether this model really corresponds to reality, since anterograde migrating mitochondria do not demonstrate a more robust morphology and functional capacity compared to retrograde migrating mitochondria[51].

2.2.4.1 Mitochondrial locomotor system

Mitochondria travel through our cells like cars on a highway. The "highways" of mitochondria are mainly microtubules on which mitochondria are carried through the cell by motor proteins. On microtubules, these motor proteins are kinesin 1 and dynein. In neurons, mitochondria are transported anterograde (away from the soma) by kinesin 1 and retrograde (towards the soma) by dynein motors[52,53]. Besides microtubule "highways", mitochondria move to a minor extent bound to myosin on actin filaments.

In contrast to microtubular motor proteins, myosin transports cargo both anterograde and retrograde. The transport along both microtubule or actin filaments by motor proteins requires energy and is fueled by ATP hydrolysis of the motor proteins. Thus, mitochondria provide the "fuel" for their own transport.

Since kinesin 1, dynein and myosin transport various organelles throughout cells, they do not directly bind to mitochondria but rely on mitochondrial anchoring proteins. The generally accepted model states that the OMM anchored proteins mitochondrial rho GTPase 1 and 2 (MIRO1/2) act as receptors that bind mitochondria to trafficking kinesin-binding protein 1 or 2 (TRAK1/2), which in turn bind to kinesin 1 or dynein[51,54] (Figure 8). Myosin only requires MIRO1/2 to bind mitochondria.

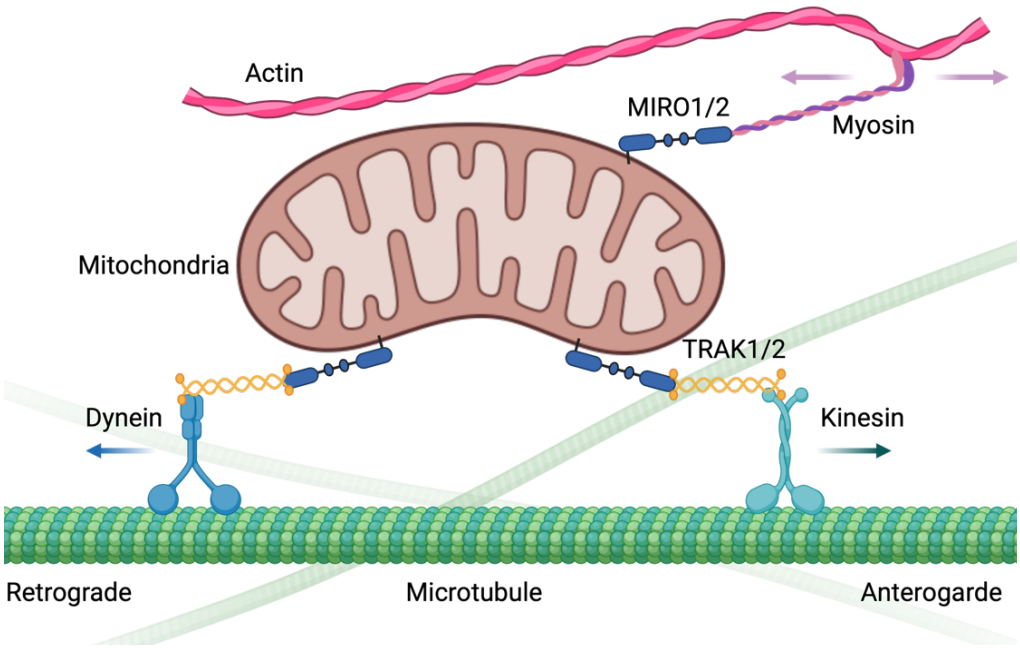

Figure 8 Mitochondria transport machinery

In summary, complexes of MIRO1/2, TRAK1/2 and kinesin 1, as well as MIRO1/2, TRAK1/2 and dynein, enable mitochondria to interfere with microtubules and control mitochondrial motility.

2.2.4.2 Arrest of mitochondrial movement

One of the most important functions of mitochondria is to provide energy in form of ATP at any cellular site energy is needed. To accomplish this, mitochondria must not

only travel to sites of high energy demand, but also arrest at those sites. In neurons, for instance, it is crucial for the release of transmitters that mitochondria provide ATP at firing synapses by anchoring themselves at these synapses.

Three different pathways are described in the literature on how mitochondria are parked at specific sites. The first major cellular signal regulating mitochondrial motility is cytosolic Ca^{2+}. Resting levels of cytosolic Ca^{2+} allow mitochondrial movement, whereas an increase in Ca^{2+} entirely inhibits mitochondrial motility[52]. In neurons, it is well known that the high energy demand required to maintain action potentials and ion gradients across membranes is accompanied by high Ca^{2+} influx. Thus, mitochondria are tethered to microtubules or actin by increased Ca^{2+} concentration to provide ATP and buffer Ca^{2+}. Responsible for the Ca^{2+} dependent arrest of mitochondrion are MIRO1/2, which function as calcium sensors binding Ca^{2+} with their two EF hands. Ca^{2+} binding by the EF hand motifs of MIRO1/2 triggers conformational changes that arrest mitochondrial movement by disrupting the interaction between kinesin 1 and microtubules or by leading to dissociation of the MIRO-TRAK complex from kinesin 1[52,54]. The same mechanism applies to the inhibition of retrograde mitochondrial migration by dynein.

Obvious, for an organelle that performs numerous metabolic processes, the nutrient status also regulates mitochondrial arrest[52]. Mitochondria accumulate at nutrient rich sites to improve ATP generation efficiency. Mitochondrial arrest during nutrient excess is regulated by the TRAK1/2 bound enzyme O-linked N-acetylglucosamine transferase (OGT)[53]. At high glucose supply, OGT catalyzes the posttranslational modification of TRAK1/2 by O-GlcNAcylation, which in turn blocks mitochondrial motility[55]. Another option to halt mitochondrial migration is via "brakes". Microtubule bound syntaphilin binds directly to mobile mitochondria tethering them to microtubules, while still being attached to motor proteins[51,52,54].

2.3 Autophagy

Autophagy (Greek „self-eating") is an evolutionarily conserved catabolic process that mediates the degradation of cellular components to maintain genomic integrity, cellular metabolism and ensure cell survival. Besides the removal of misfolded or aggregated proteins, the degradation of defective organelles and carcinogenic material, autophagy also eliminates foreign pathogens such as viruses. Various stimuli are known to trigger

selective or nonselective autophagy, among them cellular ROS, amino acid deprivation, lipid deficiency, misfolded proteins and infectious pathogens.

Three distinct types of autophagy exist: macroautophagy, microautophagy and chaperone mediated autophagy. All of which promote proteolytic degradation of cytosolic components. In macroautophagy, cytoplasmic cargo is engulfed by double membrane vesicles termed autophagosomes, which subsequently fuse with lysosomes forming autolysosomes in which the cargo is broken down. In contrast, during microautophagy, cytosolic components are incorporated and degraded directly by the lysosome. Chaperone mediated autophagy is distinct from macro- and microautophagy in that it does not rely on vesicular transport. Only proteins carrying a KFERQ motif are subject to chaperone mediated autophagy, since the cochaperone heat shock cognate 71 kDa protein (HSC70) identifies and transports these proteins to the lysosome[56]. At the lysosome, HSC70 interacts with lysosome associated membrane glycoprotein 2A (LAMP2A), promoting the transport of target proteins across lysosomal membranes into the lumen.

2.3.1.1 Macroautophagy

Macroautophagy (hereafter referred to as autophagy), the major intracellular degradation pathway, engulfs large portions of cytoplasm, organelles, proteins and infectious pathogens in double membrane vacuoles called autophagosomes to transport them to lysosomes. Following fusion with lysosomes, autophagosomal cargo is degraded by lysosomal proteases. Autophagy can either be selective or non-selective. In selective autophagy, cargo is recognized by cargo specific receptors to promote specific identification and degradation by the autolysosome, whereas in nonspecific autophagy, various cargo is degraded nonspecifically.

In mammals, the key autophagy related proteins (ATG) are divided into five subgroups: the unc51 like kinase 1 (ULK1) protein kinase complex, the class III phosphatidylinositol 3 kinases (PI3KC3) complex I, the ATG9-WIPI1 complex, the ATG5-ATG12-ATG16 complex and the microtubule associated protein 1 light chain 3 (LC3) conjugation system (Figure 9).

The underlying mechanisms on how autophagy is initiated and executed will be explained using the best characterized autophagy trigger, amino acid deprivation.

Starving on amino acids triggers autophagy by inhibition of mammalian target of rapamycin (mTOR)[56–58]. The mTOR complex 1 (mTORC1) modulates the activity of the ULK1 complex, a tetrameric complex composed of ULK1, ATG13, ATG101 and the FAK family kinase interacting protein of 200 kDa (FIP200), in response to starvation. Under nutrient rich conditions, ATG13 and ULK1 are both directly bound and phosphorylated by mTORC1 and remain inactive. However, upon nutrient deprivation ULK1 is dephosphorylated and dissociates from mTORC1. ULK1 simultaneously autophosphorylates, followed by phosphorylation of ATG13 and FIP200. The activated ULK1 kinase also phosphorylates phosphatidylinositol 3 kinase VPS34 (VPS34), which together with beclin1, VPS15, activating molecule in BECN1 regulated autophagy protein1 (AMBRA1) and ATG14 forms the PI3KC3 complex I. Phosphorylation of VPS34 mediates PI3KC3 complex I recruitment to the ER to form the phagophore (Figure 9). The membrane source for phagophore formation and proliferation is still uncertain. The most widely accepted source is the ER, but the Golgi apparatus, endosomes and mitochondria are also believed to supply membranes. VPS34 utilizes phosphatidylinositol to generate phosphatidyl inositol triphosphate (PIP_3), crucial for phagophore expansion and recruitment of other ATGs to the phagophore. Interaction of beclin1 with VPS34 promotes its catalytic activity increasing PIP_3 expression, thereby increasing phagophore elongation and maturation. Membranes required for phagophore expansion are provided by ATG9 vesicles.

Once the phagophore has formed, the ATG5-ATG12-ATG16 complex enters the scene and associates with the outer membrane of the phagophore, recruiting and integrating LC3II into the growing phagophore while preventing its premature fusion with lysosomes (Figure 9). At the phagophore, ATG4, ATG7 and ATG3 convert LC3 to LC3II by proteolytic cleavage and conjugation to phosphatidylethanolamine. LC3II is abundant on both the inner and outer surfaces of the phagophore/autophagosome, where LC3II is involved in both membrane hemifusion and binding to cargo carrying LC3 interacting region (LIR) motifs.

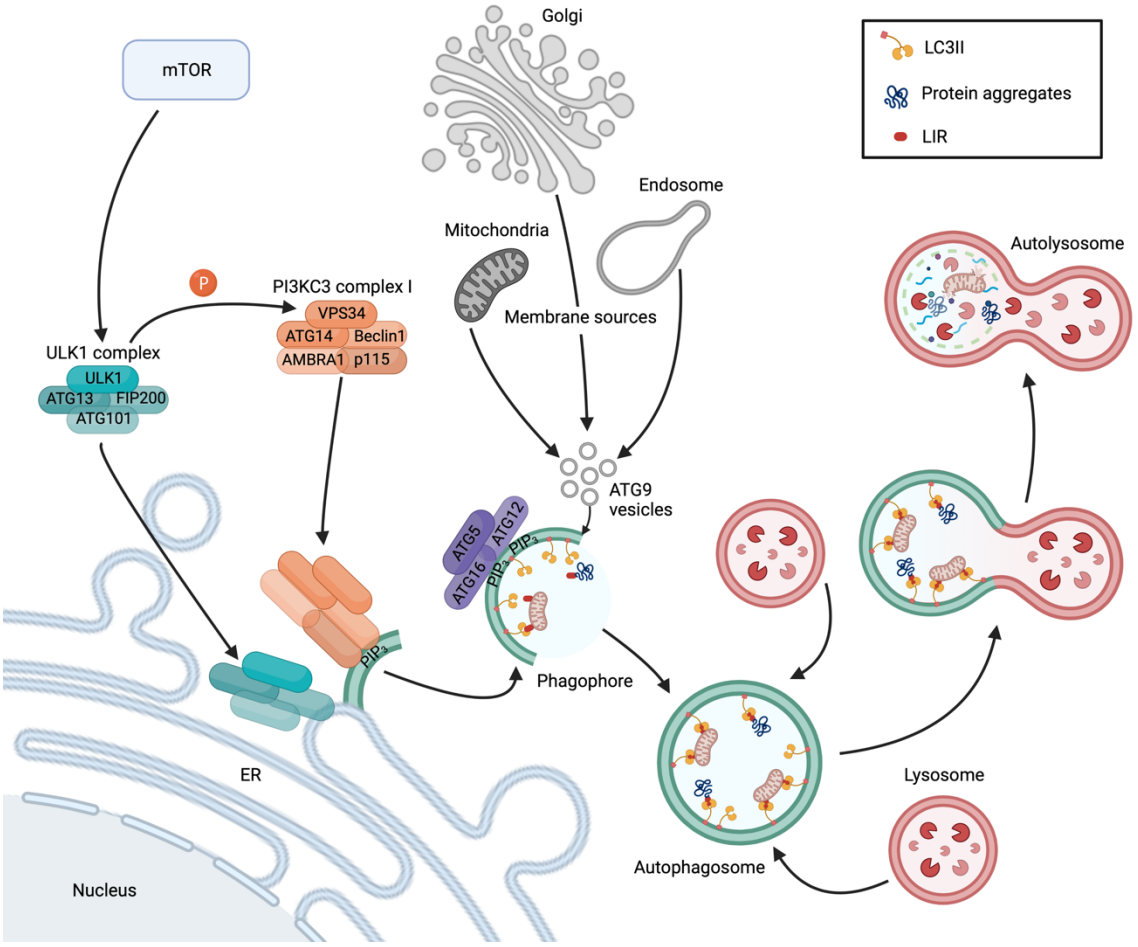

Figure 9 Macroautophagy pathway

After phagophore expansion and sealing, the autophagosome undergoes maturation which involves removal of ATGs from the outer membrane and recruitment of motor proteins and SNAREs. SNAREs on autophagosomes are syntaxin 17 (STX17) and SNAP29 and on lysosomes VAMP8. Fusion of lysosomes with autophagosomes results in release of a single membrane autophagic body into the lysosomal lumen, which is degraded along with its cargo by proteases.

2.3.1.2 Mitophagy

As mentioned earlier, autophagy occurs both selective and nonselective. Mitophagy, the selective degradation of mitochondria, is one of these selective mechanisms important for mitochondrial quality control. Being a subtype of autophagy, mitophagy and autophagy share most of their pathways and proteins. The main differences are mitochondria specific induction and selective anchoring of mitochondria to the

phagophore in mitophagy. Several pathways are known to trigger mitophagy. The most prominent is the ubiquitin dependent pathway mediated by phosphatase and tensin homologs (PTEN)-induced putative kinase 1 (PINK1) and the E3 ubiquitin ligase parkin. In addition, several mitophagy receptor mediated pathways exist where mitochondria are directly bound to the phagophore via specific receptors.

2.3.1.2.1 The PINK1/Parkin pathway

PINK1, a kinase carrying both a mitochondrial targeting sequence and transmembrane domain, is imported into functioning mitochondria via TOM and TIM complexes, where it undergoes proteolytic cleavage. Depolarization of mitochondria disrupts the transport of PINK1 across mitochondrial membranes, leading to accumulation of uncleaved PINK1 at the OMM[59–62]. PINK1 stuck at the OMM is activated by autophosphorylation whereupon it regulates the recruitment and activation of cytosolic parkin. PINK1 associated phosphorylation of parkin alters parkin's conformation, which promotes parkin's binding to the OMM and triggers its E3 ligase activity. Despite parkin, PINK1 also phosphorylates ubiquitin on dysfunctional mitochondria. Inactive parkin binds those phospho-ubiquitins generated by PINK1, facilitating its activation. Once activated parkin produces polyubiquitin chains, boosting mitophagy signaling. Parkin mediated polyubiquitination of mitochondrial proteins prompts their recognition by autophagy adaptors such as p62, optineurin (OPTN) and calcium binding and coiled-coil domain containing protein 2 (NDP52)[59–62]. LC3II recognizes these autophagy adaptor molecules, interacts with them via their LIR motifs and promotes the engulfment of targeted mitochondria by the phagophore. Prominent substrates of PINK1/Parkin mediated ubiquitination include MFN1+2, MIRO1 and VDAC1. The PINK1/Parkin mechanism is illustrated in Figure 10.

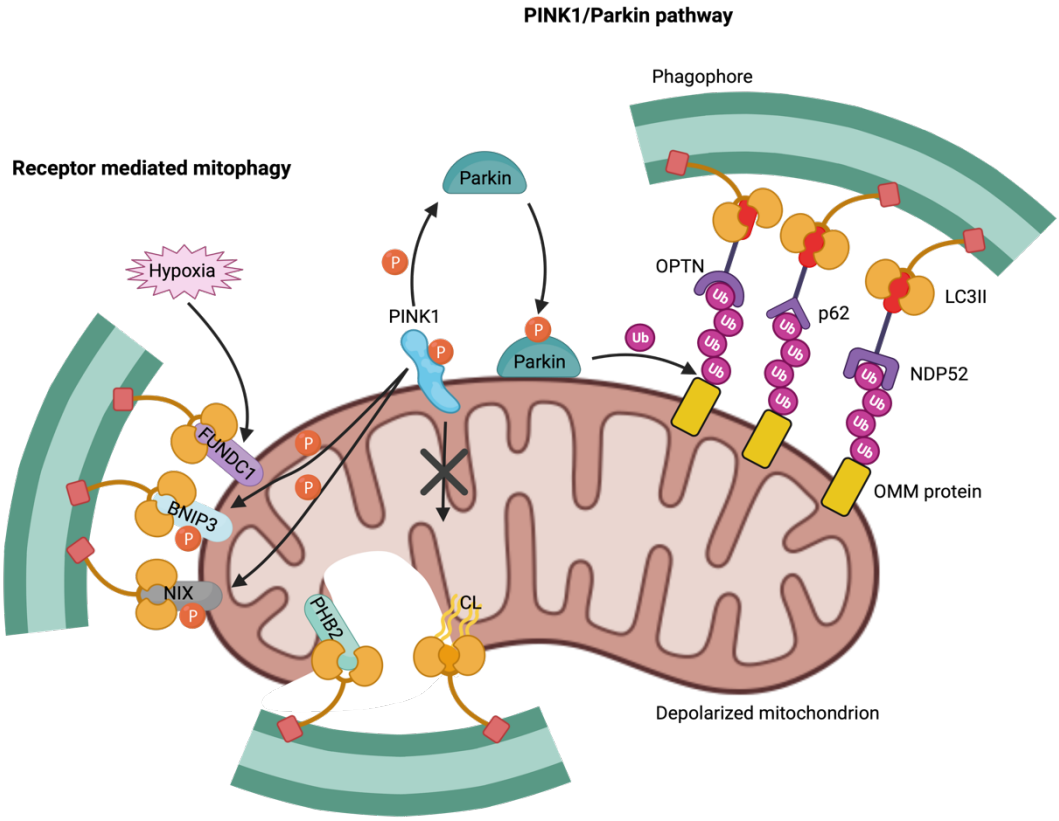

Figure 10 PINK1/Parkin and mitophagy receptor mediated mitophagy

2.3.1.2.2 Receptor mediated mitophagy

The OMM proteins NIP3-like protein X (NIX), BNIP3, FUN14 domain-containing protein 1 (FUNDC1), FK506-binding protein 8 (FKBP8) and IMM protein proinhibitin 2 (PHB2) as well as cardiolipin are mitophagy receptors that trigger mitophagy in response to various stimuli[59–62]. The mechanism of receptor mediated mitophagy is illustrated in Figure 10.

OMM proteins NIX and BNIP3 are members of the pro-apoptotic BCL2 family carrying LIR motifs which allow them to tether mitochondria to phagophores via LC3II. Interestingly, the NIX/BNIP3 and PINK1/Parkin pathway act synergistically to promote mitophagy. Phosphorylation of BNIP3 and NIX by parkin promotes their association with LC3II, whereas NIX and BNIP3 help translocate parkin to mitochondria. Where in turn NIX is ubiquitinated by parkin and recognized by autophagy adaptors that promote mitophagy along the PINK1/Parkin pathway. In addition, BNIP3 disrupts mitochondrial

dynamics by degradation of OPA1 while recruiting DRP1 to the mitochondrial surface, resulting in organelles sized to undergo mitophagy.

FUNDC1 is involved in hypoxia induced mitophagy. Under normoxic conditions, FUNDC1 is phosphorylated which suppresses the activity of its LIR motif and in turn mitophagy. During hypoxia, the mitochondrial phosphatase PGAM5 dephosphorylates FUNDC1 activating its LIR motif which binds to LC3II. Dephosphorylation of FUNDC1, similar to BNIP3, recruits DRP1 and promotes mitochondrial fragmentation. Consequently, FUNDC1 promotes mitophagy in two ways: by fragmentation of mitochondria and tethering fragmented mitochondria to the phagophore. FUNDC1 is also a substrate of ULK1 which phosphorylates FUNDC1 to promote mitophagy.

FKBP8 is a novel mitophagy receptor of the OMM which interacts with LC3II via its LIR motif to initiate mitochondrial degradation.

As mentioned, not only proteins of the OMM function as mitophagy receptors, but also proteins and lipids from inside mitochondria. One of them is PHB2, an IMM protein that has been identified as a putative mitophagy receptor under stress conditions. Upon disruption of the OMM, PHB2 interacts with LC3II via its LIR motif, leading to the formation of phagophores and subsequent elimination of dysfunctional mitochondria. Similar to autophagy receptors located on the OMM cytoplasmic PHB2 also stabilizes PINK1 on the OMM and promotes mitochondrial recruitment of parkin. Cardiolipin, a mitochondrial phospholipid of the IMM, is also externalized to the OMM upon mitochondrial fragmentation, where it binds to LC3II labeling damaged mitochondria for mitophagy.

2.4 Alzheimer's disease

2.4.1 Epidemiology

The world population ages year by year thanks to advances in medicine and healthcare. According to the World Health Organization (WHO), the global average life expectancy increased by more than 6 years, from 66.8 years in 2000 to 73.4 years in 2019[63]. In first world countries, life expectancy is even higher. German citizens born in 2019 will reach an average age of 81.7 years. As a result, the incidence of dementia will also increase dramatically.

Dementia is an umbrella term for various diseases that progressively impair memory function, other cognitive abilities and behavior. Currently, more than 55 million people worldwide suffer from dementia, a number that is expected to increase to 78 million by 2030 and to 139 million by 2050. Among them, Alzheimer's disease is the most common form, contributing to 60-70 % of dementia cases[64]. Every year about 9.9 million people worldwide develop dementia, which equals a new case every three seconds. The prevalence of AD in the European Union was estimated at 5.05 % in 2017, rising sharply among the elderly[65]. Dementia has physical, psychological, social and economic implications, not only for those affected, but also for their caretakers, families and society in general. In 2019, the estimated total cost of dementia worldwide was $1.3 trillion and is expected to soar to over $2.8 trillion by 2030 as both the number of individuals with dementia and the cost of healthcare will increase[64]. Although dementia related deaths are difficult to identify, dementia is currently the seventh leading cause of death among all diseases and one of the leading causes of disability and need for care among the elderly worldwide. On average, patients die four to eight years after the diagnosis of AD, commonly in association with aspiration pneumonia[66]. Given the heavy burden on patients and society, its rapid progression, the lack of adequate diagnostics and treatment options, the WHO considers dementia a public health priority. Therefore, the WHO launched the *"Global action plan on the public health response to dementia 2017-2025"* in May 2017. The action plan represents a comprehensive approach designed to improve the lives of patients, their caretakers and families while reducing the impact of dementia on communities and countries[67].

2.4.2 Forms of dementia

Citing the International Statistical Classification of Diseases and Related Health Problems, 11. Revision (ICD 11) Version 2022, dementia is an “acquired brain syndrome characterized by a decline from a previous level of cognitive functioning. Memory impairment is present in most forms of dementia, but cognitive impairment is not restricted to memory (i.e., there is impairment in other areas such as executive functions, attention, language, social cognition and judgment, psychomotor speed, visuoperceptual or visuospatial abilities). The cognitive impairment is not attributable to normal aging and significantly interferes with independence in the person’s performance of activities of daily living. The symptoms are not better accounted for by disturbance of consciousness, altered mental status, Delirium, Substance Intoxication, Substance Withdrawal, or another Mental, Behavioral, or Neurodevelopmental

Disorder (e.g., Schizophrenia or Other Primary Psychotic Disorder, a Depressive Disorder). Based on available evidence, the cognitive impairment is attributed or assumed to be attributable to a neurological or medical condition that affects the brain, trauma, nutritional deficiency, chronic use of specific substances or medications, or exposure to heavy metals or other toxins"[68]. According to the German S3 guideline on dementia from 2016, which refers to the ICD 10, symptoms of dementia must be present for at least 6 months to be classified as dementia. Different forms of dementia are distinguished according to etiology, with AD and vascular dementia being the most common ones. Also mixed forms of different dementias exist, making it more difficult to diagnose a specific form of dementia.

AD the most common form of dementia accounts for 60-70 % of diagnosed dementias. Pathological hallmarks of AD are the accumulation of amyloid beta (Aβ) plaques outside neurons and hyperphosphorylated tau tangles inside of neurons. AD can be divided into early-onset or familial AD (FAD) and late-onset AD (LOAD). Unlike LOAD, FAD accounts for only a minority of AD cases worldwide (1-5.5 %) and onsets before the age of 65 leading to an early death. FAD is the result of dominant gene mutations involving proteins of the Aβ metabolism, resulting in excess of Aβ. Mutated genes include those encoding the amyloid precursor protein (APP), presenilin (PSN) 1 and PSN2[69–71]. LOAD is the most common form of AD which develops after the age of 65. Among the risk factors for LOAD are age, apolipoprotein E4 (APOE4), mitochondrial dysfunction and variety of other factors[71]. Of the LOAD risk factors mentioned, age is the major one.

The second most common form of dementia is vascular dementia. Vascular dementia is the manifestation of cerebrovascular diseases, characterized by poor blood circulation leading to inadequate oxygen and nutrient supply in brains, harming neurons and brain tissue[66,72,73]. Examples of cerebrovascular diseases are atherosclerosis and stroke. Vascular dementia accounts for only 5-10 % of total dementia cases worldwide, but its prevalence is significantly higher when mixed pathologies are taken into account, as most dementia patients exhibit cerebrovascular diseases along with AD hallmarks[66].

As mentioned in the ICD 11, secondary dementias also exist. These are often related to nutritional deficiencies, chronic use of certain substances or medications and exposure to heavy metals or other toxins[68].

2.4.3 Diagnostics of AD

If a person experiences cognitive impairment along with neuronal impairments such as attention and language deficits or personality changes over a period of at least 6 months, he or she may have developed dementia. To diagnose dementia and its approximate severity, the Mini-Mental Status Test, the DemTect, the Test for Early Detection of Dementia with Depression Distinction and the Montreal Cognitive Assessment Test are appropriate cognitive tests[74]. The Mini-Mental Status Test provides an early impression on the severity of the dementia present based on the reached score. Once dementia has been diagnosed based on anamnesis and evaluation of cognitive tests, differential diagnosis is performed to determine the type of dementia. Accurate classification of the present dementia is critical for both therapy and assessment of disease progression. During classification of the present dementia AD specific biomarkers Aβ, tau and hyperphosphorylated tau are assessed in cerebrospinal fluid and blood. Quantification of these biomarkers is also used during AD therapy to monitor the therapeutic success and progression of AD[74,75]. During the progression of Alzheimer's disease, Aβ levels in the cerebrospinal fluid decrease, while levels of tau and hyperphosphorylated tau increase compared to patients without AD. Since these changes occur already before the first cognitive manifestations of AD, Aβ and tau could serve as early biomarkers for AD to intervene as early as possible. Besides laboratory diagnostics, brain imaging is also used for the diagnosis of dementia as well as for monitoring therapy efficacy. Positron emission tomography (PET) of Aβ or tau protein tracers are used to diagnose AD and monitor its progression, while SV2A radioligands are used to assess neuronal density and dementia progression[74,75]. Another option to determine whole brain atrophy and atrophy of dementia related brain regions, such as the hippocampus, is magnetic resonance imaging (MRI). MRI is used to monitor both dementia progression and response to therapy, but MRI cannot distinguish between different forms of dementia. According to the World Alzheimer Report 2021, up to 30 % diagnosed with dementia are misdiagnosed, so new improved diagnostic tools are urgently needed[75].

2.4.4 Alzheimer's disease pathophysiology

Alzheimer's disease is a multifactorial CNS disorder characterized by cognitive decline, deficits in multiple neuronal functions and personality changes. Although AD is known for more than 120 years and has been a focus of research for many years, still only theories concerning the development of AD exist without identification of the detrimental causes behind the development of AD. To date, researchers agree that misfolded proteins accumulate in brains of affected individuals, causing inflammation and oxidative damage in neurons ultimately leading to neuronal decline. Histological examinations of postmortem brains from AD patients reveal senile plaques composed of Aβ and neurofibrillary tangles formed by hyperphosphorylated tau. Already Alois Alzheimer discovered and described the presence of these plaques in the brain of Auguste Deter the first described Alzheimer patient[76]. Progression of AD is accompanied by cognitive decline and neuronal death, particularly in the cortex and hippocampus. Shrinkage of these brain areas represents a hallmark of the underlying AD pathophysiology (Figure 11).

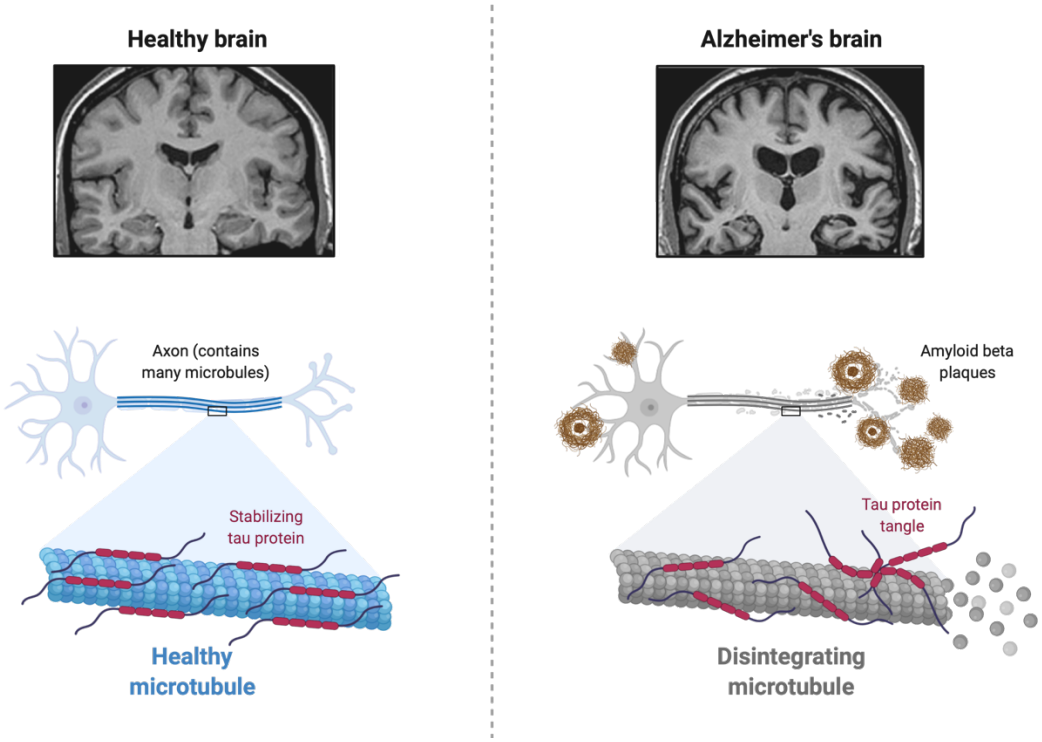

Figure 11 Comparison of healthy brain to AD brain

2.4.4.1 Amyloid beta

As the research on AD progressed scientists focused on Aβ, given the formation of Aβ plaques already at the onset of the disease and their proliferation during exacerbation of AD. In addition, crucial for the postulation of the „Amyloid Cascade Hypothesis" by Hardy & Higgins in 1992 was the discovery that FAD is predominantly caused by mutations in APP processing leading to increased formation of Aβ[77]. In short, the „Amyloid Cascade Hypothesis" postulates that Aβ is the causative agent of AD development and pathology. Nowadays, however, the mood has changed, as pharmacological reduction of Aβ failed in clinical trials[78–80]. Most experts no longer believe that Aβ is the primary cause of AD, but plays an important role in its pathology. Nevertheless in 2021, despite controversy, the first anti-Aβ antibody, aducanumab, was approved by the U.S. Food and Drug Administration (FDA) for the treatment of Alzheimer's disease in the United States[81].

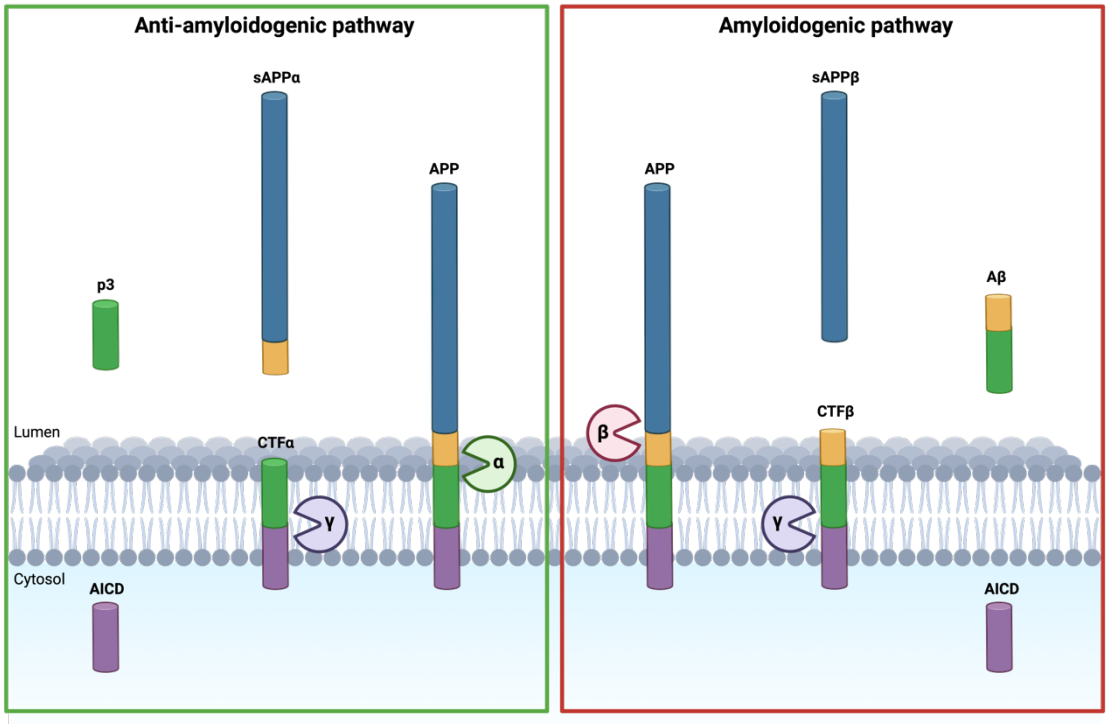

Figure 12 APP processing

Aβ is a natural cleavage product formed during the proteolytic cleavage of APP. APP is a Type I transmembrane protein frequently expressed in mammalian brain which undergoes proteolytic cleavage by α-, β-, and γ-secretases forming a series of

cleavage products. APP processing is distinguished into the amyloidogenic pathway, which leads to the formation of Aβ, and the anti-amyloidogenic pathway, which prevents Aβ formation[82–84]. Both pathways are illustrated in Figure 12.

As the name implies, the anti-amyloidogenic pathway processes APP without the formation of Aβ. Aβ formation is evaded already early in the pathway as α-secretase cuts APP within its Aβ sequence. Cleavage products of α-secretase scission are extracellular soluble APP (sAPP) α and transmembrane carboxy-terminal fragment (CTF) α. CTFα is then cleaved by γ-secretase, yielding p3 and the APP intracellular domain (AICD)[82–84]. In contrast to the anti-amyloidogenic pathway the amyloidogenic pathway produces Aβ. APP is first cut by β-secretase above the Aβ sequence, yielding sAPPβ and transmembrane CTFβ, which still contains the full Aβ sequence. The predominant β-secretase in neurons is the β-site cleaving enzyme 1 (BACE1). Aβ is then released by γ-secretase, which cleaves CTFβ into extracellular Aβ and intracellular AICD. γ-secretase is a protease complex composed of four subunits, including PSN1 and PSN2 within its catalytic domain, crucial for γ-secretase function. This explains why mutations of PSN1 and PSN2 provoke FAD as they cause a sharp increase in Aβ load by improving γ-secretase activity. Depending on where γ-secretase cleaves CTFβ, Aβ can be 36-43 amino acids long. Depending on their size, Aβ forms have different functions. In relation to the pathophysiology of AD, $Aβ_{1-40}$, the most abundant form, and $Aβ_{1-42}$ are of particular relevance. $Aβ_{1-42}$ is considered to be particular harmful and AD promoting, especially when present as soluble oligomers[82–84]. In addition, $Aβ_{1-42}$ oligomers are very aggregation prone as they carry exposed hydrophobic residues which allow them to bind additional monomers and form plaques. Since the APP gene is located on chromosome 21, individuals with trisomy 21 tend to have higher levels of APP and Aβ, which increases their prevalence for AD[85].

2.4.4.1.1 Neurotoxicity of amyloid beta

Although Aβ nowadays is controversially discussed as the causative agent of Alzheimer's disease, its influence on the pathophysiology of AD is undisputed. Intracellular Aβ oligomers, besides hyperphosphorylated tau, trigger a cascade of neurotoxic events ranging from synaptic dysfunction, oxidative stress, mitochondrial dysfunction, hyperphosphorylation of tau up to neuroinflammation[86].

In course of synaptic dysfunction, Aβ impairs synaptic plasticity by suppressing long-term potentiation (LTP) while promoting long-term depression (LTD), leading to impaired learning and memory function in affected individuals[87,88]. Neuronal oxidative stress is induced by Aβ via several pathways. Perhaps the most prominent pathway is the Aβ mediated impairment of the mitochondrial OXPHOS system, which increases leakage of ROS[89]. Furthermore, senile plaques which form during the progression of AD contain, besides Aβ, metal ions such as copper, iron and zinc. These redox active ions catalyze the generation of ROS when bound to Aβ[90]. In addition, Aβ increases intracellular ROS and exacerbates the progression of AD by stimulating microglial activation[91]. Besides, Aβ mediates neurotoxicity by facilitating the neurotoxicity of its partner in crime tau. As such, Aβ facilitates the conversion of tau into its toxic hyperphosphorylated state and accelerates the propagation of neurofibrillary tangles (NFT). Those NFTs later cause neuronal lesions and exacerbate Aβ toxicity in a vicious circle[92–94]. In terms of mitochondrial disruption, Aβ and APP are known to be located in mitochondrial membranes, where they disrupt the import of nuclear encoded mitochondrial proteins and impair mitochondrial functionality. Among mitochondrial impairments associated with Aβ are depolarization, decreased ATP levels, elevated generation of ROS owing to impairment of OXPHOS (Inhibition of complex I and IV) and altered mitochondrial morphology and motility[86,95,96]. AD is a chronic inflammatory disease of the CNS. In postmortem brains of AD patients, clusters of reactive microglia and astrocytes were found migrating to and surrounding Aβ plaques. Brain inflammation is thought to emerge initially as a protective response against dementia, with activated microglia phagocytizing Aβ oligomers. Regarding activated microglia, it should be noted that they exhibit a protective or neurotoxic phenotype depending on the environment. Aβ promotes the neurotoxic phenotype of microglia, which involves the release of cytokines that cause tissue damage and contribute to the development and progression of AD[97–99]. All of the aforementioned Aβ driven noxious mechanisms are considered key factors in neuronal cell loss and the exacerbation of AD.

2.4.4.2 Tau pathology in Alzheimer's disease

Tau the second hallmark of AD is a crucial microtubule associated protein found predominantly in the axons of CNS neurons. Here, tau is responsible for the assembly and stability of microtubules, although secondary functions like binding to enzymes and cellular structures are reported[100–102]. Microtubules are critical for neuronal morphology, and build intracellular highways along which organelles, vesicles and proteins are

carried by motor proteins, as described detailed in section *2.2.4.1 "Mitochondrial Movement System"*. Regulating and stabilizing microtubules, tau influences structural and regulatory functions of and across neurons. Posttranslational phosphorylation of tau is critical for both microtubule stabilization and disintegration observed in tauopathies. Tau must be phosphorylated to attach to microtubules physiologically. However, when tau is additionally phosphorylated at Ser262 and Ser214, it becomes hyperphosphorylated, detaches from microtubules and aggregates to form NFTs[100–102] (Figure 13). Formation of NFTs by hyperphosphorylated tau leads to loss of tau function, disruption of axonal morphology, impaired axonal transport and neuronal decline. All of which known hallmarks of AD and other tauopathies. Lack of microtubule stabilization and axonal transport further contributes to synaptic dysfunction, characterized by impaired synaptic plasticity, which may climax in the development of AD. Tau is also known to impair mitochondria by disruption of OXPHOS, mitochondrial dynamics and mitophagy[103–106]. The resulting mitochondrial dysfunction exacerbates the neurotoxicity of tau further.

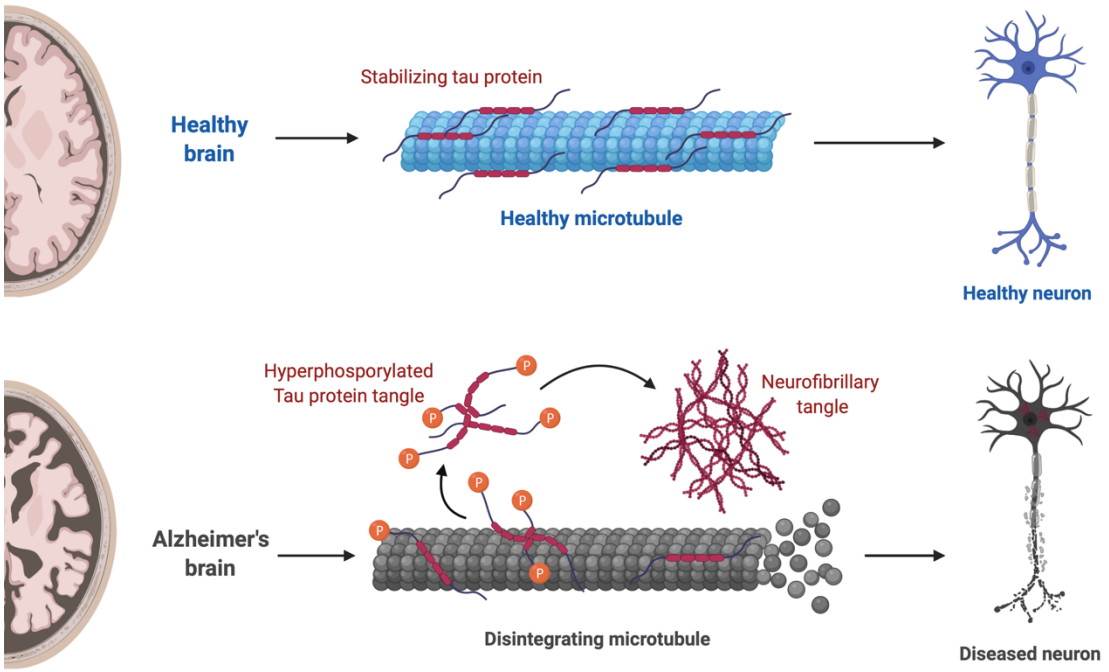

Figure 13 Tau pathology

2.4.4.3 Mitochondrial dysfunction in Alzheimer's disease

Mitochondrial dysfunction associated with decreased ATP levels and increased ROS levels is a common phenotype of aging brains. It is therefore not surprising that mitochondrial dysfunction plays a key role in the pathology of Alzheimer's disease. The hypothesis on mitochondrial dysfunction being the causative agent for the development of AD is today widely spread. Mitochondrial impairment is already present in MCI, the early stage of AD, when Aβ- and tau-aggregations are not yet detectable, and progresses proportionally to the patient's symptoms[107]. Mitochondrial dysfunction has been described in brains[108], fibroblasts and blood cells[109,110] of AD patients, in AD transgenic mouse models, cell lines expressing mutant APP, cells treated with Aβ and cybrid cell lines carrying mtDNA from AD patients[13,111–113]. Mitochondrial dysfunction is characterized by mitochondrial fragmentation, disrupted ATP synthesis, increased oxidative damage, impaired calcium homeostasis and apoptotic processes. The human brain consumes 20 % of the total oxygen consumed daily, although it represents only 2 % of the body weight. The reason is the high energy demand of CNS neurons, which requires high rates of OXPHOS, in turn generating large amounts of ROS in CNS neurons. Due to high ROS burden and low antioxidant protection, the brain is considered to be particularly susceptible to oxidative stress[114,115]. Thus, mitochondrial malfunction induces neuronal damage by energy deficiency along with elevated ROS load exacerbating the pathology of Aβ and tau once AD has developed.

As AD progresses, oxidation of proteins, lipids, ribonucleic acids and whole organelles accelerates, likely fueled by mitochondrial ROS, as mitochondria are the major intracellular source of ROS. It is well known that dysfunction of the OXPHOS system causes electron leakage and increased ROS formation throughout the progression of AD. In this context, most publications agree on an impairment of complex I and IV activity in the development and progression of AD[116]. Mitochondria themselves are the first victims of their own increased ROS production, as ROS target mitochondrial membrane lipids, leading to depolarization of the MMP, while oxidation of ETC complexes further exacerbates ROS formation and toxicity. ROS also account for many mutations within the mitochondrial genome. The mtDNA is highly vulnerable to mutations due to missing histones, reduced DNA repair system capacity and close proximity to sites of ROS generation. Analysis of mtDNA mutations in AD brains revealed a threefold increase in mtDNA mutations linked to oxidation processes compared to age matched controls[117,118]. Mutations of the mitochondrial genome are

particularly severe since mtDNA, despite encoding only for a small fraction of mitochondrial proteins, encodes core subunits of complexes I, III and IV as well as the F_0F_1 ATP synthase, all of which necessary for functioning OXPHOS. Taken together, oxidative stress depolarizes mitochondria, disrupts ETC complexes and mutates mtDNA, causing the synthesis of dysfunctional ETC proteins. These ROS mediated mitochondrial dysfunctions ultimately lead to an amplification of cellular ROS, insufficient energy supply and apoptosis of the affected neurons - a vicious circle.

That ROS derived from inhibition of complex I also trigger amyloidogenic APP processing in vitro and in vivo has been previously shown by our group. In HEK-293 cells, SH-SY5Y cells and two AD mouse models, $A\beta_{1-40}$ levels increased significantly upon complex I disruption[96,119]. Increased Aβ expression triggered by mitochondrial ROS seems to be the result of amplified APP processing by upregulated BACE1 and γ-secretase activity[120]. Based on the findings of Leuner et al. (2012) and since, as already mentioned in section *2.4.4.1. "Neurotoxicity of amyloid beta"*, Aβ likewise impairs mitochondria, Leuner and colleagues proposed that starting from mitochondrial dysfunction a vicious circle is triggered that contributes to the pathogenesis of LOAD[96]. Tau is neither a saint when it comes to mitochondrial dysfunction. P301L tau mice overexpressing the human P301L tau mutant exhibit dysfunctional mitochondria characterized by impaired complex I activity, mitochondrial respiration, ATP synthesis, and decreased expression of antioxidant enzymes[116,121].

Furthermore, mitochondria are important for intracellular calcium homeostasis. Accordingly, impaired calcium buffering capacity of dysfunctional mitochondria causes calcium dyshomeostasis. Given the role of calcium in proper synaptic functioning and induction of apoptosis, mitochondria may as well contribute to AD by disrupting intracellular calcium homeostasis[122,123].

In contrast to age matched controls, neurons of AD subjects are characterized by significantly higher numbers of abnormal and damaged mitochondria. Phenotypically, these aberrant mitochondria are characterized by reduced mitochondrial length along with a rounder and swollen morphology, which has also been demonstrated in various AD cell lines and animal models[124–126]. Mitochondrial fragmentation in AD is attributable to an increased fission rate and alterations in the expression of mitochondrial fission and fusion proteins including DRP1, OPA1 and MFN1/2[124,127]. Both Aβ and

hyperphosphorylated tau induce mitochondrial fragmentation, presumably by interacting with DRP1, which has been coimmunoprecipitated with APP and Aβ oligomers[128].

As explained in section *2.2.2.2 "Induction of apoptosis – Intrinsic pathway"*, mitochondria are the major regulators of the intrinsic apoptotic pathway. Thus, damage to mitochondria can trigger apoptosis of neurons. Opening of the mitochondrial permeability transition pore (mPTP) is one mechanism that initiates a sudden increase in mitochondrial membrane permeability, resulting in uncoupling of the OXPHOS system, swelling of the mitochondrial matrix, loss of MMP, increased ROS production and release of proapoptotic proteins (cytochrome c and DIABLO). In respect to AD, the formation and opening of mPTP can be triggered by an interaction of $A\beta_{1-42}$ with cyclophilin D[129].

It is obvious that Aβ pathology, tau pathology and mitochondrial dysfunction are intertwined in the pathology of AD given their interaction with each other. In general, all three pathologic hallmarks of AD reinforce each other's pathology triggering multiple viscous circles. To date, it remains uncertain which of the three, or perhaps a different cause, is the trigger for the onset of AD. The only certainty is that Aβ, tau and mitochondrial dysfunction play major roles in the pathogenesis and progression of AD.

2.4.5 Therapy of Alzheimer's disease

Therapy of dementia, including Alzheimer's disease, involves pharmacotherapy and psychosocial interventions for those affected including their relatives. Given the variability of symptoms and challenges, therapy must always be tailored to the individual patient and adapted to the severity of the disease[74]. None of the pharmacological treatments (drugs) currently approved in Germany are considered disease modifying as they only treat symptoms. This means they neither alter the course of Alzheimer's disease nor reverse or slow its progression.

2.4.5.1 Registered AD pharmacotherapies (European Union and USA)

2.4.5.1.1 Acetylcholinesterase inhibitors

The equilibrium and fine tuning of different neurotransmitter systems such as acetylcholine, noradrenalin, dopamine, γ-aminobutyric acid (GABA), serotonin and

glutamate is necessary for proper brain function. During the progression of AD, loss of cholinergic neurons, among other types of neurons, disrupts balanced neurotransmission in affected brains. Although the cholinergic system is not the only neurotransmitter system affected, a deficient cholinergic neurotransmission is involved in the pathophysiology of learning and memory impairment occurring in AD. To counteract the reduced cholinergic neurotransmission, acetylcholinesterase inhibitors are nowadays used for symptomatic treatment of AD. Inhibition of acetylcholinesterase prevents the breakdown of acetylcholine in the synaptic cleft, which prolongs the effect acetylcholine in the brain. In the European Union and the United States, acetylcholinesterase inhibitors donepezil, galantamine and rivastigmine are approved and indicated for the treatment of mild to moderate Alzheimer's disease over a period of 24 weeks[66,74,130].

The German Institut für Qualität und Wirtschaftlichkeit im Gesundheitswesen (Institute for Quality and Efficiency in Health Care) (IQWiG) confirms patient related benefits in mild to moderate AD on everyday life and cognitive performance during 24 weeks of use. Interestingly no clear evidence on the optimal duration of acetylcholinesterase inhibitor therapy exists, as the majority of clinical trials were limited to 6 months. Therefore, discontinuation of drug treatment based on the 24 week criterion is not reasonable according to the German S3 guideline on dementia[74,130].

2.4.5.1.2 Memantine

The N-methyl-D-aspartate (NMDA) receptor antagonist memantine is approved in the European Union and the United States for the treatment of moderate to severe Alzheimer's disease. Memantine shows no effects on mild forms of AD. By antagonizing the NMDA glutamate receptor, memantine protects neurons from NMDA overstimulation, occurring in AD and the consequent glutamate and calcium mediated neurotoxicity. The efficacy of memantine is controversial. Even various analyses by the IQWiG led to divergent conclusions. Ultimately, the IQWiG confirmed patient related benefits primarily related to cognition and minor to activities of daily living and mental or behavioral disorders[74,131]. Treatment of moderate to severe Alzheimer's disease with memantine is recommended.

2.4.5.1.3 Ginkgo Biloba (EGb 761)

In the German S3 guideline on dementia, Ginkgo Biloba, more precisely the EGb 761 extract, is recommended for the symptomatic treatment of cognitive disorders up to dementia[74]. EGb 761 is a standardized dry extract of Ginkgo Biloba leaves quantified for flavonoid glycosides and terpene lactones, including ginkgolides and bilobalide[132]. EGb 761 exhibits neuroprotective effects related to improved oxygen and nutrient supply to the brain by increasing cerebral blood flow, reducing ROS induced brain damage and preserving mitochondrial function[132–134]. In particular, the antioxidant effects of EGb 761 by scavenging ROS through flavonoids and stabilizing mitochondria seem to account for its neuroprotective effects in the treatment of dementias. Based on the heterogeneity of the data, the IQWiG concludes that only a high dose therapy at 240 mg EGb 761 daily improves cognitive function and increases activities of daily living. For low dosage treatment (120 mg daily), no conclusive statement of benefit could be made[74].

2.4.5.1.4 Aducanumab (Amyloid beta directed antibody)

In June 2021, despite some controversy, the FDA approved aducanumab for the treatment of MCI and mild stages of Alzheimer's disease. The Aβ monoclonal antibody aducanumab is the first approved drug with a putative disease modifying mechanism. The antibody specifically targets Aβ and helps eliminate Aβ burden in the AD brain to delay disease progression. Controversy surrounds aducanumab not only because it is the first registered Aβ targeted drug therapy after a series of failures, but also since, similar to its predecessors, clinical trial outcomes were inconclusive. Although aducanumab proved to lower the Aβ load in brains of study participants, the correlation between the reduction and clinical improvements could not be clearly demonstrated as the results of the two main studies were conflicting and overall did not prove that aducanumab was effective in treating early AD[135]. In addition, uncertainties arose regarding the safety of aducanumab as images of brain scans in some patients showed abnormalities indicating swelling or hemorrhage which could potentially cause harm. Due to conflicting study results and potential safety issues, the European Medicines Agency recommended in December 2021 to refuse the marketing authorization of aducanumab in the European Union[136].

2.4.5.2 Alternative or not registered pharmacotherapies for AD treatment

2.4.5.2.1 Piracetam

Piracetam is a cyclic GABA derivative which belongs to the class of nootropics. Although piracetam is a derivative of GABA, its mechanism of action does not appear to be related to GABA, although its exact mode of action still remains unknown. Growing evidence suggests that piracetam increases or restores cell membrane fluidity, regardless of cell type and especially when normal membrane fluidity is disturbed, for instance in aging or AD. In this context, piracetam is known to affect neuronal, vascular and mitochondrial function, perhaps in correlation with its effect on membrane fluidity[137].

In Germany, piracetam is approved for the symptomatic treatment of chronic cognitive impairment in primary degenerative dementia, for the adjunctive treatment of chronic sequelae of stroke, for the adjunctive treatment of myoclonus syndromes of cortical origin, for the adjunctive post concussion treatment and for the adjunctive treatment of dyslexia in children[138]. However, the current German S3 guideline on dementia does not recommend treatment of dementia with piracetam since the underlying studies are of poor quality and from heterogeneous patient groups, thus lacking proof of efficacy according to the authors[74].

The procognitive effects of piracetam may account to its modulation of neurotransmission and improvement of neuroplasticity, associated with learning and memory performance. In addition, Piracetam shows neuroprotective and anticonvulsive effects. Concerning the vascular system, piracetam decreases coagulation, improves cerebral blood flow and facilitates movement of erythrocytes through the circuit[137]. Furthermore, it is known for a long time that piracetam enhances glucose uptake and utilization as well as ATP production, pointing towards effects on mitochondria[139]. Based on these observations and since piracetam improves membrane fluidity mitochondria moved into focus as potential targets of piracetam. As suspected, piracetam exerts beneficial effects on mitochondria even in AD cell models, as evidenced by increased MMP, ATP levels and mitochondrial elongation, perhaps by increasing mitochondrial membrane fluidity[140–144]. Interestingly, in addition to parameters directly related to mitochondrial function, neurite growth improved and Aβ levels reduced in cells and AD transgenic animals[142]. The procognitive effects of piracetam seem to be the result of modulated neurotransmission, enhanced

neuroplasticity and increased cerebral blood flow. However, they could also be related to the influence of piracetam on mitochondria, which would reinforce the role of mitochondria in the development and progression of AD.

2.4.5.2.2 Levetiracetam

As explained in section *2.1.3 "SV2A ligands"*, levetiracetam, the ethyl analogue of piracetam, is a prescription drug for the treatment of epilepsy that differs from classic anticonvulsants in its target (SV2A) and mode of action. In preclinical studies LEV showed strong anticonvulsant effects in both epilepsy mouse models and patients, but failed conventional tests for antiepileptic drugs, revealing its unique mode of action[18]. Besides epilepsy, the therapeutic use of levetiracetam is also being discussed in neurodegenerative diseases such as AD.

The hypothesis of LEV targeting AD originally arose from its structural similarity to piracetam, a drug approved for the treatment of dementia, despite marked differences in their pharmacologic profiles. Furthermore, since MCI patients are characterized by increased hippocampal activity, which also occurs in carriers of FAD mutations and in patients at risk of LOAD before the onset of AD symptoms[145–147]. In contrast, patients with late MCI and early AD display lower hippocampal activity. Recent Ca^{2+} imaging and patch clamp data of McGill R-Thy1 APP rats published by Sosulina et al. (2021) demonstrate that CA1 pyramidal neurons are responsible for the hippocampal hyperactivity at the onset of AD[148]. Furthermore, epileptic seizures are known to occur more frequently in AD patients, again emphasizing the importance of neuronal hyperactivity in the development of AD. Using a human APP expressing mouse model, Sanchez et al. (2012) demonstrated that the occurring aberrant network activity can be effectively suppressed by LEV thereby reversing cognitive decline[20]. Clinical data supported the data of Sanchez et al. (2012) demonstrating efficacy of levetiracetam in suppressing aberrant CNS activity in patients with MCI or LOAD in association with improved cognitive functions[21,22,149]. Increased neuronal activity prior to the onset of AD appears to promote and accelerate AD progression rather than being a protective mechanism. Otherwise, suppression of hippocampal hyperactivity by early intervention with antiepileptic drugs would not improve cognitive function. Thus, early suppression of neuronal hyperactivity appears to be another tool to combat AD.

Given its structural similarity to piracetam and piracetam's protective effects on mitochondria, researchers started to investigate whether LEV exerts effects on mitochondria, perhaps accounting for the described neuroprotection and enhancement of cognition in AD. LEV was found to exert protective effects on mitochondria increasing MMP, ATP levels and mitochondrial size in healthy cells, AD cell models and cells treated with mitochondrial stressors[13,25]. Therefore, effects on mitochondria may contribute to the effects of LEV described in epilepsy and AD, especially considering that, according to the mitochondrial cascade theory, mitochondrial deterioration may be the trigger for the development of AD. In addition, the role of mitochondria in epilepsy receives growing attention.

3 OBJECTIVES OF THIS SCIENTIFIC WORK

Even 120 years after the first encounter of Alois Alzheimer and Auguste Deter, which is generally regarded as the starting point of Alzheimer's disease research, neither a successful therapy nor the primary cause for the development and progression of Morbus Alzheimer have been discovered. For many years, Aβ was considered the detrimental cause of AD. Consequently, Aβ became the focus of research to slow down and stop the progression of AD. However, in clinical trials, pharmacological reduction of Aβ failed to achieve the desired outcome[78–80]. In this context, it is surprising that in 2021, the first anti-Aβ antibody, aducanumab, was approved by the FDA for the treatment of AD in the United States[81]. Nevertheless, given the general failure of Aβ targeted therapies, it has become widely accepted that AD must be considered in a broader context beyond Aβ and tau. A milestone for new approaches in AD research marked the mitochondrial cascade hypothesis proposed by Swerdlow and Khan in 2004[150]. The mitochondrial cascade hypothesis places the mitochondrion at the center of AD pathogenesis and proposes that at the onset of AD mitochondrial dysfunction triggers neuronal damage by increased ROS levels and energy deprivation in neuronal cells. As a result, active compounds targeting mitochondria moved into the spotlight of AD pharmacotherapy. One of the first compounds known for its procognitive effects tested on mitochondria was piracetam. Piracetam showed positive effects on mitochondrial function, such as elevated MMP, ATP levels and mitochondrial dynamics, even in AD cell models[141–144]. Given the procognitive and mitochondrial effects of piracetam as well as neuronal hyperactivity occurring early in the development of AD, levetiracetam, a piracetam derivative approved for the treatment of epilepsy, was investigated in AD. LEV was found to ameliorate molecular abnormalities and reverse cognitive decline in AD mouse models, which was supported by clinical data demonstrating enhanced cognition in patients with MCI or LOAD[20,21,23]. Moreover, LEV treatment of healthy cells, AD model cells and cells treated with mitochondrial stressors demonstrated similar effects on mitochondria as piracetam (increase in MMP, ATP levels and mitochondrial dynamics)[13]. These results raised the question of how LEV acts on mitochondria when its target SV2A is a synaptic vesicle protein? The likely hypothesis is that SV2A is expressed in both mitochondria and synaptic vesicles. To address this question, Stockburger et al. (2016) already demonstrated that SV2A is expressed in isolated mitochondria.

Based on these findings, the aim of this scientific work was to investigate, first, if SV2A is a mitochondrial protein, second, if it is a mitochondrial protein, where exactly SV2A is located in the mitochondrion, third, how SV2A and levetiracetam mediate their effects on mitochondrial morphology, and fourth, to identify other mitochondria or cellular functions regulated by SV2A and LEV.

4 MATERIALS AND METHODS

4.1 Materials

4.1.1 Instruments

Table 2 Instruments

Instrument	Manufacturer
ACCU-jet pro	Brand
AG245 Analytic Balance	Mettler Toledo
Biowave S2100 UV/Vis Diode Array Spectrophotometer	WPA
Coulter Counter	Beckman Coulter
Digital dual timer C5080	TFA Dostmann
Direct-Q® 3UV	Merck Millipore
EZ-Vac Vacuum Manifold	Zymo Research
Fom/B50 Autoclave	Fedegari Autoclavi
Fusion Pulse TS	Vilber
Heracell CO_2 Incubator	Heraeus Instruments
IKAMAG™ RET	IKA-Werke GmbH
Labofuge 400R Centrifuge	Heraeus Instruments
LaminAir HB 2448	Heraeus Instruments
Liebherr MediLine	Liebherr
MaxQ™ 4000 Benchtop Orbital Shaker	Thermo Fisher Scientific
Miele professional PG 8583	Miele
Mini Star Microcentrifuge	VWR
NanoDrop One	Thermo Fisher Scientific
PB3002 DeltaRange	Mettler Toledo
pHenomenal pH 1100L	VWR
PIPETMAN Classic (P20, P100, P200, P1000)	Gilson
Potter S	B. Braun Biotech International
PowerPac™ HC Power Supply	Bio-Rad Laboratories

QuantStudio 5 Real-Time PCR	Thermo Fisher Scientific
Rocking Platform	VWR
Rotary Microtom RM2255	Leica
SR GSDIM Super-Resolution Microscope	Leica
TCS SP5 Confocal Microscope	Leica
Tissue embedding center EG1150	Leica
Tissue processor TP1020	Leica
UNIVERSAL 320R centrifuge	Andreas Hettich GmbH
Visitron Spinning Disc Microscope	Visitron
Vortex-Genie 2	Scientific Industries
Water bath type 3044	Koettermann
Water Bath WNB 22	Memmert

4.1.2 Computer software

Table 3 Computer software for data analysis

Software	Publisher
FIJI (Version: 2.3.0/1.53f)	Open Source
Just Another Colocalization Plugin (JACoP)	Cordelieres, Bolte
MATLAB, R2018b V5 with Toolboxes	The MathWorks
Microsoft Excel (Version: 16.57)	Microsoft
GraphPad Prism (Version: 9.2.0)	GraphPad Software
ThunderSTORM	Ovesný, Křížek, Borkovec, Švindrych, Hagen

Table 4 Computer software for writing the dissertation

Software	Publisher
Mendeley Desktop (Version: 1.19.8)	Mendeley Ltd.
Microsoft Word (Version: 16.57)	Microsoft

Table 5 Computer software for the creation of figures

Software	Publisher
BioRender	Science Suite Inc
Microsoft PowerPoint (Version: 16.57)	Microsoft

4.1.3 Materials

Table 6 Materials

Material	Manufacturer
10 ml Gilson-Style Graduated Macro Tip	Starlab
Adhesion slides SuperFrost Plus	Thermo Fisher Scientific
Beakers in different sizes	Simax
Buffer Tank and Lid	Bio-Rad Laboratories
CELLSTAR® Cell Culture Dishes (60/15 mm, 100/20 mm)	Greiner Bio One
CELLSTAR® Tubes (15 ml, 50 ml)	Greiner Bio One
Cell Scraper 28 cm	Greiner Bio One
Coverslips Ø 24 mm	Paul Marienfeld GmbH & Co. KG
Duran Bottles (2 L, 1 L, 500 ml, 250 ml, 100 ml)	Schott
Fiber Pads	Bio-Rad Laboratories
Gel blotting sheets GB003	GE Healthcare
Gel Releasers	Bio-Rad Laboratories
KIMTECH Science Tissues	Kimberly-Clark
Latex gloves	VWR
Microtube (0.5 ml, 1.5 ml, 2 ml)	Sarstedt
Mini Cell Buffer Dams	Bio-Rad Laboratories
Mini Gel Holder Cassette	Bio-Rad Laboratories
Mini-PROTEAN Casting Stand	Bio-Rad Laboratories
Mini-PROTEAN Clamps	Bio-Rad Laboratories
Mini-PROTEAN Comb (10-well, 15-well)	Bio-Rad Laboratories

Mini-PROTEAN Tetra Electrode Assembly	Bio-Rad Laboratories
Mini-PROTEAN Short Plates	Bio-Rad Laboratories
Mini-PROTEAN Spacer Plates	Bio-Rad Laboratories
Nalgene Dewar flask	Thermo Fisher Scientific
Polycarbonate Baffled Culture Flasks	Thermo Fisher Scientific
Nitrile gloves	VWR
Nunc EasYFlask Cell Culture Flasks (25 cm^2, 75 cm^2, 175 cm^2)	Thermo Fisher Scientific
µ-Dish 35 mm, high Glass Bottom	Ibidi
Parafilm M	Pechiney Plastic Packaging
Pipette Tips (10 µl, 20 µl, 200 µl, 1000 µl)	Sarstedt
PVDF Transfer Membrane, 0.2 µm	Thermo Fisher Scientific
Roller	Bio-Rad Laboratories
SafeSeal Tips Premium 1000 µl sterile	Biozym Scientific
Sterilization tape for autoclaves	A. Hartenstein
SuperFrost Microscope Slides	Thermo Fisher Scientific
Super PAP Pen	Daido Sangyo
Serological Pipette (2 ml, 5 ml, 10 ml, 25 ml)	Sarstedt
TC-Plate 6 Well	Sarstedt
Tetra Cooling Unit	Bio-Rad Laboratories
TipOne Tips (20 µl, 200 µl), sterile	Starlab
Tissue embedding cassettes	Kartell Spa
Volumetric flask 100 ml	Simax

4.1.4 Reagents, kits & media

Table 7 Reagents, kits & media

Reagents; kits; media	Manufacturer
0.05 % Trypsin-EDTA	Thermo Fisher Scientific
Albumin Fraction V, protease-free	Carl Roth

Amersham ECL Prime Western Blotting Detection Reagent	GE Healthcare
Bacto Agar	Becton Dickinson
Bacto Tryptone	Becton Dickinson
BLOCK-iT Alexa Fluor Red Fluorescent Control	Thermo Fisher Scientific
COULTER ISOTON II Diluent	Beckman Coulter
Digitonin 5 % solution	Thermo Fisher Scientific
DMEM, high glucose, GlutaMAX	Thermo Fisher Scientific
DMEM, high glucose, no glutamine, no phenol red	Thermo Fisher Scientific
EBSS, calcium, magnesium, phenol red	Thermo Fisher Scientific
Effectene Transfection Reagent	QIAGEN
GenElute HP Plasmid Midiprep Kit	Sigma-Aldrich
GlutaMAX Supplement (100x)	Thermo Fisher Scientific
High-Capacity cDNA Reverse Transcription Kit	Thermo Fisher Scientific
Hygromycin B (50 mg/ml)	Thermo Fisher Scientific
Fetal bovine serum	Thermo Fisher Scientific
Lipofectamine RNAiMAX	Thermo Fisher Scientific
LysoTracker Red DND-99	Thermo Fisher Scientific
MassRuler DNA Ladder Mix	Thermo Fisher Scientific
MEM Non-Essential Amino Acids Solution (100x)	Thermo Fisher Scientific
MEM Vitamin Solution (100x)	Thermo Fisher Scientific
Mini Protease Inhibitor Cocktail	Roche
MitoTracker Deep Red FM	Thermo Fisher Scientific
Nuclease-Free Water	Life Technologies
Penicillin-Streptomycin (10,000 U/mL)	Thermo Fisher Scientific
Pierce BCA Protein Assay Kit	Thermo Fisher Scientific
Proteinase K (20 mg/ml)	Thermo Fisher Scientific
Protein Assay Dye Reagent	Bio-Rad Laboratories

ProLong Glass Antifade Mountant with NucBlue	Thermo Fisher Scientific
RNaseZap	Thermo Fisher Scientific
ROTILoad 1 (4x)	Carl Roth
Rotiphorese®Gel 30 (37,5:1)	Carl Roth
ROTIZol RNA	Carl Roth
Sodium Pyruvate (100 mM)	Thermo Fisher Scientific
TaqMan™ Fast Advanced Master Mix	Thermo Fisher Scientific
Technical Buffer (pH 10, 7, 4.01, 2)	Xylem Analytics Germany
Yeast extract BioChemica	AppliChem

4.1.5 Chemicals

Table 8 Chemicals

Chemical	Manufacturer
2-Mercaptoethanol	Sigma-Aldrich
2-Propanol	Sigma-Aldrich
3-(N-Morpholino)-propane sulphonic acid (MOPS) ≥99.5 %	Carl Roth
Ammonium persulfate (APS)	Thermo Fisher Scientific
Bafilomycin A1	Enzo Life Science
Calcium chloride dihydrate ≥99 %, Ph. Eur., USP	Carl Roth
Carbonyl cyanide 3-chlorophenylhydrazone (CCCP)	Sigma-Aldrich
Chloroform ≥99.5 %	Sigma-Aldrich
D-Sorbitol ≥98 %	Carl Roth
di-Sodium hydrogen phosphate dihydrate ≥99.5 %	Carl Roth
Dimethyl sulfoxide (DMSO) ≥99.8 %	Carl Roth
Ethanol ≥99 %	Fisher Chemical
Ethanol ≥99.5 %, Ph.Eur., extra pure	Carl Roth
Ethylenediamine tetraacetic acid (EDTA) disodium salt dihydrate ≥99 %	Carl Roth

Ethylene glycol bis(β-aminoethylether) tetraacetic acid (EGTA)	Carl Roth
Glycine ≥99 %	Carl Roth
Hydrogen peroxide 30 %	Sigma-Aldrich
Hydrochloric acid 37 %	VWR Chemicals
Kanamycin sulfate	Sigma-Aldrich
Levetiracetam	Sigma-Aldrich
Magnesium chloride hexahydrate ≥99 %	Carl Roth
Methanol ≥99.9 %	Fisher Chemical
N-2-Hydroxyethylpiperazine-N'-2-ethane sulphonic acid (HEPES) ≥99.5 %	Carl Roth
Paraformaldehyde (PFA)	Carl Roth
Phenylmethyl sulphonyl fluoride (PMSF) ≥99 %	Carl Roth
Polyethylene glycol alkylphenyl ether (Triton-X 100)	Carl Roth
Potassium chloride (KCl) ≥99,5 %	Carl Roth
Potassium dihydrogen phosphate	Merck
Rotenone	Sigma-Aldrich
Sodium chloride (NaCl)	VWR Chemicals
Sodium dihydrogen phosphate monohydrate ≥98 %	Carl Roth
Sodium dodecyl sulfate (SDS)	Carl Roth
Sodium hydroxide (NaOH) pellets	Carl Roth
Sucrose	Grüssing
TEMED ≥99 %	Carl Roth
Trichloroacetic acid ≥99 %, Ph.Eur	Carl Roth
Polysorbate 20 (Tween 20)	Carl Roth
Tris-(hydroxymethyl)-amino methane ≥99,9 % (TRIS)	Carl Roth
TRIS hydrochloride	SERVA Electrophoresis

4.1.6 Antibodies

Table 9 Primary antibodies

Antibody	Dilution	Catalog no.	Manufacturer
Rabbit monoclonal **Anti-Adenylate kinase 2**	WB: 1:2500	MA5-29016	Thermo Fisher Scientific
Mouse monoclonal **Anti-α-tubulin**	WB: 1:5000	ab7291	Abcam
Mouse monoclonal **Anti-β-actin**	WB: 1:2000	A1978	Sigma-Aldrich
Mouse monoclonal **Anti-Citratesynthetase**	WB: 1:1000	SAB2702186	Sigma-Aldrich
Rabbit monoclonal **Anti-DRP1**	ICC: 1:250 SRM: 1:250	ab184247	Abcam
Rabbit monoclonal **Anti-GAPDH**	WB: 1:10000	ab181602	Abcam
Rabbit polyclonal **Anti-LC3II**	WB: 1:500	L7543	Sigma-Aldrich
Rabbit monoclonal **Anti-LC3II**	ICC: 1 µg/ml	ab192890	Abcam
Rabbit polyclonal **Anti-SV2A**	WB: 1:500	ab32942	Abcam
Mouse monoclonal **Anti-SV2A**	ICC: 1:200 SRM: 1:100	119 011	Synaptic Systems
Mouse monoclonal **Anti-TIMM23**	WB: 1:1000	MA5-27384	Thermo Fisher Scientific
Rabbit monoclonal **Anti-TOMM20**	IHC: 1:50 WB: 1:1000	ab186735	Abcam
Rabbit monoclonal **Anti-TOMM20 (Alexa Fluor 647)**	SRM: 1:1000	ab205487	Abcam
Mouse monoclonal **Anti-VAMP2**	SRM: 1:1000	104 211	Synaptic Systems
Rabbit monoclonal **Anti-VAMP2**	ICC: 1:1000	104 008	Synaptic Systems
Camelid monoclonal **Anti-VGlut1 (ATTO 488)**	IHC: 1:250	N1602-At488-L	NanoTag Biotechnologies

Table 10 Secondary antibodies

Antibody	Dilution	Catalog no.	Manufacturer
FluoTag-X2 **Anti-Mouse (ATTO 488)**	SRM: 1:200	N1202-At488-S	NanoTag Biotechnologies
FluoTag-X4 **Anti-Rabbit (Alexa Fluor 647)**	IHC: 1:250 SRM: 1:200	N2404-AF647-S	NanoTag Biotechnologies
Goat **Anti-Mouse (Alexa Fluor 488)**	ICC: 1:200	ab150117	Abcam
Goat **Anti-Rabbit (Alexa Fluor 568)**	ICC: 1:1500	ab175471	Abcam
Goat **Anti-Mouse-Horseradish peroxidase (HRP) conjugated**	WB: 1:5000	31430	Thermo Fisher Scientific
Goat **Anti-Rabbit–Peroxidase conjugated**	WB: 1:10000	A0545	Sigma-Aldrich

4.1.7 Plasmids

mEos2-Mito-7

- Selective staining of mitochondria by transcription of cytochrome c oxidase subunit 8A-tagged photoactivable mEOS2.
- mEOS2 is a green fluorescent protein (Em: 516 nm) in resting state, which transitions to its active red fluorescent state (Em: 581 nm) upon UV irradiation of ~390 nm (Figure 14).
- Enables photoconversion of stained mitochondria in live cells.

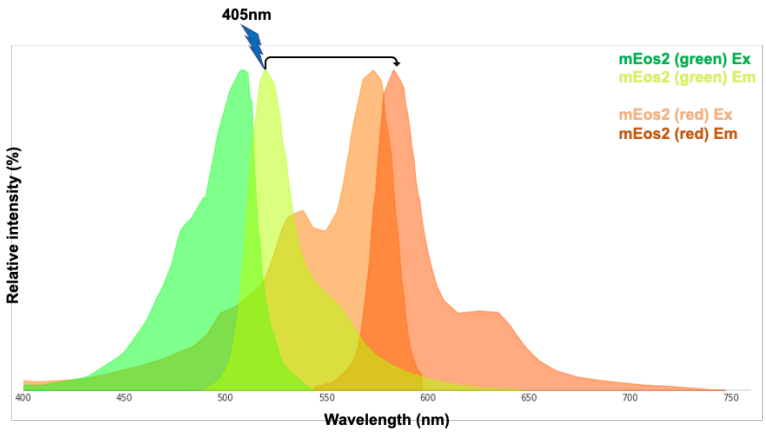

Figure 14 Emission and excitation of mEos2. Modified according to FPbase.org

4.1.8 TaqMan Assays

Table 11 TaqMan Assays

Gene	Assay ID	Manufacturer
GAPDH	Hs99999905_m1	Thermo Fisher Scientific
SV2A	Hs01059458_m1	Thermo Fisher Scientific

4.1.9 siRNAs

Table 12 siRNAs

siRNA	Assay ID	Manufacturer
Silencer Select Negativ control	4390843	Thermo Fisher Scientific
Silencer Select SV2A siRNA	s19182	Thermo Fisher Scientific

4.1.10 Buffers

10x Phosphate Buffered Saline without Ca^{2+} and Mg^{2+} (PBS CMF)

80 g	NaCl
2 g	KCl
17.8 g	$Na_2HPO_4 \times 2H_2O$
2.4 g	KH_2PO_4
ad 1 L	Ultrapure water

Autoclave.

1x PBS CMF

100 ml	10x PBS CMF
900 ml	Ultrapure water

Autoclave.

1x PBS

500 ml	1x PBS CMF
500 ml	$CaCl_2/MgCl_2$ Solution

1 M Tris/MOPS

12.1 g Tris

70 ml Ultrapure water

Adjust pH to 7.4 by adding dry MOPS.

Fill up to 100 ml with ultrapure water and filter sterile.

10x Running Buffer pH 8.45

30.2 g Tris

144 g Glycine

50 ml 20 % SDS solution

ad 1 L Ultrapure water

1x Running Buffer

100 ml 10x Running Buffer

900 ml Ultrapure water

10x Transfer Buffer

30.3 g Tris

144 g Glycine

ad 1 L Ultrapure water

Autoclave.

1x Transfer Buffer

100 ml 10x Transfer Buffer

200 ml Methanol

700 ml Ultrapure water

10x Tris Buffered Saline (TBS)

24.2 g Tris

87.8 g NaCl

700 ml Ultrapure water

Adjust pH to 6.8 by adding concentrated HCl.

Fill up to 1 L with ultrapure water, control pH and autoclave.

0.1 % TBST

100 ml	10x TBS
1 ml	Tween 20
ad 1 L	Ultrapure water

0.5 % TBST

100 ml	10x TBS
5 ml	Tween 20
ad 1 L	Ultrapure water

200 mM EGTA/Tris

3.8 g	EGTA
10 ml	Ultrapure water
30-40 ml	1M Tris/MOPS

Once EGTA dissolved fill up to 50 ml with 1M Tris/MOPS and filter sterile.
pH is ~6.7.

HS-Buffer

4.77 g	HEPES
109.31 g	Sorbitol
ad 1 L	Ultrapure water

HS-Buffer + 1 mM PMSF

100 µl	100 mM PMSF
9.9 ml	HS-Buffer

5x KCl-$CaCl_2$-$MgCl_2$ (KCM) Buffer

5 ml	1 M KCl
1.5 ml	1 M $CaCl_2$
2.5 ml	1 M $MgCl_2$
1 ml	Ultrapure water

Mitochondrial Isolation Buffer (MIB)

50 ml	400 mM Saccharose
1 ml	1 M Tris/MOPS
500 µl	200 mM EGTA/Tris
48.5 µl	Ultrapure water

Filter sterile.

Radioimmunoprecipitation Assay (RIPA) Buffer

50 mM	1 M Tris-HCl, pH 7.4
150 mM	1 M NaCl
1 %	Triton-X 100
0.5 %	Sodium deoxycholate
0.1 %	20 % SDS
5 mM	0.5 M EDTA

Tris-EDTA Buffer

1.21 g	Tris
370 mg	EDTA
ad 1 L	Ultrapure water

pH should be 9.

Add 0.5 ml of Tween 20 and mix well.

Tris-HCl pH 8.8

121.1 g	Tris
800 ml	Ultrapure water

Adjust pH to 8.8 with concentrated HCl.

Fill up to 1 L with ultrapure water, control pH and autoclave.

Tris-HCl pH 7.4

121.1 g	Tris
800 ml	Ultrapure water

Adjust pH to 7.4 by adding concentrated HCl.

Fill up to 1 L with ultrapure water, control pH and autoclave.

Tris-HCl pH 6.8

121.1 g Tris

800 ml Ultrapure water

Adjust pH to 6.8 by adding concentrated HCl.

Fill up to 1 L with ultrapure water, control pH and autoclave.

4.1.11 Solutions

0.1 % Tween 20/PBS CMF

50 µl Tween 20

ad 50 ml PBS CMF

0.5 % Triton-X 100/PBS

250 µl Triton-X 100

49.750 ml PBS CMF

0.5 M EDTA

23.26 g EDTA x $2H_2O$

100 ml Ultrapure water

Adjust pH to 8.0 by adding droplets of concentrated NaOH and autoclave.

1 M NaCl

292 mg NaCl

5 ml Ultrapure water

Autoclave.

1 M NaOH

40 g NaOH

ad 1 L Ultrapure water

1 M KCl

7.46 g KCl

10 ml Ultrapure water

Autoclave.

1 M $CaCl_2$

11.1 g $CaCl_2$

10 ml Ultrapure water

Autoclave.

1 M $MgCl_2$

20.33 g $MgCl_2 \times 6\ H_2O$

10 ml Ultrapure water

Autoclave.

4 % Paraformaldehyde solution

40 g Paraformaldehyde

500 ml Ultrapure water

10 ml 1 M NaOH

Heat up to 65 °C for dissolution.

100 ml 10x PBS CMF

Let solution cool down to room temperature.

Adjust pH to 7.4 by adding droplets of concentrated HCl.

Fill up to 1 L with ultrapure water, control pH and filter sterile.

10 % APS

100 mg APS

1 ml Ultrapure water

20 % SDS

20 g SDS

80 ml Ultrapure water

Heat up to 68 °C for dissolution.

Once solution is clear, adjust pH to 7.2 by adding droplets of concentrated HCl.

100 mM PMSF

175 mg PMSF

10 ml Isopropanol

100 % Trichloroacetic acid (TCA)

500 g TCA

227 ml Ultrapure water

400 mM Sucrose

13.7 g Saccharose

Ad 100 ml Ultrapure water

Filter sterile.

Antibody Dilution Solution for microscopy (1 % BSA)

500 mg Bovine Serum Albumin (BSA)

49.5 ml 1x PBS CMF

Blocking Solution for microscopy (5 % BSA)

2.5 g BSA

47.5 ml 1x PBS CMF

Blocking/Antibody Dilution Solution for histology (3 % BSA)

1.5 g BSA

48.5 ml PBS CMF

Blocking/Antibody Dilution Solution for WB (5 % BSA)

12.5 g BSA

237.5 ml 0.1 % TBST

$CaCl_2/MgCl_2$ Solution

147 mg $CaCl_2 \times 2H_2O$

102 mg $MgCl_2 \times 6H_2O$

ad 500 ml Ultrapure water

Autoclave.

Permeabilization solution (0.2 % Triton-X 100)

100 µl Triton-X 100

49.9 ml 1x PBS CMF

Protease Inhibitors

1 Tablet	Mini Protease Inhibitor Cocktail (Roche)
1 ml	Ultrapure water

Quenching solution

394 mg	TRIS HCl
292 mg	NaCl
50 ml	1x PBS CMF

Adjust pH to 8.0

Stripping Solution

10 ml	20 % SDS solution
12.5 ml	Tris-HCl 6.8
77.5 ml	Ultrapure water
0.8 ml	2-mercaptoethanol

4.1.12 Cell culture media

Full medium untransfected SH-SY5Y cells

500 ml	DMEM, high glucose, GlutaMAX supplement
50 ml	FBS (heat inactivated)
5.7 ml	Penicillin-Streptomycin (10,000 U/ml)
5 ml	MEM Vitamin Solution (100x)
5 ml	MEM Non-Essential Amino Acids (100x)
5 ml	Sodium Pyruvate (100 mM)

Reduced medium untransfected SH-SY5Y cells

500 ml	DMEM, high glucose, GlutaMAX supplement
10 ml	FBS (heat inactivated)
5.7 ml	Penicillin-Streptomycin (10,000 U/ml)
5 ml	MEM Vitamin Solution (100x)
5 ml	MEM Non-Essential Amino Acids (100x)
5 ml	Sodium pyruvate (100 mM)

Full medium transfected SH-SY5Y cells

500 ml	DMEM, high glucose, GlutaMAX supplement
50 ml	FBS (heat inactivated)
3.4 ml	Hygromycin B (50 mg/ml)
5.7 ml	Penicillin-Streptomycin (10,000 U/ml)
5 ml	MEM Vitamin Solution (100x)
5 ml	MEM Non-Essential Amino Acids (100x)
5 ml	Sodium pyruvate (100 mM)

Reduced medium transfected SH-SY5Y cells

500 ml	DMEM, high glucose, GlutaMAX supplement
10 ml	FBS (heat inactivated)
3.4 ml	Hygromycin B (50 mg/ml)
5.7 ml	Penicillin-Streptomycin (10,000 U/ml)
5 ml	MEM Vitamin Solution (100x)
5 ml	MEM Non-Essential Amino Acids (100x)
5 ml	Sodium pyruvate (100 mM)

Reduced medium for live cell imaging of untransfected SH-SY5Y cells

490 ml	DMEM, high glucose, no glutamine, no phenol red
10 ml	GlutaMAX supplement (100x)
10 ml	FBS (heat inactivated)
5.7 ml	Penicillin-Streptomycin (10,000 U/ml)
5 ml	MEM Vitamin Solution (100x)
5 ml	MEM Non-Essential Amino Acids (100x)
5 ml	Sodium pyruvate (100 mM)

Full medium untransfected HEK-293 cells

500 ml	DMEM, high glucose
50 ml	FBS (heat inactivated)
5.7 ml	Penicillin-Streptomycin (10,000 U/ml)

Freezing medium

95 %	Full medium
5 %	DMSO

4.1.13 Bacteria

Table 13 Bacteria strains

Strain	Species	Advantage	Application
DH5α	*e. coli*	Engineered to maximize transformation efficiency	Plasmid transfection and amplification
JM105	*e. coli*	Engineered to maximize transformation efficiency	Plasmid transfection and amplification

4.1.14 Cell lines

4.1.14.1 SH-SY5Y cells

This human cell line, derived from a bone marrow biopsy of a female neuroblastoma patient, grows very adherently and serves as a neuronal in vitro model. To develop a model for the early form of LOAD, SH-SY5Y cells were stably transfected with the human APP695 gene on a pCEP4 vector. These cells, carrying an additional copy of the human wildtype (wt) APP695 gene, are called SH-SY5Y APPwt. The corresponding control cell line carrying the empty pCEP4 vector is called SH-SY5Y Mock[13,151,152]. SH-SY5Y APPwt and SH-SY5Y Mock cells were transferred from the Institute of Pharmacy at the Goethe University Frankfurt to our facilities by Prof. Dr. Friedland. Untransfected SH-SY5Y cells were kindly provided by Prof. Dr. Christian Behl (Mainz, Germany).

4.1.14.2 Human Embryo Kidney-293 cells

Human Embryo Kidney-293 (HEK-293) cells are an immortalized cell line originally derived from embryonic kidney cells of a female human fetus exposed to sheared fragments of adenovirus type 5 DNA[153]. HEK-293 cells were used in the present research, as they are fast growing and easy to transfect. HEK-293 cells were transferred from the Institute of Pharmacy at the Goethe University Frankfurt to our facilities by Prof. Dr. Friedland.

4.1.15 Mice

The Rogister group (Liège, Belgium) developed a hippocampus specific SV2A KO mouse model where SV2A is only knocked out in glutamatergic neurons of the dentate gyrus (DG) and the cornu ammonis 3 (CA3) region[154]. This new mouse model was created performing a Cre/loxP recombination based approach. At the beginning SV2A flox/flox mice were generated by flanking exon 3 of the SV2A gene with LoxP sites in mouse embryonic stem cells and injecting these embryonic stem cells into the blastocysts of C57BL/6 mice. The later born chimeric mice were then crossed with C57BL/6 wildtype mice to create SV2A flox/flox homozygous mice. Next SV2A flox/flox mice were crossed with glutamate receptor, ionotropic, kainate 4 (Grik4)-Cre mice. Since the Cre recombinase expression in Grik4-Cre mice is controlled by the endogenous promoter elements of the Grik4 gene, which primarily occurs in the hippocampus, SV2A is solely knocked out in hippocampal regions. As a result, in the hippocampus of Grik4-Cre/+; SV2A flox/flox heterozygous mice, due to the occurred recombination, the deletion of exon 3 introduced an open reading frame shift producing an early stop codon disrupting the transcription of SV2A in the dentate gyrus and CA3 region. As control serve both Grik4+/+ and SV2A flox/flox homozygous mice, since their hippocampal SV2A gene function and protein levels are not altered. The brains of 12 weeks old SV2A KD and control mice were kindly provided by Prof. Dr. Bernard Rogister (Liège, Belgium).

4.2 Methods

4.2.1 Bacteria

4.2.1.1 Pouring lysogeny broth-agar plates

Fresh lysogeny broth (LB) medium is prepared, mixed with 15 g agar per liter and then autoclaved. During autoclavation the agar solubilizes. Following autoclavation the solution is kept in a water bath at 70 °C to prevent solidifying. Antibiotics such as ampicillin can be added to the solution once it has cooled down to below 80 °C. Agar plates are poured under a hood (20 ml per dish), stored at room temperature (RT) overnight and afterwards kept at 4 °C for long time storage.

4.2.1.2 Growing bacteria

Bacteria are either grown in liquid LB medium cultures under constant agitation at 37 °C or on LB-agar plates at 37 °C. Bacterial growth is exponential and can be graded

into four different phases: 1. Lag phase; 2. Log phase; 3. Stationary phase; 4. Death phase (Figure 15). Bacterial growth can be slowed down by storing bacteria at 4 °C.

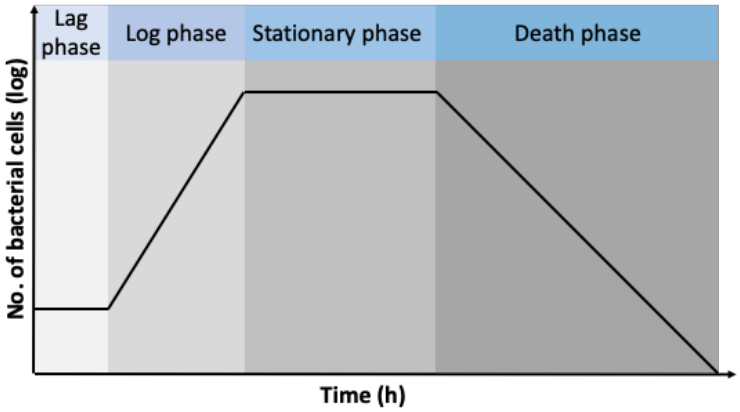

Figure 15 Bacterial growth curve

4.2.1.3 Freezing bacteria

An overnight culture is set up and bacteria are grown in LB medium (+ selective antibiotic) under constant agitation at 37 °C. The next day optical density of the overnight culture is measured at 600 nm using a photometer. Once an optical density of ~1 is reached, glycerol is added to a final concentration of 20 %, bacterial stocks are snap frozen in liquid nitrogen and afterwards stored at -80 °C.

4.2.1.4 Transformation of competent bacteria

Competent bacteria are gently thawed on ice for 1 h. Once thawed, 20 µl 5x KCM buffer, 100 ng plasmid and 70 µl ultrapure water are mixed with 100 µl competent bacteria (c= $4x10^9$ bacteria/ml). Bacteria treated with additional ultrapure water instead of plasmid serve as control. Both samples and controls are incubated for 20 min on ice, followed by a 10 min incubation at RT and subsequent dilution in 1 ml LB medium (without antibiotics). Afterwards bacteria are grown for 50 min at 37 °C under constant agitation, spread onto agar plates containing a selective antibiotic and grown in an incubator over night at 37 °C. The next day, plates containing transfected or control bacteria are screened for bacterial growth and an overnight culture of the transfected bacteria is set up (including antibiotics). If colony forming units (CFU) are found on control plates, the whole transformation must be repeated, as control bacteria should lack the antibiotic resistance inherited through the plasmid. Finished overnight cultures

of transfected bacteria can either be frozen for later use as described in *4.2.1.3 "Freezing bacteria"* or used for plasmid preparation.

4.2.1.5 Plasmid preparation

Plasmid preparation is performed using the GenElute HP Plasmid Midiprep Kit (Sigma Aldrich). 50 ml of the prepared overnight culture are centrifuged (5,000 g, 10 min, RT) and the bacteria pellet is resuspended in 4 ml Resuspension/RNAse Solution. Next 4 ml Lysis Buffer are added to the resuspended pellet and after gently inversion the mixture is left to stand for 5 min. After cell lysis 4 ml cooled Neutralization Solution are added to the lysate, which triggers the formation of a white aggregate. Once 3 ml Binding Solution are added, the whole lysate is poured into an open syringe and the column is installed onto the vacuum manifold. The loaded syringe is placed on top of the column and the lysate is sucked through the filter of the column. Once the cell lysate is filtered, Wash Solution 1 and 2 are sucked through the filter and the column is dried for at least 10 min. As soon as the column dried it is placed into a tube, 800µl Elution Buffer are added and the column is centrifuged (5,000g, 10 min, RT). In the end plasmid concentration of the solution is determined photometric and aliquots are stored at -20 °C.

4.2.2 Cell culture

4.2.2.1 Splitting & seeding cells

Splitting and seeding cells starts by discarding the old cell culture medium. While HEK-293 cells are only washed off with fresh cell culture medium, the more adherent SH-SY5Y are first washed with cold PBS CMF to remove FBS residues and are then treated with trypsin in an incubator at 37 °C. Once SH-SY5Y begin to detach, they are resuspended in prewarmed cell culture medium. After harvesting, both cell lines are centrifuged (1,000 g, 5 min, RT) and the resulting pellets are resuspended in warm cell culture medium. Following resuspension, 200 µl cell suspension are diluted in 9.8 ml "Coulter Isoton" and the cell number/ml is counted using the Beckman Coulter Cell Counter. For maintenance, $2.5x10^6$ SH-SY5Y Mock cells, $2.5x10^6$ SH-SY5Y APPwt cells, $4x10^6$ SH-SY5Y ut cells and $2.5x10^6$ HEK-293 cells are seeded into 175 cm^2 cell culture flasks. Each cell line is grown in an incubator at 37 °C and 5 % CO_2 until ~80 % confluency is reached.

4.2.2.2 Freezing cells

Cells are harvested as described in *4.2.2.1 "Splitting & seeding cells"*. After counting the cells, DMSO is added to the cell suspension until a final concentration of 5 % is reached. Afterwards 3-5x10^6 cells are quickly filled into cryotubes, placed into a freezing container and stored at -80 °C overnight for gentle freezing (-1 °C/min). The next day frozen cells are transferred to liquid nitrogen for long time storage.

4.2.2.3 Thawing cells

A cryotube containing the desired cell line is thawed in hands. Once the cell suspension starts thawing, cells are transferred to 9 ml cold full medium, centrifuged (1,000 g, 5 min, RT), resuspended in prewarmed full medium and seeded into a fresh cell culture flask. Cell culture medium is exchanged the following day to remove dead cells.

4.2.2.4 SV2A KD in SH-SY5Y cells

7x10^5 SH-SY5Y cells are either seeded in empty 6-well plates or in 6-well plates loaded with untreated glass coverslips depending on the performed experiment. Cells are grown for 24 h in full medium or until 60-80 % confluency is reached. Once cells are ready for transfection the lipofectamine mastermix is prepared by diluting 9 µl Lipofectamine RNAiMAX in 150 µl Opti-MEM Reduced Serum Medium (Opti-MEM). Similar to lipofectamine a SV2A siRNA and a negative control (neg. ctl) siRNA mastermix is prepared by diluting 3 µl of the respective 10 µM siRNA stock in Opti-MEM. Optional 1.5 µl positive control (Alexa Flour 555) can be added to visualize successfully transfected cells under a microscope. The negative control siRNA serves as a control being a non-targeting siRNA. Before transfection 150 µl of the lipofectamine and siRNA mastermixes are mixed and incubated for 5 min at RT. In the meantime, full medium is removed from the cells and replaced by 2.25 ml reduced medium per well. 250 µl of the prepared siRNA-lipofectamine complexes are added to each well and cells are transfected for 48 h in an incubator at 37 °C and 5 % CO_2. Modified according to *"Silencer Select Libraries: Transfection protocol - Pub. No. MAN0014605 Rev. A.0" - Thermofisher Scientific*

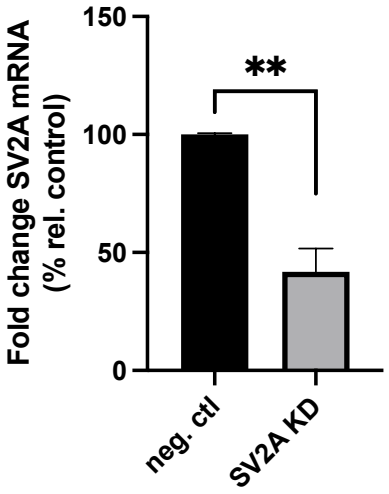

Figure 16 SV2A mRNA fold change following SV2A KD

Reduction of SV2A messenger RNA (mRNA) levels in SH-SY5Y cells upon treatment with SV2A siRNA (10 nM/48 h). Neg. ctl cells were treated with scrambled siRNA (10 nM/48 h). 3 independent qPCR experiments were performed. Data are expressed as mean ± standard error of the mean (SEM); student's unpaired t-test (*p <0.05; **p <0.01, ***p <0.001).

4.2.3 Histology

4.2.3.1 Paraffin embedding of tissue

PFA fixed tissue is cut to appropriate size and shape and placed into an embedding cassette. Afterwards tissue is dehydrated by ascending ethanol dilutions, xylene substitutes and finally infiltrated with paraffin by a semiautomatic tissue processor. 18 h later, the dehydrated and paraffin infiltrated tissue is embedded in paraffin using the Leica Tissue Embedding Center. Finished paraffin blocks are stored at 4 °C.

4.2.3.2 Tissue sectioning with microtome

Paraffin blocks are trimmed and placed on a cooling plate with the specimen side facing the plate. Once the microtome is set up, the paraffin block is placed into the cooling specimen clamp and its angle is adjusted by moving and tilting the specimen clamp. Before cutting 10 µm thick slices, the paraffin block is trimmed until the desired area is reached. During sectioning, the resulting paraffin ribbon is placed into a 40 °C water bath to remove wrinkles and sections are afterwards mounted onto charged slides. Once sections dried for 30 min at 35 °C on a heating plate they are baked overnight at 47 °C. Finished slides are either stained immediately or stored at 4 °C.

4.2.4 Confocal microscopy

4.2.4.1 Immunocytochemistry (ICC)

$5x10^5$ SH-SY5Y cells are seeded in full medium on untreated glass coverslips inside 6-well plates. The following day cell culture medium is exchanged to remove non adhered cells and cells are cultivated for another day. On day three cell culture medium is removed and mitochondria are stained with 200 nM preheated MitoTracker Deep Red FM for 45 min at 37 °C protected from light. Afterwards MitoTracker is replaced by a 4 % PFA solution and cells are fixed for 20 min at RT. Once cells are fixed, PFA is removed and samples are washed with quenching buffer for 5 min. Cells are then permeabilized using permeabilization buffer at RT for 20 min followed by washing the cells with PBS CMF 5x5 min. Next samples are blocked using blocking buffer for 1 h at RT, followed by a 1 h incubation with primary antibodies at RT. Once the primary antibodies have been removed and cells have been washed with PBS CMF 5x5 min, secondary antibodies are added to the cells for 1h at RT protected from light. By the time the secondary antibody incubation is completed, samples are washed with PBS CMF 5x5 min and coverslips are mounted on to slides with ProLong Glass Antifade Mountant with NucBlue Stain. Images of stained cells are later acquired with the 63x oil immersion objective on the Leica TCS SP5 confocal microscope.

To mimic mitochondrial dysfunction and oxidative stress occurring during the progression of AD, SH-SY5Y cells can be treated with either 5 µM complex I inhibitor rotenone or 1 µM mitochondrial uncoupler carbonyl cyanide 3-chlorophenylhydrazone (CCCP) for 24 h at 37 °C. Complex I inhibitor rotenone causes mitochondrial impairment associated with increased intracellular ROS levels, decreased MMP, decreased ATP levels and mitochondrial shortening[96,155,156]. CCCP, described in the literature as a potent mitochondrial uncoupler decreases ATP levels, depolarizes mitochondria, increases ROS levels and induces mitochondrial fragmentation up to mitophagy[157,158]. It is important that mitochondrial toxins are added to both cell culture medium and MitoTracker solution to ensure mitochondrial stress until cell fixation.

4.2.4.1.1 Measuring of mitochondrial length

Samples for the determination of mitochondrial length are prepared almost exactly as described in *4.2.4.1 "Immunocytochemistry (ICC)"*. The only difference is that incubations with primary or secondary antibodies are replaced by incubations with

antibody dilution buffer. Due to the prolonged procedure with several washing steps, clearer images with lower background are obtained. Mitochondrial length is measured with FIJI software and mitochondria are classified into four groups according to their size (Figure 17). 100 mitochondria measured account for one n.

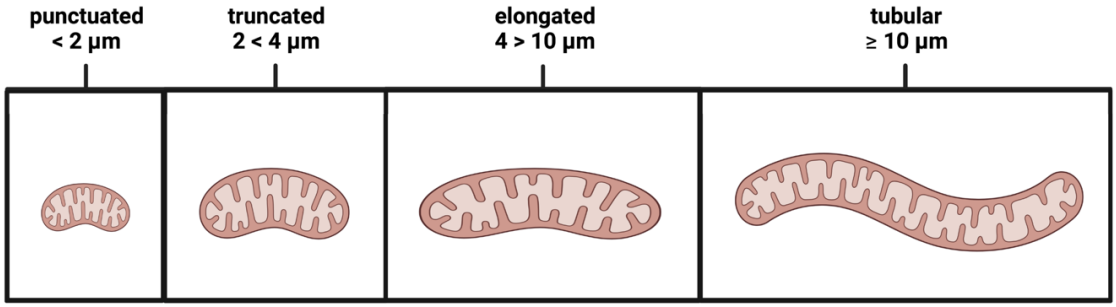

Figure 17 Mitochondrial length classification adapted from Stockburger et al. (2016)

4.2.4.1.2 Staining of autophagic vacuoles and lysosomes

Staining of autophagic vacuoles by LC3II is performed as described in *4.2.4.1 "Immunocytochemistry (ICC)"*, except that cells are additionally treated with 600 nM bafilomycin A1 (Bafi) for 4 h prior to cell fixation to prevent degradation of autophagic vacuoles.

Staining of lysosomes is also performed for the most part as described in *4.2.4.1 "Immunocytochemistry (ICC)"*. Lysosomes are stained with 75 nM LysoTracker Red DND-99 for 45 min at 37 °C prior to fixation. To increase the number of lysosomes, cells can be starved in EBSS for 2 h prior to fixation (Figure 18). When starving the cells, it is important to starve them with EBSS until fixation, consequently lysotracker must be diluted in EBSS. Raising lysosome numbers by bafilomycin A1 is not an option since bafilomycin A1 inhibits the acidification of lysosomes (Inhibition of vacuolar-type H+ -ATPase (V-ATPase)) necessary for the staining of lysosomes by LysoTracker Red DND-99 (Figure 18C).

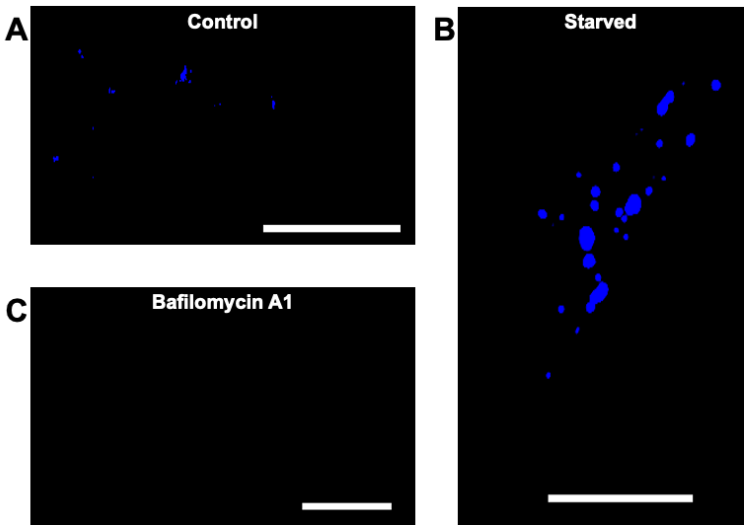

Figure 18 Starving increases the number of lysosomes

(A) Representative confocal image of untreated and non-starved SH-SY5Y cells stained for lysosomes

(B) Representative confocal image of EBSS starved (2 h) SH-SY5Y cells stained for lysosomes. Starving increases the number of lysosomes.

(C) Representative confocal image of EBSS starved (2 h) SH-SY5Y cells treated with bafilomycin A1 (600 nM/4 h) stained for lysosomes. Lysosomes were not stained by LysoTracker Red DND-99 as bafilomycin A1 inhibits the acidification of lysosomes. Proof of lysosome staining specificity.

Lysosomes were stained by LysoTracker Red DND-99 (75 nM/2 h), Scale bar: 10 µm.

4.2.4.2 Immunohistochemistry (IHC)

Tissue sections are deparaffinized and rehydrated by incubation with xylene substitutes followed by descending ethanol dilutions. Rehydrated tissue is encircled by a hydrophobic pen to build a hydrophobic barrier necessary for applying reagents such as antibodies to the tissue. Afterwards, Tris-EDTA buffer induced antigen retrieval is performed boiling the sections at 95 °C in preheated TRIS-EDTA Buffer for 15 min. After cooling, sections are washed with 0.1 % Tween20/PBS CMF buffer at RT for 5 min followed by PBS CMF at RT for 5 min. Permeabilization of the tissue is achieved by treating the sections with 0.5 % Triton-X 100/PBS CMF solution for 1h at RT. Subsequently sections are washed twice with PBS CMF for 5 min and are then blocked with 3 % BSA/PBS CMF buffer for 1h at RT. After blocking, slices are incubated with primary antibody dilutions overnight at 4 °C in a humified chamber. The next day samples are washed 3x5 min with PBS CMF followed by a 1 h incubation with

secondary antibodies at RT protected from light. After washing the slides on last time with PBS CMF (3x5 min), coverslips are mounted onto sections using ProLong Glass Antifade Mountant with NucBlue Stain. Image acquisition is performed as described in *4.2.4.1 "Immunocytochemistry (ICC").*

4.2.4.3 Live cell imaging of SV2A KD cells

Cell transfection is performed according to the protocol described in *4.2.2.4 "SV2A KD in SH-SY5Y cells"*, except that 600 µg mEos2-Mito7 plasmid are added to the siRNA master mix and the incubation of the siRNA/plasmid mastermix with the lipofectamine mastermix is increased to 15 min. After successful transfection, the transfection complex is removed from the cells and replaced by cell culture medium lacking phenol red. Live cell imaging is performed using the 100x oil immersion objective on the Visitron Spinning Disc microscope. During the imaging process, cells are kept at 37 °C and 5 % CO_2 in a humified chamber. Every 30 sec an image is acquired for a total duration of 10 min. FIJI software is used to analyze the recordings for fission and fusion events, distance traveled and velocity. Fission and fusion events are determined visually during a 10 minute period, while distance traveled and velocity are measured for three individual mitochondria per cell using the FIJI tracking plugin.

4.2.4.4 Staining for confocal microscopy

Proteins and organelles are stained for ICC as listed in table 14 and for IHC as listed in table 15. Dilutions of the respective antibodies are provided in table 9-10.

Table 14 Staining of proteins and organelles for ICC

Protein or organelle	Staining
DRP1	Anti-DRP1 primary antibody + Alexa Fluor 568 tagged secondary antibody
LC3II	Anti-LC3II primary antibody + Alexa Fluor 568 tagged secondary antibody
Lysosomes	LysoTracker Red DND-99
Mitochondria	MitoTracker Deep Red FM
SV2A	Anti-SV2A primary antibody + Alexa Fluor 488 tagged secondary antibody

VAMP2	Anti-VAMP2 primary antibody + Alexa Fluor 568 tagged secondary antibody

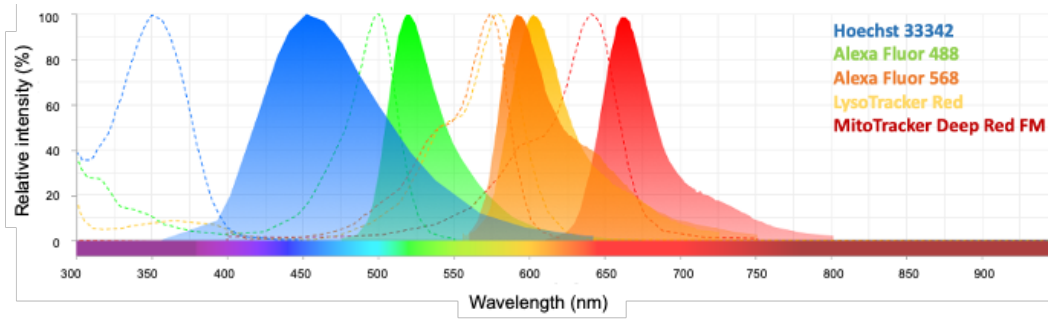

Figure 19 Emission and excitation of dyes used for confocal microscopy; created with Spectraviewer

Table 15 Staining of proteins and organelles for IHC

Protein or organelle	Staining
TOM20	Anti-TOMM20- Alexa Fluor 647 primary antibody
VGlut1	Anti-VGlut1-ATTO 488 primary antibody

4.2.4.5 Confocal raw data processing

Confocal images are acquired in xy- and z-direction to capture and analyze each layer of the cell. Recorded z-stacks are processed and analyzed using FIJI software. First, stacks of each staining per cell are merged (Command: merge channels) and if necessary, brightness or contrast of the respective stainings are adjusted for higher resolution (Brightness & Contrast tool). Afterwards, an overall image of the respective cell is created by merging all stacks (z-project). Following analysis of each individual layer of the cell the z project is analyzed and compared to the results of each cell layer. This step is necessary to ensure integrity of the results. If the results of the z-project match the results of the individual layers, the z-project is further analyzed, e.g. by determining Pearson's correlation coefficient (Pearson's r) or measuring mitochondrial length. The Pearson's r is a colocalization parameter that ranges from -1 to 1, with -1 representing anti-correlation and 1 representing correlation. A Pearson's r of ≥0.5 indicates colocalization of two stained proteins. During live cell imaging, cells are also imaged in the xy- and z- direction.

4.2.5 Super-resolution microscopy

Super-resolution microscopy (SRM) breaks the diffraction barrier postulated by Ernst Abbe in the 19th century and enables the acquisition of images with 8-16x higher resolution in xy-direction and about 15x higher resolution in z-direction compared to confocal microscopy (Table 16, Figure 20). This advantage in resolution is ideal for colocalization experiments.

Table 16 Resolution of confocal and super-resolution microscopy

	Confocal microscope	**Super-resolution microscope**
Resolution in xy-direction	320 nm	20-40 nm
Resolution in z-direction	772 nm	50 nm

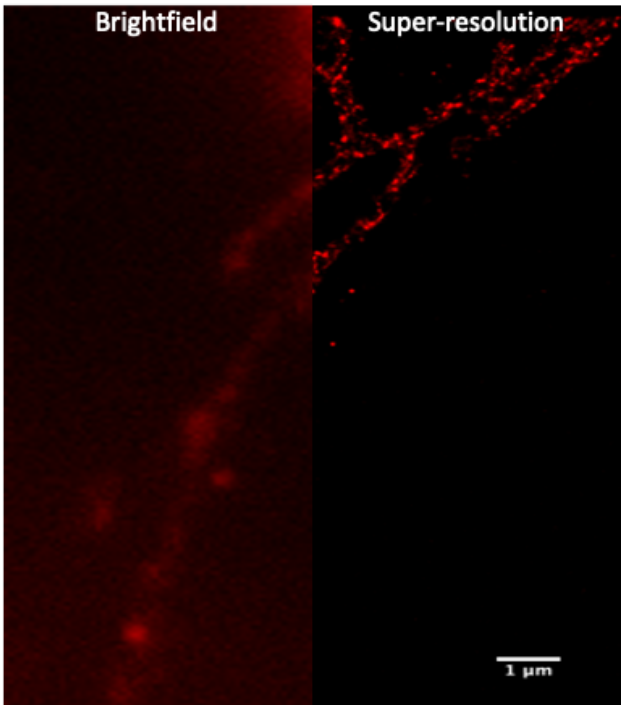

Figure 20 Resolution of brightfield microscopy compared to super-resolution microscopy

$5x10^5$ SH-SY5Y cells are seeded in full medium on 35 mm µ-Dish dishes. The following day, cell culture medium is changed to remove non-adhered cells and cells are cultivated for another day. On the third day, cell culture medium is replaced with 4 %

PFA solution and cells are fixed for 20 min at RT. Once cells are fixed, PFA is removed and cells are washed with quenching buffer for 5min. Next cells are permeabilized using permeabilization buffer for 20 min at RT followed by washing with PBS CMF 5x5 min. The samples are then blocked using blocking buffer for 1 h at RT, followed by a 1 h incubation with primary antibodies at RT. Once the primary antibodies have been removed and cells have been washed with PBS CMF 5x5 min, secondary antibodies are added to the cells for 1 h at RT protected from light. By the time the secondary antibody incubation is completed, samples are washed with PBS CMF 5x5 min and in the end stained cells are embedded in PBS CMF.

Before analyzing the samples, a 1:500 dilution of TetraSpeck microspheres is applied to a fresh 35 mm µ-dish and measured. TetraSpeck microspheres,100 nm in size and stained with four different fluorophores, yield beads which are used to determine the shift between the green and the red channel whilst the recording of the samples (Figure 21). This step is important since even a slight shift of a few nm between the two channels alters the correct localization of the stained proteins, yielding false results. After the microspheres had time to settle for 30 min, they are embedded in freshly prepared Pyranose Oxidase Buffer + MEA and measured for each channel before and after the microscopy session.

Once TetraSpeck were measured, PBS CMF is removed from the samples, they are embedded in Pyranose Oxidase Buffer + MEA and imaged with the 160x 1,47 oil immersion objective of the Leica GSD 3D Widefield Super-Resolution microscope. Approximately 10,000 frames per protein are recorded.

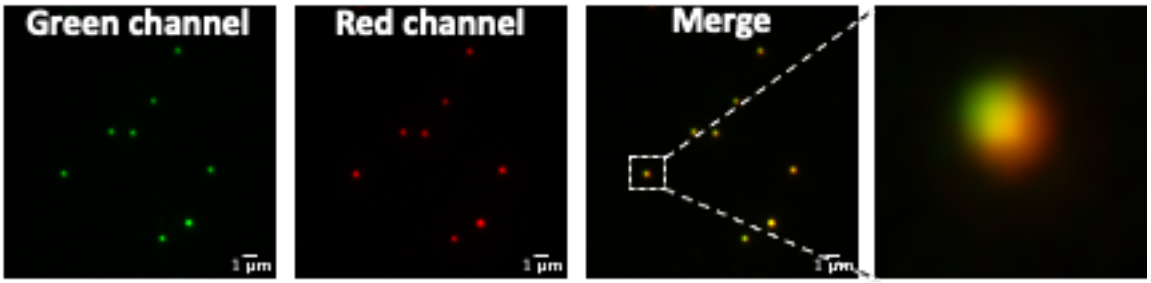

Figure 21 Representation of unshifted TetraSpeck beads

4.2.5.1 Staining for super-resolution microscopy

Mitochondria are visualized by staining of TOM20 as described in Huang et al. (2008) and Wurm et al. (2011)[159,160]. Vesicles by staining of VAMP2.

Proteins are stained according to table 17. Dilutions of the respective antibodies are provided in table 9-10.

Table 17 Staining of proteins for super-resolution microscopy

Protein	Staining
DRP1	Anti-DRP1 primary antibody + Alexa Fluor 647 tagged secondary antibody
SV2A	Anti-SV2A primary antibody + ATTO 488 tagged secondary antibody
TOM20	Anti-TOMM20- Alexa Fluor 647 primary antibody
VAMP2	Anti-VAMP2 primary antibody + ATTO 488 tagged secondary antibody

4.2.5.2 Data processing and analyzation

SRM raw data are acquired in xy-direction and consist of thousands of frames per channel containing the coordinates of the stained proteins. ThunderSTORM is used to extract and convert these data into result tables, which are used for data processing (e.g. shift correction) and turning the coordinates into images. The shift between the green and the red channel is calculated with a MATLAB software written and kindly provided by Dr. Márton Gelléri from the Institute of Molecular Biology (Mainz, Germany). The software measures the shift of TetraSpeck beads between the two channels and simultaneously calculates a matrix to adjust the red channels data (coordinates), leading to a higher reliability of the data (Figure 22). Once the red channels coordinates have been transformed, images of the green and the red channel are merged. In addition to just visually analyzing the merged images, ThunderSTORM offers a colocalization tool called Coordinate-based colocalization (CBC). The CBC value is calculated for each coordinate over the distance between two coordinates in a 50 nm radius and ranges from -1 (100% anti-correlation) to 1 (100% correlation). The CBC values for every coordinate are displayed in a histogram (Figure 22).

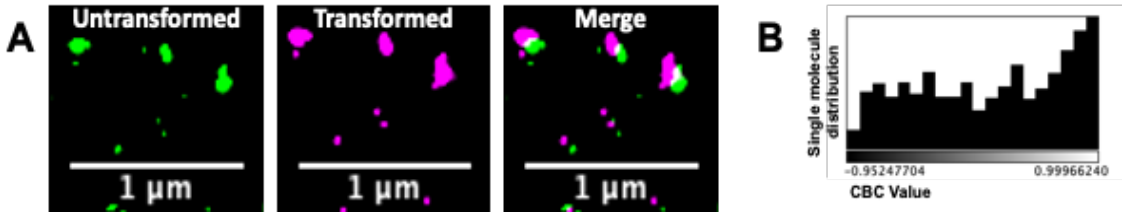

Figure 22 Data processing and analyzation of super-resolution data

(A) Comparison of protein localization untransformed and transformed.
(B) Representative CBC histogram

4.2.5.2.1 Determination of SV2A molecules within mitochondrial areas

First the number of SV2A molecules per super-resolution image is determined using the FIJI 3D object counter at a threshold of 75. Afterwards, mitochondrial areas are assessed using the TOM20 staining, which represents the OMM. The number of SV2A molecules within these mitochondrial regions is then determined using the 3D object counter at a threshold of 75. At the end, the percentage of mitochondrial SV2A molecules is calculated.

4.2.6 Western blot

4.2.6.1 Protein extraction from cells

Cells are cultivated up to sub confluency on 58 cm^2 culture plates. Upon sub confluency, cells are placed on ice, cell culture medium is removed and cells are washed once with ice cold PBS CMF. Afterwards cell lysis is initiated by adding 200 µl RIPA buffer + PMSF to the cells. After a 15 min incubation on ice, adherend cells are harvested with a cell scraper and the cell lysate is transferred to a precooled 1.5 ml tube. Once additional 30 min on ice have passed, the cell lysate is centrifuged (10,000 g, 10 min, 4 °C) and the supernatant is transferred to a new precooled tube. Finally, a 20 µl sample is taken to determine the protein concentration by Bradford assay, protease inhibitors are added to the cell extract and it is stored at -80 °C.

4.2.6.2 Bradford assay

The Bradford assay is used to quantify the unknown protein concentration of a solution by measuring the color shift of Coomassie G-250 when bound to proteins. Unbound Coomassie G-250 is red with an absorbance maximum at 470 nm. Bound to proteins Coomassie G-250 turns blue and its absorbance maximum shifts to 595 nm. This

change in color of Coomassie G-250 from red to blue upon binding protein is measured spectroscopic after a 5 min incubation protected from light. Since the amount of blue Coomassie G-250 is proportional to the amount of protein, the protein concentration of a sample can be determined by measuring its absorbance at 595 nm. To determine the unknown protein concentration of a cell extract, the cell extract is first diluted 1:1000 with ultrapure water. Then a serial dilution of BSA (20-1.25 µg/ml), including blank, is measured to create a standard curve. To determine the unknown protein concentration, 200 µl Bradford reagent are added to 800 µl diluted cell extract, the absorbance is measured at 595 nm and the protein concentration is calculated using the equation of the BSA standard curve.

4.2.6.3 Western blot (WB) performance

Samples are diluted to the desired protein concentration (20-30 µg) with ultrapure water, 4x loading buffer is added and samples are boiled 5 min at 95 °C. Samples and protein ladder are then loaded onto a polyacrylamide gel, where proteins are separated according to their size by running the gel first at 80 V for 30 min following 1-1.5 h at 120 V. Afterwards, the denatured proteins are blotted for 1 h at 100 V and 4 °C onto a polyvinylidene difluoride (PVDF) membrane that has been activated with methanol. After successful blotting, the membrane is cut at the desired bands and blocked with 20 ml blocking buffer for 1h at RT. The blocked membrane is then embedded in 5-10 ml primary antibody solution for 1h at RT or overnight at 4 °C. Once the primary antibody incubation is completed, the membrane is washed 3x (15 min, 10 min, 5 min) with 0.5 % TBST and incubated with 10 ml secondary antibody solution for 1h at RT. Afterwards, the membrane is washed once more with 0.5% TBST for 30 min and analyzed using Vilber's Fusion Pulse. For analysis, the membrane is incubated with Amersham ECL-Prime reagent for 5 min protected from light. Oxidation of luminol by HRP bound to the secondary antibody generates a chemiluminescent signal, of which an image is taken. Intensity of the protein bands on the acquired image can be measured using FIJI. The analyzed membrane can be further investigated removing all previously bound antibodies by incubating the membrane for 30 min at 50 °C with prewarmed stripping buffer. The membrane is afterwards washed twice with 0.5% TBST for 10 min each and analyzed using Amersham ECL Prime reagent. If no signal is detected, displaying that all antibodies have been removed, the immunoassay is repeated by blocking the membrane for 1 h at RT.

4.2.6.4 Autophagic flux WB

To determine the autophagic flux by WB, protein extraction is performed as described in *4.2.6.1 "Protein extraction from cells"*, except that cells are treated with autophagy inhibitor bafilomycin A1 (600 nM/4 h) prior to extraction. For the determination of autophagic flux, it is mandatory to have a control group of untreated cells with functional autophagy. These will later serve as a benchmark to compare LC3II levels under normal conditions with LC3II levels of bafilomycin A1 treated samples. Autophagic flux is calculated from the WB data by subtracting the intensity of the control LC3II band from those of the bafilomycin A1 treated samples (Equation 1). The difference represents the amount of LC3II molecules that would have been degraded during this period under normal conditions, hence the autophagy rate (Figure 23+24). Bradford assay (*4.2.6.2 "Bradford assay"*) and WB (*4.2.6.3 "Western blot performance"*) are performed as described above.

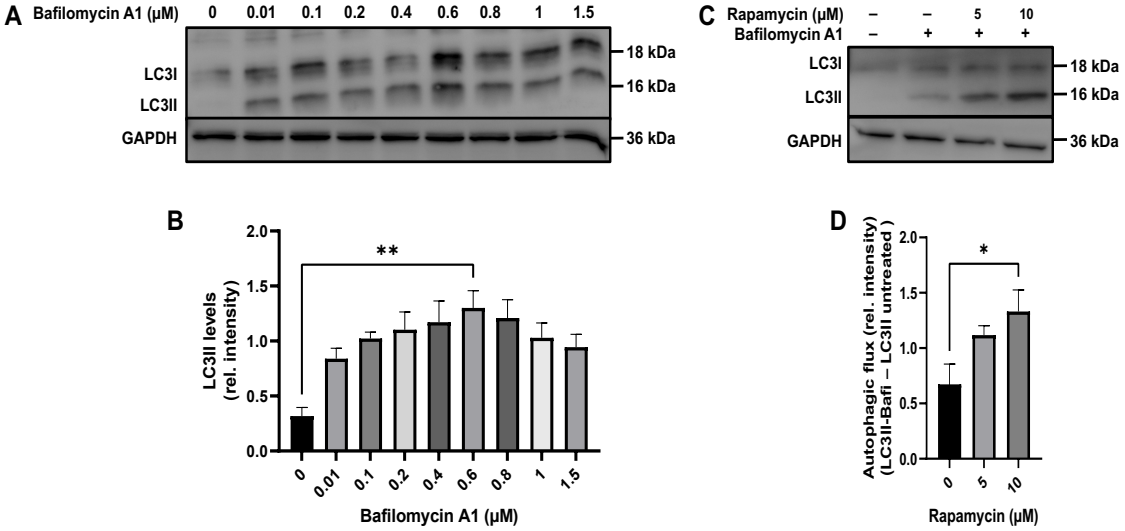

Figure 23 Verification of bafilomycin A1 and rapamycin concentrations

(A) Representative LC3II western blot of SH-SY5Y Mock cells treated with different bafilomycin A1 concentrations for 4 h. 20 µg protein were loaded per well. Glyceraldehyde 3-phosphate dehydrogenase (GAPDH) serves as internal control. **(B)** Graphical representation of relative LC3II intensities depending on bafilomycin A1 concentrations. **(C)** Representative LC3II western blot of SH-SY5Y Mock cells treated with bafilomycin A1 (600 nM/4 h) along with either 5 µM or 10 µM rapamycin for 4 h. 20 µg protein were loaded per well. GAPDH serves as internal control. **(D)** Graphical representation of autophagic flux depending on rapamycin concentrations. Analyzed were 3 independent cell extracts. Data are expressed as mean ± SEM; student's unpaired t-test (*p <0.05; **p <0.01, ***p <0.001).

$$\boldsymbol{Autophagic\ flux = Control\ (untreated) - Samples\ (Bafilomycin\ A1\ treated)}$$

Equation 1 Autophagic flux

The autophagic flux of an AD cell model can be investigated by seeding 2x10^6 SH-SY5Y Mock or APPwt cells on 60 mm cell culture dishes and proceeding as describe above. The effects of LEV on autophagic flux can be tested by incubating these cells with 200 µM LEV for 2 h whilst bafilomycin A1 treatment.

To investigate whether SV2A affects autophagy, 7x10^5 SH-SY5Y cells are seeded per well of a 6-well plate. One whole 6-well plate is harvested per sample. SV2A KD is performed as described in *4.2.2.4 "SV2A KD in SH-SY5Y cells"*, and bafilomycin A1 is added to the transfection cocktail 4 h before protein extraction.

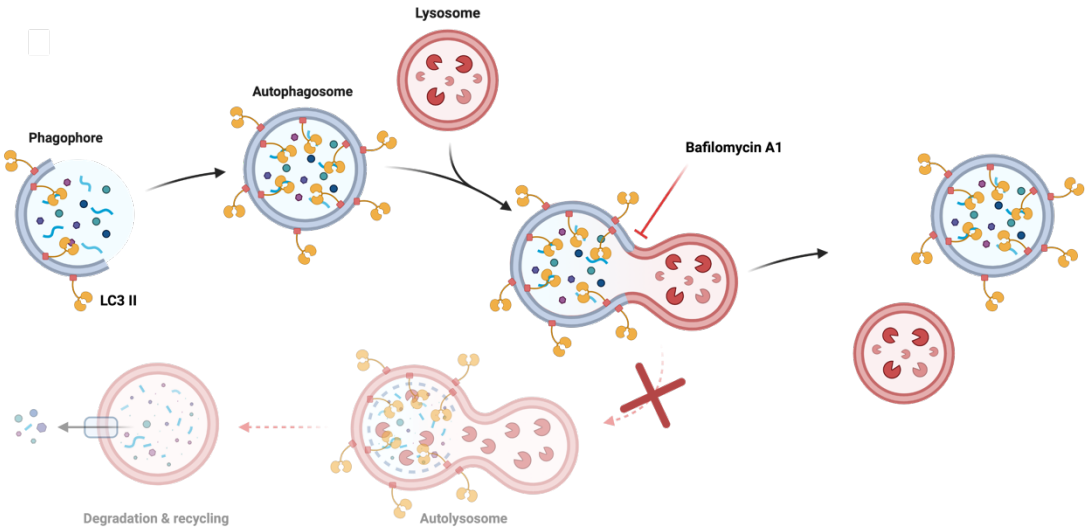

Figure 24 Bafilomycin A1 mode of action and principle of autophagic flux WB

4.2.7 Mitochondrial fractioning

4.2.7.1 Isolation of mitochondria

2.5x10^6 HEK-293 cells are seeded per 175 cm^2 flask in full medium and are grown for 96 h until ~90 % confluency is reached. All following steps are performed on ice. Isolation of mitochondria starts by aspirating cell culture medium. Cells are then washed once with PBS CMF and harvested using cell scrapers. Detached cells are collected in 15 ml PBS CMF, centrifuged in a swinging bucket rotor (700 g, 5 min, 4 °C)

and the resulting pellet is resuspended in 1 ml Mitochondrial Isolation Buffer (MIB). Resuspended cells are then transferred to a glass potter vessel, MIB is added until the first line is reached, the potter is set to 1000 rounds per minute (rpm) and 3 passages are performed. The homogenized cell suspension is transferred to a 50 ml conical tube and cell disruption is continued by drawing the suspension into a syringe with a 18 gauge needle and expelling it against the wall of the tube with a 27 gauge needle. Drawing and expelling is repeated four more times until a total number of five times is reached. Broken up cells are transferred to a 15 ml conical tube and centrifuged in a swinging bucket rotor (600 g, 5 min, 4 °C). The supernatant is carefully removed, distributed among 1.5 ml tubes and centrifuged in a fixed-angle rotor (10,000 g, 5 min, 4 °C). After centrifugation, the pellet is resuspended in 100 µl HS buffer and mitochondria concentration is determined using biuret assay.

4.2.7.2 Determination of mitochondria concentration – Biuret Assay

Mitochondria concentration is measured using biuret assay. The biuret assay combines the reduction of Cu^{2+} cations to Cu^{1+} cations by proteins in alkaline medium with the highly sensitive and selective colorimetric detection of formed Cu^{1+} using bicinchoninic acid (BCA). The purple colored reaction product is formed by chelation of one Cu^{1+} cation by two molecules of BCA during a 30 min incubation at 37 °C protected from light. After cooling to RT, the absorbance of the purple complexes is measured with a photometer at 562 nm. The biuret assay is performed using the Pierce BCA Protein Assay Kit. First fresh working reagent is prepared by diluting solution B (Cu^{2+} solution) in a 1:50 ratio with solution A (BCA solution). When performing the high range assay, 100 µl samples are diluted with 2 ml working reagent. Blank, BSA serial dilution (2-0.125 g/ml) and 1:10 mitochondrial dilutions are incubated with working reagent for 30 min at 37 °C. After cooling to RT, the purple complexes of blank and serial dilution samples are measured before the mitochondria samples. Finally, concentration of mitochondria in µg/ml is calculated using the equation of the BSA standard curve.

4.2.7.3 Mitochondrial fractioning and TCA protein precipitation

Aim of this experiment is to identify the mitochondrial fraction a protein of interest is located in. This is accomplished by treating isolated mitochondria with ascending concentrations of the detergent digitonin, causing mitochondrial membranes to dissolve depending on the digitonin concentration. Consequently, mitochondria are separated into their four fractions (OMM, IMS, IMM, matrix). To obtain pure fractions, proteins

released during membrane dissolution are digested by proteinase K. The proteins of each fraction are afterwards precipitated with TCA. Precipitated proteins of each sample are analyzed by western blot.

It is important that the entire experiment is performed on ice. At the beginning of the experiment, 800 µg mitochondria are dissolved in 150 µl HS buffer per sample and the same volume of digitonin solution is added. The digitonin concentration of the samples ranges from 0 % to 0.105 %. A total of thirteen samples are prepared, of which the first two samples receive no digitonin. In the remaining eleven samples, the digitonin concentration increases by 0.01% for each ascending sample, starting at 0.005% until the highest concentration of 0.105% is reached at sample thirteen. Immediately after the addition of digitonin, 1.5 µl proteinase K stock solution (20 mg/ml) is added to all samples except the first one and mitochondria are left to disrupt into their fractions for 30 min with occasional inverting. To stop mitochondrial digestion, 3 µl 100 mM PMSF solution is pipetted into each sample and samples are incubated 5 min. Afterwards samples are centrifuged (13,000 g, 10 min, 4 °C), the supernatant is removed and the pellet is resuspended in 1 ml HS buffer/1 mM PMSF. After successful mitochondrial fractioning, remaining proteins are precipitated by TCA protein precipitation. 250 µl 100% TCA solution is added to each sample and incubated for 10 min. After centrifugation (14,000 rpm, 5 min, 4 °C), the supernatant is removed and the pellet is washed with 200 µl ice cold acetone. This procedure is repeated for a total of three times and afterwards the pellet is dried on ice for 30 min. The dried pellet is taken up in 4x ROTILoad 1 and boiled for 10 min at 95 °C to dissolve the pellet. Finished samples are stored at -80 °C and later analyzed by WB. When performing Western blot, marker proteins for each mitochondrial fraction must be detected to determine in which mitochondrial fraction the protein of interest is located.

4.2.8 Real time quantitative polymerase chain reaction (qPCR)

4.2.8.1 RNA extraction from cells

The entire experiment is performed on ice. Cells are cultivated on 8.7 cm^2 culture dishes up to 80 % confluency. Once 80 % confluency is reached, cell culture medium is removed and cells are harvested by adding 1 ml ROTIZol. The cell lysate is transferred to a 2 ml RNAse free tube and thoroughly vortexed. Afterwards 200 µl chloroform is added to the sample, the sample is thoroughly vortexed, left to stand for 10 min and centrifuged (10,000 rpm, 15 min, 4 °C). In the meantime, 1 µl glycogen is

pipetted into a fresh RNAse free 2 ml tube. As a result of the centrifugation the cell lysate separates into three phases. The clear upper phase contains the RNA, the white interphase consists of precipitated DNA floating on top of the lower green phenol chloroform phase (Figure 25). The upper phase is removed carefully and transferred to the glycogen containing tube, while the other two phases are discarded. At this point, it is important that none of the DNA and phenol chloroform phase are transferred to the new tube along with the RNA. Next 500 µl isopropanol is added to the RNA solution, the sample is thoroughly vortexed, left to stand for 10 min and centrifuged (13,000 rpm, 15 min, 4 °C). The supernatant is discarded, while the precipitated RNA is washed with 1 ml 70 % ethanol and centrifuged (13,000 rpm, 10 min, 4 °C). After centrifugation the entire ethanol is removed and the white RNA pellet is air dried on ice until it turns transparent. In the final step the RNA pellet is resuspended in RNAse free water and its concentration and purity are determined by UV/VIS spectroscopy.

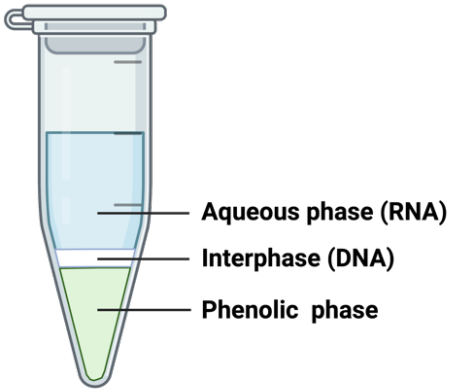

Figure 25 Phases of ROTIZol centrifugation

4.2.8.2 Conversion of messenger RNA (mRNA) to cDNA

The conversion of extracted mRNA into cDNA is performed using the High-Capacity cDNA Reverse Transcription Kit. A 10 µl RNA sample, containing 2 µg RNA, is mixed with 10 µl freshly prepared 2x mastermix. The mastermix consists of 10x buffer, dNTPs, random primers and reverse transcriptase, all diluted in nuclease-free water. In addition, a Mock sample (Mastermix replaced by nuclease free water) is prepared. The samples are placed into a polymerase chain reaction (PCR) cycler and run 10 min at 25 °C, followed by 120 min at 37 °C and finally 5 min at 85 °C. Once the PCR is finished, the cDNA is cooled to 4 °C and either used immediately or stored at -20 °C for later use. All described steps, except the PCR, are performed on ice.

4.2.8.3 qPCR performance

TaqMan based qPCR is performed in a transparent 96-well plate using QuantStudio 5 Real-Time PCR. TaqMan assays contain gene specific forward and reverse primers as well as a sequence specific oligonucleotide called Probe. Probe holds a fluorescent molecule called Promotor at the 5’ end, a Quencher molecule at the 3’ end and cannot be extended due to the absence of a free hydroxyl group. When the Promotor and Quencher are close to each other, as they are bound to the oligonucleotides, the energy absorbed by the Promotor is transferred to the Quencher thereby suppressing the fluorescence emission. During the PCR, single stranded DNA is extended by the AmpliTaq Fast DNA Polymerase. Once the DNA polymerase reaches a Probe bound to the DNA it cleaves the Probe with its exonuclease activity and releases the Promotor and Quencher. Now that the Promotor is freed from the Quencher, it emits a fluoresce signal proportional to the duplication of the DNA, which is measured in real time by the instrument. TaqMan based qPCR starts by pipetting 18 µl Mastermix, containing TaqMan Fast Advanced Master Mix and the gene specific TaqMan Assay into each well, followed by 2 µl cDNA solution (c= 5 ng/µl) or 2 µl nuclease-free water for the blank. For each sample, as well as for blank and Mock samples, triplets for the gene of interest and housekeeping gene are prepared. Once each well is loaded, the plate is sealed with an optical adhesive film, centrifuged (900 g, 2 min, RT) to remove bubbles, placed into the instrument and the PCR is run.

4.3 Statistical analysis

Statistical analysis of the data was performed using GraphPad Prism software. The measured values are presented as mean values with standard error of the mean (±SEM). Student's unpaired t-test was performed to test for statistically significant differences between two data sets.

5 RESULTS

5.1 Mitochondrial localization of SV2A

5.1.1 SV2A is located at mitochondria

To investigate whether SV2A is expressed at mitochondria, SH-SY5Y cells were analyzed using confocal microscopy. On confocal images, SV2A appears as the expected vesicular structures evenly distributed throughout the cell. Interestingly, SV2A is frequently found at mitochondria, indicated by yellow spots across mitochondria (Figure 26A). Notably, high density areas of SV2A are particularly abundant at mitochondria. Localization of SV2A at mitochondria is further confirmed by an average Pearson's r of 0.75 (Figure 26B).

To get a closer look on the mitochondrial localization of SV2A, SH-SY5Y cells were analyzed using ground state depletion microscopy followed by individual molecule return (GSDIM) super-resolution microscopy. With its resolution ~15 times higher in xy-direction than conventional confocal microscopy, super-resolution microscopy allowed the fine mapping of cellular structures and differentiation of single molecules. On super-resolution images mitochondria are visualized by staining of translocase of the outer mitochondrial membrane subunit 20 (TOM20). The close proximity and colocalization of SV2A and TOM20 observed on super-resolution images support the confocal data and confirm that SV2A is located at mitochondria. Colocalization of SV2A and TOM20 on super-resolution images indicates that SV2A and TOM20 are less than 40 nm apart (Figure 26C). CBC values calculated for the interaction of SV2A with TOM20 reveal that 14.1 % of SV2A molecules possess CBC values ≥0.5, therefore colocalize with TOM20 and are present at mitochondria (Figure 26E).

As the name implies, super-resolution microscopy is very precise thus visualizing and analyzing the localization of SV2A at TOM20, rather than of SV2A at the entire mitochondrion. To obtain super-resolution data on the localization of SV2A across entire mitochondria, SV2A localization was assessed in mitochondrial regions defined by TOM20. 34.5 % of SV2A molecules are located in mitochondrial regions, which is three times higher than the CBC values of SV2A at TOM20 and proves again that SV2A is located at mitochondria (Figure 26F).

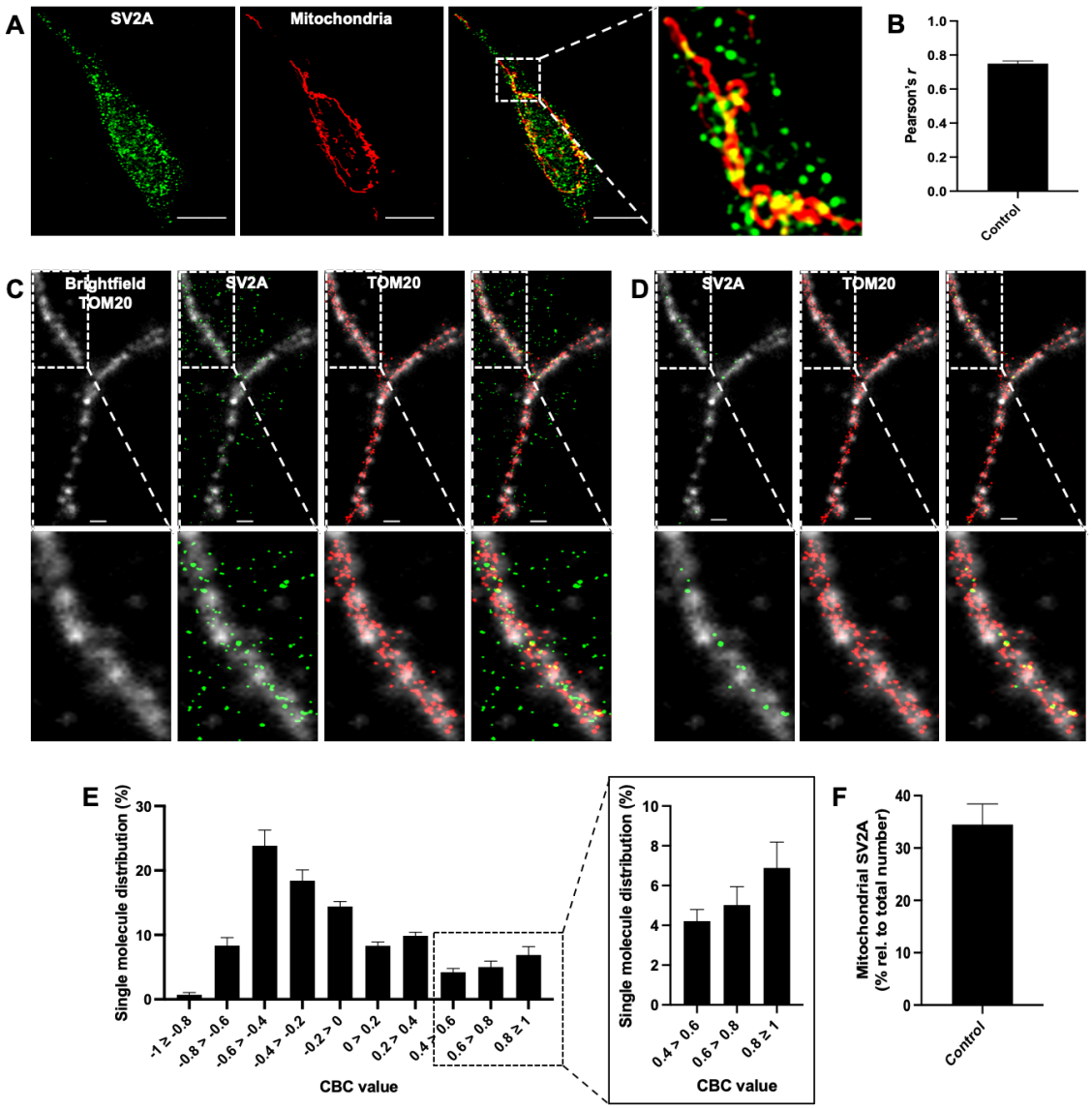

Figure 26 SV2A is located at mitochondria

(A-B) Representative confocal images of SH-SY5Y cells stained for SV2A and mitochondria. Colocalization of SV2A and mitochondria is indicated by yellow spots. Enlarged image of the boxed area is displayed at the end of the image series (A). Mean of Pearson's r values calculated for each imaged cell demonstrates the colocalization of SV2A and mitochondria (B). Analyzed were 54 cells. Scale bar: 10 µm. **(C-D)** Representative super-resolution images of SH-SY5Y cells stained for SV2A and TOM20 (C). Representative super-resolution images of TOM20 and SV2A proteins with CBC values ≥0.5, indicating that these SV2A molecules colocalize with TOM20 (D). Mitochondrial area is displayed by gray brightfield image of TOM20. Enlarged images of boxed areas are displayed underneath. Scale bar: 1 µm. **(E)** Histogram of CBC value distribution for the colocalization of SV2A and TOM20. Enlarged are CBC values corresponding to colocalization of the two proteins. **(F)** Percentage of SV2A molecules within

mitochondrial areas**.** Staining according to Table 14+17. Analyzed were 11 cells. Data are expressed as mean ± SEM.

5.1.2 Mitochondrial stress increases the localization of SV2A at mitochondria

5.1.2.1 Effect of complex I inhibitor rotenone on SV2A localization

Since LEV improves cognition of AD patients, 5xFAD mice and attenuates mitochondrial dysfunction in cell models of AD, the question arose if mitochondrial stress increases or decreases levels of SV2A at mitochondria. Since the progression of Alzheimer's disease is associated with the disruption of complex I of the ETC causing increased ROS levels, AD like mitochondrial disruption and elevated ROS levels were simulated by treating SH-SY5Y cells with 5 µM complex I inhibitor rotenone for 24 h.

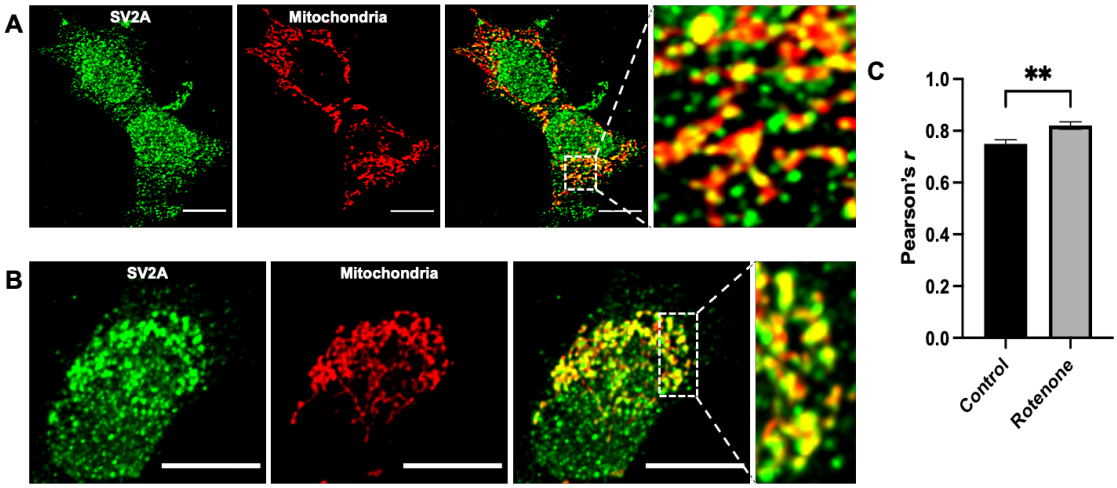

Figure 27 Mitochondrial localization of SV2A increases upon mitochondrial stress

(A-B) Representative confocal images of rotenone (5 µM/24 h) treated SH-SY5Y cells stained for SV2A and mitochondria. Increased colocalization of SV2A and mitochondria compared to control is indicated by yellow spots (A). The more severe mitochondria are fragmented, the more SV2A is present (B). Enlarged images of boxed areas are displayed at the end of each image series. Scale bar: 10 µm. **(C)** Mean of Pearson's r values calculated for each imaged cell confirm the increased colocalization of SV2A and mitochondria upon mitochondrial stress induced by rotenone. Staining according to Table 14. Cells analyzed: control: 54; rotenone treated: 36. Data are expressed as mean ± SEM; student's unpaired t-test (*p <0.05; **p <0.01, ***p <0.001).

As a result of complex I inhibition, mitochondria are fragmented, spherical and no longer demonstrate a tubular, interconnected network. SV2A, on the other hand, again resembles vesicular structures spread throughout the cell, with some areas of high density. As expected SV2A is also found at mitochondria experiencing mitochondrial stress. Indeed, SV2A seems to be particularly abundant at highly fragmented and spherical mitochondria (Figure 27A, B). As indicated by the images, Pearson's r rose significantly from 0.75 to 0.82 compared to control cells. Especially high density areas of SV2A interact with mitochondria.

Confocal images of rotenone treated cells demonstrate that SV2A increasingly resides at impaired mitochondria, especially when highly fragmented. For a more detailed examination, SH-SY5Y cells treated with 5 µM rotenone for 24 h were imaged using a super-resolution microscope. Super-resolution images also display that SV2A is more abundant among damaged mitochondria, especially when they are highly fragmented and spherical (Figure 28). Figure 28 features super-resolution images of mildly and highly fragmented mitochondria derived from the same image and cell. Surprisingly, only a minor enhancement in localization of SV2A to TOM20 is observed when mitochondria are slightly fragmented (Figure 28A, B). In contrast, highly fragmented mitochondria express increased localization of SV2A to TOM20, as predicted from the confocal data (Figure 28C). The increased localization of SV2A at fragmented mitochondria is also confirmed by images displaying only SV2A molecules colocalizing with TOM20 (CBC ≥0.5) (Figure 28D). Surprisingly CBC values ≥0.5 decrease by 1.1 % in rotenone treated cells (13 %) compared to control (14,1 %) (Figure 28E). Nevertheless, super-resolution data demonstrate that localization of SV2A increases among fragmented mitochondria, matching the confocal data.

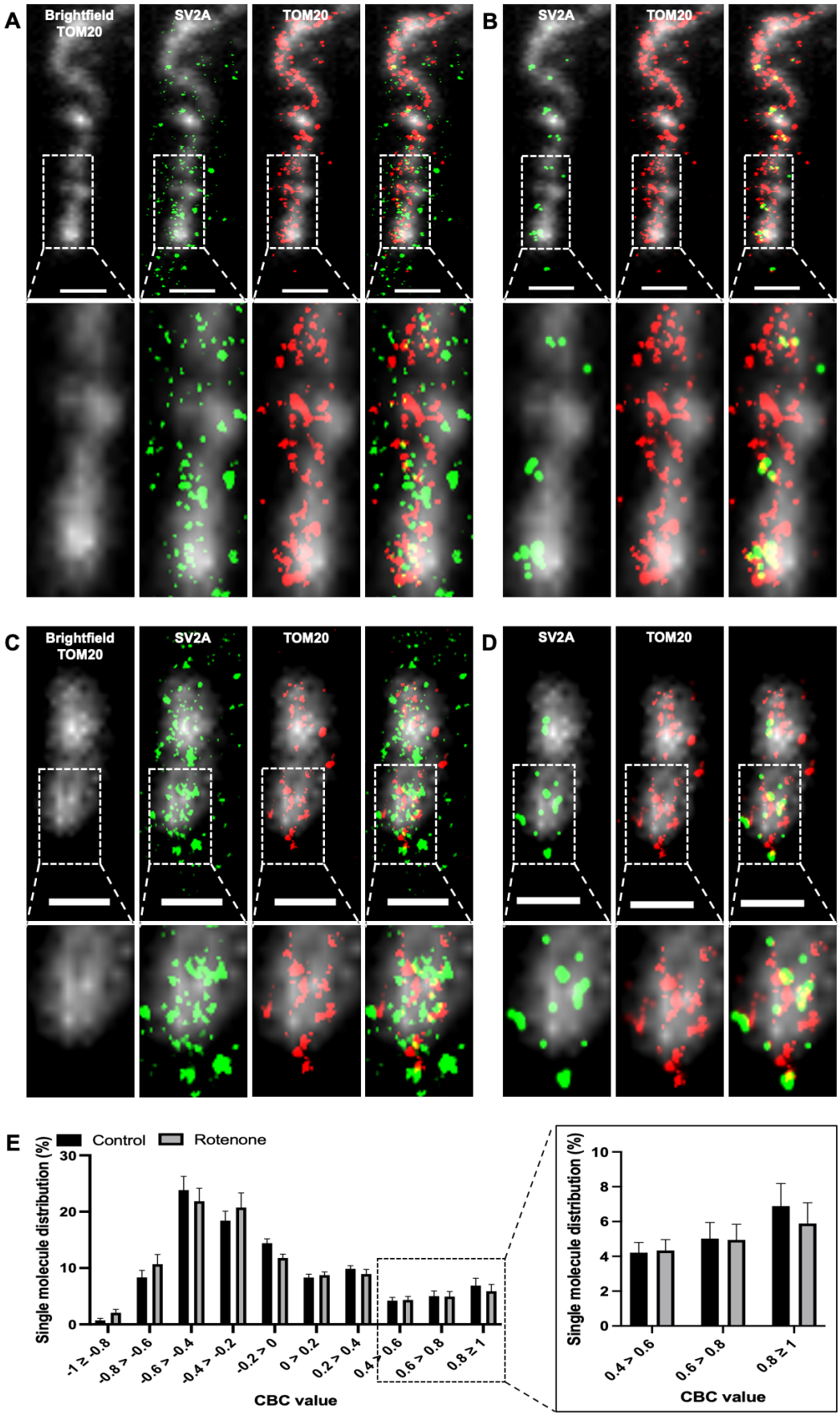
A
Brightfield
TOM20
SV2A
TOM20
B
SV2A
TOM20
C
Brightfield
TOM20
SV2A
TOM20
D
SV2A
TOM20
E
Control
Rotenone
Single molecule distribution (%)
30
20
10
0
-1 ≥ -0.8
-0.8 > -0.6
-0.6 > -0.4
-0.4 > -0.2
-0.2 > 0
0 > 0.2
0.2 > 0.4
0.4 > 0.6
0.6 > 0.8
0.8 ≥ 1
CBC value
Single molecule distribution (%)
10
8
6
4
2
0
0.4 > 0.6
0.6 > 0.8
0.8 ≥ 1
CBC value

Figure 28 Mitochondrial localization of SV2A increases upon mitochondrial stress

(A-B) Representative super-resolution images of SH-SY5Y cells treated with rotenone (5 µM/24 h) stained for SV2A and TOM20 (A). Representative images of TOM20 and SV2A proteins with CBC values ≥ 0.5, indicating that these SV2A molecules colocalize with TOM20. Mitochondrial area is displayed in gray. Enlarged images of boxed areas are displayed underneath. Scale bar: 1 µm. **(C-D)** Representative super-resolution images displaying that SV2A is more abundant at severely fragmented mitochondria. Mitochondrial area is displayed by gray brightfield image of TOM20. Enlarged images of boxed areas are displayed underneath. Scale bar: 1 µm. **(E)** Histogram comparing the mean CBC value distribution of SV2A and TOM20 in control and rotenone treated SH-SY5Y cells. Enlarged are CBC values corresponding to colocalization of the two proteins (E). Staining according to Table 17. Cells analyzed: control: 11; rotenone treated: 9. Data are expressed as mean ± SEM; student's unpaired t-test (*p <0.05; **p <0.01, ***p <0.001).

5.1.2.2 Effect of mitochondrial uncoupler CCCP on SV2A localization

Confocal and super-resolution data of rotenone treated cells, demonstrate that mitochondrial localization of SV2A increases especially at highly fragmented mitochondria. To assess if greater mitochondrial fragmentation accelerates mitochondrial localization of SV2A, SH-SY5Y cells were treated with 1 µM CCCP for 24 h. As a mitochondrial uncoupler, CCCP is a more potent stressor than rotenone and disrupts the internal mitochondrial proton gradient, crucial for ATP synthesis. As expected, CCCP treatment caused severe fragmentation of mitochondria. On super-resolution images SV2A occurs similar to control and rotenone treated cells, yet the overall expression of SV2A appears to have increased (Figure 29). Moreover, as expected, SV2A is present in increased levels at CCCP damaged mitochondria (Figure 29A). However surprisingly, the percentage of SV2A molecules bearing CBC values ≥0.5 is 9.9 % in CCCP treated cells, hence lower than in control (14.1 %) and rotenone treated cells (13 %) (Figure 29C).

As already indicated by the super-resolution images, cellular expression of SV2A increases upon mitochondrial stress, doubling in cells treated with CCCP and increasing slightly in cells treated with rotenone (Figure 30A). To investigate if the localization of SV2A increases at dysfunctional mitochondria, the number of SV2A molecules in mitochondrial regions was determined in cells treated with rotenone and CCCP.

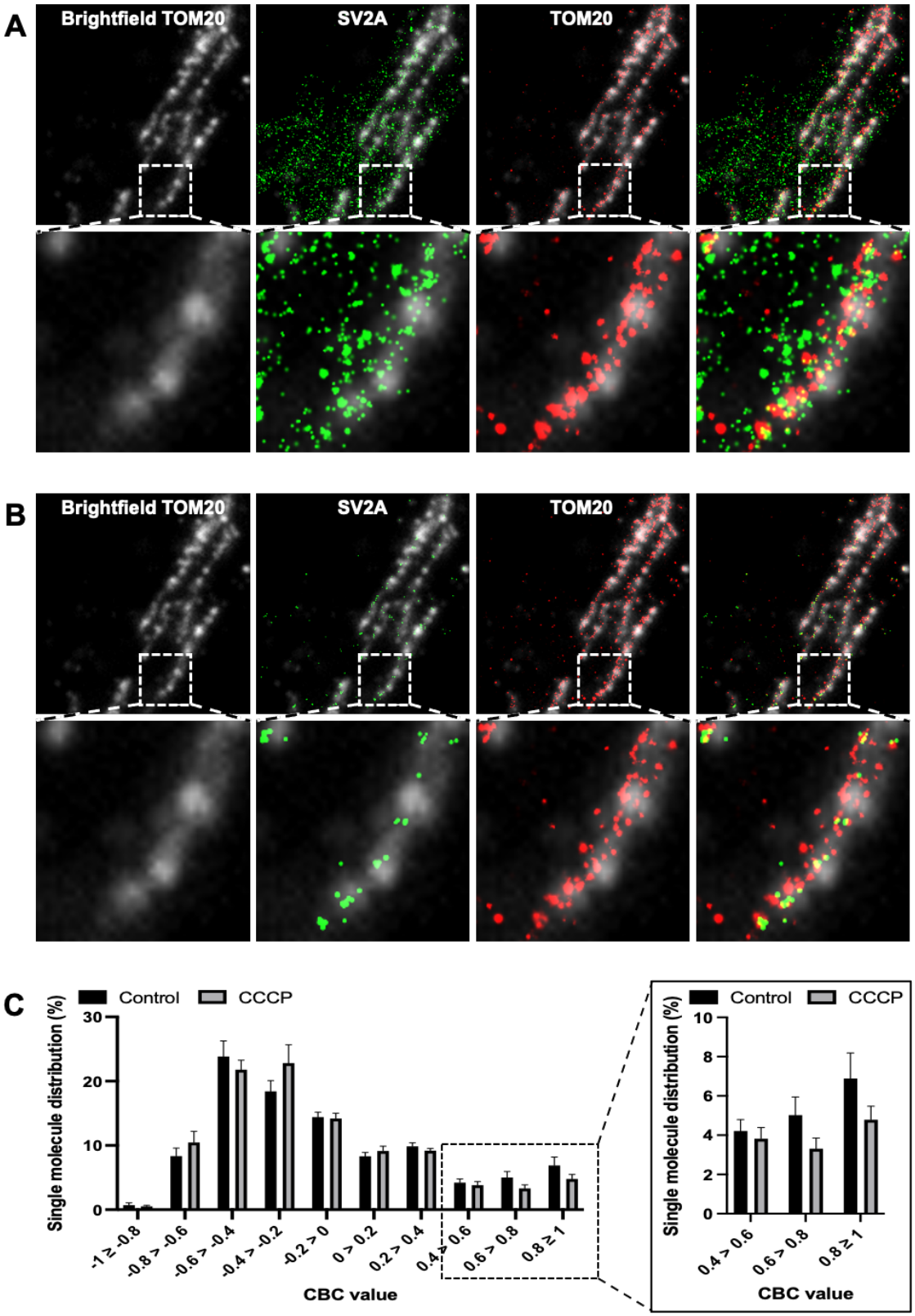
A
Brightfield TOM20
SV2A
TOM20
B
Brightfield TOM20
SV2A
TOM20
C
Control
CCCP
Single molecule distribution (%)
30
20
10
0
-1 ≥ -0.8
-0.8 > -0.6
-0.6 > -0.4
-0.4 > -0.2
-0.2 > 0
0 > 0.2
0.2 > 0.4
0.4 > 0.6
0.6 > 0.8
0.8 ≥ 1
CBC value
Control
CCCP
Single molecule distribution (%)
10
8
6
4
2
0
0.4 > 0.6
0.6 > 0.8
0.8 ≥ 1
CBC value

Figure 29 Mitochondrial localization of SV2A in CCCP treated cells

(A-B) Representative super-resolution images of SH-SY5Y cells treated with mitochondrial uncoupler CCCP (1 µM/24 h) stained for SV2A and TOM20 (A). Representative super-resolution images of TOM20 and SV2A proteins with CBC values ≥0.5, indicating that these SV2A molecules colocalize with TOM20 (B). Mitochondrial area is displayed by gray brightfield image of TOM20. Enlarged images of boxed areas are displayed underneath. Scale bar: 1 µm. **(C)** Histogram comparing the CBC value distribution of SV2A and TOM20 in control and CCCP treated SH-SY5Y cells. Enlarged are data of CBC values corresponding to colocalization of the two proteins. Staining according to Table 17. Cells analyzed: control: 11; CCCP treated: 9. Data are expressed as mean ± SEM; student's unpaired t-test (*p <0.05; **p <0.01, ***p <0.001).

The hypothesis that mitochondrial SV2A localization increases in relation to the severity of mitochondrial stress is proven, as SV2A is most abundant among mitochondria in CCCP treated cells and least abundant in control cells (Figure 31B).

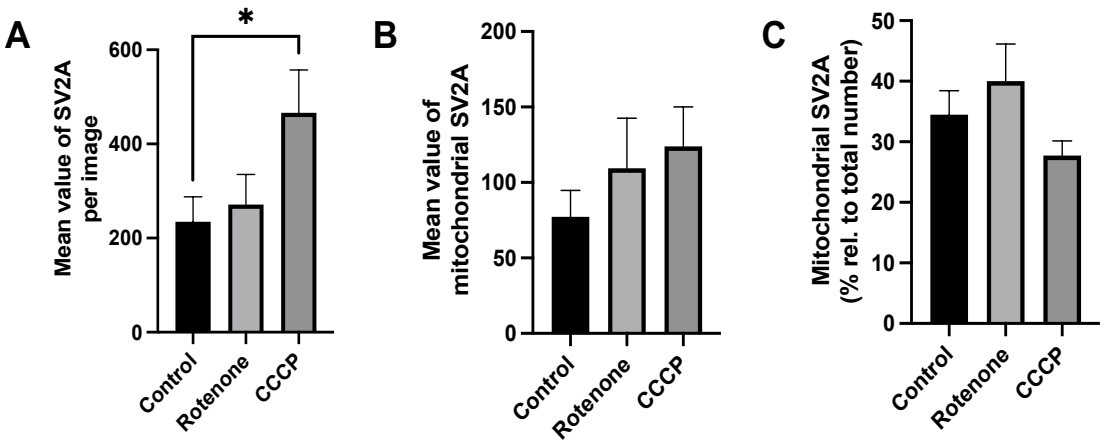

Figure 30 SV2A number increases in stressed cells and at mitochondria

(**A)** Mean values of SV2A molecules per cell in rotenone (5 µM/24 h) and CCCP (1 µM/24 h) treated cells compared to control. **(B)** Mean values of mitochondrial SV2A in rotenone (5 µM/24 h) and CCCP (1 µM/24 h) treated cells compared to control. **(C)** Percentage of mitochondrial SV2A relative to the total number of SV2A molecules per cell in rotenone (5 µM/24 h) and CCCP (1 µM/24 h) treated cells compared to control. Cells analyzed: control: 11; rotenone treated: 9; CCCP treated: 9. Data are expressed as mean ± SEM; student's unpaired t-test (*p <0.05; **p <0.01, ***p <0.001).

Moreover, the percentage of SV2A molecules in mitochondrial regions increased to 40 % in rotenone treated cells compared to 34.5 % in control cells, while surprisingly decreasing to 27.7 % upon CCCP treatment (Figure 30C). Interestingly, CCCP perturbed mitochondria express the highest number of SV2A molecules but the lowest percentage of mitochondrial SV2A (Figure 30A).

5.1.3 SV2A is located at the outer mitochondrial membrane

SV2A is located at mitochondria, where it accumulates in response to mitochondrial stress. But where exactly on or in mitochondria SV2A is located remains to be elucidated. Being a transmembrane protein, SV2A is most likely located in either the OMM or the IMM. Other, rather unlikely possibilities are the IMS and the mitochondrial matrix. Isolated mitochondria were exposed to increasing concentrations of digitonin, to disintegrate mitochondria into their individual fractions. Samples were afterwards analyzed by WB using specific marker proteins for the respective mitochondrial fractions. As expected, SV2A is located at the outer mitochondrial membrane, as the SV2A band appears in the first well, where the OMM marker TOM20 band is also still present and the joint disappearance of the SV2A and TOM20 bands in the second well (Figure 31). The purity of isolated mitochondria is verified by the absence of the cytosolic marker α-tubulin.

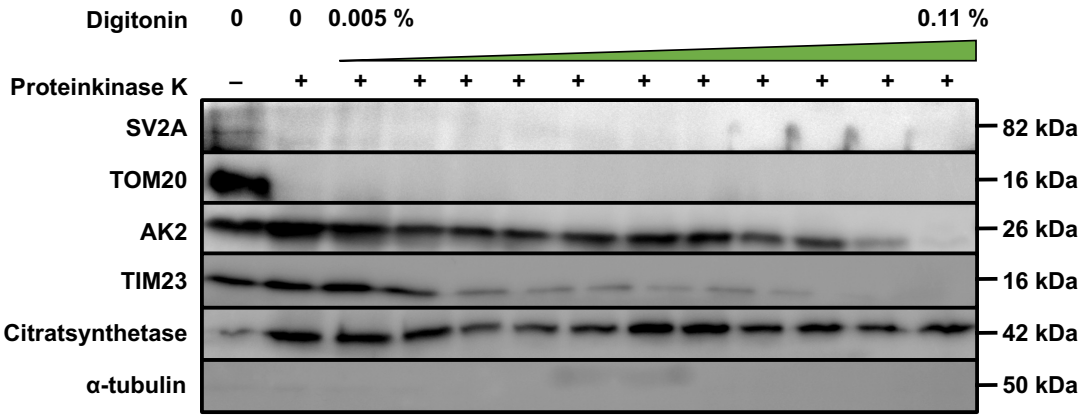

Figure 31 SV2A is located at the outer mitochondrial membrane

Western blot of mitochondrial fractions. 30 µg protein were loaded per well. For each mitochondrial fraction, a marker protein was detected to visualize the existing fractions per lane. SV2A (protein of interest), TOM20 (OMM), AK2 (IMS), TIM23 (IMM), Citrasynthetase (matrix), α-tubulin (cytosolic marker). 3 independent extracts were analyzed.

5.2 Vesicular interactions of SV2A with mitochondria

5.2.1 Physiological conditions

Having demonstrated that SV2A is located at the outer mitochondrial membrane, it was of interest to determine whether the mitochondrial localization of SV2A has a vesicular background, since SV2A is located at the outer mitochondrial membrane, where synaptic vesicles could interact with mitochondria. Confocal microscopy was performed to characterize the interaction of SV2A, vesicles defined by staining of VAMP2 and mitochondria in SH-SY5Y cells. On confocal images, SV2A and mitochondria appear similar as on previous images of untreated cells, with SV2A being located at mitochondria (Figure 32B). The mitochondrial localization of SV2A is confirmed by a Pearson's r of 0.66 (Figure 32E). Resembling vesicles VAMP2 is distributed throughout the cell with some areas of high density similar to SV2A. As they are both synaptic vesicle proteins, SV2A and VAMP2 frequently colocalize with each other, also reflected by a Pearson's r of 0.69 (Figure 32C, F). Interestingly, although SV2A and VAMP2 are vesicular proteins, they also exist separated from each other. Unexpectedly, VAMP2 is present at mitochondria, as reflected by Pearson’s r of 0.6 (Figure 32D, G). Consequently, it is not surprising that SV2A is present along with VAMP2 at mitochondria (white arrows) (Figure 32 A). SV2A occurs either alone or in association with VAMP2 at mitochondria, whereas VAMP2 commonly occurs in association with SV2A at mitochondria. Nevertheless, the two proteins behave alike on the images, and Pearson's r values show no significant difference between the two proteins at mitochondria, despite a tendency that SV2A is more abundant.

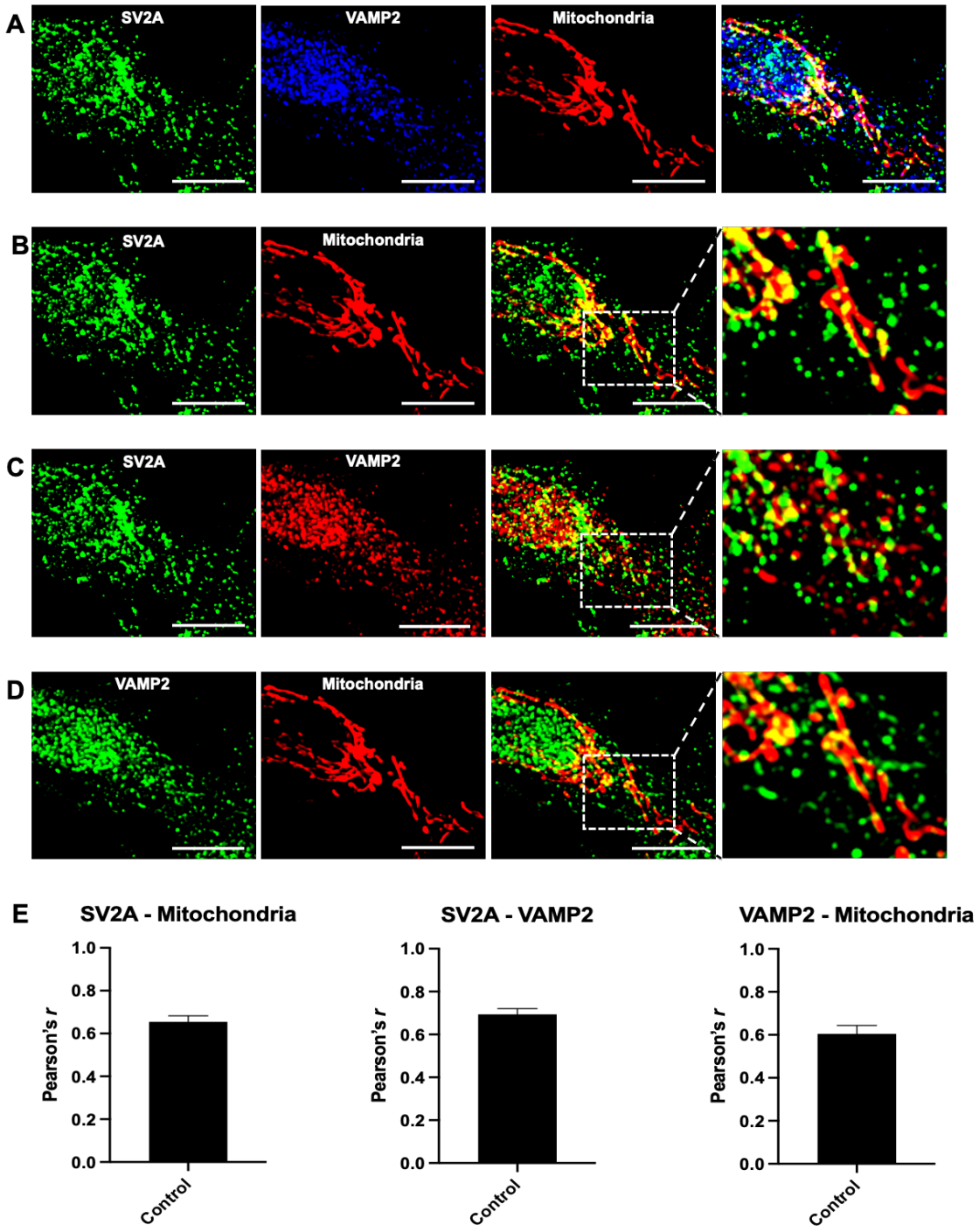

Figure 32 Localization of SV2A and VAMP2 at mitochondria

(A) Representative confocal images of SH-SY5Y cells stained for SV2A, VAMP2 and mitochondria. Colocalization of the three is indicated by bright white spots. **(B)** Representative confocal images of cells stained for SV2A and mitochondria. Yellow indicates colocalization. **(C)** Representative confocal images of cells stained for SV2A and VAMP2. Yellow indicates colocalization. **(D)** Representative confocal images of cells stained for VAMP2 and

mitochondria. Yellow indicates colocalization. **(E-G)** Pearson's r values display colocalization of SV2A with mitochondria, SV2A with VAMP2 and VAMP2 with mitochondria. Enlarged images of boxed areas are displayed at the end of each image series. Staining according to Table 14. Analyzed were 9 cells. Scale bar: 10 µm. Data are expressed as mean ± SEM.

To verify that SV2A is higher abundant at mitochondria than VAMP2 and that SV2A interacts with mitochondria detached from vesicles, the interaction between VAMP2 and TOM20 (mitochondria) was analyzed using super-resolution microscopy. Super-resolution data confirm that VAMP2 is present at mitochondria (Figure 33A). As for SV2A, direct colocalization of VAMP2 and TOM20 exists. When only VAMP2 molecules with CBC values ≥0.5 are displayed, it is obvious that the majority of VAMP2 molecules are located at small mitochondria rather than tubular ones, similar to SV2A (Figure 33B). 9.7 % of VAMP2 molecules exhibit CBC values ≥0.5 (Figure 33C).

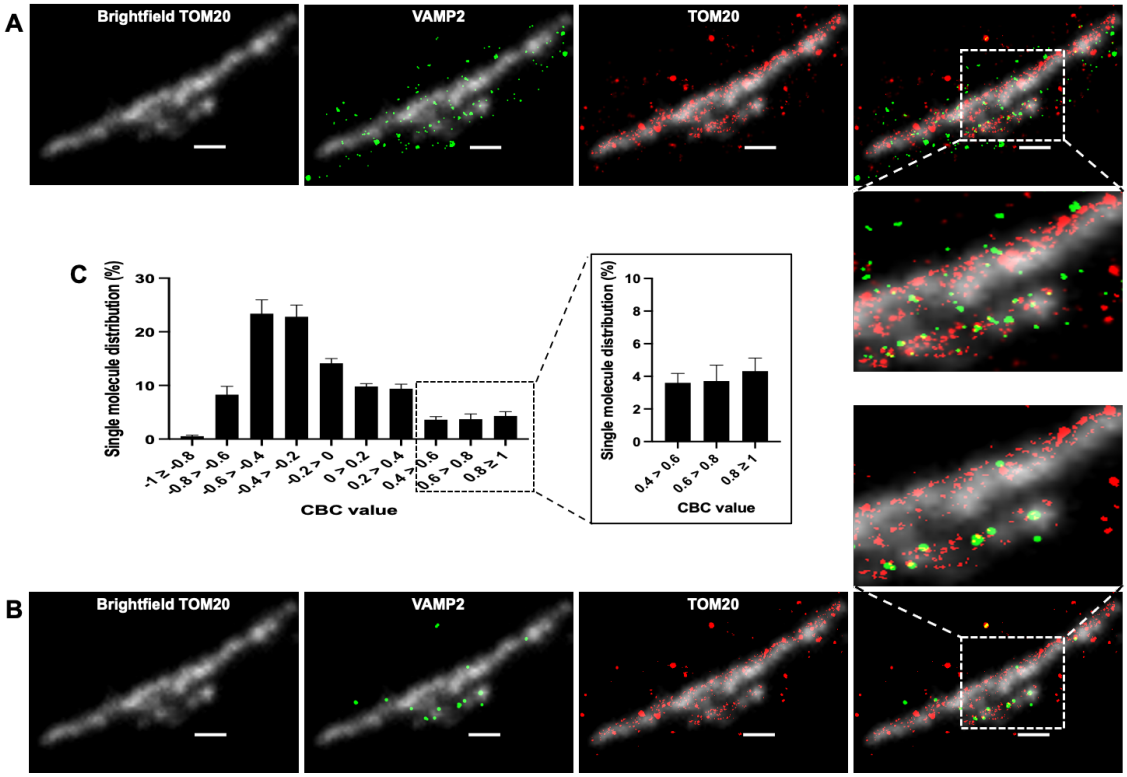

Figure 33 VAMP2 is present at mitochondria

(A-B) Representative super-resolution images of SH-SY5Y cells immunostained for VAMP2 and TOM20 (A). Representative super-resolution images of TOM20 and VAMP2 proteins with CBC values ≥0.5, indicating that these VAMP2 molecules colocalize with TOM20 (B). Mitochondrial area is displayed by gray brightfield image of TOM20. Enlarged images of boxed areas are displayed underneath (A) or above (B) the image series. Scale bar: 1 µm. **(C)** Histogram of

CBC value distribution for the colocalization of VAMP2 and TOM20. Enlarged are data of CBC values corresponding to colocalization of the two proteins. Staining according to Table 17. Analyzed were 13 images. Data are expressed as mean ± SEM.

5.2.2 Effect of rotenone on VAMP2 localization

Investigations on the relationship of SV2A and VAMP2 (vesicles) by confocal and super-resolution microscopy revealed that SV2A occurs both attached and detached from vesicular structures in the cytosol and at mitochondria. Surprisingly, as SV2A and VAMP2 share similar localization patterns, an interaction between VAMP2 and mitochondria was also detected, although the localization of SV2A appeared to be higher at mitochondria. Moreover, super-resolution microscopy showed that the localization of VAMP2 is higher at short mitochondria, analogous to SV2A. Consequently, it was investigated if the interaction of VAMP2 and SV2A as well as their mitochondrial localization is altered in SH-SY5Y cells treated with 5 µM complex I inhibitor rotenone for 24 h.

Rotenone induced mitochondrial stress, caused mitochondrial fragmentation (Figure 34A). SV2A appears similar to previous images of rotenone treated cells in that mitochondrial localization of SV2A is greater at impaired mitochondria, demonstrated also by a significant increase in Pearson's r from 0.66 to 0.84 compared to untreated cells (Figure 34B, E). Not surprising for two vesicle proteins, SV2A and VAMP2 still colocalize upon rotenone treatment. Colocalization of the two vesicle proteins even increases as the Pearson's r rose from 0.69 to 0.77 compared to control (Figure 34C, F). As expected from previous data of untreated cells, VAMP2 behaves similarly to SV2A in that it is more abundant among fragmented mitochondria, as demonstrated by Pearson's r significantly rising from 0.6 to 0.77 upon rotenone treatment (Figure 34D, G). It is therefore not surprising that the colocalization of SV2A and VAMP2 at mitochondria also increases (Figure 34A). Despite their increased colocalization at mitochondria, SV2A remains to be separated from VAMP2 sometimes and is more abundant at mitochondria, whereas VAMP2 continues to rely on SV2A at mitochondria.

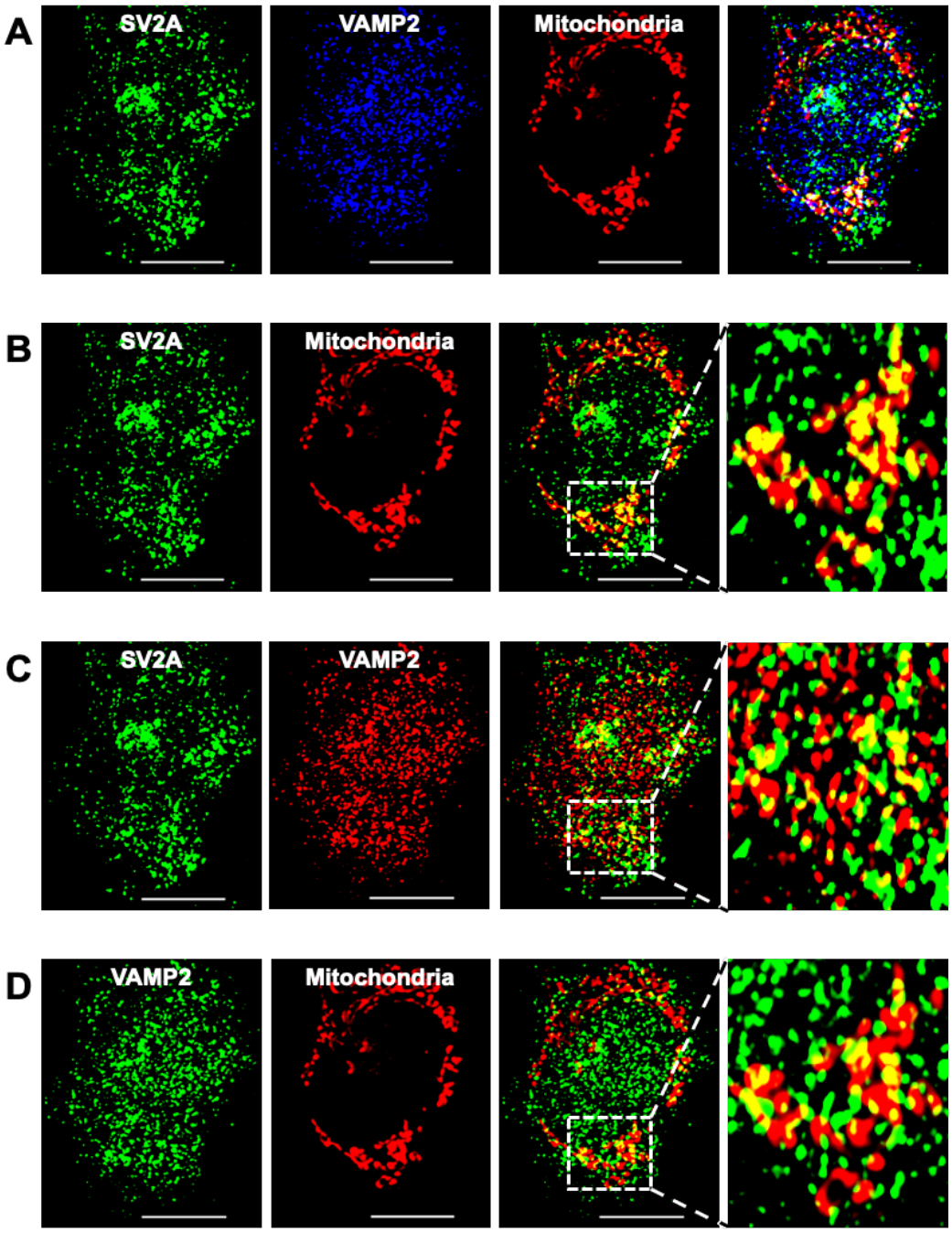
A
SV2A
VAMP2
Mitochondria
B
SV2A
Mitochondria
C
SV2A
VAMP2
D
VAMP2
Mitochondria

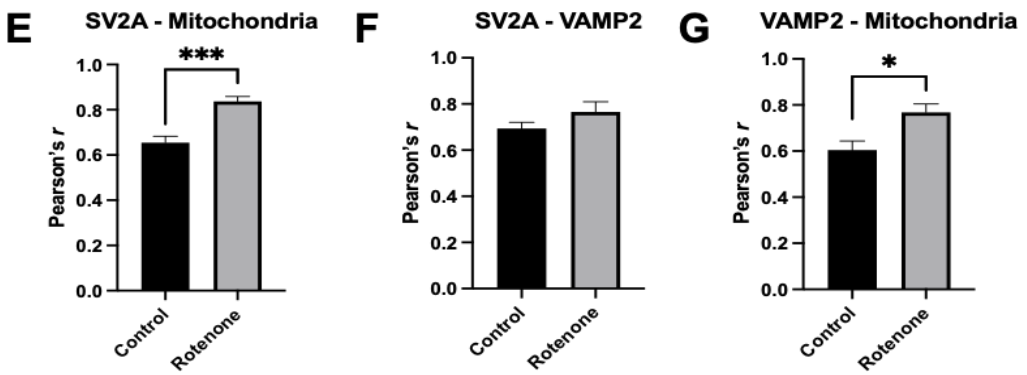
E
SV2A - Mitochondria
***
Pearson's r
1.0
0.8
0.6
0.4
0.2
0.0
Control
Rotenone
F
SV2A - VAMP2
Pearson's r
Control
Rotenone
G
VAMP2 - Mitochondria
*
Pearson's r
Control
Rotenone

Figure 34 Mitochondrial localization of SV2A and VAMP2 increase upon mitochondrial stress

(A) Representative confocal images of rotenone (5 µM/24 h) treated SH-SY5Y cells stained for SV2A, VAMP2 and mitochondria. Colocalization of the three is indicated by bright white spots. **(B)** Representative confocal images of rotenone (5 µM/24 h) treated cells stained for SV2A and mitochondria. Yellow indicates colocalization. **(C)** Representative confocal images of rotenone (5 µM/24 h) treated cells stained for SV2A and VAMP2. Yellow indicates colocalization. **(D)** Representative confocal images of rotenone (5 µM/24 h) treated cells stained for VAMP2 and mitochondria. Yellow indicates colocalization. **(E-G)** Mean of Pearson's r values calculated for each imaged cell confirm the increased colocalization of SV2A with mitochondria (E), of SV2A with VAMP2 (F) and of VAMP2 with mitochondria (G) upon mitochondrial stress. Enlarged images of boxed areas are displayed at the end of each image series. Staining according to Table 14. Cells analyzed: control: 9; rotenone treated: 6. Scale bar: 10 µm. Data are expressed as mean ± SEM; student's unpaired t-test (*p <0.05; **p <0.01, ***p <0.001).

Based on the confocal data of rotenone treated cells, super-resolution images of the interplay between VAMP2 and TOM20 (mitochondria) during mitochondrial stress were acquired. SH-SY5Y cells were treated with 5 µM rotenone for 24 h. Mitochondria affected by rotenone are fragmented, swollen and feature aberrant morphologies (Figure 35). VAMP2 expression increases during rotenone treatment throughout the cell, building large agglomerates especially at fragmented mitochondria (Figure 35A). Enhanced colocalization of VAMP2 and TOM20 is the result, which is also confirmed by images displaying only VAMP2 molecules with CBC values ≥0.5 (Figure 35B). VAMP2 is again most abundant among fragmented mitochondria. Indeed, the increased colocalization of VAMP2 and TOM20 is reflected in CBC values ≥0.5, which increased to 11.7 %, indicating greater colocalization of VAMP2 and mitochondria in rotenone treated cells (Figure 35C). As CBC values represent only the localization of VAMP2 at TOM20, but not at the whole mitochondrion, VAMP2 molecules located in mitochondrial regions were also quantified. In untreated cells, 28.5 % of VAMP2 molecules are located in mitochondrial regions, which increases significantly to 41.2 % in the presence of mitochondrial stressors (Figure 35D). Confocal data, super-resolution data and assessment of mitochondrial VAMP2 molecules demonstrate that VAMP2 attaches to mitochondria in a stress dependent manner.

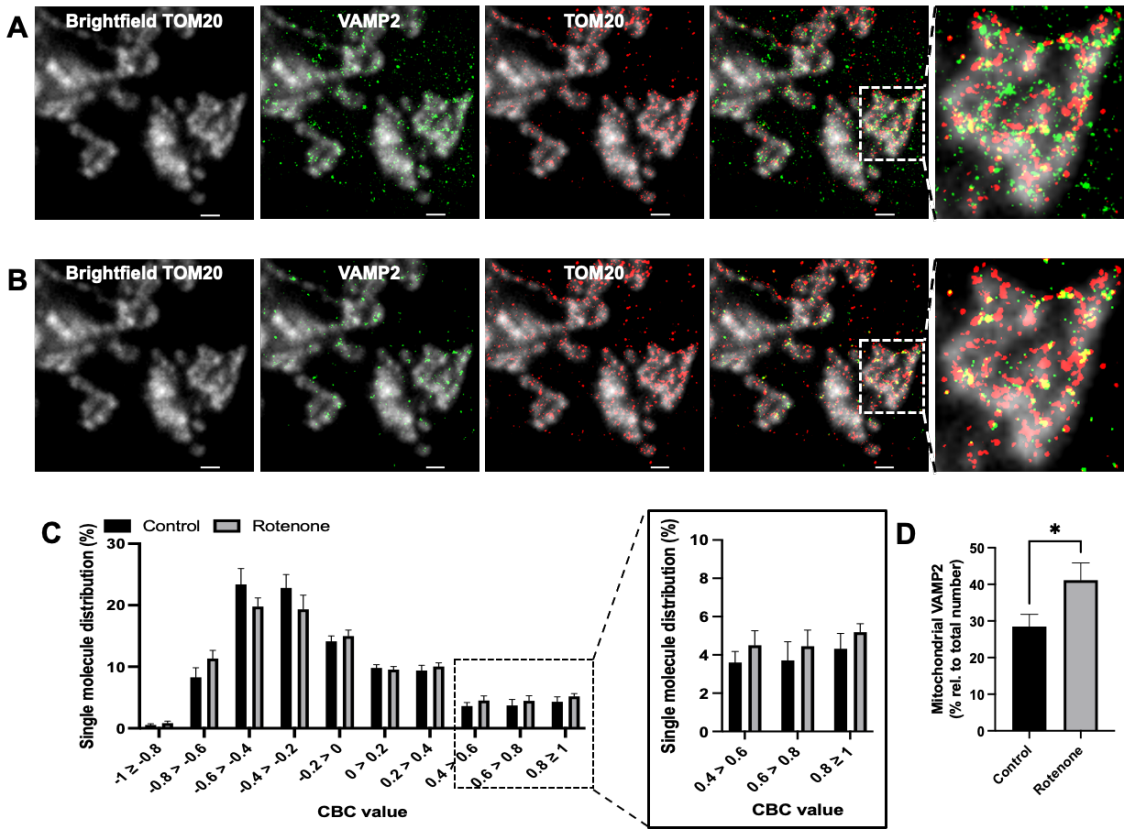

Figure 35 Mitochondrial localization of VAMP2 increases upon mitochondrial stress

(A-B) Representative super-resolution images of SH-SY5Y cells treated with rotenone (5 µM/24 h) stained for VAMP2 and TOM20 (A). Representative super-resolution images of TOM20 and VAMP2 proteins with CBC values ≥0.5, indicating that these VAMP2 molecules colocalize with TOM20 (B). Mitochondrial area is displayed by gray brightfield image of TOM20. Enlarged images of boxed areas are displayed at the end of each image series. Scale bar: 1 µm. **(C)** Histogram of CBC value distribution for the colocalization of VAMP2 and TOM20 in rotenone treated (5 µM/24 h) cells compared to control. Enlarged are data of CBC values corresponding to colocalization of the two proteins. **(D)** Percentage of VAMP2 molecules located in mitochondrial areas in rotenone treated (5 µM/24 h) cells compared to control. Staining according to Table 17. Cells analyzed: control: 13; rotenone treated: 6. Data are expressed as mean ± SEM; student's unpaired t-test (*p <0.05; **p <0.01, ***p <0.001).

5.2.3 Comparison of super-resolution data on SV2A and VAMP2 at mitochondria

SV2A and VAMP2 behave similar at mitochondria in that both are present at mitochondria, with SV2A displaying a tendency to be more abundant at healthy

mitochondria than VAMP2 and both experiencing greater localization at mitochondria during mitochondrial stress. Since only confocal data of SV2A and VAMP2 have been compared so far, the super-resolution data are now compared in terms of CBC values and molecules within mitochondrial regions.

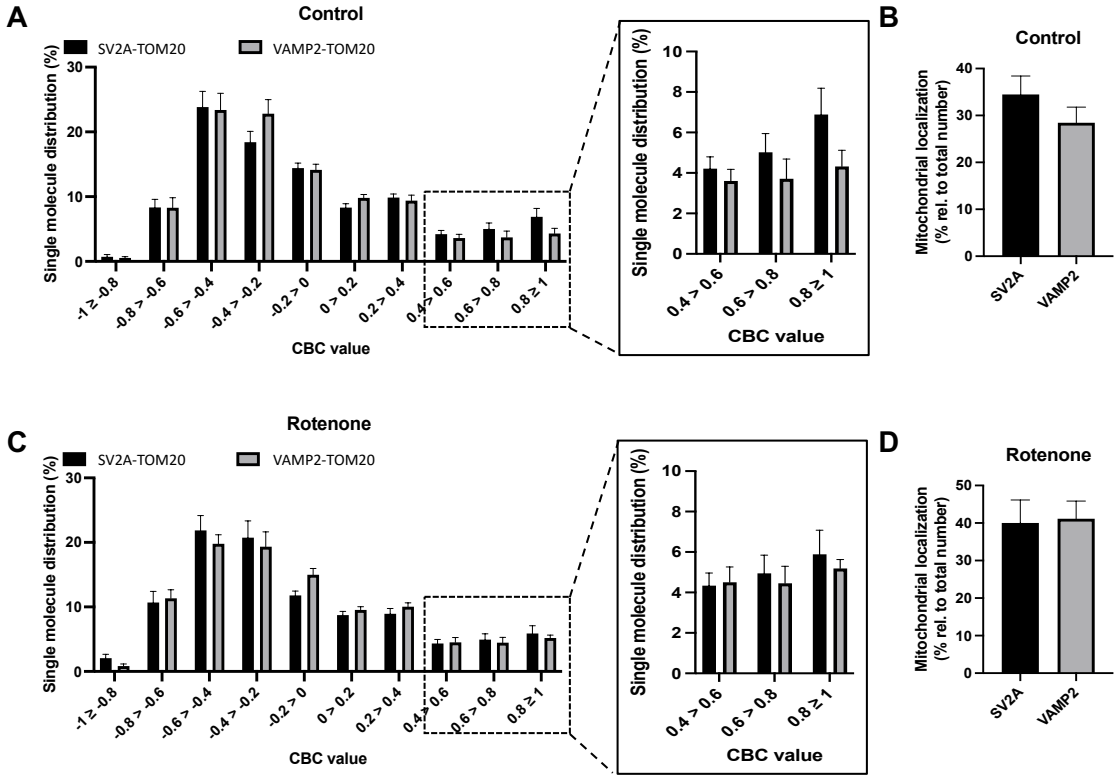

Figure 36 Comparison of super-resolution data of SV2A and VAMP2 at TOM20

(A-B) Comparison of CBC value distribution calculated for SV2A-TOM20 and VAMP2-TOM20 in untreated cells (A). Comparison of the percentage of SV2A and VAMP2 molecules located in mitochondrial areas (B). Analyzed cells: SV2A-TOM20: 11; VAMP2-TOM20: 13. **(C-D)** Comparison of CBC value distribution calculated for SV2A-TOM20 and VAMP2-TOM20 in rotenone (5 µM/24 h) treated cells (C). Comparison of the percentage of SV2A and VAMP2 molecules located in mitochondrial areas in rotenone treated (5 µM/24 h) cells (C). Analyzed cells: SV2A-TOM20: 9; VAMP2-TOM20: 6. Data are expressed as mean ± SEM; student's unpaired t-test (*p <0.05; **p <0.01, ***p <0.001).

Starting with untreated cells, CBC values ≥0.5, show a tendency for SV2A to be more abundant at mitochondria than VAMP2 as the percentage of SV2A molecules with CBC values ≥0.5 is 4.4 % higher (14.1 %) when compared to VAMP2 (9.7 %) (Figure 36A). The same trend is observed as 34.5 % of SV2A molecules in control cells are

located in mitochondrial regions compared to 28.5 % of VAMP2 molecules, although this difference is not significant (Figure 36B). Data obtained from untreated cells point to an interaction of mitochondria with both proteins which is more pronounced for SV2A. Examination of data from rotenone treated cells demonstrate that SV2A and VAMP2 behave alike in terms of colocalization with TOM20 when analyzed by CBC values ≥0.5. Although the percentage of CBC values ≥0.5 increases for VAMP2 and simultaneously decreases for SV2A, their percentages are almost the same albeit slightly higher for SV2A (13 %) compared to VAMP2 (11.7 %) (Figure 37C). Comparing the localization of SV2A and VAMP2 in mitochondrial regions of rotenone treated mitochondria, the percentage of SV2A increased to 40 % (+5.5 %) and for VAMP2 to 41.2 % (+12.7 %) (Figure 36D). These data are of particular interest as they demonstrate that both SV2A and VAMP2 localization increase markedly at dysfunctional mitochondria. Both comparison of CBC values ≥0.5 and localization of molecules in mitochondrial regions show that SV2A is more abundant among mitochondria in untreated cells, although not significant. Surprisingly, VAMP2 and SV2A behave in a similar manner during mitochondrial stress, as following rotenone treatment the greater abundance of SV2A compared to VAMP2 disappears.

5.3 SV2A affected mitochondrial and cellular processes

5.3.1 Mitochondrial dynamics

SV2A is abundant at mitochondria, more precisely at the OMM. Subsequently, potential mitochondrial functions of SV2A were investigated. In particular, how SV2A affects and controls mitochondrial dynamics. LEV is described to affect mitochondrial morphology and prolong mitochondria in control cells and cell models of FAD[13]. Moreover, Stockburger et al. (2016) demonstrated that knockdown of SV2A disrupts mitochondrial morphology resulting in mitochondrial fragmentation. These data strongly suggest that SV2A plays a role in mitochondrial dynamics, although the mode of action remains to be elucidated. Most likely, SV2A acts as a fission or fusion factor or regulates the activity of such factors. SV2A regulating mitochondrial processes seems plausible, considering that synaptic proteins and SNAREs affect mitochondria. For example, SNARE protein STX17 regulates mitochondrial fission by controlling the localization and activity of DRP1[161]. Conversely, there is evidence that mitochondrial fission and fusion factors are involved in vesicle transport, as DRP1 acts on synaptic vesicle retrieval together with Bcl-xL[162].

5.3.1.1 SV2A KD alters mitochondrial morphology

To investigate the effect of SV2A on mitochondrial dynamics, first mitochondrial morphology in SV2A KD cells was compared to rotenone treated cells. The experiment was designed to determine the severity of SV2A KD on mitochondrial morphology compared to a positive control rotenone. SH-SY5Y cells were used as in previous experiments.

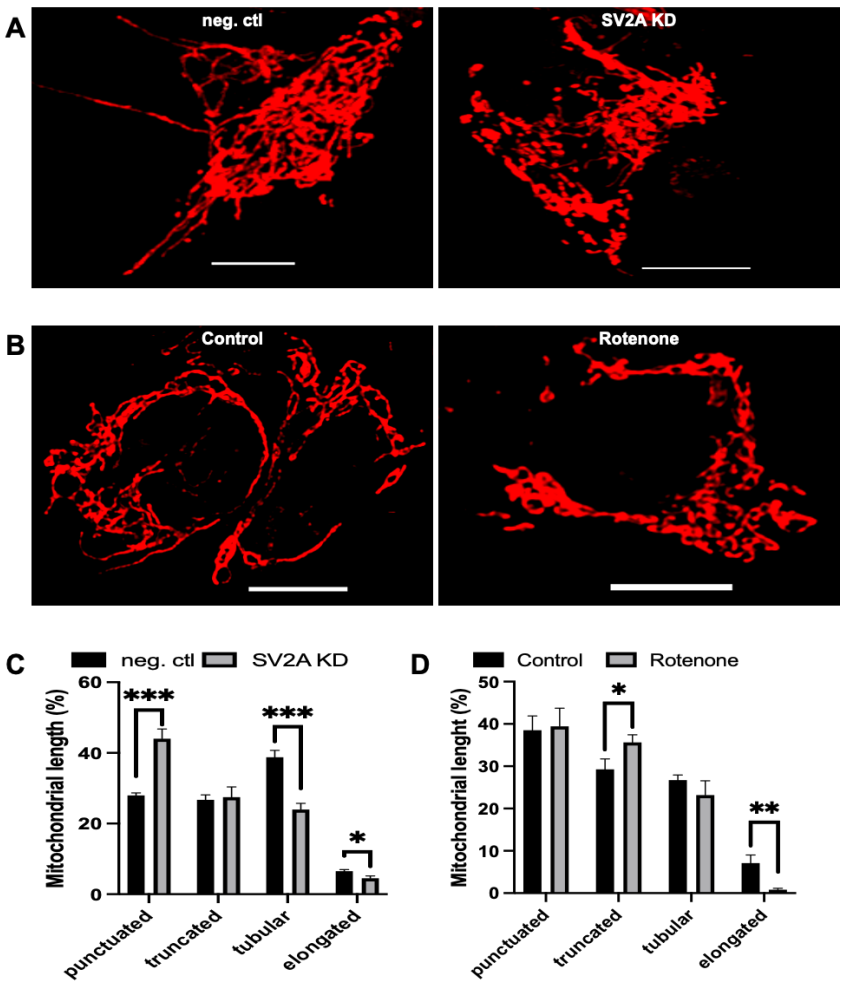

Figure 37 SV2A KD disrupts mitochondrial morphology similar to rotenone

(A) Representative confocal images of mitochondria in SV2A KD cells and cells treated with scrambled siRNA (10 nM/48 h). **(B)** Representative confocal images of mitochondria in rotenone (5 µM/24 h) treated and control cells. **(C)** Length distribution of mitochondria in SV2A KD cells compared to cells treated with scrambled siRNA, n= 7 **(D)** Length distribution of mitochondria in rotenone (5 µM/24 h) treated cells compared to control, n= 4. Scale bar: 10 µm. Staining according to Table 14. Data are expressed as mean ± SEM; student's unpaired t-test (*p <0.05; **p <0.01, ***p <0.001). n= 1 equals 100 mitochondria measured.

On confocal images, control cells treated with scrambled siRNA demonstrate tubular mitochondria and low numbers of fragmented mitochondria, whereas mitochondria of SV2A KD cells are smaller, swollen and fragmented (Figure 37A). In terms of mitochondrial length, SV2A KD induces a significant shift towards short punctuated mitochondria (+16 %), while the number of tubular (-14,8 %) and elongated (-2 %) mitochondria decrease compared to control (Figure 37C). Interestingly, mitochondria treated with 5 µM rotenone for 24 h appear similar to those of SV2A KD cells, including a shift in mitochondrial length towards smaller mitochondria (Figure 30B, D). Both SV2A knockdown and complex I inhibitor rotenone cause mitochondrial fragmentation, which surprisingly is severer in SV2A KD.

5.3.1.2 SV2A KD perturbs mitochondrial fission and fusion

So far, alterations in mitochondrial morphology by SV2A KD have only been analyzed in fixed cells. To verify whether the mitochondrial phenotype of SV2A KD persists in living cells and to examine changes in fission and fusion events, SV2A was knocked out in SH-SY5Y cells while mitochondria were stained by mEOS-Mito7. Mitochondrial dynamics and morphology of live cells were analyzed for 10 min using a confocal microscope.

As expected, SV2A knockdown in living cells also results in mitochondrial fragmentation (Figure 38A, B). An interesting observation upon SV2A KD is that the majority of mitochondria are located in the cell center. The tubular mitochondria of control cells confirm that mitochondrial fragmentation in SV2A KD cells is specific to SV2A knockdown and not the result of the live cell imaging process. Not surprising given the mitochondrial phenotype, fission and fusion events decreased by an average of 20 events/10 min in SV2A-KD cells (Figure 38C). Moreover, fission events decreased by 14 events/10 min in SV2A KD cells compared to control (Figure 38D). Based on mitochondrial fragmentation upon SV2A KD, a decrease in fission events is unexpected. Fusion events likewise decreased in SV2A KD cells compared to cells treated with scrambled siRNA, which was expected given the fragmentation of mitochondria (-11.4 events/10 min) (Figure 38E). Interestingly, despite mitochondrial fragmentation the balance between fission and fusion is unchanged in SV2A KD cells (Figure 38F, G). A shift towards fission was hypothesized before the experiment. However, a general impairment of the fission and fusion machinery exists.

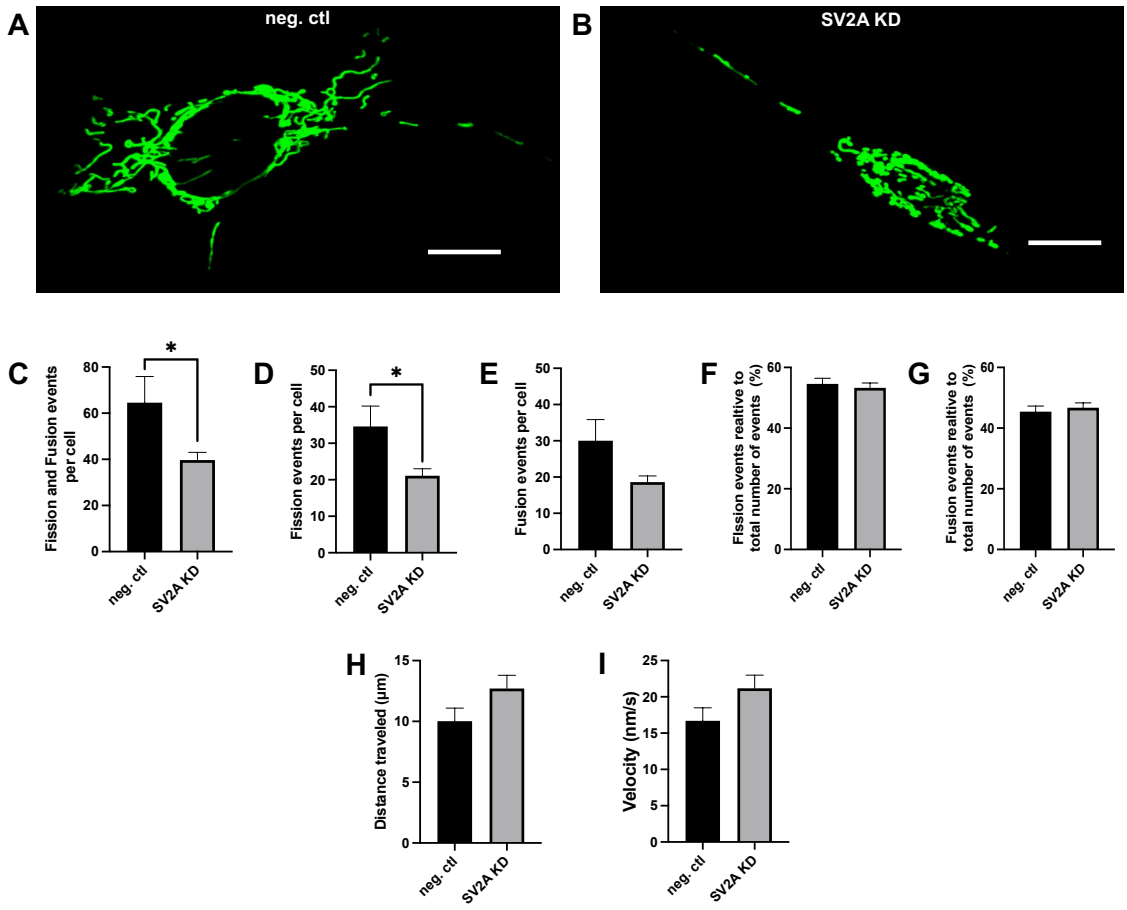

Figure 38 SV2A KD impairs mitochondrial dynamics in living cells

(A) Representative confocal image of mitochondria stained with mEOS-Mito7 in live SH-SY5Y cells treated with scrambled siRNA (10 nM/48 h). **(B)** Representative confocal image of mitochondria stained with mEOS-Mito7 in live SH-SY5Y cells treated with SV2A siRNA (10 nM/48 h). **(C-G)** Mitochondrial fission and fusion events in SV2A KD cells compared to negative control. **(H-I)** Velocity and distance traveled of mitochondria in SV2A KD cells compared to negative control. Scale bar: 10 µm. 11 cells were analyzed for both negative control and SV2A KD. Data are expressed as mean ± SEM; student's unpaired t-test (*p <0.05; **p <0.01, ***p <0.001).

In addition, the distance traveled and velocity of mitochondria in SV2A KD cells were measured during a 10 min timeframe and compared to control. Interestingly, fragmented mitochondria of SV2A KD cells traveled longer distances (12.7 µm) compared to mitochondria treated with scrambled siRNA (10 µm) (Figure 38H). Consequently, these mitochondria also moved faster (SV2A KD: 21.2 nm/s; control: 16.7 nm/s) (Figure 38I).

5.3.1.3 Mitochondrial fragmentation in SV2A KO mouse hippocampus

Since mitochondrial fragmentation and disruption of mitochondrial morphology following knockdown of SV2A have only been demonstrated in vitro, it was interesting to study SV2A knockout in vivo in mice. Considering that homozygous SV2A knockout causes juvenile death in mice, the SV2A KO mouse model introduced by Menten-Dedoyart et. al. (2016) was analyzed, because of its unique hippocampus restricted SV2A knockout[154]. The advantages of this mouse model over the other available SV2A KO mouse models are, first, that mice of any age can be studied since these animals do not die juvenile, second, these animals do not experience seizures which would have a strong negative impact on mitochondrial morphology and third, the hippocampus is the essential brain region for cognition and the development of AD. Mitochondrial morphology was investigated among glutamatergic neurons in the CA3 region of the hippocampus from SV2A KO and control animals using confocal microscopy. It is evident from the images that the mitochondrial phenotype of SV2A KD cells exists in vivo in SV2A KO mice. In control mice, mitochondria are tubular and build an interconnected network, whereas mitochondria in SV2A KO mice are highly fragmented (Figure 39A, B). Double blinded measurements of mitochondrial length in SV2A KO hippocampi of both female and male animals reflect a shift in mitochondrial length towards smaller, punctuated mitochondria compared to control. The percentage of punctuated mitochondria increased, accompanied by a substantial loss in mitochondria within the size range of truncated mitochondria (Figure 39C). For mitochondria, classified as elongated and tubular, numbers are equally low in both SV2A KO and control. As the importance of gender is increasingly emphasized in science, mitochondrial length was also examined for males or females. Surprisingly, mitochondrial morphology and length is not altered in males experiencing SV2A KO (Figure 39D). However in females, SV2A KO has devastating effects on mitochondrial morphology, resulting in a 10 % increase in punctuated mitochondria and a simultaneously 10.2 % loss in truncated mitochondria (Figure 39E). These fascinating data suggest that reduction of SV2A protein levels primarily affect mitochondria in females.

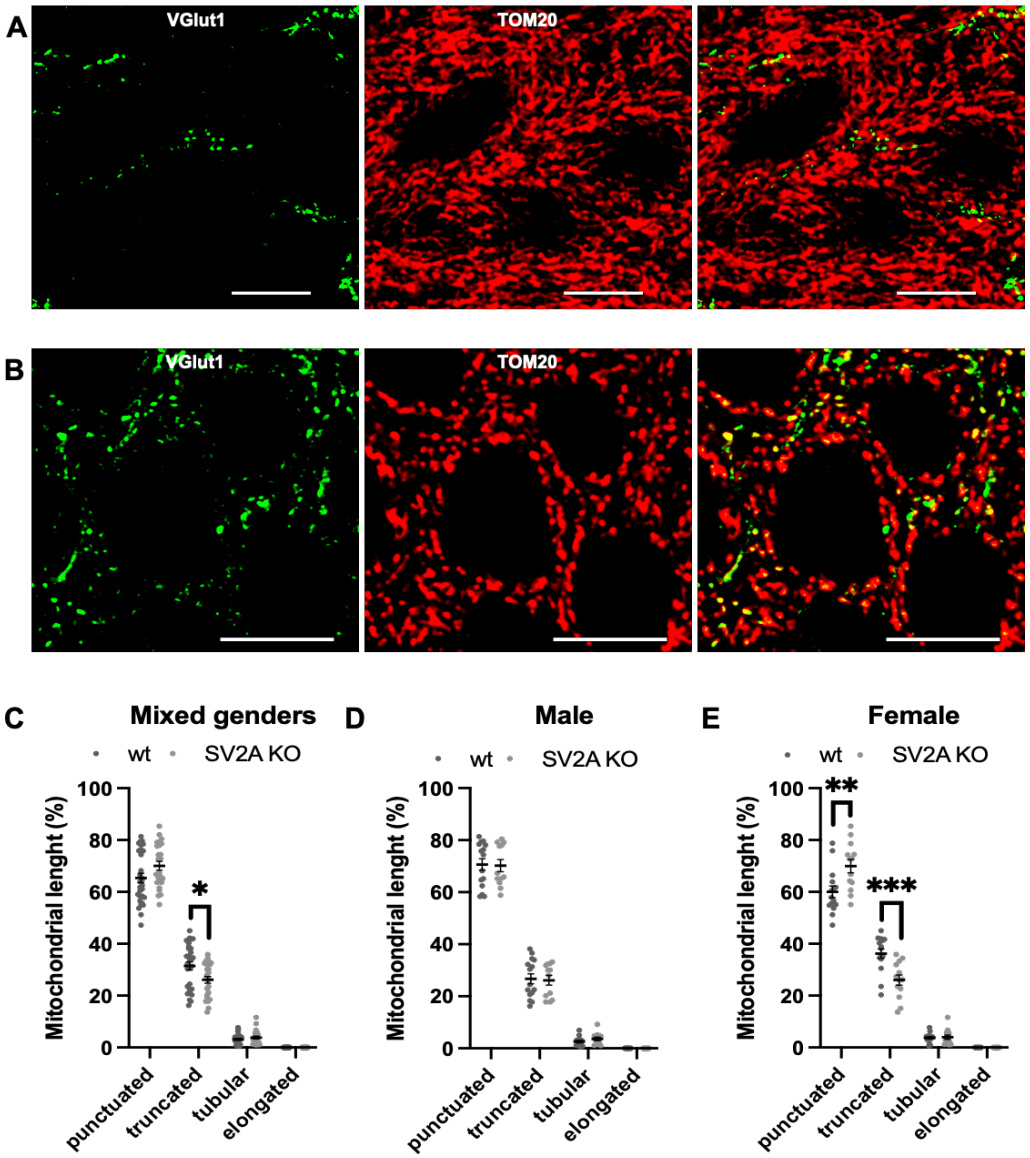

Figure 39 Mitochondrial fragmentation in the CA3 region of SV2A KO mice

(A) Representative confocal images of CA3 pyramidal cells of wildtype female mice stained for VGlut1 and TOM20. **(B)** Representative confocal images of CA3 pyramidal cells of CA3 specific SV2A KO female mice stained for VGlut1 and TOM20. **(C)** Length distribution of mitochondria in CA3 pyramidal cells of control and SV2A KO mice. Control: 30 images of 10 mice were analyzed; SV2A KD: 24 images of 8 mice were analyzed. **(D)** Length distribution of mitochondria in CA3 pyramidal cells of male control and SV2A KO mice. Control: 15 images of 5 mice were analyzed; SV2A KD: 12 images of 4 mice were analyzed. **(E)** Length distribution of mitochondria in CA3 pyramidal cells of female control and SV2A KO mice. Control: 15 images of 5 mice were analyzed; SV2A KD: 13 images of 4 mice were analyzed. Scale bar: 10 µm. Staining according to Table 15. Data are expressed as mean ± SEM; student's unpaired t-test (*p <0.05; **p <0.01, ***p <0.001).

5.3.1.4 Colocalization of SV2A and DRP1 is restricted to mitochondria

Both in vitro and in vivo, it has been demonstrated that reduction of SV2A protein levels causes mitochondrial fragmentation. But how does SV2A mediate its effects? The most likely explanation is that SV2A serves as a mitochondrial fission or fusion factor, like DRP1 a GTPase responsible for mitochondrial fission. SV2A resembles DRP1 in that both proteins are located in the cytosol and at mitochondria since DRP1 translocates from the cytosol to mitochondria to exert fission. Additionally, both proteins lack mitochondrial targeting sequences and exert effects on vesicles. Hence, DRP1 and SV2A behave very similar, except that DRP1 KD causes mitochondrial elongation, whereas SV2A KD induces mitochondrial fragmentation. However, as inhibition of DRP1 by mitochondrial division inhibitor 1 (mdivi-1) induces mitochondrial elongation like LEV treatment and SV2A KD on the other hand causes mitochondrial fragmentation, we hypothesize that SV2A might regulate DRP1 activity[163]. Based on this hypothesis, mitochondrial fragmentation downstream of SV2A KD would be understood as unleashed DRP1 activity in the absence of its physiological regulator. Certainly, SV2A may as well be part of the fusion machinery, as knockdown of fusion factors such as MFN2 and DRP1 causes mitochondrial fragmentation, similar to knockdown of SV2A. However, we decided to investigate whether SV2A regulates DRP1 activity, which has already been described for SNARE protein STX17[161].

The interaction of SV2A and DRP1 in respect to mitochondria was examined in SH-SY5Y cells by confocal microscopy. On confocal images, SV2A is uniformly distributed like on previous images, mitochondria are healthy and elongated and DRP1 is distributed throughout the cell, with higher abundance among mitochondria. In the case of SV2A and mitochondria, their previously described colocalization is again visible and confirmed by a Pearson's r of 0.78 (Figure 40B, E). In line with the literature, DRP1 is located both at mitochondria and in the cytosol, although more frequently at mitochondria (Figure 40D). The known mitochondrial localization of DRP1 is also confirmed by a Pearson's r of 0.74 (Figure 40G). Interestingly, SV2A and DRP1 colocalize with each other, but almost exclusively at mitochondria (white arrows) (Figure 40A, C). Nevertheless, both SV2A and DRP1 are also located at mitochondria by themselves. The Pearson's r of SV2A and DRP1 is 0.78 (Figure 40F).

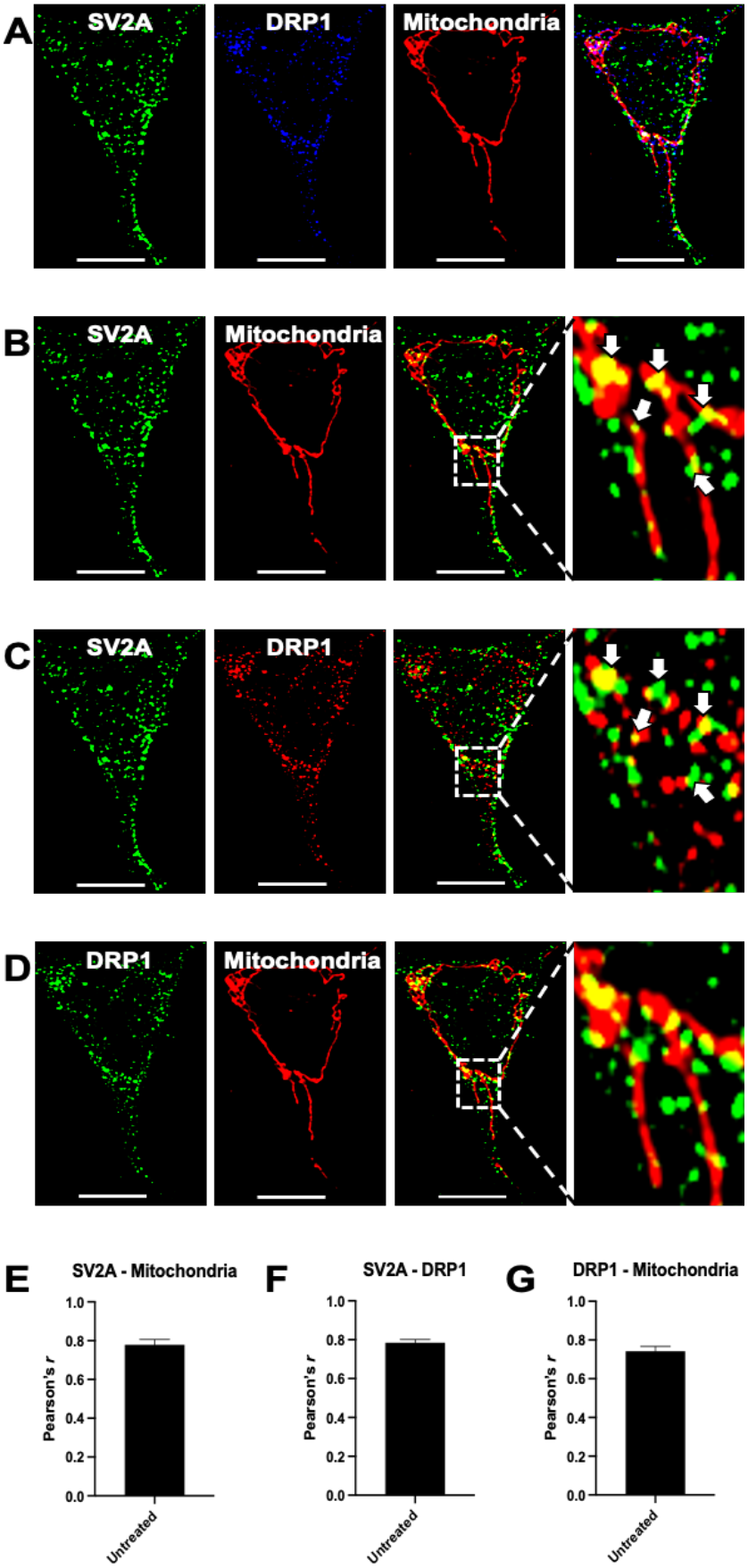
A
SV2A
DRP1
Mitochondria
B
SV2A
Mitochondria
C
SV2A
DRP1
D
DRP1
Mitochondria
E
SV2A - Mitochondria
F
SV2A - DRP1
G
DRP1 - Mitochondria
Pearson's r
1.0
0.8
0.6
0.4
0.2
0.0
Untreated

Figure 40 Colocalization of SV2A and DRP1 is restricted to mitochondria

(A) Representative confocal images of SH-SY5Y cells stained for SV2A, DRP1 and mitochondria. Colocalization of the three is indicated by bright white spots. **(B)** Representative confocal images of cells stained for SV2A and mitochondria. Yellow indicates colocalization. **(C)** Representative confocal images of cells stained for SV2A and DRP1. Yellow indicates colocalization. **(D)** Representative confocal images of cells stained for DRP1 and mitochondria. Yellow indicates colocalization. **(E-G)** Mean of Pearson's r values calculated for each imaged cell display colocalization of SV2A with mitochondria, SV2A with DRP1 and DRP1 with mitochondria. Staining according to Table 14. Analyzed were 16 cells. Scale bar: 10 µm. Enlarged images of boxed areas are displayed at the end of each image series. Data are expressed as mean ± SEM.

Super-resolution microscopy was performed to clarify whether the observed interaction between SV2A and DRP1 at mitochondria represents a specific or false positive interaction owing to the low resolution of confocal microscopy. Colocalization of DRP1 and SV2A is present in line with the confocal data, but to a minor extent and only at a some sites (Figure 41A). Additional, many regions exist where SV2A and DRP1 are close to each other yet not close enough to colocalize on super-resolution microscopy. When only SV2A molecules with a CBC ≥0.5 are displayed, only a small fraction of SV2A and DRP1 molecules colocalize with each other (Figure 41B). The present but low colocalization is supported as 7.1 % of SV2A molecules possess CBC values ≥0.5 (Figure 41C).

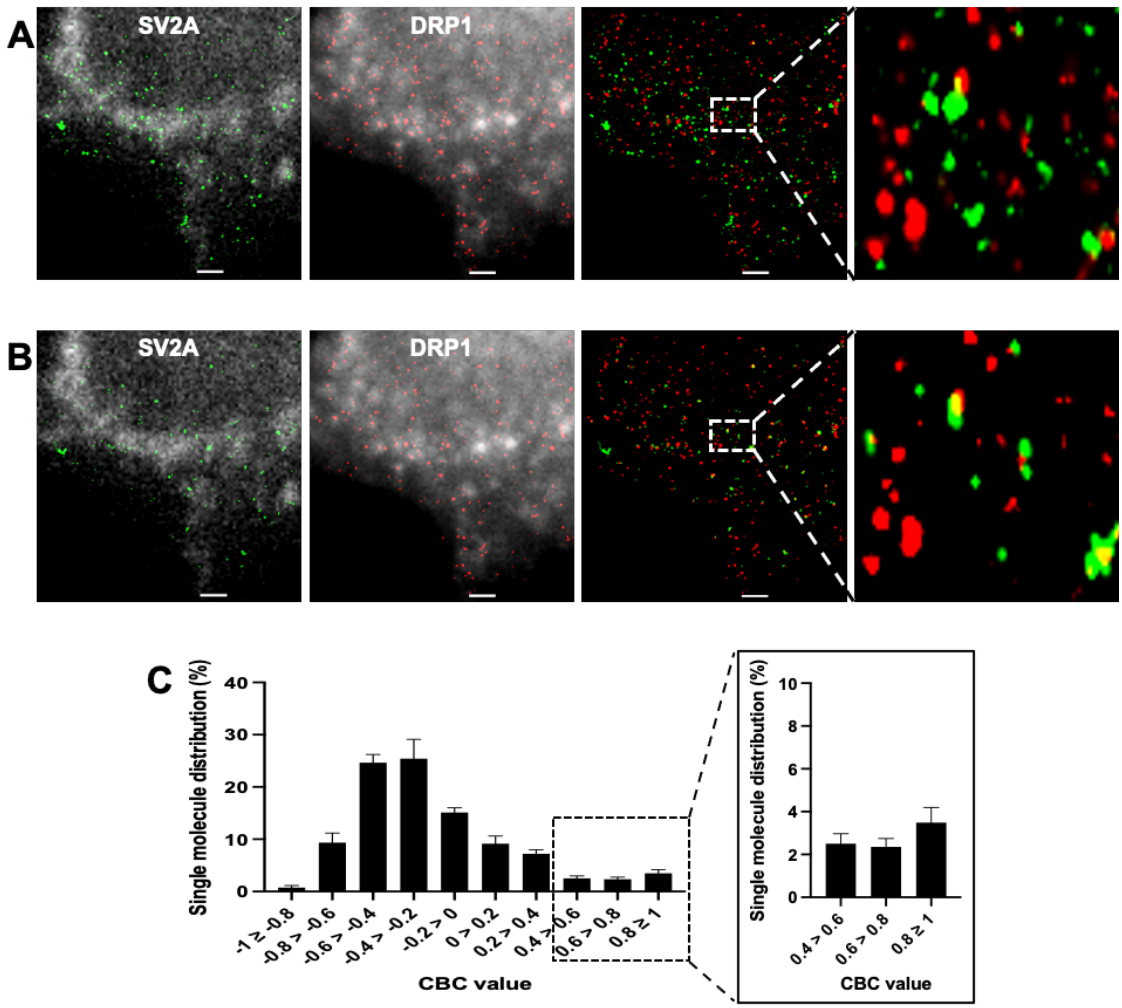

Figure 41 Colocalization of SV2A and DRP1 appears to be coincidental

(A-B) Representative super-resolution images of untreated SH-SY5Y cells stained for SV2A and DRP1 (A). Representative super-resolution images of DRP1 and SV2A proteins with CBC values ≥0.5, indicating that these SV2A molecules colocalize with DRP1 (B). Brightfield images of stained proteins are displayed in gray. Enlarged images of boxed areas are displayed at the end of each image series. Scale bar: 1 µm. **(C)** Histogram of mean CBC value distribution calculated for the colocalization of SV2A and DRP1. Enlarged are data of CBC values corresponding to colocalization of the two proteins. Staining according to Table 17. Analyzed were 9 images. Data are expressed as mean ± SEM.

5.3.1.4.1 Rotenone treatment increases colocalization of SV2A and DRP1

In untreated cells, mitochondria restricted colocalization of SV2A and DRP1 exists. Super-resolution microscopy displayed that the colocalization of SV2A and DRP1 is minor and therefore may represent mitochondrial localization of each protein rather than an interaction of the two proteins. Considering that mitochondrial translocation of

DRP1 and fission increase at dysfunctional mitochondria, we investigated whether mitochondrial stress alters the colocalization of SV2A and DRP1. If SV2A regulates the activity of DRP1, changes in colocalization of the two proteins should occur.

Colocalization of DRP1 and SV2A at mitochondria in SH-SY5Y cells treated with 5 µM rotenone for 24 h was examined by confocal microscopy. As expected, complex I inhibitor rotenone induced both mitochondrial fragmentation and increased translocation of DRP1 to mitochondria (Figure 42D). The increased mitochondrial localization of DRP1 during rotenone treatment is also reflected by Pearson's r, which increased from 0.74 to 0.83 (Figure 42G). In addition, localization of SV2A at defective mitochondria increased, consistent with observations from previous images (Figure 42B). Elevated mitochondrial localization of SV2A by inhibition of complex I is also confirmed by an increase in Pearson's r from 0.78 to 0.84 (Figure 42E). Furthermore, colocalization of SV2A and DRP1 increases during rotenone treatment and is again almost exclusively restricted to mitochondria (Figure 42A, C). Nevertheless, both proteins still occur separated from each other at mitochondria. Accordingly, Pearson's r of SV2A and DRP1 rose from 0.78 to 0.86 compared to control (Figure 42F). The increased colocalization upon rotenone treatment was expected given that both SV2A and DRP1 target mitochondria upon mitochondrial stress.

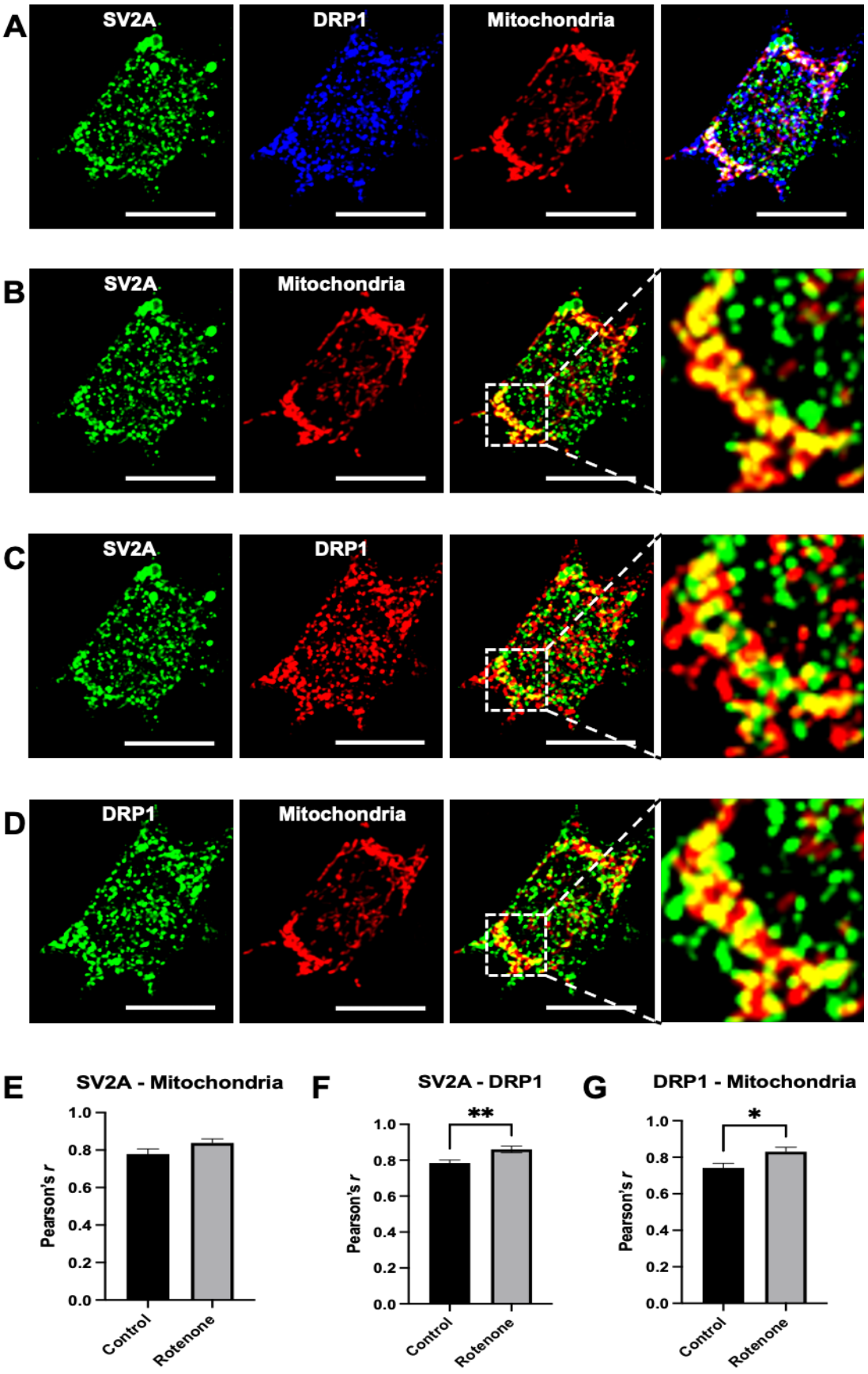
A
SV2A
DRP1
Mitochondria
B
SV2A
Mitochondria
C
SV2A
DRP1
D
DRP1
Mitochondria
E
SV2A - Mitochondria
Pearson's r
1.0
0.8
0.6
0.4
0.2
0.0
Control
Rotenone
F
SV2A - DRP1
**
Pearson's r
1.0
0.8
0.6
0.4
0.2
0.0
Control
Rotenone
G
DRP1 - Mitochondria
*
Pearson's r
1.0
0.8
0.6
0.4
0.2
0.0
Control
Rotenone

Figure 42 Colocalization of SV2A and DRP1 increases upon mitochondrial stress

A) Representative confocal images of rotenone (5 µM/24 h) treated SH-SY5Y cells stained for SV2A, DRP1 and mitochondria. Colocalization of the three is indicated by bright white spots. **(B)** Representative confocal images of rotenone (5 µM/24 h) treated cells stained for SV2A and mitochondria. Yellow indicates colocalization. **(C)** Representative confocal images of rotenone (5 µM/24 h) treated cells stained for SV2A and DRP1. Yellow indicates colocalization. **(D)** Representative confocal images of rotenone (5 µM/24 h) treated cells stained for DRP1 and mitochondria. Yellow indicates colocalization. **(E-G)** Mean of Pearson's r values calculated for each imaged cell confirm the increased colocalization of SV2A with mitochondria, of SV2A with DRP1 and of DRP1 with mitochondria upon mitochondrial stress. Enlarged images of boxed areas are displayed at the end of each image series. Staining according to Table 14. Cells analyzed: control: 16; rotenone treated: 11. Scale bar: 10 µm. Data are expressed as mean ± SEM; student's unpaired t-test (*p <0.05; **p <0.01, ***p <0.001).

Confocal data on the interaction of SV2A, DRP1 and mitochondria demonstrate stress induced elevation of SV2A and DRP1 colocalization at mitochondria. To determine whether the increased colocalization is the result of enhanced interaction between the two proteins or due to increased mitochondrial localization of both proteins upon mitochondrial stress, rotenone treated SH-SY5Y cells were analyzed using super-resolution microscopy. Interestingly super-resolution data confirm the increased colocalization of SV2A and DRP1 under the influence of rotenone even when only SV2A molecules with CBC values ≥0.5 are displayed (Figure 43A, B). Indeed, the amount of SV2A molecules bearing CBC values ≥0.5 rose from 7.1 % to 12.8 % (Figure 43C).

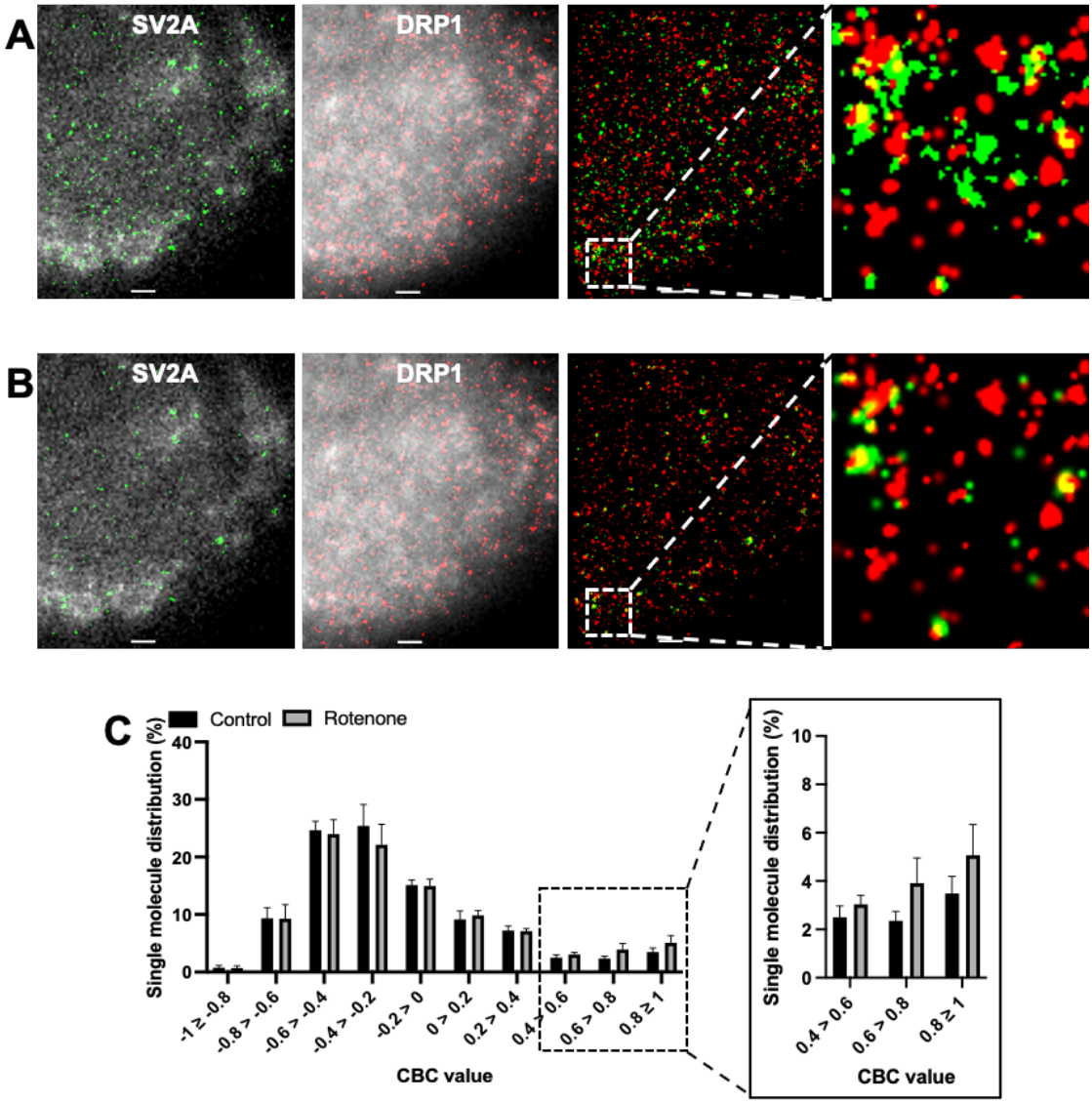

Figure 43 Colocalization of SV2A and DRP1 increases during rotenone treatment

(A-B) Representative super-resolution images of SH-SY5Y cells treated with rotenone (5 µM/24 h) stained for SV2A and DRP1 (A). Representative super-resolution images of DRP1 and SV2A proteins with CBC values ≥0.5, indicating that these SV2A molecules colocalize with DRP1 (B). Brightfield images of stained proteins are displayed in gray. Enlarged images of boxed areas are displayed at the end of each image series. Scale bar: 1 µm. **(C)** Histogram of CBC value distribution for the colocalization of SV2A and DRP1 in control and rotenone treated cells. Enlarged are CBC values corresponding to colocalization of the two proteins. Staining according to Table 17. Cells analyzed: control: 9; rotenone treated: 9. Data are expressed as mean ± SEM; student's unpaired t-test (*p <0.05; **p <0.01, ***p <0.001).

5.3.2 Autophagy

In recent years, the involvement of both mitochondrial fission and fusion proteins as well as SNARE proteins in autophagy and mitophagy has received increasing attention. For example, MFN2 performs autophagosome-lysosome fusion during autophagy and is involved in PINK1-Parkin mediated mitophagy[164,165]. Among SNARE proteins, family members of the VAMP and syntaxin family are responsible for phagophore formation and elongation as well as the fusion of autophagosome and lysosome[166,167]. Therefore, it is plausible that SV2A, as a hybrid of vesicular and mitochondrial protein, exerts similar functions in autophagy. Since both mitochondrial shortening by SV2A KD and elongation by LEV are defined by changes in the percentage of mitochondrial length distribution, changes in mitochondrial length may be the result of the induction or inhibition of autophagy. An increased autophagy rate would reduce the percentage of small punctuated mitochondria, which in turn would increase the percentage of tubular mitochondria. On the other hand, inhibition of autophagy would increase the percentage of punctuated mitochondria accompanied by a decrease in elongated mitochondria. To determine whether SV2A affects mitochondrial length distribution reducing punctuated mitochondria via autophagy or mitophagy, alterations in autophagic flux during knockdown of SV2A were examined as well as if SV2A is a constituent of the autophagosome or lysosome.

5.3.2.1 SV2A KD reduces autophagic flux

First the impact of SV2A KD on autophagic flux was examined in SH-SY5Y cells. This involved knocking down SV2A by siRNA and blocking the degradation of autophagosomes by 600 nM V-ATPase inhibitor bafilomycin A1 4 h prior to protein extraction. LC3II was used as an autophagy marker since LC3II is generated during the initiation of autophagy and degraded during the final step of autophagy as part of the autophagosome. As bafilomycin A1 blocks the degradation of autophagosomes it increases LC3II levels within the cell. Autophagic flux is determined by WB subtracting the LC3II band intensity of samples with intact autophagy from those treated with bafilomycin A1 (Equation 1). The difference is equivalent to LC3II molecules that would have been degraded in the absence of bafilomycin A1.

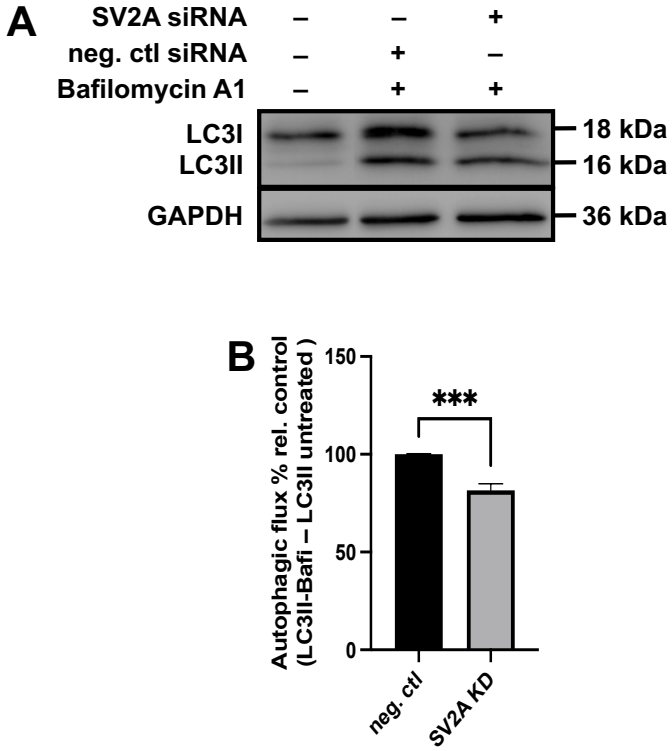

Figure 44 Autophagic flux is reduced in SV2 KD cells

(A) Representative LC3II western blot of SV2A KD and neg. ctl SH-SY5Y cells treated with bafilomycin A1 (600 nM/4 h). 20 µg protein were loaded per well. GAPDH serves as an internal control. 1. well: control cells neither treated with bafilomycin A1 nor with siRNA, 2. well: cells treated with scrambled siRNA (10 nM/48 h) and bafilomycin A1 (600 nM/4 h), 3. well: cells treated with SV2A siRNA (10 nM/48 h) and bafilomycin A1 (600 nM/4 h). **(B)** Autophagic flux in SV2A KD cells compared to cells treated with scrambled siRNA. Analyzed were 3 independent cell extracts. Data are expressed as mean ± SEM; student's unpaired t-test (*p <0.05; **p <0.01, ***p <0.001).

The WB membrane displays LC3I, LC3II and glyceraldehyde 3-phosphate dehydrogenase (GAPDH) band intensities in correlation to bafilomycin A1 and SV2A KD (Figure 44A). GAPDH serves as an internal control for the normalization of LC3II band intensities. A sample neither treated with bafilomycin A1 nor siRNA was loaded onto the first well to visualize physiological LC3II levels. Physiological intracellular LC3II levels are low, reflected by the faint band in the first well (Figure 44A). A protein extract of cells treated with both scrambled siRNA and bafilomycin A1 was loaded onto the second well. Since autophagy was inhibited by bafilomycin A1, a strong LC3II band is visible in the second well (Figure 44A). The third well was loaded with a protein

extract from cells treated with both SV2A siRNA and bafilomycin A1. An LC3II band with lower intensity than the LC3II band of scrambled siRNA treated samples is visible (Figure 44A). Autophagic flux in SV2A KD cells is significant reduced by 18.4 %. (Figure 44B). As band intensities of the internal standard GAPDH are uniform, each well was loaded with the same amount of protein.

5.3.2.2 SV2A colocalizes with LC3II at mitochondria and in the cytosol

The reduction in autophagic flux by SV2A KD suggests that SV2A affects autophagy. Therefore, the question arose of how SV2A regulates autophagy. One possibility is that SV2A resides in the membrane of autophagosomes and regulates either thei fusion with lysosomes or the maturation of phagophores, similar to SNAREs VAMP7 and syntaxin7/8[168]. The interaction of SV2A and LC3II was examined by confocal microscopy in SH-SY5Y cells treated with 600 nM bafilomycin A1 for 4 h. Bafilomycin A1 was used to increase the number of LC3II positive structures.

On confocal images, SV2A displays uniformly distributed vesicular structures similar to previous images while mitochondria are fragmented and swollen. LC3II is evenly distributed throughout the cell and occurs at mitochondria. Knowing that SV2A, is located at mitochondria and LC3II binds to mitochondria during mitophagy it is not surprising that SV2A, LC3II and mitochondria colocalize (Figure 45A). SV2A is located at mitochondria as previously described and confirmed by a Pearson's r of 0.74 (Figure 45B, E). SV2A and LC3II colocalize at mitochondria (white arrows) and in the cytosol, although LC3II is often found apart from SV2A (Figure 45C). Colocalization of SV2A and LC3II is also confirmed by a Pearson's r of 0.76 (Figure 45F). As expected for an autophagosomal protein, LC3II is frequently found at mitochondria given that autophagosomes are critical for mitophagy (Figure 45D). Pearson's r of 0.74 supports the localization of LC3II at mitochondria (Figure 45G).

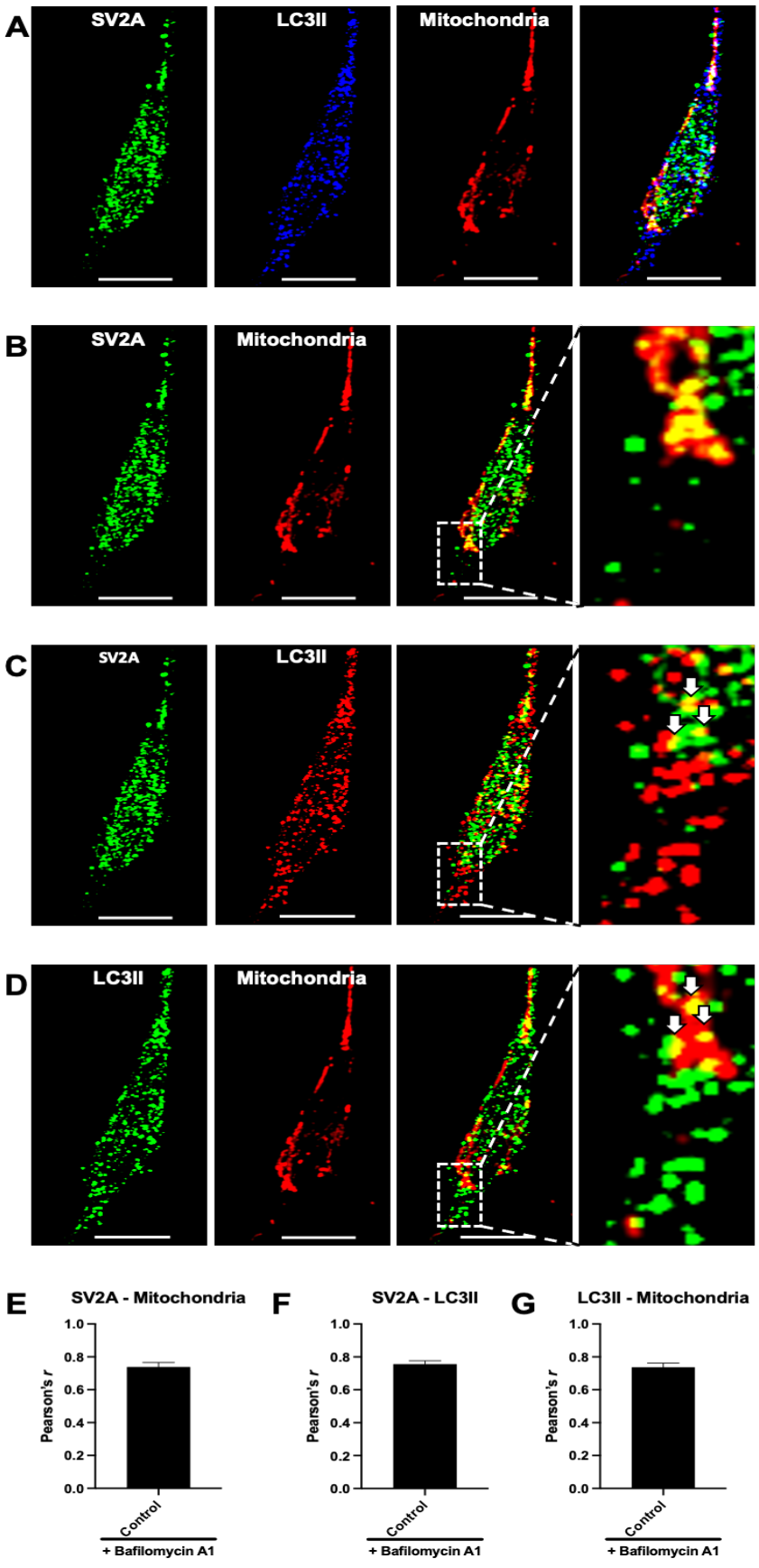
A
SV2A
LC3II
Mitochondria
B
SV2A
Mitochondria
C
SV2A
LC3II
D
LC3II
Mitochondria
E
SV2A - Mitochondria
F
SV2A - LC3II
G
LC3II - Mitochondria
Pearson's r
1.0
0.8
0.6
0.4
0.2
0.0
Control
+ Bafilomycin A1

Figure 45 SV2A is not a constituent of the autophagosome

(A) Representative confocal images of SH-SY5Y cells stained for SV2A, LC3II and mitochondria treated with bafilomycin A1 (600 nM/4 h). Colocalization of the three is indicated by bright white spots. **(B)** Representative confocal images of cells stained for SV2A and mitochondria. Yellow indicates colocalization. **(C)** Representative confocal images of cells stained for SV2A and LC3II. Arrows mark LC3II molecules colocalizing with SV2A. Yellow indicates colocalization **(D)** Representative confocal images of cells stained for LC3II and mitochondria. Arrows mark the same LC3II molecules as in (C). Yellow indicates colocalization. **(E-G)** Mean of Pearson's r values calculated for each imaged cell display colocalization of SV2A with mitochondria (E), SV2A with LC3II (F) and LC3II with mitochondria (G). Enlarged images of boxed areas are displayed at the end of each image series. Staining according to Table 14. Analyzed were 18 cells. Scale bar: 10 µm. Data are expressed as mean ± SEM.

5.3.2.2.1 Interaction of SV2A and LC3II during induced auto- or mitophagy

While investigating if SV2A is part of the autophagosome or phagophore, colocalization of SV2A and LC3II was found both in the cytosol and at mitochondria. The data suggest that the interaction of SV2A and LC3II at mitochondria is related to mitophagy. To assess whether the induction of autophagy or mitophagy alters the interaction of SV2A with LC3II, SH-SY5Y cells were treated with bafilomycin A1 for 4 h to inhibit autophagosomal degradation. At the same time mitophagy was induced by 10 µM mitochondrial uncoupler CCCP for 1 h and autophagy by 10 µM rapamycin for 4 h. Rapamycin induces autophagy by inhibition of mTORC1 at the onset of autophagy.

CCCP treatment impaired mitochondria and caused severe fragmentation. SV2A is again uniformly distributed inside the cell and at mitochondria, while forming larger SV2A agglomerates. Likewise, LC3II is higher expressed and widely distributed upon CCCP treatment in combination with inhibition of autophagosome degradation. LC3II agglomerates occur at mitochondria. As expected, based on previous data, colocalization of SV2A, LC3II and mitochondria increases by mitochondrial stress compared to cells treated with only bafilomycin A1 (Figure 46A). Furthermore, SV2A increasingly localizes to dysfunctional mitochondria, as previously described for CCCP treated cells (Figure 46B). As in control cells, SV2A and LC3II colocalize at mitochondria and in the cytosol, but greater at mitochondria (Figure 46C). During severe mitochondrial stress, SV2A still not always associates with LC3II. Compared to untreated cells, LC3II is located mainly at CCCP disrupted mitochondria (Figure 46D).

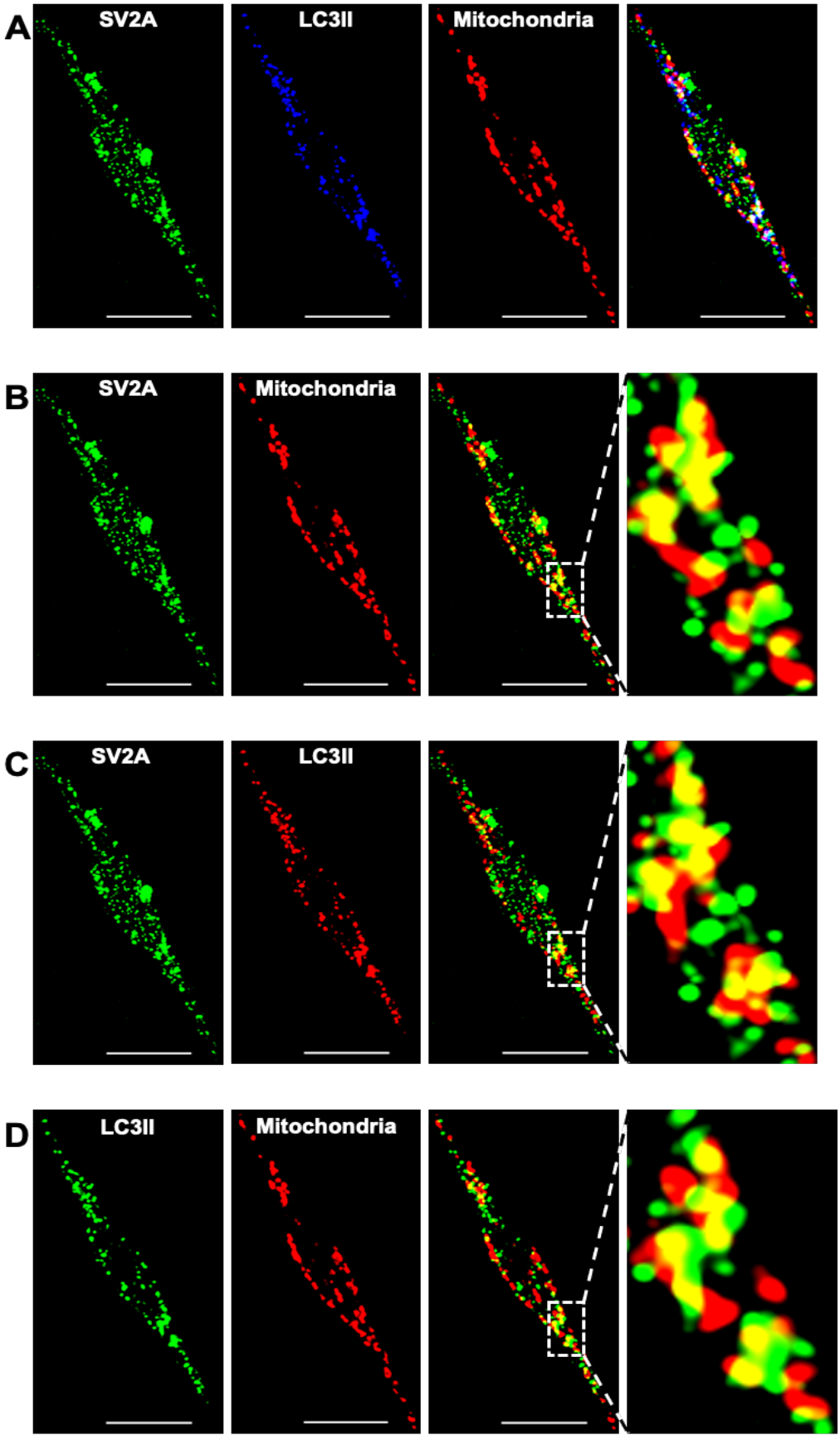
A
SV2A
LC3II
Mitochondria
B
SV2A
Mitochondria
C
SV2A
LC3II
D
LC3II
Mitochondria

Figure 46 LC3II is greater abundant at CCCP disrupted mitochondria

A) Representative confocal images of CCCP (10 µM/1 h) and bafilomycin A1 (600 nM/4 h) treated SH-SY5Y cells stained for SV2A, LC3II and mitochondria. Colocalization of the three is indicated by bright white spots. **(B)** Representative confocal images of CCCP (10 µM/1 h) and bafilomycin A1 (600 nM/4 h) treated cells stained for SV2A and mitochondria. Yellow indicates colocalization. **(C)** Representative confocal images of CCCP (10 µM/1 h) and bafilomycin A1 (600 nM/4 h) treated cells stained for SV2A and LC3II. Yellow indicates colocalization. **(D)** Representative confocal images of CCCP (10 µM/1 h) and bafilomycin A1 (600 nM/4 h) treated cells stained for LC3II and mitochondria. Yellow indicates colocalization. Enlarged images of boxed areas are displayed at the end of each image series. Scale bar: 10 µm. Staining according to Table 14. Analyzed were 11 cells.

After examining how mitochondrial stress affects the interaction of LC3II and SV2A, it was investigated how induction of autophagy by inhibition of mTORC1 using rapamycin affects their interaction. Surprisingly induction of autophagy alters the distribution of SV2A. SV2A is no longer evenly distributed as seen on previous confocal images of control and stressed cells. SV2A is most abundant at the edges of the cell where fragmented mitochondria reside and forms large agglomerates at these sites. LC3II is also predominantly expressed at the edges of the cell and forms large agglomerates. Mitochondria appear fragmented as in control cells treated with bafilomycin A1. As expected, based on previous data and since LC3II is an autophagy protein, colocalization of SV2A, LC3II and mitochondria increase during induced autophagy (Figure 47A). Unexpectedly, induced autophagy leads to increased localization of SV2A at mitochondria (Figure 47B). Furthermore, as in CCCP treated cells, SV2A and LC3II colocalize at both mitochondria and in the cytosol, but cytosolic colocalization is again lower (Figure 47C). Despite the induction of autophagy, SV2A is not always associated with LC3II. Induction of autophagy causes LC3II to mainly locate to severely fragmented mitochondria, like in CCCP treated cells (Figure 47D).

After analyzing SH-SY5Y cells either exposed to mitochondrial stress by CCCP or experiencing elevated autophagy by rapamycin, the Pearson's r values of these samples are compared to control. For SV2A localization at mitochondria, CCCP and rapamycin demonstrate increased Pearson's r values. The increased Pearson's r values agree well with the images showing that CCCP and rapamycin enhance localization of SV2A at mitochondria, which is more pronounced for rapamycin.

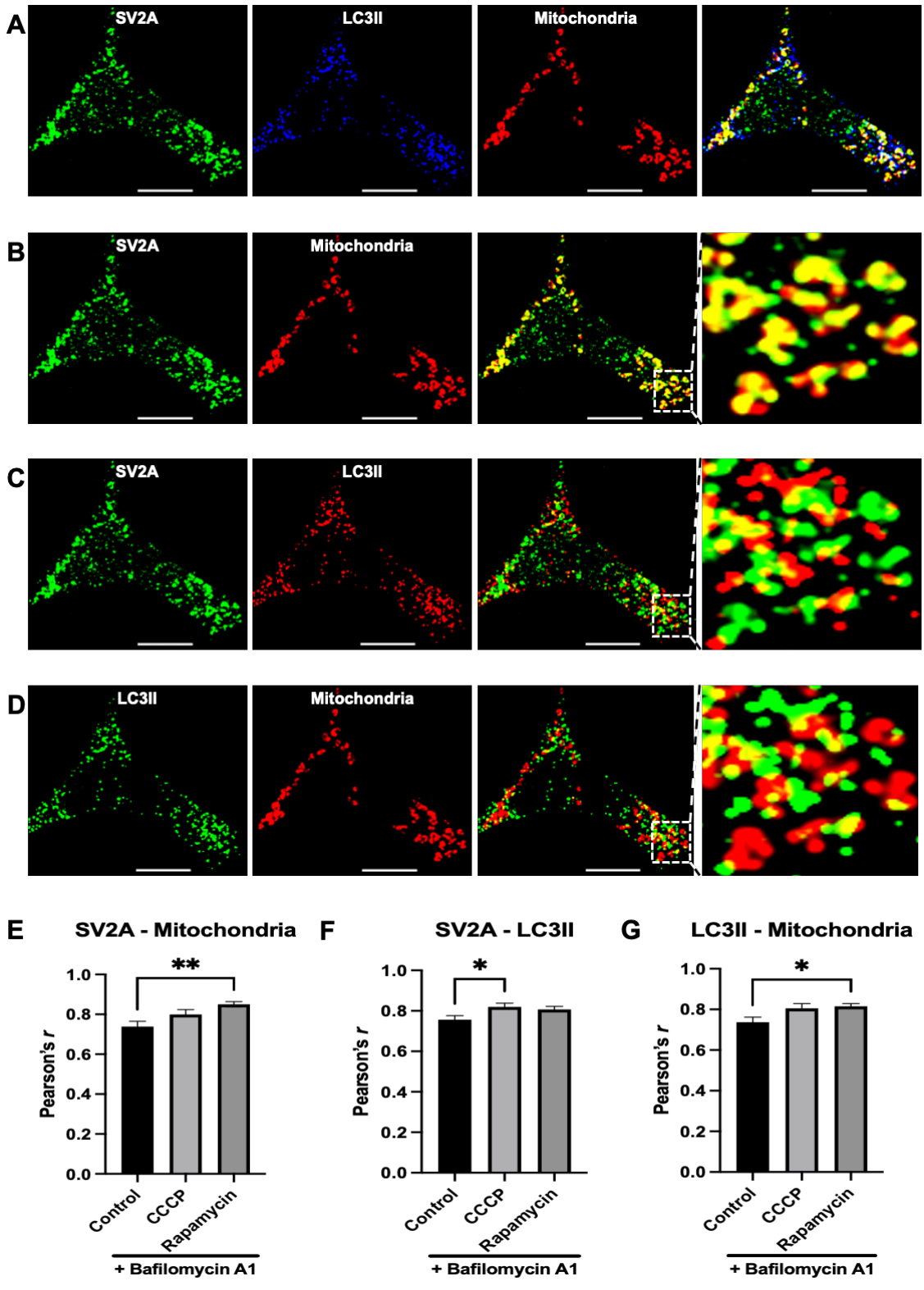
A
SV2A
LC3II
Mitochondria
B
SV2A
Mitochondria
C
SV2A
LC3II
D
LC3II
Mitochondria
E
SV2A - Mitochondria
**
Pearson's r
1.0
0.8
0.6
0.4
0.2
0.0
Control
CCCP
Rapamycin
+ Bafilomycin A1
F
SV2A - LC3II
*
Pearson's r
1.0
0.8
0.6
0.4
0.2
0.0
Control
CCCP
Rapamycin
+ Bafilomycin A1
G
LC3II - Mitochondria
*
Pearson's r
1.0
0.8
0.6
0.4
0.2
0.0
Control
CCCP
Rapamycin
+ Bafilomycin A1

Figure 47 Induction of autophagy enhances mitochondrial localization of SV2A

A) Representative confocal images of rapamycin (10 µM/4 h) and bafilomycin A1 (600 nM/4 h) treated SH-SY5Y cells stained for SV2A, LC3II and mitochondria. Colocalization of the three is indicated by bright white spots. **(B)** Representative confocal images of rapamycin (10 µM/4 h) and bafilomycin A1 (600 nM/4 h) treated cells stained for SV2A and mitochondria. Yellow indicates colocalization. **(C)** Representative confocal images of rapamycin (10 µM/4 h) and bafilomycin A1 (600 nM/4 h) treated cells stained for SV2A and LC3II. Yellow indicates colocalization. **(D)** Representative confocal images of rapamycin (10 µM/4 h) and bafilomycin A1 (600 nM/4 h) treated cells stained for LC3II and mitochondria. Yellow indicates colocalization. **(E-G)** Mean Pearson's r values calculated for each imaged cell confirm the increased colocalization of SV2A with mitochondria (E), of SV2A with LC3II (F) and of LC3II with mitochondria (G) upon mitochondrial stress or induction of autophagy in autophagy deficient cells. Enlarged images of boxed areas are displayed at the end of each image series. Staining according to Table 14. Cells analyzed: control: 18; CCCP treated: 11, rapamycin treated: 13. Scale bar: 10 µm. Data are expressed as mean ± SEM; student's unpaired t-test (*p <0.05; **p <0.01, ***p <0.001).

Pearson's r increased from 0.74 to 0.8 during CCCP treatment and to 0.85 by rapamycin (Figure 47E). Furthermore, as predicted by the images, Pearson's r values of SV2A and LC3II increased in CCCP and rapamycin treated cells. In CCCP treated cells, Pearson's r rose from 0.76 to 0.82, while the induction of autophagy by rapamycin caused an increase to 0.81 (Figure 47F). Finally, Pearson's r values of LC3II at mitochondria increased as well in both CCCP and rapamycin treated cells. Pearson's r values rose from 0.74 to 0.81 for CCCP treated cells and to 0.82 in rapamycin treated cells (Figure 47G).

5.3.2.3 SV2A is located at lysosomes

Analysis of LC3II (autophagosomes) and SV2A suggests that SV2A controls mitophagy. However, unlikely as a constituent of the autophagosome or phagophore, as colocalization of SV2A and LC3II is missing especially in the cytosol. Anyway, SV2A may act in autophagy apart from autophagosomes being a lysosome constituent.

To induce lysosome formation, cells were starved for 2 h in EBSS medium lacking amino acids. Cells respond to starvation with increased autophagy rates, accompanied by elevated expression of lysosomes to restore their energy and amino acid supply.

SV2A is evenly distributed across control and starved cells, except that SV2A expression is elevated in starved cells, forming regions of higher density (Figure 48A, B). As expected, lysosomes are present in both control and starved cells, meanwhile the number and size of lysosomes per cell increased by starvation (Figure 48A, B).

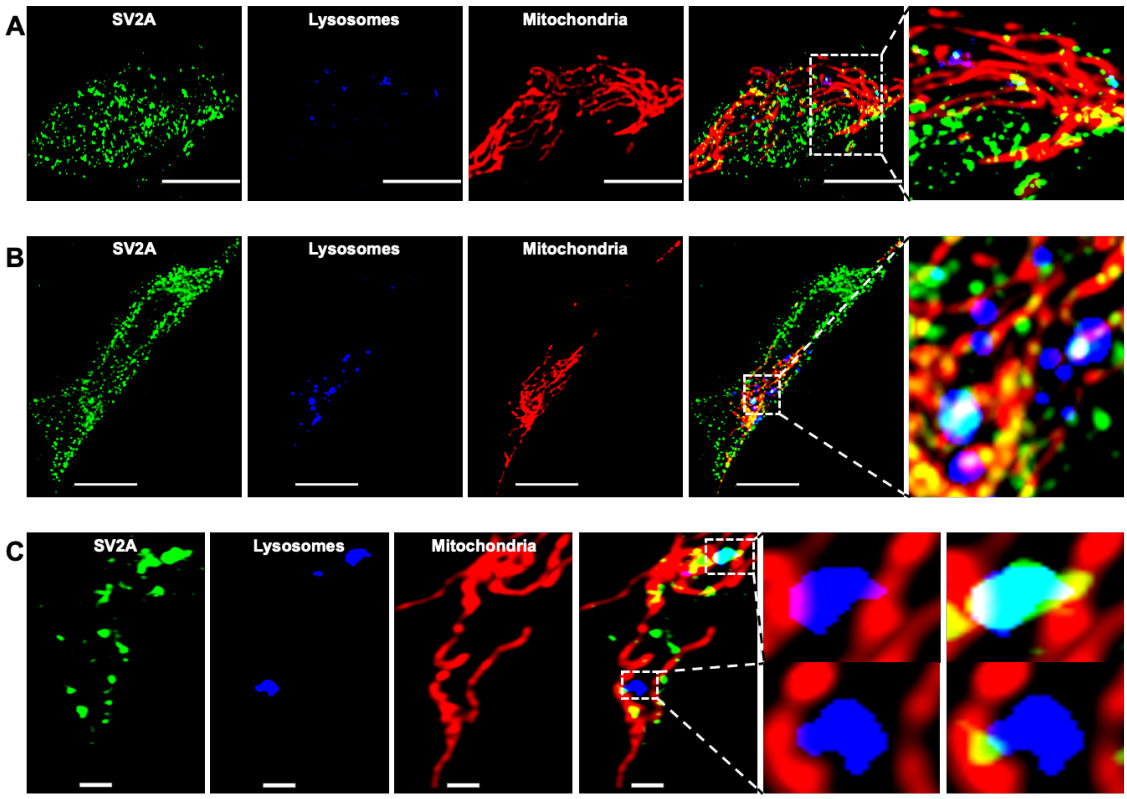

Figure 48 SV2A is located at lysosomes

(A) Representative confocal images of non starved SH-SY5Y cells stained for SV2A, lysosomes and mitochondria. Analyzed were 11 cells. **(B-C)** Representative confocal images of EBSS starved (2 h) cells stained for SV2A, lysosomes and mitochondria. Colocalization of SV2A with mitochondria is indicated by yellow color, of SV2A with lysosomes by turquoise color, of lysosomes with mitochondria by pink color and of the three by bright white spots. SV2A seems to be an anchoring protein for lysosomes at the mitochondrion (C). Analyzed were 20 cells. Scale bar: 10 µm. Enlarged images of boxed areas are displayed at the end of each image series. Staining according to Table 14.

Interestingly, starvation had no effect on mitochondrial morphology, since mitochondria are tubular and interconnected, similar to control. As expected, SV2A is frequently present at lysosomes, but not at all of them. Lysosomes of starved cells reside mainly in regions where mitochondria are present, resulting in colocalization of lysosomes with

SV2A and mitochondria. Moreover, lysosomes frequently attach to mitochondria at sites where SV2A is present.

5.4 Impact of levetiracetam on SV2A affected cellular processes

Previous experiments demonstrate that SV2A is present at mitochondria, especially when mitochondria are severely damaged and fragmented. Moreover, SV2A affects mitochondrial morphology, as reduction of SV2A protein levels causes mitochondrial fragmentation both in vitro and in vivo. After all, SV2A was demonstrated to affect autophagy, as knockdown of SV2A decreases the autophagic flux. Hereafter, the effects of SV2A ligand LEV on mitochondrial morphology and autophagy are examined.

5.4.1 Levetiracetam elongates mitochondria via its target SV2A

To analyze if LEV influences mitochondrial morphology in SH-SY5Y cells, mitochondrial length of control cells and cells treated with 200 µM LEV for 2 h was measured. Confocal images demonstrate that LEV induces changes in mitochondrial morphology compared to untreated control, as mitochondria are elongated and healthier in appearance (Figure 49A). The percentage of small punctuated mitochondria dropped by 7.4 % during LEV treatment, whereas the percentage of tubular (+5.5 %) and elongated mitochondria (+1.7 %) increased (Figure 49C).

Whether LEV depends on SV2A for its mitochondrial effect was analyzed by treating SV2A KD cells with LEV and later examination of mitochondrial morphology. If LEV acts independently of SV2A on mitochondria, mitochondrial morphology should still improve despite SV2A KD. As previously described, mitochondria in cells treated with scrambled siRNA appear healthy and tubular, whereas knockdown of SV2A results in severe fragmentation and swelling of mitochondria (Figure 49B). Moreover, mitochondrial fragmentation and swelling observed in SV2A KD cells is not ameliorated by LEV, which was expected given that LEV is a SV2A ligand (Figure 49B). The percentage of punctuated mitochondria increased by ~17 % in both SV2A KD and SV2A KD+LEV cells compared to negative control. In addition, levels of truncated mitochondria decreased by 6.2 % in SV2A KD cells, whereas in SV2A KD+LEV cells no difference compared to control is observed. Tubular mitochondria experienced a 9.1 % loss in SV2A KD cells, which is even exceeded by the 15.6 % reduction in cells

additional treated with LEV (Figure 43D). Furthermore, the amount of elongated mitochondria declined in SV2A KD and SV2A KD+LEV cells.

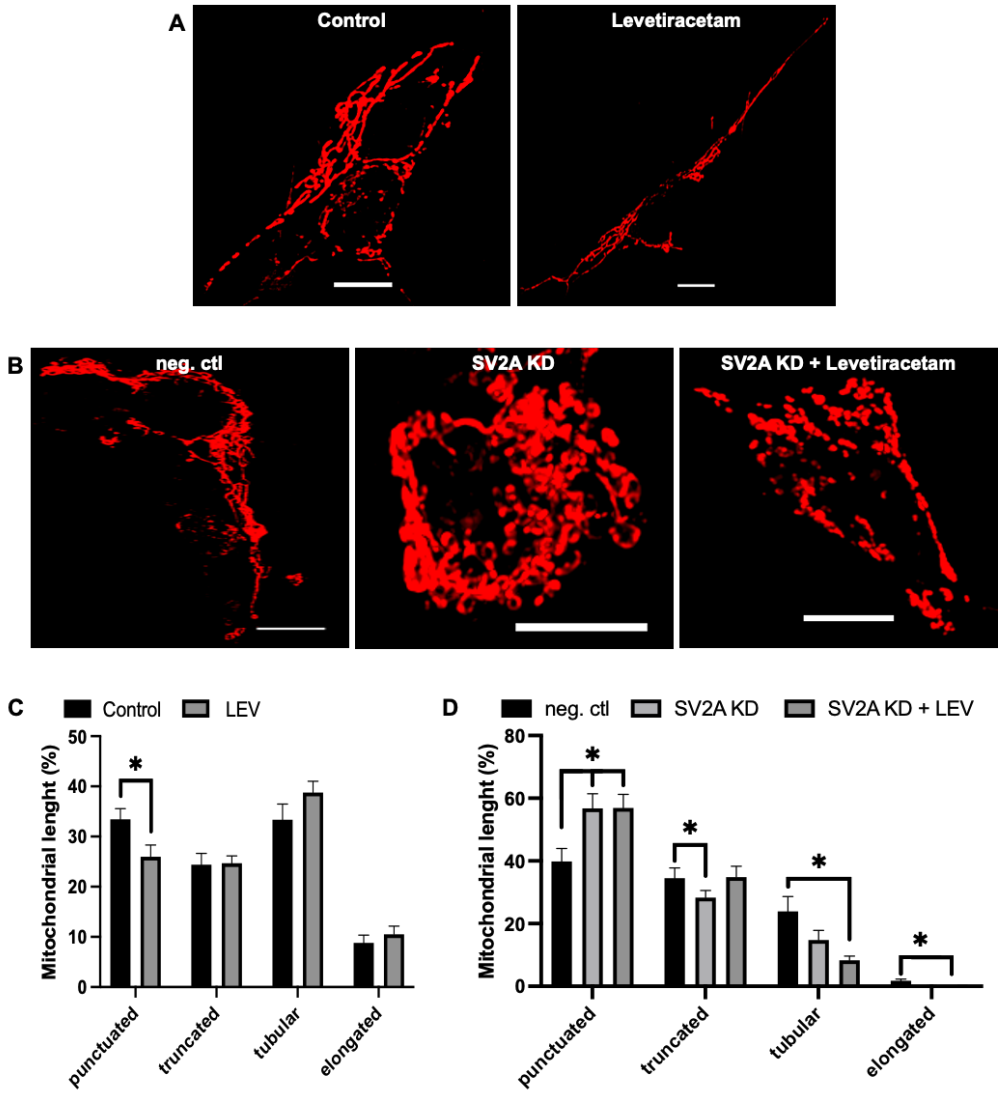

Figure 49 Levetiracetam mediates elongation of mitochondria acting on SV2A

(A) Representative confocal images of mitochondrial morphology in LEV (200 µM/2 h) treated SH-SY5Y cells. **(B)** Representative confocal images of mitochondrial morphology in SH-SY5Y cells treated with scrambled siRNA (10 nM/48 h), SV2A siRNA (10 nM/48 h) and SV2A siRNA (10 nM/48 h) along LEV (200 µM/2 h). **(C)** Length distribution of mitochondria in LEV treated cells compared to untreated control. LEV elongates mitochondria. n= 11. **(D)** Length distribution of mitochondria in SV2A KD cells treated with LEV (200 µM/2 h) compared to SV2A KD cells and negative control. Effect of LEV on mitochondria vanishes during SV2A KD. n= 4-6**.** Staining according to Table 14. Scale bar: 10 µm. Data are expressed as mean ± SEM; student's unpaired t-test (*p <0.05; **p <0.01, ***p <0.001). n= 1 equals 100 mitochondria measured.

5.4.2 Autophagy

As reported previously, loss of SV2A impairs autophagic flux. Since one of the underlying ideas of this scientific work was to explore the effects of LEV in context of AD, autophagic flux was first investigated in our SH-SY5Y AD cell model, followed by examining the effects of LEV on autophagic flux in AD.

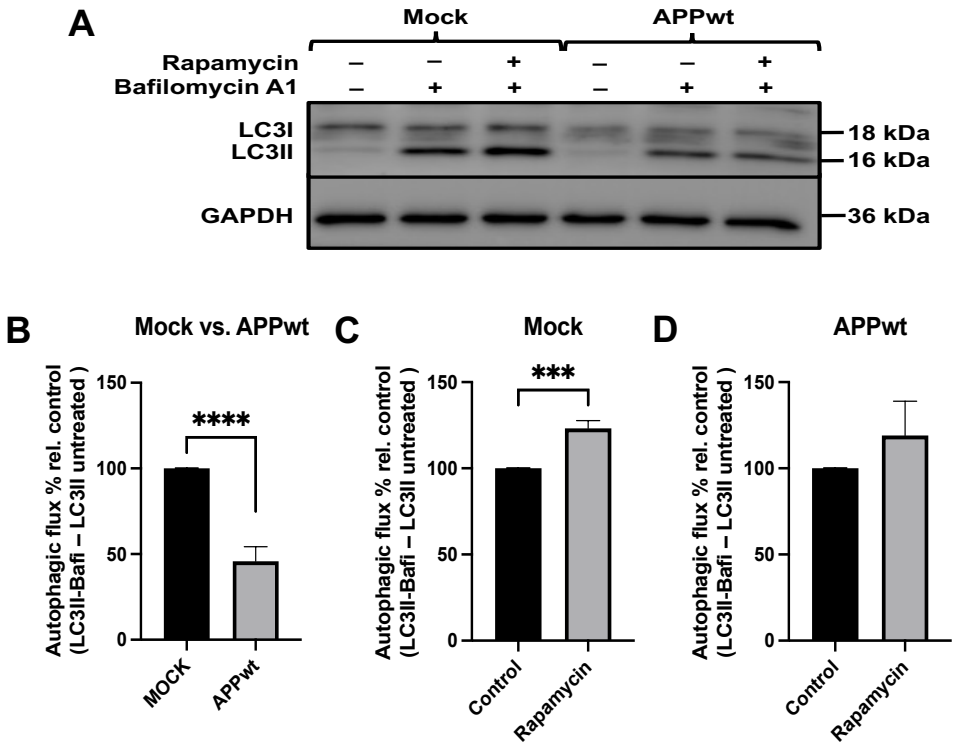

Figure 50 Autophagy is impaired in Alzheimer's disease

(A) Representative LC3II western blot of SH-SY5Y Mock and APPwt cells treated with bafilomycin A1 (600 nM/4 h) and rapamycin (10 µM/4 h). 20 µg protein were loaded per well. GAPDH serves as internal control. The first three wells were loaded with Mock extracts and wells 4-6 with APPwt extracts. Gel was loaded for both cell lines as follows: 1. well: control cells, 2. well: cells treated with bafilomycin A1, 3. well: cells treated with bafilomycin A1 and rapamycin. **(B-D)** Autophagic flux in Mock cells compared to APPwt cells suffering from increased Aβ load (B). Autophagy is still inducible in both Mock and APPwt cells (C-D). Analyzed were 3 independent cell extracts. Data are expressed as mean ± SEM; student's unpaired t-test (*p <0.05; **p <0.01, ***p <0.001).

Cell extracts of SH-SY5Y Mock and APPwt cells were treated with 600 nM bafilomycin A1 for 4 h to inhibit autophagosome degradation as previously described. In addition,

to investigate whether autophagy is still inducible in AD, a third sample treated with bafilomycin A1 and 10 µM rapamycin for 4 h was prepared for both cell lines. LC3II expression was again analyzed as an autophagy marker. The representative western blot displays LC3I, LC3II and GAPDH bands in correlation to bafilomycin A1 and rapamycin treatment. GAPDH serves as internal control. As expected, the band intensity of LC3II increases significantly in both Mock and APPwt cells in response to treatment with bafilomycin A1 (Figure 50A). Interestingly, the intensity of LC3II bands is stronger in Mock cells regardless of autophagy induction compared to APPwt cells, indicating impaired autophagy in cells with high Aβ burden. The band intensities of internal control GAPDH are equal in all wells, proving that the same amount of protein was loaded onto each well. As expected according to the band intensities, autophagic flux fell significantly to 54.2 % in APPwt cells compared to Mock cells. (Figure 50B). Moreover, inhibition of mTORC1 induced a significant 23.2 % increase of autophagic flux in Mock cells and a 19 % increase in APPwt cells (Figure 50C, D).

Autophagy is impaired in our AD cell model. Consequently, the effect of 200 µM LEV for 2 h on autophagy in Mock and APPwt cells was investigated by WB. Interestingly, the LC3II band intensity increases in Mock cells treated with LEV compared to control, corresponding to a 12.5 % rise in autophagic flux (Figure 51A, B). Surprisingly, upon LEV treatment the LC3II band intensity is weaker in APPwt cells compared to control. Likewise, autophagic flux is reduced by 8% (Figure 51C). The band intensities of internal control GAPDH are equal in all wells, proving that the same amount of protein was loaded into each well.

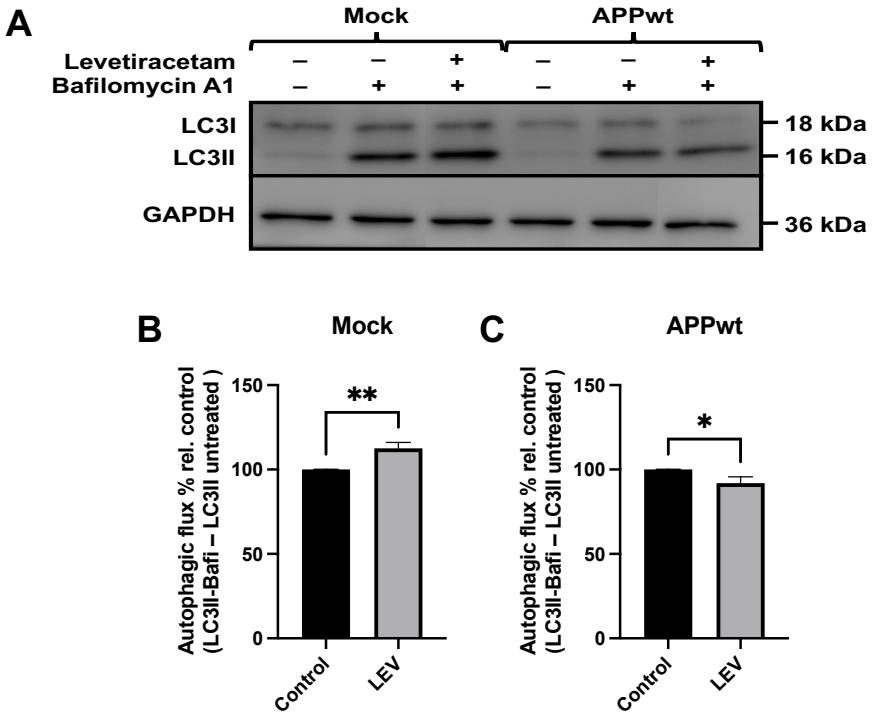

Figure 51 Levetiracetam affects autophagy

(A) Representative LC3II western blot of SH-SY5Y Mock and APPwt cells treated with bafilomycin A1 (600 nM/4 h) and LEV (200 µM/2 h). 20 µg protein were loaded per well. GAPDH serves as internal control. The first three wells were loaded with Mock extracts and wells 4-6 with APPwt extracts. Gel was loaded for both cell lines as follows: 1. well: control cells, 2. well: cells treated with bafilomycin A1, 3. well: cells treated with bafilomycin A1 and levetiracetam. **(B-C)** Changes in autophagic flux in Mock (B) and APPwt (C) cells treated with LEV. Analyzed were 3 independent cell extracts. Data are expressed as mean ± SEM; student's unpaired t-test (*p <0.05; **p <0.01, ***p <0.001).

5.4.3 Impact of levetiracetam on SV2A transcription

Levetiracetam affects autophagy, as LEV increases autophagic flux in Mock cells and decreases it in APPwt cells. This impact is presumably mediated via SV2A, since SV2A is the accepted target of LEV and its effects on mitochondria disappear upon SV2A KD. To investigate the discrepancy of LEV on autophagy in APPwt and Mock cells, SV2A mRNA expression was determined in LEV treated APPwt and Mock cells by qPCR.

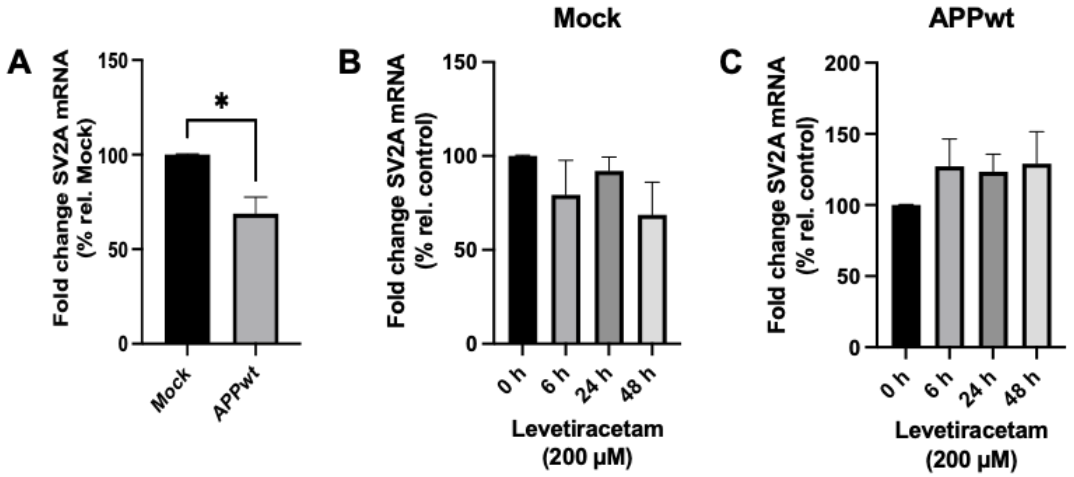

Figure 52 SV2A transcription is impaired in Alzheimer's disease

(A) Fold change of SV2A mRNA in SH-SY5Y APPwt cells compared to Mock cells. **(B)** Fold change of SV2A mRNA in Mock cells treated with 200 µM LEV for 6 h, 24 h and 48 h. **(C)** Fold change of SV2A mRNA in APPwt cells treated with 200 µM LEV for 6 h, 24 h and 48 h. 4 independent qPCR experiments were performed. Data are expressed as mean ± SEM; student's unpaired t-test (*p <0.05; **p <0.01, ***p <0.001).

In APPwt cells, a cell model of LOAD, mRNA fold change is 31.1 % lower compared to Mock cells (Figure 52A). AD cells experience a minor SV2A KD. To analyze the impact of LEV on the transcription of SV2A, SH-SY5Y Mock and APPwt cells, were treated with 200 µM LEV for 6 h, 24 h and 48 h. Surprisingly, LEV reduces SV2A transcription in Mock cells, as SV2A mRNA levels decreased to 79.3 % at 6 h, increased to 92.1 % at 24 h and decreased to 68.8 % at 48 h (Figure 52B). In contrast, in APPwt cells LEV increases SV2A transcription, although not significantly. After 6 h, mRNA levels already increased to 127.3 %, which remained stable over 48 h (Figure 52C). LEV increases SV2A transcription in APPwt cells while reducing it in Mock cells.

6 DISCUSSION

6.1 Mitochondrial localization of SV2A

6.1.1 SV2A is located at the outer mitochondrial membrane

Since SV2A is the accepted target of LEV and LEV exhibits protective effects on mitochondria, we hypothesized that SV2A is a mitochondrial protein. First evidence supporting our hypothesis came from Stockburger et al. (2016), who detected SV2A in isolated mitochondria from mouse brains performing WB technique[13]. Interestingly, in the literature, very little is known about the mitochondrial localization and effects of SV2A and other synaptic vesicle proteins, therefore this research could revolutionize the understanding of SV2A.

As hypothesized, both confocal and super-resolution images of SH-SY5Y cells stained for SV2A and mitochondria/TOM20, show mitochondrial localization of SV2A. This marks a breakthrough as these are the first images to confirm that SV2A is located at mitochondria. On super-resolution images the localization of SV2A at mitochondria is lower compared to confocal data, presumably owing to the 15-fold higher resolution of super-resolution microscopy. Since the resolution of super-resolution microscopy is ~40 nm in xy-direction, the colocalization of SV2A and TOM20 is analyzed and not the overall mitochondrial localization of SV2A as on confocal images where whole mitochondria are stained. Due to the lower resolution of the confocal images, the amount of SV2A located at mitochondria may have also been incorrectly determined. Moreover, an interaction between TOM20 and SV2A is unlikely given that SV2A lacks mitochondrial targeting sequences required for mitochondrial import of nuclear-encoded proteins via the TOM complex, which are recognized by TOM20, the TOM complex receptor[169,170]. Nevertheless, CBC values of super-resolution images confirm that colocalization of SV2A and TOM20 exists, as SV2A molecules colocalize with TOM20. As CBC values only account for the colocalization of SV2A and TOM20, SV2A molecules within mitochondrial regions were determined based on super-resolution images. 34.5 % of SV2A molecules are located in mitochondrial regions on super-resolution images, which agrees with the impression of confocal and super-resolution images. The strong discrepancy in SV2A at TOM20 and within mitochondrial regions suggests that SV2A is present at mitochondria but does not primarily interact with

TOM20. As SV2A is located at mitochondria, SV2A of course sometimes colocalizes with TOM20 despite not being transported by the TOM complex.

Interestingly, SV2A forms areas of higher abundance commonly found at mitochondria, which could represent an accumulation of either synaptic vesicles or SV2A proteins targeting mitochondria in response to certain stimuli. Greater mitochondrial localization following various stimuli, such as increased ROS levels, is already known for several proteins associated with mitochondrial dynamics or mitophagy, but is unknown for any synaptic vesicle proteins because of the lack of data on those proteins at mitochondria.

Since SV2A is present at mitochondria and colocalizes with TOM20 but cannot be imported into the mitochondrion lacking a mitochondrial target sequence, SV2A likely resides in the OMM or interacts with the OMM. Western blot of mitochondrial fractions confirmed this assumption, with SV2A present only in the OMM fraction and disappearing once the IMS is reached.

TOM20 is unlikely the primary mitochondrial interaction partner of SV2A, therefore super-resolution experiments could be repeated involving other OMM proteins to identify interaction partners of SV2A. Given that the entire TOM complex is only ~120 Å wide and ~90 Å high (12 nm/9 nm), experiments with different TOM subunits will be of little use as even super-resolution microscopy cannot distinguish between the individual subunits[171,172].

6.1.2 Mitochondrial localization of SV2A increases upon mitochondrial dysfunction and fragmentation

As mentioned in the introduction, SV2A ligand levetiracetam exerts particularly strong effects on mitochondria in cells suffering from severe oxidative or mitochondrial stress[13,25,173]. In context of increased colocalization observed at certain mitochondria in control cells, it was hypothesized that mitochondrial localization of SV2A correlates with mitochondrial health. To test this hypothesis, SH-SY5Y cells were treated with either 5 µM rotenone or 1 µM CCCP for 24 h to simulate chronic elevated ROS levels and mitochondrial perturbation known to be associated with AD[13,150]. Rotenone inhibits complex I of the ETC, triggering electron leakage and impairment of the ETC associated with increased intracellular ROS levels, decreased MMP, decreased ATP levels and mitochondrial fragmentation. CCCP is a potent mitochondrial uncoupler

which transports protons across the IMM, thereby disrupting the proton gradient and MMP necessary for ATP synthesis, causing decreased ATP levels, depolarization of mitochondria, increased ROS levels and mitochondrial fragmentation.

As expected, confocal images of rotenone treated cells demonstrate increased mitochondrial localization of SV2A among rotenone damaged mitochondria, especially when highly fragmented. This is also reflected in a significant increase in Pearson's r. Likewise, super-resolution images of both rotenone and CCCP treated cells demonstrate increased localization of SV2A at highly fragmented mitochondria, whereas no increase at tubular mitochondria despite exposure to CCCP or rotenone. This indicates that mitochondrial fragmentation and disruption are stimuli for the elevated localization of SV2A at mitochondria.

Surprisingly, the increase in SV2A at fragmented mitochondria displayed on super-resolution and confocal images is not reflected in the percentage of SV2A molecules with CBC values ≥0.5 resembling colocalization with TOM20 (mitochondria). CBC values ≥0.5 decreased in rotenone and CCCP treated cells compared to control. The discrepancy between super-resolution images and CBC values accounts to decreased colocalization of SV2A and TOM20, which does not necessarily indicate reduced localization of SV2A at mitochondria. In this context, it is important that the distribution of CBC values does not state whether the number of SV2A molecules at TOM20 (mitochondria) has increased, as observed on the images, but whether SV2A at TOM20 has increased or decreased relative to the total number of SV2A molecules inside the cell. Consequently, if both the SV2A expression within the cell and the interaction between SV2A and TOM20 increase, the increased colocalization of SV2A and TOM20 is not reflected in the percentage of CBC values ≥0.5. This appears to be the case in both rotenone and CCCP treated cells, as the total number of intracellular SV2A increased significantly in CCCP treated cells and slightly in rotenone treated cells compared to control, explaining the lower percentage of CBC values ≥0.5 most pronounced in CCCP treated cells. In agreement, the percentage of SV2A within mitochondrial regions relative to the total number of SV2A per image is the lowest in cells exposed to CCCP (27.7 %). Interestingly, the total number of mitochondrial SV2A is highest following CCCP treatment, although this represents a trend and is not significant. However, in cells treated with rotenone, a milder stressor, the percentage of

mitochondrial SV2A increased from 34.5 % to 40 %, in contrast to the decrease in CBC levels ≥0.5 calculated for TOM20.

Mitochondrial localization of SV2A and its cellular expression appear to depend on the degree of mitochondrial stress and the severity of mitochondrial damage. SV2A may be present at damaged mitochondria to prevent them from entering mitophagy or to protect the cell from intrinsic apoptosis. However, when mitochondria and cells are severely damaged, SV2A is increased in the cytosol, perhaps indicating increased vesicle formation or the initiation of cellular mechanisms that may trigger apoptosis, which is known to be induced by CCCP[174,175]. The increased intracellular SV2A expression, especially under the influence of CCCP, could thus be part of the pathogenicity of the two mitochondrial toxins. In this context, Nowack et al. (2011) already suggested that normal synaptic function is affected likewise by both elevated and decreased SV2A expression as the phenotype of SV2A overexpression is consistent with that of neurons from SV2A KO mice[176].

Evaluation of SV2A molecules within mitochondrial regions of cells treated with either rotenone or CCCP confirmed elevation of mitochondrial SV2A upon mitochondrial stress. The localization of SV2A molecules in mitochondrial regions is again particularly pronounced in severely distorted mitochondria treated with CCCP. It appears that the increased mitochondrial localization of SV2A reflects increased levels of ROS and mitochondrial dysfunction up to mitophagy. As cells suffering from CCCP display the strongest increase in mitochondrial SV2A, SV2A may be involved in autophagy or mitophagy, since CCCP induces mitophagy by disruption of the MMP[157,158]. Another possibility regarding the increased localization of SV2A at mitochondria could be that SV2A is involved in apoptosis, as intrinsic apoptosis is induced by mitochondrial disruption and CCCP.

As hypothesized, mitochondrial stress and increased ROS levels appear to be stimuli enhancing localization of SV2A to mitochondria. Stress induced intracellular translocation is also known for SNARE proteins, a family of proteins also present on vesicles where their activity is regulated by SV2A. Arasaki et al. (2015) reported that SNARE protein STX17 localizes to the ER and mitochondria following oxidative stress to initiate mitochondrial fission by controlling the localization and activity of DRP1[161]. Moreover, as mentioned previously SNARE proteins are involved in autophagy as

well[166,167,177]. The literature suggests that mitochondrial stress induced accumulation of SV2A at mitochondria is plausible. Whether the enhanced localization of SV2A at mitochondria causes mitochondrial degradation or rescue remains to be investigated.

6.1.3 Interaction of SV2A and mitochondria could be vesicle related

SV2A has been considered a vesicular protein ever since its discovery by Buckley, K. & Kelly, R. B. (1985)[178]. This changed with the discovery of SV2A in isolated mitochondria by Stockburger et al. (2016), although no evidence was provided that SV2A was present in theses mitochondrial fractions apart from vesicles[13]. In the literature, synaptic vesicles are neither described as mitochondrial interactors, nor have they ever been identified at mitochondria by electron microscopy or any other imaging method. However, mitochondria shed mitochondria derived vesicles (MDV), a mechanism which dates back to archaebacteria, the ancestors of mitochondria[179]. MDV are believed to transport damaged mitochondrial compounds to peroxisomes or lysosomes for degradation without inducing mitophagy, playing an important role in mitochondrial homeostasis[179–182]. Furthermore, mitochondrial compounds are transferred by MDV to recipient cells, even whole mitochondria encapsulated in vesicles can be transferred[183]. The previously demonstrated mitochondrial localization of SV2A suggests that vesicular interactions may occur at mitochondria.

VAMP2 representing synaptic vesicles, colocalizes with SV2A on confocal images, as expected for two synaptic vesicle proteins. Surprisingly and more exciting, VAMP2 is also present at mitochondria on confocal and super-resolution images. The colocalization of VAMP2 and SV2A observed at mitochondria may represent vesicles at mitochondria. Nevertheless, SV2A is frequently found at mitochondria, separate from VAMP2, as also indicated by a higher, but not significantly higher, Pearson's r for SV2A at mitochondria (0.66) compared to VAMP2 at mitochondria (0.6), suggesting that SV2A may also be present at mitochondria without vesicles. Synaptic vesicles are ~40 nm in size, making confocal microscopy with its resolution of ~320 nm in xy-direction incapable of resolving individual proteins of vesicles separately[184]. Consequently, SV2A molecules separated from VAMP2 on confocal images are more than 320 nm apart from VAMP2 and thereby detached from vesicles. Only colocalization of SV2A and VAMP2 on confocal images represents mutual vesicular localization of SV2A. It is evident on super-resolution images that the localization of VAMP2 at TOM20 is lower compared to that described previously for SV2A. The

percentage of CBC values ≥0.5 is 4.4 % higher for SV2A (14.1 %) compared to VAMP2 (9.7 %), which does not represent a significantly higher colocalization of SV2A and TOM20, but suggests that SV2A is located to a greater extent at mitochondria than VAMP2. These data support the aforementioned theory that SV2A is present at mitochondria both in form of vesicles and by itself. However, since SV2A and VAMP2 behave similar at mitochondria and the differences in mitochondrial localization are not significant, it cannot be excluded that the localization of SV2A at mitochondria in fact reflects an interaction of vesicles with mitochondria.

As previously the CBC data, do not represent all VAMP2 molecules at mitochondria, but only those located at TOM20. Like SV2A, VAMP2 does not feature a mitochondrial targeting sequence, therefore, pronounced colocalization with TOM complex receptor TOM20 was not to be expected. Comparing the amount of SV2A and VAMP2 within mitochondrial regions, the higher abundance of SV2A over VAMP2 is still evident, as 34.5 % of SV2A molecules are located at mitochondria compared to 28.5 % of VAMP2 molecules. The difference, although not significant, suggests once again that SV2A may be present at mitochondria apart from VAMP2 (vesicles). Since members of the VAMP family perform many different functions and have different cellular localizations, staining of vesicles by VAMP2 may not 100 % guarantee that only synaptic vesicles are stained, even though a specific monoclonal antibody for VAMP2 was used. To define synaptic vesicles more precisely, a second vesicular protein could be stained. SV2A would not be suitable as we suspect functions and localizations for SV2A apart from vesicles.

Upon rotenone treatment, mitochondrial localization of SV2A and VAMP2 increases likewise on confocal images, yet greater for SV2A as SV2A is present at mitochondria even in the absence of VAMP2, whereas VAMP2 seems to require SV2A to bind to mitochondria. The increased mitochondrial localization induced by rotenone is also confirmed by the significant increase in Pearson's r for SV2A (0.66 to 0.84) and VAMP2 (0.6 to 0.77). Interestingly, the Pearson's r regarding colocalization of SV2A and VAMP2 (0.77) matches exactly those of VAMP2 and mitochondria, again suggesting that VAMP2 is present only along SV2A at mitochondria. However, this also indicates that vesicular interactions with mitochondria exist and increase due to mitochondrial stress and may account for a large proportion of the interactions of SV2A with mitochondria. On super-resolution images of rotenone treated cells, colocalization

of VAMP2 and TOM20 also increases, similar to SV2A previously. Interestingly, in contrast to SV2A mentioned earlier, the increased colocalization of VAMP2 and TOM20 is reflected in the percentage of CBC values ≥0.5, which increased from 9.7 % to 11.7 %. However, the percentage of CBC values ≥0.5 is still higher for SV2A (13%), but only slightly and not significant. The corresponding mitochondrial localization of VAMP2 rose from 28.5 % to 41.2 % following rotenone treatment, even surpassing those of SV2A (40 %). This is surprising in light of previous data, as SV2A has previously been consistently more abundant at mitochondria than VAMP2, although not significantly. The sharp increase in VAMP2 at mitochondria, as evidenced by the increase in CBC levels ≥0.5 and VAMP2 molecules in mitochondrial regions, suggests stress induced accumulation of vesicles at mitochondria and agrees with the SV2A data. Since SV2A and VAMP2 always behave alike, even though SV2A is usually a little more abundant at mitochondria without reflecting significant differences, it cannot be excluded that the localization of SV2A at mitochondria in fact reflects vesicles present at mitochondria. To ensure that the enhanced localization of SV2A at mitochondria indeed reflects a localization of SV2A, further experiments and data are needed.

In the literature, little evidence exists regarding the localization of VAMP2 at mitochondria, as in most experiments involving VAMP2 and mitochondria, VAMP2 is either used as a marker for synaptic vesicles or active synapses[185]. However, synaptic vesicles displayed by VAMP2 are frequently described to occur close to mitochondria prior to transmitter release as mitochondria provide the ATP required. Griesche et al. (2019), for instance, demonstrated by confocal microscopy that VAMP2 is in close proximity to mitochondria during insulin release from granules of B-cells[186]. Interestingly, Isenmann et al. (1998) reported the existence of a VAMP1 splice variant, VAMP1B, which is present at mitochondria and contains a mitochondrial targeting sequence[187,188]. They performed confocal microscopy of FLAG-labeled VAMP1B demonstrating distinct localization of VAMP1B at mitochondria stained by TOM20, even sharing structural similarities[187]. In addition, radiolabeled VAMP1B, but not VAMP1A, was detected by WB in isolated mitochondria[188]. Surprisingly, according to the confocal images, VAMP1A is also present at mitochondria, albeit to a lower extent. These results are similar to ours showing colocalization of VAMP2 with TOM20 and suggest that vesicles may indeed interact with mitochondria or perhaps that VAMPs and SV2A interact with mitochondria beyond vesicles. Since VAMP1 and VAMP2 are

both synaptic vesicle proteins and their protein sequences are 85.87 % homologous (e-value: $1e^{54}$) according to NCBI's Basic Local Alignment Search Tool (BLAST), a similar splice variant for VAMP2 may exist which would explain the mitochondrial localization of VAMP2. Given that both VAMP1 and VAMP2 are involved in membrane fusion, VAMP1B and the hypothetical VAMP2B may be involved in mitochondrial fusion, as previously suggested by Isenman et al. (1998). Despite these exciting findings, no mitochondrial functions for VAMP1B have been published to date.

The colocalization of SV2A and VAMP2 at mitochondria could also represent the involvement of both vesicular proteins in the formation or maturation of MDV. Soubannier et al. (2012) already demonstrated MDV formation for selective disposal of ROS damaged mitochondrial proteins by lysosomes via a PINK1-Parkin mediated mechanism which protects mitochondria and cells from impairment and apoptosis[181]. Another hypothesis related to the increased colocalization and intracellular expression of SV2A and VAMP2 is impairment of vesicle transport, loading and release caused by reduced ATP levels and Ca^{2+} buffering due to mitochondrial dysfunction, thereby increasing the number of vesicles within the cell[189–191]. Moreover, the increased expression of SV2A and VAMP2 may reflect autophagic or apoptotic processes, as already postulated for SV2A. VAMP2 regulating autophagy seems plausible, since members of the VAMP family (VAMP7/8) are already known to be involved in the fusion of autophagosome and lysosome[166,167].

6.2 SV2A regulates mitochondrial morphology

SV2A is present at mitochondria, precisely at the OMM, where its depletion causes mitochondrial fragmentation, while levetiracetam elongates mitochondria by targeting SV2A. This led to the hypothesis that SV2A either itself functions as a fission or fusion factor or regulates the activity of related proteins. Indeed, it is plausible that SV2A exerts mitochondrial functions via SNAREs as SV2A regulates SNARE activity on vesicles and SNARE protein STX17 is described to regulate mitochondrial fission by controlling the localization and activity of fission protein DRP1[161]. Conversely, evidence exist involving mitochondrial fission and fusion factors in vesicle transport, as DRP1 is involved in synaptic vesicle recovery along with Bcl-xL[162].

6.2.1 Knockdown of SV2A impairs mitochondrial morphology

The presented confocal data on mitochondrial morphology in SV2A KD cells demonstrate a significant 16 % increase in punctuated mitochondria compared to cells treated with scrambled siRNA, leaving 44 % of mitochondria smaller than 2 µm, resembling mitochondrial impairment. Furthermore, the percentage of tubular and elongated mitochondria decreased. The data on the impairment of mitochondrial morphology by SV2A KD are consistent with those of Stockburger et al. (2016), who demonstrated impairment of mitochondrial morphology and shrinkage of mitochondria following SV2A KD similar by confocal microscopy[13]. Interestingly, mitochondrial fragmentation following reduced SV2A protein levels is greater than under rotenone treatment. The observed mild mitochondrial fragmentation by inhibition of complex I using 5 µM rotenone for 24 h matches those reported in the literature[13,144,192]. Based on the severity of mitochondrial fragmentation, we hypothesize that SV2A KD and rotenone cause mitochondrial fragmentation via different pathways. In other words, SV2A does not act along the respiratory chain. This hypothesis is supported by the literature reporting no elevation of ROS levels in SV2A KD cells as well as SV2A KO animals, whereas rotenone is known to induce ROS by inhibition of complex I of the respiratory chain[1,9]. However, based on the mitochondrial phenotype of SV2A KD and KO, an increase in ROS levels is likely, but seems to have never been investigated. Interestingly knockdown of SV2B is reported to lower $A\beta_{25-35}$ induced oxidative stress caused by mitochondrial dysfunction, although rather by reducing Aβ burden than directly effecting mitochondria[193].

Based on the mitochondrial phenotype upon knockdown of SV2A, it is likely that SV2A functions as a fusion factor, since both knockout and knockdown of fusion factors MFN1/2 and OPA1 also cause mitochondrial fragmentation[194–199]. However, defects in mitochondrial morphology upon reduced protein levels of MFN1/2 and OPA1 are more severe than those associated with knockdown of SV2A, leaving only small spherical mitochondria. In the literature, mitochondrial length has not been measured in MFN1/2 or OPA1 depleted cells, likely due to the undeniably high degree of mitochondrial fragmentation visible on confocal images. Despite SV2A also bears strong resemblance to fission factor DRP1 in that both proteins are located in the cytosol and at mitochondria, as DRP1 translocates from the cytosol to mitochondria in response to certain stimuli, such as mitochondrial dysfunction associated with elevated ROS levels, to carry out fission. Additionally, SV2A and DRP1 both lack mitochondrial targeting

sequences and impact vesicles[162]. Resuming, DRP1 and SV2A behave very similar, except that DRP1 KD leads to mitochondrial elongation, whereas SV2A KD causes fragmentation[200,201]. Nevertheless, since inhibition of DRP1 by mdivi-1 similar to LEV causes mitochondrial elongation while SV2A KD on the other hand mitochondrial fragmentation, we hypothesize that SV2A might regulate DRP1 activity, which would understand mitochondrial fragmentation upon SV2A KD as a consequence of unleashed DRP1 activity in the absence of its physiological regulator[163]. As mentioned previously regulation of DRP1 activity has already been demonstrated for SNARE protein STX17 by Arasaki et al. (2015), who found that STX17 regulates mitochondrial localization and activity of DRP1, thereby controlling mitochondrial fission[161].

An interesting thought regarding the defects in mitochondrial morphology by SV2A KD is that some of the small spherical mitochondria may be mistaken for mitochondria but in reality are MDV. Since SV2A is a synaptic vesicle protein that regulates vesicle functions via SNARE proteins, knockdown of SV2A could lead to proliferation of MDV or impair their degradation by lysosomes. That MDV are stained by MitoTracker and form both under physiological and cellular stress conditions was already published by Soubannier et al. (2012)[181]. Therefore, the increase in punctuated mitochondria (<2 µm) by SV2A KD may indeed represent an increase in MDV, even though they are only 60-150 nm in size according to electron microscopy. However, the number of mitochondria 60-150 nm in size measured is definitely too small to be solely responsible for the observed mitochondrial fragmentation induced by SV2A KD. Consequently, SV2A likely influences mitochondrial fission and fusion rather than MDV. The fact that MDV size is below the resolution of a conventional confocal microscope, which perhaps makes MDV appear larger, does not change this assumption.

6.2.2 SV2A KO impairs mitochondrial morphology in a sex specific manner

SV2A KD impairs mitochondrial morphology in vitro as demonstrated in this scientific work and in the literature. However, it has never been studied how knockout of SV2A affects mitochondrial morphology in vivo, as common homozygous SV2A KO mouse models die during early PD expressing seizures[1,9]. Considering that homozygous SV2A knockout leads to juvenile death associated with seizures in rodents, mitochondrial morphology was investigated in the SV2A KO mouse model introduced by Menten-

Dedoyart et. al. (2016)[154]. Because of their unique SV2A knockout restricted to glutamatergic neurons in the CA3 region and dentate gyrus of the hippocampus, these animals do not experience seizures causing mitochondrial fragmentation and survive into adulthood[154]. In a double-blind approach using confocal microscopy mitochondrial morphology was investigated among glutamatergic neurons in the CA3 region from 12 weeks old SV2A KO and control animals.

When female and male animals are pooled, mitochondrial morphology in the CA3 region of SV2A KO animals is found to be impaired compared to control animals, consistent with our in vitro observations. More precisely mitochondria appear fragmented and length measurements reveal that the percentage of punctuated mitochondria increased, whereas the percentage of truncated mitochondria decreased significantly. These are the first data showing that mitochondrial fragmentation also manifests in vivo in SV2A KO mice. As interesting as these data already are, they become even more exciting when gender differences are incorporated. No difference in mitochondrial morphology is observed in SV2A KO males, whereas in females, SV2A KO has devastating effects on mitochondrial morphology. In female mice, the percentage of punctuated mitochondria increased by 10 %, and at the same time, the number of truncated mitochondria decreased by 10.2 % compared to control female mice. These data are particularly exciting given that mitochondria are maternally inherited, meaning that brothers and sisters inherit the same set of mitochondria at the beginning of their lives[202]. However, several studies indicate that female mitochondria are more functional and robust than male mitochondria, especially at younger ages[203]. Female mitochondria in rodent brains are described to suffer less from oxidative damage, exhibit increased ETC transport and consequently generate more ATP than mitochondria in males. This is of special interest in terms of aging, as women tend to live longer than men as their mitochondria produce less ROS and exert a higher capacity of antioxidant defense. In contrast, male animals were only reported to have enhanced mitochondrial biogenesis in brain, as indicated by higher expression of key regulators e.g. PGC-1α. The key player behind the differences between male and female mitochondria is probably the influence of estrogen on mitochondrial function. Mitochondria possess both estrogen receptors (ESR) and androgen receptors. Little is known about the effect of androgens on mitochondrial function. In contrast, ESR are known to bind to nuclear and mtDNA regulating their transcription and replication, whereby estrogens increase the expression of mitochondrial proteins encoded by

nuclear and mitochondrial genomes and promote mitochondrial biogenesis. The observation that the incidence of AD is lower in young females compared to males, but increases after menopause then exceeding the incidence of males, emphasizes the importance of estrogens on mitochondria especially in females.

That male mitochondria are generally inferior to female mitochondria is also evident from the SV2A KO mouse data, as male control animals exhibit greater mitochondrial fragmentation in comparison to female control animals. Male control animals exhibit an average percentage of punctuated mitochondria as high as 70.2 %, whereas in females it is only 60 %, increasing to 69.9% during SV2A-KO, then matching male control animals. Similar is the trend for truncated mitochondria, where the percentage is already lower in male controls compared to female controls. This may explain why SV2A KO has no effect in males, as mitochondria of control males are already as fragmented as those of SV2A KO females. Although the question remains as to why mitochondrial fragmentation experienced in female SV2A KO mice fails to occur in males, already expressing impaired mitochondria? Perhaps greater mitochondrial fragmentation would be lethal or as SV2A is not solely responsible for mitochondrial dynamics, greater fragmentation is prevented by the intervention of other proteins.

The mitochondrial phenotype associated with SV2A KO is sex specific. For the SV2A KO mouse model analyzed, Serrano et al. (2019) also reported sex differences in anxiety and memory performance[204]. They examined anxiety using the Elevated Plus Maze and found that male SV2A KO animals were more anxious compared to control animals as they exhibited a significant reduction in entries and a non-significant reduction in time spent in the open arm. Among females, however, entries remained at control levels and time spent in the open arm even increased, yet not significant. Additional they employed contextual fear conditioning tests in which both female and male SV2A KO mice responded more anxiously following electric shocks, indicated by freezing of the mice, while memory performance also decreased compared to controls. The authors also reported that SV2A KO mice behaved more anxiously in general, for example, they frequently attempted to climb the wall to avoid electric shocks during the contextual fear conditioning test. Finally, they investigated the effect of SV2A KO on spatial memory by Barnes Maze. Spatial memory impairment occurred primarily in females, among whom errors (wrong hole) increased, while, interestingly, errors decreased in males. In short, animals exhibiting SV2A KO in the hippocampus behave

more anxiously and show signs of memory impairment, with males being more anxious and females showing greater impairment of spatial memory. Thus, Serrano et al. (2019) also showed sex differences in this SV2A KO mouse model supporting our data. Regarding the sex specific effects of SV2A KO, it is worth mentioning that SH-SY5Y are a cell line from a female donor, therefore the observed effects in SH-SY5Y cells may also be related to their "gender"[205]. In this context, it would be of interest to study the effects of SV2A KD in a cell line of male origin.

6.2.3 Fission and fusion events decrease upon SV2A knockdown

Based on the mitochondrial phenotype of SV2A KD and KO, the effects of reduced SV2A protein levels on mitochondrial dynamics were investigated performing live cell imaging of SH-SY5Y cells. SV2A KD in live cells induced the same phenotype observed in fixed cells and brains, characterized by pronounced mitochondrial fragmentation compared to scrambled siRNA treated control. Mitochondrial fragmentation in living cells proves that mitochondrial fragmentation observed in fixed cells and brains is the result of reduced SV2A protein levels and not an artefact of the fixation process. Regarding the distribution of mitochondria within the cell, mitochondria from SV2A KD cells are most abundant in the cell center compared to control cells. The accumulation of mitochondria in the cell center is reminiscent of the phenomenon already known in neurons, where dysfunctional mitochondria disengage from axonal anchorage during stress and migrate to the soma to be degraded; some of them already in autophagosomes[206–208]. The increased number of fragmented mitochondria in the center of SV2A KD cells may hence reflect this stress induced neuronal phenomena or a perturbation of mitophagy. Of course, despite their neuronal background, SH-SY5Y cells cannot be equated 100 % to neurons, especially in terms of size.

In terms of fission and fusion events during a 10 min time period, a significant decrease in fission and fusion events is evident in SV2A KD cells compared to control as previously hypothesized. Surprisingly, knockdown of SV2A causes a uniform decrease in fission and fusion events compared to control, whereas a shift towards fission would have been expected based on the mitochondrial phenotype. This is also confirmed since the balance between fission and fusion is unchanged in SV2A KD cells compared to control. Interestingly, with respect to mitochondrial dynamics, Cagalinec et al. (2013) published that over 80 % of fission or fusion events are followed by the

opposite event in control cells[209]. This implies that the balance between fission and fusion shifts towards fusion for shorter mitochondria and towards fission for longer mitochondria. In their experiments, they discovered that overexpression of DRP1 causes shorter mitochondria, yet the balance between fission and fusion remained equal to control. When DRP1 was knocked out, they found a slight shift in favor of fission in the balance of fission and fusion, accompanied by an elongation of mitochondria. They also investigated overexpression of MFN2 and found a 76 % increase in mitochondrial fusion rate accompanied by a 68 % increase in fission suggesting that the fission rate adjusts to the fusion rate and vice versa. When they silenced MFN2, mitochondrial length decreased, while the balance between fission and fusion was again maintained. The data of Cagalinec et al. (2013) confirm the presented data on the impairment of mitochondrial dynamics by depletion of SV2A, as KD of SV2A, like MFN2 KD, shortens mitochondria associated with a lower incidence of fission and fusion events, whereas the balance between fission and fusion is not altered. Thus, like MFN2 KD, SV2A KD perhaps induces a reduction in fusion events while simultaneously reducing the fission rate as a counter regulation of the cell to prevent excessive mitochondrial fragmentation. SV2A again proves to be similar to MFN2.

6.2.4 Knockdown of SV2A affects mitochondrial migration

Another parameter accounting for mitochondrial health is mitochondrial migration. Mitochondrial movement and velocity are essential for degradation and fusion of mitochondria. Therefore, impaired migration of mitochondria causes shortening of mitochondria. Interestingly, fragmented mitochondria in SV2A KD cells traveled 12.7 µm in 10 min, compared to only 10 µm in control cells. Due to the longer distances traveled, the velocity of mitochondria increased upon SV2A KD (21.2 nm/s) compared to control (16.7 nm/s). Although the differences are not significant, the fact that mitochondria migrate faster the smaller they are has also been demonstrated by Arnold et al. (2011) performing live imaging of cortical neurons[210]. Compared to the literature, our measured distances traveled and velocities are low given that mitochondria can move at velocities of ~100-2000 nm/s in neurons[211,212]. The large discrepancy is likely related to the fact that measurements in the literature have been performed on neurons much larger than SH-SY5Y cells.

Mitochondria cannot move by themselves, instead they are transported along microtubules by motor proteins dynein and kinesin[213]. Since knockdown of SV2A does not impair mitochondrial transport, but facilitates it, SV2A is not involved in mitochondrial transport. As mentioned earlier, in neurons, dysfunctional mitochondria are transported back to the soma for degradation. Therefore, the increased velocity of fragmented mitochondria in SV2A KD cells in combination with the increased expression of mitochondria in the cell center may reflect this neuronal phenomenon. In other words, impaired mitochondria move faster than control mitochondria because they are on their way to be degraded in the cell center. An explanation for the slower migration of control mitochondria is provided by Arnold et al. (2011) and Cagalinec et al. (2013) who found that fused mitochondria (control) move slower than small mitochondria created by fission (SV2A KD)[209,210]. They also claim that small mitochondria need to migrate through the cell faster to encounter fusion partners. Unfortunately, SH-SY5Y cells are not large enough to confirm increased retrograde transport of damaged mitochondria, as in neurons. It would therefore be of interest to repeat these experiments in primary neurons to investigate mitochondrial retrograde and anterograde migration during SV2A KD.

6.3 Interaction of DRP1 and SV2A

6.3.1 Minor colocalization of SV2A and DRP1

Since it is plausible that SV2A acts on mitochondria via fission or fusion, it remains to be elucidated how SV2A performs fission or fusion. As mentioned, SV2A appears to act as a fusion factor like MFN2 on mitochondria. However, a regulatory function for fission factor DRP1, which is known to be controlled by SNARE proteins, cannot be ruled out either[161]. DRP1 activity was hypothesized to be regulated by SV2A as both SV2A and DRP1 interact increasingly with mitochondria upon mitochondrial stress, and loss of either protein results in mortality of juvenile mice. According to the hypothesis, fragmentation induced by SV2A KD and KO would be understood as an unleashing of DRP1 activity, implying that SV2A acts as a DRP1 inhibitor counteracting STX17. The activity of DRP1 is also known to be regulated by posttranslational modifications such as phosphorylation, sumoylation or ubiquitination[214,215]. For example, protein kinase A inhibits DRP1 activity by phosphorylating S637, while calcineurin increases DRP1 activity by dephosphorylating S637[216–218]. Since SV2A is neither known to phosphorylate nor ubiquitinate proteins, it presumably requires direct binding to DRP1

for controlling DRP1 activity. Interestingly a physiological inhibitor that binds directly to DRP1, is not known.

On confocal images SV2A and DRP1 colocalize predominantly at mitochondria, surpassing their cytosolic colocalization. There are two possible explanations for the stronger mitochondrial colocalization of SV2A and DRP1. The first theory is that SV2A and DRP1 are located independently of each at mitochondria, and colocalization is falsely assumed given the low confocal microscope resolution. Another possibility is that SV2A functions as an anchoring partner for DRP1 at mitochondria, similar to FIS1 and MFF, although reduction of FIS1 and MFF protein levels results in mitochondrial elongation[219–221]. Since the Pearson's r of SV2A and mitochondria (0.78) is higher than that of DRP1 and mitochondria (0.74), SV2A is more prominent at mitochondria than DRP1 under physiological conditions, providing further evidence that SV2A is either an anchoring partner of DRP1 or functions beside DRP1. The low cytosolic colocalization of SV2A and DRP1 compared to mitochondria suggests that SV2A does not control DRP1 activity at least apart from mitochondria. If SV2A would regulate the activity of DRP1, equal colocalization of DRP1 and SV2A in the cytosol and at mitochondria would have been expected. In this regard, it is interesting that Arasaki et al. (2015), who were often cited regarding the regulation of DRP1 by SNAREs, demonstrated the regulatory function of STX17 on DRP1 not by colocalization of the two proteins but by proximity ligation assay (PLA)[161]. PLA fluorescently detects the in situ interactions of two proteins or their presence within 30-40 nm. Performing PLA they found positive signals for STX17 and DRP1. As we lack comparative images of the colocalization of STX17 and DRP1, we cannot say with certainty whether SV2A would interact with DRP1 equally in the cytosol and at mitochondria if it is a physiological interactor.

Super-resolution data on the interaction of SV2A and DRP1 support the concept that mitochondrial colocalization of SV2A and DRP1 may be nonspecific and represents, at least in part, a shared but separate mitochondrial localization. Interestingly, regions exist where both proteins are more abundant, perhaps reflecting mitochondria. However, even in these regions colocalization is low. CBC values ≥0.5 also indicate minor colocalization, as the percentage of SV2A molecules colocalizing with DRP1 is 7.1 %, which is only half of that of SV2A at TOM20 (14.1 %).

6.3.2 Colocalization of SV2A and DRP1 increases upon mitochondrial stress proving that SV2A is not an DRP1 repressor

The activity of mitochondrial fission factor DRP1, and thus its mitochondrial localization, can be induced by mitochondrial stressors such as rotenone[222,223]. Therefore, rotenone induced mitochondrial stress was used to investigate the stress related interaction of DRP1 and SV2A. If SV2A indeed regulates the activity and localization of DRP1, this will be reflected by alterations in the colocalization of SV2A and DRP1. According to our theory, we assumed decreased colocalization of SV2A and DRP1 as SV2A inhibits DRP1 activity, which is known to increase during mitochondrial stress.

As described in the literature, mitochondrial localization of DRP1 increased markedly following rotenone treatment. Moreover, increased colocalization of SV2A and DRP1 is found, especially at mitochondria. The Pearson's r for SV2A and DRP1 (0.86) even exceeds those of SV2A or DRP1 with mitochondria. Interestingly, the Pearson's r accounting for the colocalization of SV2A and mitochondria (0.84) matches those of DRP1 and mitochondria (0.83), again supporting mitochondrial stress induced binding of SV2A to mitochondria. The increased presence of both proteins at mitochondria was expected based on previous data regarding SV2A and the mode of action of DRP1. However, elevated colocalization of DRP1 and SV2A contradicts our hypothesis and rules out the possibility that SV2A functions as an inhibitor of DRP1 activity. Since super-resolution images also demonstrate enhanced colocalization of SV2A and DRP1, the enhanced colocalization observed by confocal microscopy is confirmed and not attributable to the lower resolution. Increased interaction of SV2A and DRP1 is reflected in CBC values ≥0.5, which increased to 12.8 %, approaching the 13 % of SV2A at TOM20 from previous rotenone experiments. Considering that CBC values ≥0.5 match those of SV2A at TOM20, the increased colocalization of DRP1 and SV2A may be related to DRP1 forming a chain around mitochondria where SV2A is located.

On the other hand the increased colocalization of SV2A and DRP1 could perhaps represent enhanced vesicular localization and activity of DRP1, as described by Li et al. (2013)[162]. Using electron microscopy of primary neurons and immunoblots they found that DRP1 is present at both mitochondria and on synaptic vesicles. They also demonstrated that DRP1 binds to vesicles along with Bcl-xL interacting with clathrin and, surprisingly, MFF. Interacting with clathrin, DRP1 influences endocytosis and the

release ready pool of synaptic vesicles. In this context, depletion of DRP1 is said to impair the recovery of synaptic vesicles into release ready pools, whereas physiological translocation of Bcl-xL-DRP1 to synaptic vesicle membranes increases the rate of recovery. Based on their data, Li et al. (2013) hypothesized that the protein complex of Bcl-xL-DRP1 is necessary for efficient endocytosis and presynaptic plasticity. Our data on SV2A and DRP1 perhaps align with their hypothesis, as increased DRP1 activity may have led to increased vesicle retrieval, whereby SV2A increasingly colocalizes with DRP1 as part of these retrieved synaptic vesicles. However, if this would be the case, it is unlikely that the associated colocalization is primarily related to mitochondria. Since vesicular colocalization of SV2A and DRP1 is possible according to the data of Li et al. (2013), it is certainly responsible for some of their colocalization, but minor compared to their stress induced mitochondrial colocalization.

The previous raised hypothesis that SV2A, like MFF, acts as an anchoring partner for DRP1 at mitochondria agrees well with the stress related enhanced colocalization of DRP1 and SV2A at mitochondria as well as the enhanced mitochondrial fragmentation. However, not to the mitochondrial fragmentation induced by SV2A KD. According to Li et al. (2013), DRP1 is recruited to synaptic vesicles by MFF, as MFF was co-immunoprecipitated with DRP1 and synaptotagmin from purified synaptic vesicle lysates[162]. The fact that mitochondrial DRP1 receptor MFF acts on vesicles supports the idea of SV2A serving as a vesicular and mitochondrial interactor of DRP1, thereby controlling mitochondrial morphology. If SV2A does not directly bind to DRP1, SV2A could also interact with MFF at both vesicles and mitochondria to control DRP1 activity. SV2A interacting with MFF would also be displayed by increased mitochondrial colocalization of DRP1 and SV2A. In addition, synaptotagmin 1 is a known interactor of SV2A on synaptic vesicles, whose activity is controlled by SV2A.

Considering that SV2A is a fusion factor, since the effects of SV2A on mitochondrial morphology are similar to those of MFN1/2 and OPA1, the increased colocalization of SV2A and DRP1 may reflect the phenomenon previously described by Cagalinec et al. (2013)[209]. Accordingly, the increased colocalization of DRP1 and SV2A at mitochondria upon rotenone treatment would be understood as enhanced fission mediated by DRP1 bound to mitochondria, accompanied by increased fusion of the resulting smaller mitochondria, whereupon localization of SV2A at mitochondria increases. If SV2A is a

fusion factor, LEV acts as an SV2A agonist and elongation of mitochondria would be the result of increased SV2A activity. In this context, Rocha et al. (2018) already demonstrated elongation of mitochondria by MFN2 agonists similar to the effects of LEV[224].

6.4 SV2A and its role in autophagy/mitophagy

The data discussed so far suggest that SV2A acts as a mitochondrial fusion factor. However, analysis of the SV2A KD data raised another hypothesis on how loss of SV2A causes mitochondrial fragmentation, namely that SV2A functions in autophagy and mitophagy. The involvement of SV2A in autophagy would explain the elongation of mitochondria under the influence of LEV and the increase in fragmented mitochondria caused by knockdown of SV2A due to changes in autophagy/mitophagy rate. Accordingly, SV2A KD would inhibit autophagy, leading to the observed higher percentage in punctuated mitochondria as these short mitochondria (<2 µm) could no longer be efficiently degraded, decreasing the percentage of elongated mitochondria. The accumulation of dysfunctional mitochondria due to depletion of SV2A would also trigger a vicious cycle, as increased ROS production by dysfunctional mitochondria would facilitate fragmentation of neighboring mitochondria, which could likewise not be degraded, eventually leading to apoptosis.

The hypothesis is supported by increasing knowledge on mitochondrial fission and fusion proteins as well as SNARE proteins being involved in autophagy and mitophagy. In this regard, mitochondrial fusion factor MFN2 was identified to play a key role in the fusion of autophagosomes and lysosomes during autophagy, resulting in inhibition of autophagy following MFN2 KD[164]. Furthermore, MFN2 is involved in PINK1-Parkin mediated mitophagy[165]. Among SNARE proteins, VAMP and syntaxin family members are involved in the formation and expansion of the phagophore as well as autophagosome-lysosome fusion[166,167]. Considering the effects of MFN2, a dual mechanism of SV2A acting both as a fusion factor and on autophagy is possible. Moreover, SV2A could affect autophagy by regulating the activity of SNARE proteins, as SV2A regulates the activity of SNAREs on vesicles.

6.4.1 SV2A knockdown impairs autophagy

Since, according to the theory, reduction in SV2A protein levels would cause an impairment of autophagy, autophagic flux was determined in SH-SY5Y cells experiencing SV2A KD under the influence of autophagy inhibitor bafilomycin A1. Bafilomycin A1 blocks the acidification of lysosomes by inhibiting V-ATPase, thereby preventing the degradation of autophagosomes by lysosomes, leading to an accumulation of autophagosomes. A significant, decline in autophagic flux was detected upon knockdown of SV2A, confirming the theory of SV2A influencing autophagy. The modest decrease in autophagic flux may be related to the likelihood that SV2A, as a mitochondrial protein, only regulates mitophagy, which accounts for a small fraction of cellular autophagy.

6.4.2 SV2A may regulate autophagy like mitochondrial dynamics proteins

SV2A KD results in decreased LC3II protein levels and thus autophagic flux when degradation of autophagosomes is inhibited by bafilomycin A1. In contrast MFN2 KD and KO cause autophagosome accumulation by inhibiting autophagosome-lysosome fusion, reflected by increased LC3II protein levels by WB[164,225–227]. As such, depletion of MFN2 has similar effects on autophagy as bafilomycin A1. This implies that SV2A, unlike MFN2, intervenes further upstream in the autophagy cascade than fusion of autophagosomes and lysosomes. Otherwise, no effect or rather an increase in LC3II expression should have been observed under the influence of bafilomycin A1 compared to control. Despite mediating fusion of autophagosomes and lysosomes, MFN2 has been described by Zhao et al. (2012) to exert additional effects on autophagy[164]. They detected ER derived MFN2 in autophagosomal membranes, where MFN2 interacts with ras related protein Rab 7 (RAB7) mediating the maturation of autophagosomes. In addition, Sebastián et al. (2016) analyzed the overexpression of MFN2 and described upregulation of transcription and protein levels of parkin and LC3II, indicating promotion of mitophagy by MFN2[228]. In this regard, Chen et al. (2013) demonstrated that MFN1 und MFN2 are ubiquitination substrates of parkin, that parkin is co-immunoprecipitated with MFN2 and fails to translocate to mitochondria in MFN2 null cells despite stimulation by mitochondrial stressors[229]. Recent liquid chromatography-tandem mass spectrometry (LC-MS/MS) data of Hoffmann-Conaway et al. (2020) state that SV2A is a parkin substrate, which would fit to both the reduction in autophagic flux upon SV2A KD and the higher abundance of SV2A at fragmented mitochondria[230]. Although MFN2 and SV2A behave similar in respect to mitochondrial

dynamics, loss of these proteins causes opposite effects on autophagy, corresponding to the mitochondria detached effects of MFN2 on autophagy.

Regulation of autophagy or mitophagy is known for most mitochondrial fission and fusion proteins and not unique to MFN2. However, despite MFN2, they usually do not act directly on autophagy, but rather on mitochondrial morphology, which in turn promotes or inhibits mitophagy by the size of mitochondria. According to the literature, loss of OPA1 is associated with an increase in autophagy and mitophagy, owing to a decrease in mitochondrial size and associated mitochondrial dysfunction[231,232]. The two fission factors FIS1 and MFF are also known to affect mitophagy. Not surprisingly, overexpression of FIS1 increases autophagic flux by reducing mitochondrial size while knockdown of FIS1 impairs autophagy[233,234]. MFF is described to act as a second messenger in the induction of mitophagy being phosphorylated by AMP-activated protein kinase (AMPK) and recruiting DRP1 to mitochondria[235]. Upon recruitment, DRP1 promotes fission of mitochondria, a prerequisite for the engulfment of mitochondria by the autophagosome. Talking about DRP1, knockdown and knockout of DRP1 generally result in lower autophagosome formation accompanied by impairment of autophagic flux[236,237]. Of course, on the one hand, this is attributable to increased mitochondria size but, on the other hand, according to Ikeda et al. (2015), DRP1 interacts with Bcl-2/Bcl-xL. Depletion of DRP1 promotes the interaction of beclin 1 with its endogenous inhibitors Bcl-2/Bcl-xL thereby suppressing autophagy[236]. Of interest is also the hypothesis of Inbal et al. (2002), who claimed based on immunogold staining that DRP1 is a resident protein of the autophagosome itself, which has not been confirmed by other groups[238].

Compared to the effects of fission and fusion factors on autophagy, the effects of SV2A seem to occur before the completion of autophagosome formation, since despite shortening of mitochondria, which usually facilitates LC3II expression, LC3II levels decreased in SV2A KD cells. Based on the data, SV2A seems to be involved either directly in the formation of autophagosomes or in targeting of mitochondria during mitophagy. Furthermore, the extension of phagophores by delivery of membrane parts would be possible for SV2A, a vesicular and mitochondrial protein, as this has already been demonstrated for SNARE proteins VAMP7, syntaxin 7/8, VTI1B and fusion factor MFN2[166]. Since Hailey et al. (2010) demonstrated that outer mitochondrial membranes are largely found within membranes of autophagosomes not associated with

mitophagy, mitochondria appear to be involved in the biogenesis of autophagosomes providing membranes[239]. The hypothesis on OMM as part of the autophagosome suggests that SV2A bound to the OMM may influence autophagy by elongation of the phagophore. However, it should not be excluded that the reduced autophagic flux in SV2A KD cells may also be related to impaired autophagy of vesicles, which would imply that SV2A is critical for the degradation of synaptic vesicles.

6.4.3 SV2A may influence autophagy by regulating the activity of SNARE proteins

Besides the aforementioned regulatory functions of mitochondrial fission and fusion factors on autophagy, SNARE proteins are also known to be involved in autophagy[166,240]. The involvement of SNAREs in autophagy is of particular interest given that they are also present in synaptic vesicles where their activity, is regulated by SV2A via interaction with SYT1. Thus, SV2A may affect and promote autophagy by regulating the activity of SNAREs. According to this hypothesis, SNAREs would experience a loss of function by knockdown of SV2A, resulting in suppression of autophagic flux. As already mentioned, SNAREs VAMP7, syntaxin 7/8 and VTI1B are known to regulate homotypic fusion of phagophore precursors. These membrane fusions are crucial for autophagy, as they promote the growth of membrane structures forming phagophores and autophagosomes. Furthermore, the SNARE complex of VAMP8, STX17 and SNAP29 mediates fusion of autophagosomes with lysosomes. The spectrum of SNARE functions in autophagy also covers the formation of lysosomes from the ER by syntaxin 5. Neither a direct interaction with nor a regulatory function of SV2A on the above mentioned SNARE proteins has been described so far. As mentioned SV2A interacts with SYT1 at synaptic vesicles[8,16], although SYT1 is not known to be involved in autophagy, its relatives the extended synaptotagmins (E-SYTs) are. E-SYTs are involved in autophagosome formation by participating in the local targeting of PI3P-synthesizing complexes via mobilization of vacuolar membrane protein 1, a step known to be responsible for the initiation of autophagosome biogenesis[241]. The main functional difference between SYT1 and E-SYTs is that SYT1 mediates fusion of secretory vesicles, whereas E-SYTs are ER resident membrane proteins that bridge ER and phospholipid membranes for lipid exchange without membrane fusion. However, as they are related E-SYTs, especially E-SYT1, contain conserved structural elements of SYT1. Binding of SV2A to E-SYTs has not yet been described, but seems promising given their structural similarities to SYT1.

6.4.4 Interaction of SV2A and autophagosomes

Knockdown of SV2A proved that SV2A affects autophagy or mitophagy, but not how. So far, based on the SV2A KD data it can be excluded that SV2A, like MFN2, performs fusion of lysosomes and autophagosomes, as otherwise an accumulation of LC3II proteins should have occurred. Nor is it plausible that SV2A, like mitochondrial fission and fusion factors, acts on mitophagy by shifting mitochondrial dynamics, as mitochondrial fragmentation induced by SV2A KD did not increase LC3II expression. Accordingly, SV2A seems to affect autophagy at a stage prior to autophagosome degradation, either at the initiation of autophagy or at the formation of autophagosomes. Hence, SV2A may be part of the autophagosome, perhaps located in parts of the outer mitochondrial membrane or as a parkin substrate like MFN2[229,239].

6.4.4.1 Interaction of SV2A and autophagosomes

Striking about the images on the interaction of SV2A and autophagosomes is that even in control samples exposed only to bafilomycin A1, mitochondria are swollen and fragmented. Since the only difference between these cells and untreated cells expressing tubular and healthy mitochondria is bafilomycin A1, bafilomycin A1 itself or the resulting accumulation of autophagosomes must have led to a deterioration of mitochondrial dynamics. The impaired degradation of dysfunctional mitochondria may have increased intracellular ROS levels, which in turn caused mitochondrial dysfunction and deterioration of mitochondrial morphology. However, the most plausible explanation for the swelling and partial fragmentation of mitochondria is bafilomycin A1 itself. In the literature, bafilomycin A1 is described to induce K^+ influx into the mitochondrial matrix causing mitochondrial depolarization, swelling and even release of cytochrome c[225,242,243].

On confocal images LC3II and SV2A colocalize at mitochondria and in the cytosol. Notably, LC3II is frequently separated from SV2A in the cytosol, suggesting that autophagosomes are formed and exist without SV2A. Consequently, SV2A is not an integral component of autophagosomes, as otherwise SV2A would be expressed in every autophagosome. Accordingly, the hypothesis of SV2A residing in parts of the OMM used for the formation of phagophores and later autophagosomes, as suspected based on the data of Hailey et al. (2010), becomes unlikely[239]. Nevertheless, some autophagosomes may contain OMM parts that carry SV2A, but since not every autophagosome is built on OMM parts and perhaps not every OMM part contains

SV2A, some autophagosomes do not harbor SV2A. The cytosolic colocalization of SV2A and LC3II rather seems to reflect autophagy of synaptic vesicles engulfed by autophagosomes at the moment of imaging.

More interesting than the cytosolic colocalization of SV2A and LC3II is their colocalization at mitochondria, reflecting mitophagy. When LC3II is located at mitochondria, it almost entirely colocalizes with SV2A, similar to the observations of VAMP2 and DRP1 previously, implying that SV2A may induce or facilitate mitophagy. In mitophagy, SV2A could either serve as a mitophagy receptor or as a signaling protein at the OMM, perhaps ubiquitinated by parkin, to which LC3II binds. As hypothesized earlier the involvement of SV2A in mitophagy would explain why SV2A KD causes only a small, albeit significant, decrease in autophagic flux, as loss of SV2A would only affect mitophagy, a small fraction of total cellular autophagy. Furthermore, it would explain why SV2A occurs preferentially at fragmented mitochondria. Regarding an interaction of SV2A with parkin, little is known in the literature. However, recently Hoffmann-Conaway et al. (2020) discovered ubiquitinated SV2A by LC-MS/MS analysis, believed to be ubiquitinated by parkin in the course of vesicular autophagy[230]. The involvement of SV2A in mitophagy would also explain why LC3II protein levels are lower in SV2A KD cells compared to MFN2 KD cells despite the inhibition of autophagosomal degradation by bafilomycin A1, as the engulfment of mitochondria into autophagosomes would be impaired in the absence of SV2A. The lower induction of mitophagy would thus lead to lower formation of LC3II and autophagosomes.

6.4.4.2 Increased interaction of SV2A and autophagosomes at mitochondria upon induction of mitophagy

Since SV2A is hypothesized to be involved in mitophagy, mitophagy was induced by CCCP and rapamycin, in combination with bafilomycin A1. Autophagy inducer rapamycin induces autophagy by inhibiting mTOR, the master regulator of autophagy associated with nutrient deprivation. Mitophagy was successfully induced by both CCCP and rapamycin, as LC3II localization at mitochondria increased compared to control. Elevated mitochondrial localization of LC3II is also evident by an increase in Pearson's r from 0.74 to 0.81 for CCCP and to 0.82 for rapamycin. As in control cells treated with bafilomycin A1, cells treated with CCCP or rapamycin display altered mitochondrial morphology characterized by fragmentation and swelling. Mitochondrial fragmentation in CCCP treated cells is related to CCCP mediated disruption of the

MMP. On the other hand, the pronounced fragmentation of mitochondria under rapamycin treatment seems to be related to bafilomycin A1, because in contrast to the observed mitochondrial fragmentation, mitochondria protective effects are commonly described for rapamycin, mediated by an increase in autophagic flux[244–246].

In respect to SV2A, both substances cause formation of larger SV2A agglomerates, indicating stress or autophagy related agglomeration of SV2A. That the number of SV2A increases in CCCP treated cells has already been observed in previous CCCP experiments. These SV2A agglomerates could reflect impaired vesicle transport, loading and release owing to decreased ATP levels and Ca^{2+} buffering arising from mitochondrial dysfunction. However, because autophagy inducer rapamycin in particular induces SV2A agglomerates, it is reasonable to hypothesize that these SV2A agglomerates may represent autophagic vacuoles. Although SV2A proves again not to be a constituent of every autophagosome, SV2A agglomerates colocalize with mitochondria and autophagosomes, especially during rapamycin treatment, suggesting they may represent autophagosomes loaded with mitochondria not degraded in response to bafilomycin A1 treatment. The hypothesis that these SV2A agglomerates are autophagosomes is supported by their average size of 1514 nm, which falls within the size range of autophagosomes and autolysosomes (300-2000 nm)[247,248].

The theory that SV2A controls mitophagy by acting as a mitochondrial LC3II receptor is supported by the increased colocalization of SV2A and LC3II at dysfunctional mitochondria. When, talking about the mitochondrial colocalization of SV2A and LC3II, it should not be excluded that their colocalization could also reflect the degradation of SV2A positive mitochondria without an interaction of SV2A and LC3II. However, the impact of SV2A KD on autophagic flux supports the theory of a mitophagy related interaction between SV2A and LC3II. SV2A's role in autophagy or mitophagy is also demonstrated as treatment with autophagy inducer rapamycin causes greater localization of SV2A to mitochondria than mitochondrial uncoupler CCCP. Pearson's r values of SV2A at mitochondria support this, as the value of rapamycin (0.85) is markedly higher than that of CCCP (0.8). Interestingly, 0.85 is the highest Pearson's r value calculated in all experiments analyzing colocalization of SV2A and mitochondria, indicating once again that SV2A is associated with mitophagy.

6.4.5 Interaction of lysosomes with SV2A

SV2A is not native to autophagosomes but appears to be involved in mitophagy as SV2A colocalizes with LC3II at mitochondria and appears to link autophagosomes to mitochondria. Another explanation for the frequent yet inconsistent colocalization of SV2A and LC3II is that SV2A interacts with autophagosomes as part of lysosomes forming LC3II and SV2A rich autolysosomes upon fusion.

In SH-SY5Y cells starved on amino acids mitochondria appear healthy similar to control cells. Given that mitochondria respond rapidly to noxious stimuli by fragmentation, the 2 h starvation in EBSS did not induce severe mitochondrial damage. In fact, the literature even reports mitochondrial elongation in response to short term starvation, related to an increase in cAMP activating protein kinase A, which upon activation phosphorylates DRP1, thereby arresting DRP1 in the cytoplasm, which promotes mitochondrial fusion[249,250]. In addition, intracellular SV2A expression increased following amino acid deprivation, consistent with previously described data demonstrating elevated SV2A protein levels following mitochondrial stress.

Similar to autophagosomes, SV2A is not a lysosomal protein as although lysosomes frequently colocalize with SV2A, not every lysosome does. Interestingly, lysosomes behave like autophagosomes at mitochondria, as they interact with mitochondria almost exclusively in contact with SV2A. This supports the hypothesis of SV2A serving as an anchoring or marker protein for autophagosomes, especially since stained lysosomes with a size of ≥1 µm at these contact sites likely represent autolysosomes derived from the fusion of autophagosomes and lysosomes. However, despite large autolysosomes, lysosomes are also found among mitochondria, displayed by structures ≤500 nm in size[248]. That lysosomes attach to mitochondria without an underlying mitophagy background has been reported by Wong et al. (2018)[50]. They identified lysosomal contact sites on mitochondria that mark sites of mitochondrial fission and allow the regulation of mitochondria by lysosomes. Accordingly, SV2A may control mitochondrial dynamics, enabling the interaction between mitochondria and lysosomes. This implies that SV2A promotes mitochondrial fission by attracting lysosomes to mitochondria, which would also explain why SV2A is more abundant at smaller mitochondria. Moreover, Wong et al. (2018) claimed that mitochondrial proteins, perhaps SV2A, in turn control lysosome activity, as mitochondrial protein TBC1D15 regulates RAB7 hydrolysis, a mechanism known to modulate lysosomal

dynamics by turning off active RAB7, which regulates lysosomal transport, fusion and maturation[50].

6.5 Effects of levetiracetam on mitochondrial morphology, autophagy and SV2A transcription

Data describing the role of SV2A on mitochondria and autophagy revealed that SV2A is involved in regulating mitochondrial morphology and dynamics along with autophagy/mitophagy. To gain further insight into the effects of SV2A, the effects of SV2A ligand LEV on mitochondrial morphology and autophagy were examined as well as if LEV functions as an SV2A transcription factor. These experiments also aimed to determine whether LEV is an SV2A agonist or antagonist, which is still unknown and remains controversial.

6.5.1 Levetiracetam elongates mitochondria by targeting SV2A

Confocal images of cells treated with levetiracetam (200 µM/2 h) show marked improvements in mitochondrial morphology reflected by an elongation of mitochondria compared to control. LEV treatment decreased the percentage of punctuated mitochondria by 7.4 %, whereas the percentage of tubular and elongated mitochondria increased. These data agree with those of Stockburger et al. (2016), who also examined the effects of levetiracetam on mitochondrial morphology using confocal microscopy and observed elongation of mitochondria. In contrast to our experiments, they applied 20 µM or 200 µM LEV to their cells for 24 h[13]. Interestingly, LEV has opposite effects on mitochondrial morphology compared to knockdown of SV2A, which has been shown to induce mitochondrial fragmentation and deterioration of mitochondrial function.

To ensure that the effect of levetiracetam on mitochondria is mediated by its postulated target SV2A, the effects of levetiracetam on mitochondrial morphology were additionally examined in SV2A KD cells. As expected, LEV targets mitochondria via SV2A, as evidenced by mitochondrial fragmentation and swelling in SV2A KD cells despite treatment with LEV. The previously described elongation of mitochondria by LEV no longer exists, as the percentage of punctuated mitochondria increased similar in SV2A KD cells and SV2A KD cells treated with LEV. As already reported for SV2A KD cells, the number of elongated and tubular mitochondria likewise decreased in

SV2A KD cells treated with LEV. These results agree with those of Stockburger et al. (2016), who also discovered by confocal microscopy that the effect of LEV on mitochondrial morphology disappears once SV2A protein levels are reduced by knockdown of SV2A[13].

As of today, it remains unknown and controversial whether LEV is an SV2A agonist or antagonist. Our data suggest that LEV is an SV2A agonist enhancing the physiological effects of SV2A on mitochondria, thereby inducing mitochondrial elongation. If LEV were an SV2A antagonist, LEV would cause mitochondrial fragmentation equivalent to that reported for SV2A KD and KO. The fact that SV2A KO mice exhibit severe seizures, whereas levetiracetam as an anticonvulsant suppresses seizures, also supports the hypothesis that LEV functions as an SV2A agonist. If LEV were an antagonist, it would induce seizures in mice like SV2A KO and not suppress them. Since the mode of action of LEV is uncertain, the literature also suggests that LEV may function as an SV2A antagonist, especially since it suppresses neuronal hyperexcitability and seizures, which can be interpreted as an inhibition of SV2A which blocks vesicular SNARE complexes from releasing transmitters. The dilemma regarding whether LEV is an SV2A agonist or antagonist is that several contrary data or data which can be interpreted either way exist. Our data clearly suggest that LEV is an agonist.

6.5.2 Levetiracetam affects autophagy as an SV2A agonist

Given the impairment of autophagic flux following SV2A KD, we examined whether SV2A ligand LEV affects autophagy as well. Since this scientific work builds on the concept of LEV improving mitochondrial functions and cognition in AD patients, the effect of LEV on autophagy was investigated in a human APP overexpressing SH-SY5Y cell model.

The literature agrees on an impairment of autophagy in AD both in cell and animal models, presumably mediated by decreased activity of beclin1[251–254]. Similarly, autophagic flux is impaired in our AD cell model, as autophagic flux decreased to 54.5 % compared to Mock control. Interestingly despite impaired autophagy in APPwt cells, inhibition of mTORC1 by rapamycin increases autophagic flux by ~20 % in both APPwt and Mock cells. The results on rapamycin treatment are consistent with improvements in AD pathology reported in the literature, where rapamycin treatment reduces Aβ and

tau pathology by inhibiting mTORC1, restoring previously impaired Aβ clearance[255,256]. Aβ is presumably the principal cause for the impaired autophagy in our cell model, since only APP and Aβ are overexpressed and none of the other AD associated hallmarks, such as tau tangles, are present. Since the results on impaired autophagy in AD are consistent with the literature, the determination of autophagic flux with bafilomycin A1 and LC3II proves to provide valid data.

As hypothesized, incubation of Mock cells with 200 µM LEV for 2 h significantly increased the autophagic flux by 12.5 % compared to untreated control. Accordingly, LEV proves again to act as an SV2A agonist promoting autophagy as KD of SV2A was impairs autophagy. That the 12.5 % increase in autophagic flux following LEV treatment is lower than the 23.2 % increase by rapamycin, is not surprising given that rapamycin inhibits mTORC1, one of the major regulators of autophagy associated with nutrient starvation. It would have been highly surprising if inhibition of mTORC1 has milder effects on autophagy than LEV. Unexpectedly, however, in our AD cell model, LEV decreased autophagic flux significantly by 8 % compared to untreated controls. Why LEV reduces the autophagic flux in APPwt cells remains uncertain. One explanation could be that APPwt cells express lower levels of SV2A relative to Mock cells, hindering LEV from inducing autophagy. Indeed, qPCR analysis demonstrated that APPwt cells express lower transcription of SV2A, as evidenced by a significant decrease in SV2A mRNA expression by 31.1 % compared to Mock cells. Of course, reduced mRNA levels do not reflect reduced SV2A protein levels, but they indicate that the transcription of SV2A is impaired in AD cells, which in turn may lead to lower SV2A protein levels. To confirm these data, future investigations of SV2A protein levels, for example by WB, will be required. The hypothesis is further supported as SV2A expression is known to decrease during aging and the progression of Alzheimer's disease[257]. However, the decline of SV2A levels in AD brains may perhaps reflect neuronal decline rather than decreased expression of SV2A in neurons. Boosting autophagy in APPwt cells would have been possible, given that rapamycin induced autophagic flux in these cells by 19 %. Therefore, the underlying cause for the missing effect of LEV on autophagy in APPwt cells appears to be low SV2A levels.

6.5.3 Regulation of SV2A transcription by levetiracetam

As mentioned previously, SV2A mRNA levels are significantly lower (-31.1 %) in APPwt cells compared to Mock control. These data are the first of their kind to represent

alterations in SV2A transcription and perhaps protein levels in an AD cell model instead of in AD brains, where reduction in SV2A expression is commonly used as a marker of neuronal decline, performing PET imaging of levetiracetam based radioligand 11C-UCB-J[258,259]. Impaired transcription of SV2A in our APPwt cells could explain both the impaired autophagic flux mentioned earlier and the shortening of mitochondria observed by Stockburger et al. (2016) for this cell line. Since impairment of cellular processes thought to be affected by SV2A (mitochondrial morphology and autophagy) occurs in APPwt cells similar to in SV2A KD cells and LEV treatment is known to exert beneficial effects on these processes in APPwt cells, the question arose whether LEV increases SV2A transcription and consequently SV2A protein levels in AD cells to those of healthy cells, which may explain the improvement in those SV2A affected processes.

When APPwt cells were treated with 200 µM LEV for 6 h, 24 h, and 48 h, transcription of SV2A increased, but not significantly. The observed trend is evident already after 6 h, when SV2A mRNA expression increased by ~29 % and remained stable for 48 h. LEV acts rapidly on the transcription of its target SV2A, which fits to LEV acting rapidly in patients as well, as according to the KEPPRA® (levetiracetam) professional information, the maximum plasma concentration (Cmax) of LEV is reached after 1.3 h in patients. Thus, although the data reflect only a trend, LEV appears to exert a dual mode of action in combating mitochondrial degeneration in AD. On the one hand, LEV potentially acts as an SV2A agonist on mitochondria and on the other hand raises low levels of SV2A, thereby amplifying its own effect.

Surprisingly, LEV has the opposite effect in Mock cells, as SV2A mRNA levels decreased to 68.9 % after 48 h, equivalent to SV2A mRNA levels of untreated APPwt cells (68.8 %). Considering the positive effects of LEV on mitochondrial function and autophagy in Mock cells, an increase in SV2A transcription would have been expected. Perhaps reduced SV2A transcription in Mock cells during LEV treatment represents feedback inhibition owing to increased SV2A activity by LEV. Although only trends, these data provide a first impression on LEV regulating the transcription of its target in response to the cell's state of health.

7 SUMMARY

The present work can be broadly divided into three main parts. The first part addressed the mitochondrial localization of SV2A. In SH-SY5Y cells, a human neuronal cell line, SV2A localization at mitochondria and how the localization of SV2A and mitochondria is altered by mitochondrial stressors rotenone and CCCP was investigated. Despite its vesicular background, SV2A was found to be located at mitochondria by confocal and super-resolution microscopy. In addition, western blot of isolated mitochondria, verified that SV2A is unique to the outer mitochondrial membrane. Furthermore, SV2A localized to a greater extent to mitochondria following mitochondrial stress, particularly to fragmented mitochondria. Suggesting that mitochondrial stress is a stimulus for SV2A to interact with mitochondria. To rule out the possibility of SV2A interacting with mitochondria as a vesicle, confocal and super-resolution microscopy were performed to analyze the colocalization of VAMP2 and SV2A at mitochondria. It turned out that surprisingly SV2A and VAMP2 occurred jointly at mitochondria. Notably, VAMP2 also occurred at mitochondria, suggesting that vesicles may interact with mitochondria. Although SV2A occurred more frequently and sometimes independently of VAMP2 at mitochondria, this reflected only a trend and not a significant change compared to VAMP2, which occurred less frequently at mitochondria but behaved similarly. The same pattern was observed when cells were treated with complex I inhibitor rotenone, accompanied by higher levels and colocalization of SV2A and VAMP2. SV2A again occurred more frequently at mitochondria than VAMP2 following mitochondrial stress, but not significantly, and it seemed that SV2A occurred both vesicularly and by itself at mitochondria. However, to confirm the hypothesis that SV2A occurs outside vesicles at mitochondria, future experiments are necessary. If future experiments show that synaptic vesicles interact with mitochondria, this would be extremely interesting, as this is unknown to date. The increased colocalization of SV2A and VAMP2 could also represent accumulation of synaptic vesicles resulting from the inhibition of vesicle release owing to mitochondrial impairment or represent MDV, as vesicular proteins SV2A and VAMP2 could be involved in their formation, transport or fusion during mitochondrial stress.

The second part of the thesis addressed the influence of SV2A and LEV on mitochondrial dynamics. First, it was demonstrated that knockdown of SV2A in SH-SY5Y cells causes disruption of mitochondrial dynamics, as evidenced by shrinkage of

mitochondria. SV2A KD mediated mitochondrial fragmentation proved to be severer than the deleterious effects of complex I inhibitor rotenone, leading to the assumption that SV2A doesn't damage mitochondria like toxins but rather disrupts mitochondrial dynamics by affecting mitochondrial fission or fusion. Furthermore, levetiracetam was found to require SV2A for its effect on mitochondrial morphology, as LEV induced mitochondrial elongation disappeared in SV2A KD cells, leaving fragmented mitochondria. Considering that SV2A KD leads to shortening of mitochondria, whereas LEV elongates mitochondria, it is plausible that LEV acts as an SV2A agonist amplifying the mitochondrial fusion activity of SV2A. In contrast, if LEV were an SV2A antagonist, LEV would have caused mitochondrial fragmentation similar to that observed in SV2A KD. To verify whether the mitochondrial phenotype of SV2A KD persists in vivo, the size of mitochondria was assessed in the hippocampus of SV2A KO mice, an approach that has never been attempted before. As a result, we were the first to show that mitochondrial fragmentation also occurs in brains of SV2A KO mice. Interestingly, mitochondrial fragmentation associated with SV2A KO is sex-specific, being unique to females. These results are of particular interest as female mitochondria are generally considered to be more robust compared to male mitochondria due to the effects of estrogens. In this context, it seems possible that no effect was observed in male SV2A KO mice as mitochondrial fragmentation in male controls was already at the female SV2A KO mouse level. Next, the functionality of the mitochondrial fission and fusion machinery in SV2A KD cells was examined by comparing the frequency of fission and fusion events in SV2A KD cells to control cells using live cell imaging. SV2A knockdown cells demonstrated a uniform decrease in fission and fusion events compared to control cells treated with scrambled siRNA. A uniform decrease in fission and fusion events was surprising considering mitochondrial fragmentation associated with SV2A KD. However, knockdown of mitochondrial fusion factor MFN2 has been reported in the literature to likewise cause mitochondrial fragmentation and reduce the frequency of both fission and fusion events without altering the balance of them. The data presented suggest that SV2A either acts like MFN2 as a fusion factor on mitochondria or regulates the activity of fission factor DRP1 in an inhibitory manner, whereby knockdown of SV2A increases the activity of DRP1. Since regulation of DRP1 activity is already known in the literature and DRP1, like SV2A, is present in the cytosol and at mitochondria, the potential interaction of SV2A and DRP1 was investigated. Microscopic analysis of untreated and rotenone treated SH-SY5Y cells demonstrated that colocalization of SV2A and DRP1 almost completely occurs at mitochondria.

Mitochondrial stress causing mitochondrial fragmentation enhanced the colocalization of SV2A and DRP1, as both proteins experienced stress induced elevation in mitochondrial localization. The colocalization of SV2A and DRP1, pronounced on confocal images but weak on super-resolution images, appeared to be rather nonspecific and related to the respective mitochondrial localization of the two proteins. In light of these data, it seems unlikely that SV2A antagonizes DRP1 activity, as otherwise mitochondrial stress would have reduced the interaction between SV2A and DRP1. Consequently, it is reasonable to assume that SV2A is involved in the regulation of mitochondrial dynamics as a fusion factor.

The third part of the dissertation addressed the impact of SV2A on autophagy. Interestingly, autophagic flux was impaired by knockdown of SV2A in SH-SY5Y cells. However, how SV2A affects autophagy is still unknown. The only certainty is that SV2A KD impairs the autophagic cascade during or before the formation of autophagosomes. An effect downstream of autophagosome maturation, for example, on autophagosome-lysosome fusion, is unlikely, as knockdown of SV2A should have then led to elevated LC3II levels. Increased LC3II expression upon impaired autophagosome and lysosome fusion is reported for MFN2 KD, as MFN2 mediates their fusion under normal conditions. SV2A is also not an intrinsic component of autophagosomes and lysosomes, given that SV2A did not necessarily colocalize with LC3II and lysosomes. On the other hand, SV2A is hypothesized to be involved in mitophagy, which would explain the minor decrease in autophagic flux by SV2A KD, given that mitophagy accounts for only a small fraction of autophagy. On mitochondria, SV2A may therefore serve as an anchoring partner for LC3II and facilitate mitophagy as indicated by confocal microscopy data showing colocalization of LC3II and SV2A at mitochondria. Furthermore, in cells subjected to induced mitophagy by CCCP or mTORC1 inhibitor rapamycin, LC3II was almost exclusively located at mitochondria associated with SV2A. The same is true for lysosomes and autolysosomes, which likewise were associated with SV2A at mitochondria. Via its interaction with lysosomes SV2A could also drive mitochondrial dynamics, as lysosomes are known in the literature to associate with mitochondria and trigger mitochondrial fission. The hypothesis on SV2A and mitophagy states that SV2A attaches to severely damaged mitochondria marking them for degradation by autophagosomes and lysosomes. Based on the SV2A data, it is not surprising that LEV increased autophagic flux in Mock cells, consistent with the hypothesis of LEV being an SV2A agonist. However, levetiracetam reduced autophagic

flux in our APP overexpressing cell model, perhaps due to low SV2A levels and severely impaired autophagy.

In summary, SV2A is located at mitochondria and affects mitochondrial dynamics as well as autophagy. Since the spectrum of SV2A functions is broad, it cannot be ultimately stated how SV2A contributes to mitochondrial dynamics and autophagy. However, it is certain that SV2A protects mitochondria and is responsible for the mitochondrial and neuroprotective effects of levetiracetam. Therefore, further studies on SV2A in relation to mitochondria and autophagy are promising and may help to improve the treatment of CNS diseases such as Alzheimer's disease in the future.

8 BIBLIOGRAPHY

1. Janz, R., Goda, Y., Geppert, M., Missler, M. & Südhof, T. C. SV2A and SV2B function as redundant Ca2+ regulators in neurotransmitter release. *Neuron* **24**, 1003–1016 (1999).
2. Bartholome, O. *et al.* Puzzling out synaptic vesicle 2 family members functions. *Frontiers in Molecular Neuroscience* **10**, 148 (2017).
3. Löscher, W. The holy grail of epilepsy prevention: Preclinical approaches to antiepileptogenic treatments. *Neuropharmacology* **167**, 107605 (2020).
4. Stout, K. A., Dunn, A. R., Hoffman, C. & Miller, G. W. The Synaptic Vesicle Glycoprotein 2: Structure, Function, and Disease Relevance. *ACS Chemical Neuroscience* **10**, 3927–3938 (2019).
5. Löscher, W., Gillard, M., Sands, Z. A., Kaminski, R. M. & Klitgaard, H. Synaptic Vesicle Glycoprotein 2A Ligands in the Treatment of Epilepsy and Beyond. *CNS Drugs* **30**, 1055–1077 (2016).
6. Bajjalieh, S. M., Frantz, G. D., Weimann, J. M., McConnell, S. K. & Scheller, R. H. Differential expression of synaptic vesicle protein 2 (SV2) isoforms. *J. Neurosci.* **14**, 5223–5235 (1994).
7. Schivell, A. E., Batchelor, R. H. & Bajjalieh, S. M. Isoform-specific, calcium-regulated interaction of the synaptic vesicle proteins SV2 and synaptotagmin. *J. Biol. Chem.* **271**, 27770–27775 (1996).
8. Schivell, A. E., Mochida, S., Kensel-Hammes, P., Custer, K. L. & Bajjalieh, S. M. SV2A and SV2C contain a unique synaptotagmin-binding site. *Mol. Cell. Neurosci.* **29**, 56–64 (2005).
9. Crowder, K. M. *et al.* Abnormal neurotransmission in mice lacking synaptic vesicle protein 2A (SV2A). *Proc. Natl. Acad. Sci. U. S. A.* **96**, 15268–15273 (1999).
10. Budzinski, K. L. *et al.* Large structural change in isolated synaptic vesicles upon loading with neurotransmitter. *Biophys. J.* **97**, 2577–2584 (2009).
11. Söllner, T. *et al.* SNAP receptors implicated in vesicle targeting and fusion. *Nature* **362**, 318–324 (1993).
12. Janz, R., Hofmann, K. & Südhof, T. C. SVOP, an Evolutionarily Conserved Synaptic Vesicle Protein, Suggests Novel Transport Functions of Synaptic Vesicles. *J. Neurosci.* **18**, 9269 LP – 9281 (1998).
13. Stockburger, C. *et al.* A Mitochondrial Role of SV2a Protein in Aging and

Alzheimer's Disease: Studies with Levetiracetam. *J. Alzheimer's Dis.* **50**, 201–215 (2016).

14. Südhof, T. C. & Rizo, J. Synaptic vesicle exocytosis. *Cold Spring Harb. Perspect. Biol.* **3**, (2011).
15. Rizo, J. & Xu, J. The Synaptic Vesicle Release Machinery. *Annu. Rev. Biophys.* **44**, 339–367 (2015).
16. Yao, J., Nowack, A., Kensel-Hammes, P., Gardner, R. G. & Bajjalieh, S. M. Cotrafficking of SV2 and synaptotagmin at the synapse. *J. Neurosci.* **30**, 5569–5578 (2010).
17. Madeo, M., Kovács, A. D. & Pearce, D. A. The human synaptic vesicle protein, SV2A, functions as a galactose transporter in Saccharomyces cerevisiae. *J. Biol. Chem.* **289**, 33066–33071 (2014).
18. Klitgaard, H. & Verdru, P. Levetiracetam: The first SV2A ligand for the treatment of epilepsy. *Expert Opin. Drug Discov.* **2**, 1537–1545 (2007).
19. Gillard, M., Chatelain, P. & Fuks, B. Binding characteristics of levetiracetam to synaptic vesicle protein 2A (SV2A) in human brain and in CHO cells expressing the human recombinant protein. *Eur. J. Pharmacol.* **536**, 102–108 (2006).
20. Sanchez, P. E. *et al.* Levetiracetam suppresses neuronal network dysfunction and reverses synaptic and cognitive deficits in an Alzheimer's disease model. *Proc. Natl. Acad. Sci. U. S. A.* **109**, E2895-903 (2012).
21. Zaharia, C. *et al.* Two-year follow-up study on efficacy of levetiracetam in patients with Mild Cognitive Impairment and partial epilepsy. *Journal of Neurology* **258**, S194 (2011).
22. Belcastro, V. *et al.* Levetiracetam monotherapy in Alzheimer patients with late-onset seizures: A prospective observational study. *Eur. J. Neurol.* **14**, 1176–1178 (2007).
23. NCT01044758. Levetiracetam and Memory Function in Amnestic Mild Cognitive Impairment (MCI). *Https://clinicaltrials.gov/show/nct01044758* (2010).
24. Koh, M. T., Shao, Y., Rosenzweig-Lipson, S. & Gallagher, M. Treatment with levetiracetam improves cognition in a ketamine rat model of schizophrenia. *Schizophr. Res.* **193**, 119–125 (2018).
25. Gibbs, J. E., Walker, M. C. & Cock, H. R. Levetiracetam: antiepileptic properties and protective effects on mitochondrial dysfunction in experimental status epilepticus. *Epilepsia* **47**, 469–478 (2006).
26. Klein, P., Diaz, A., Gasalla, T. & Whitesides, J. A review of the pharmacology

and clinical efficacy of brivaracetam. *Clin. Pharmacol.* **10**, 1–22 (2018).

27. Steinhoff, B. J. & Staack, A. M. Levetiracetam and brivaracetam: a review of evidence from clinical trials and clinical experience. *Therapeutic Advances in Neurological Disorders* **12**, 1–23 (2019).
28. Lukyanetz, E. A., Shkryl, V. M. & Kostyuk, P. G. Selective blockade of N-type calcium channels by levetiracetam. *Epilepsia* **43**, 9–18 (2002).
29. Vogl, C., Mochida, S., Wolff, C., Whalley, B. J. & Stephens, G. J. The Synaptic Vesicle Glycoprotein 2A Ligand Levetiracetam Inhibits Presynaptic Ca^{2+} Channels through an Intracellular Pathway. *Mol. Pharmacol.* **82**, 199 LP – 208 (2012).
30. Witt, J. A., Elger, C. E. & Helmstaedter, C. Short-term and longer-term effects of brivaracetam on cognition and behavior in a naturalistic clinical setting—Preliminary data. *Seizure* **62**, 49–54 (2018).
31. Nygaard, H. B. *et al.* Brivaracetam, but not ethosuximide, reverses memory impairments in an Alzheimer's disease mouse model. *Alzheimers. Res. Ther.* **7**, 25 (2015).
32. Eisner, V., Picard, M. & Hajnóczky, G. Mitochondrial dynamics in adaptive and maladaptive cellular stress responses. *Nature Cell Biology* **20**, 755–765 (2018).
33. Fontanesi, F. Mitochondria: Structure and Role in Respiration. *eLS* 1–13 (2015).
34. Krauss, S. Mitochondria: Structure and Role in Respiration. *eLS* 1–6 (2001).
35. Schenkel, L. C. & Bakovic, M. Formation and regulation of mitochondrial membranes. *Int. J. Cell Biol.* (2014).
36. Pakendorf, B. & Stoneking, M. MITOCHONDRIAL DNA AND HUMAN EVOLUTION. *Annu. Rev. Genomics Hum. Genet.* **6**, 165–183 (2005).
37. Bogenhagen, D. F. Mitochondrial DNA nucleoid structure. *Biochim. Biophys. Acta - Gene Regul. Mech.* **1819**, 914–920 (2012).
38. Smeitink, J., van den Heuvel, L. & DiMauro, S. The genetics and pathology of oxidative phosphorylation. *Nat. Rev. Genet.* **2**, 342–352 (2001).
39. Cogliati, S., Cabrera-Alarcón, J. L. & Enriquez, J. A. Regulation and functional role of the electron transport chain supercomplexes. *Biochem. Soc. Trans.* **49**, 2655–2668 (2021).
40. Chaban, Y., Boekema, E. J. & Dudkina, N. V. Structures of mitochondrial oxidative phosphorylation supercomplexes and mechanisms for their stabilisation. *Biochim. Biophys. Acta - Bioenerg.* **1837**, 418–426 (2014).
41. Zhao, R., Jiang, S., Zhang, L. & Yu, Z. Mitochondrial electron transport chain,

ROS generation and uncoupling (Review). *Int J Mol Med* **44**, 3–15 (2019).

42. Nolfi-Donegan, D., Braganza, A. & Shiva, S. Mitochondrial electron transport chain: Oxidative phosphorylation, oxidant production, and methods of measurement. *Redox Biol.* **37**, 101674 (2020).
43. Holley, A. K., Bakthavatchalu, V., Velez-Roman, J. M. & St. Clair, D. K. Manganese superoxide dismutase: Guardian of the powerhouse. *Int. J. Mol. Sci.* **12**, 7114–7162 (2011).
44. Pfeffer, C. M. & Singh, A. T. K. Apoptosis: A target for anticancer therapy. *Int. J. Mol. Sci.* **19**, (2018).
45. Galluzzi, L. *et al.* Molecular mechanisms of cell death: Recommendations of the Nomenclature Committee on Cell Death 2018. *Cell Death Differ.* **25**, 486–541 (2018).
46. Tilokani, L., Nagashima, S., Paupe, V. & Prudent, J. Mitochondrial dynamics: Overview of molecular mechanisms. *Essays in Biochemistry* **62**, 341–360 (2018).
47. Wai, T. & Langer, T. Mitochondrial Dynamics and Metabolic Regulation. *Trends Endocrinol. Metab.* **27**, 105–117 (2016).
48. Kraus, F. & Ryan, M. T. The constriction and scission machineries involved in mitochondrial fission. *J. Cell Sci.* **130**, 2953–2960 (2017).
49. Lee, J. E., Westrate, L. M., Wu, H., Page, C. & Voeltz, G. K. Multiple dynamin family members collaborate to drive mitochondrial division. *Nature* **540**, 139–143 (2016).
50. Wong, Y. C., Ysselstein, D. & Krainc, D. Mitochondria–lysosome contacts regulate mitochondrial fission via RAB7 GTP hydrolysis. *Nature* **554**, 382–386 (2018).
51. Saxton, W. M. & Hollenbeck, P. J. The axonal transport of mitochondria. *J. Cell Sci.* **125**, 2095–2104 (2012).
52. Lovas, J. R. & Wang, X. The meaning of mitochondrial movement to a neuron's life. *Biochim. Biophys. Acta - Mol. Cell Res.* **1833**, 184–194 (2013).
53. Barnhart, E. L. Mechanics of mitochondrial motility in neurons. *Curr. Opin. Cell Biol.* **38**, 90–99 (2016).
54. Kruppa, A. J. & Buss, F. Motor proteins at the mitochondria–cytoskeleton interface. *J. Cell Sci.* **134**, (2021).
55. Pekkurnaz, G., Trinidad, J. C., Wang, X., Kong, D. & Schwarz, T. L. Glucose regulates mitochondrial motility via Milton modification by O-GlcNAc transferase.

Cell **158**, 54–68 (2014).

56. Khandia, R. *et al.* A Comprehensive Review of Autophagy and Its Various Roles in Infectious, Non-Infectious, and Lifestyle Diseases: Current Knowledge and Prospects for Disease Prevention, Novel Drug Design, and Therapy. *Cells* **8**, 674 (2019).
57. Bento, C. F. *et al.* Mammalian Autophagy: How Does It Work? *Annu. Rev. Biochem.* **85**, 685–713 (2016).
58. Dikic, I. & Elazar, Z. Mechanism and medical implications of mammalian autophagy. *Nat. Rev. Mol. Cell Biol.* **19**, 349–364 (2018).
59. Palikaras, K., Lionaki, E. & Tavernarakis, N. Mechanisms of mitophagy in cellular homeostasis, physiology and pathology. *Nat. Cell Biol.* **20**, 1013–1022 (2018).
60. Bakula, D. & Scheibye-Knudsen, M. MitophAging: Mitophagy in Aging and Disease. *Front. Cell Dev. Biol.* **8**, 1–16 (2020).
61. Zuo, Z. *et al.* Mechanisms and Functions of Mitophagy and Potential Roles in Renal Disease. *Front. Physiol.* **11**, (2020).
62. Onishi, M., Yamano, K., Sato, M., Matsuda, N. & Okamoto, K. Molecular mechanisms and physiological functions of mitophagy. *EMBO J.* **40**, 1–27 (2021).
63. World Health Organization (WHO). Life expectancy at birth (years). Available at: https://www.who.int/data/gho/data/indicators/indicator-details/GHO/life-expectancy-at-birth-(years). (Accessed: 2nd January 2022)
64. World Health Organization (WHO). Dementia. Available at: https://www.who.int/news-room/fact-sheets/detail/dementia. (Accessed: 2nd January 2022)
65. Niu, H., Álvarez-Álvarez, I., Guillén-Grima, F. & Aguinaga-Ontoso, I. Prevalencia e incidencia de la enfermedad de Alzheimer en Europa: metaanálisis. *Neurología* **32**, 523–532 (2017).
66. Alzheimer's Association. 2021 Alzheimer's disease facts and figures special report Race, Ethnicity and Alzheimer's in America. *Alzheimers. Dement.* **17**, 327–406 (2021).
67. World Health Organization (WHO). Global action plan on the public health response to dementia 2017 - 2025. *Geneva World Heal. Organ.* 27 (2017).
68. World Health Organization (WHO). ICD-11 for Mortality and Morbidity Statistics. Available at: https://icd.who.int/browse11/l-

m/en#/http%3A%2F%2Fid.who.int%2Ficd%2Fentity%2F546689346. (Accessed: 2nd January 2022)

69. Price, D. L. & Sisodia, S. S. Mutant genes in familial Alzheimer's disease and transgenic models. *Annu. Rev. Neurosci.* **21**, 479–505 (1998).
70. Wu, L. *et al.* Early-Onset Familial Alzheimer's Disease (EOFAD). *Can. J. Neurol. Sci. / J. Can. des Sci. Neurol.* **39**, 436–445 (2012).
71. A. Armstrong, R. Risk factors for Alzheimer's disease. *Folia Neuropathol.* **57**, 87–105 (2019).
72. Iadecola, C. The Pathobiology of Vascular Dementia. *Neuron* **80**, 844–866 (2013).
73. O'Brien, J. T. & Thomas, A. Vascular dementia. *Lancet* **386**, 1698–1706 (2015).
74. Deuschl, G. & Maier, W. S3-Leitlinie / Nationale Versorgungsleitlinie: Demenz. *Dtsch. Gesellschaft für Psychiatr. Psychother. und Nervenheilkd. Dtsch. Gesellschaft für Neurol.* (2016).
75. International, A. D. & University, M. World Alzheimer Report 2021. (2021).
76. Alzheimer, A. über eigenartige Krankheitsfälle des späteren Alters. *Zeitschrift für die gesamte Neurol. und Psychiatr.* **4**, 356–385 (1911).
77. Hardy, J. A. & Higgins, G. A. Alzheimer's disease: the amyloid cascade hypothesis. *Science* **256**, 184–185 (1992).
78. Ackley, S. F. *et al.* Effect of reductions in amyloid levels on cognitive change in randomized trials: instrumental variable meta-analysis. *BMJ* **372**, n156–n156 (2021).
79. Mangialasche, F., Solomon, A., Winblad, B., Mecocci, P. & Kivipelto, M. Alzheimer's disease: clinical trials and drug development. *Lancet Neurol.* **9**, 702–716 (2010).
80. Huang, L.-K., Chao, S.-P. & Hu, C.-J. Clinical trials of new drugs for Alzheimer disease. *J. Biomed. Sci.* **27**, 18 (2020).
81. Dhillon, S. Aducanumab: First Approval. *Drugs* **81**, 1437–1443 (2021).
82. Chow, V. W., Mattson, M. P., Wong, P. C. & Gleichmann, M. An overview of APP processing enzymes and products. *Neuromolecular Med.* **12**, 1–12 (2010).
83. Zhang, Y., Thompson, R., Zhang, H. & Xu, H. APP processing in Alzheimer's disease. *Mol. Brain* **4**, 3 (2011).
84. Haass, C., Kaether, C., Thinakaran, G. & Sisodia, S. Trafficking and proteolytic processing of APP. *Cold Spring Harb. Perspect. Med.* **2**, 1–26 (2012).
85. Lott, I. T. & Head, E. Dementia in Down syndrome: unique insights for Alzheimer

disease research. *Nat. Rev. Neurol.* **15**, 135–147 (2019).

86. Leuner, K., Müller, W. E. & Reichert, A. S. From mitochondrial dysfunction to amyloid beta formation: Novel insights into the pathogenesis of Alzheimer's disease. *Mol. Neurobiol.* **46**, 186–193 (2012).
87. Shankar, G. M. *et al.* Amyloid-β protein dimers isolated directly from Alzheimer's brains impair synaptic plasticity and memory. *Nat. Med.* **14**, 837–842 (2008).
88. Wang, H.-W. *et al.* Soluble oligomers of β amyloid (1-42) inhibit long-term potentiation but not long-term depression in rat dentate gyrus. *Brain Res.* **924**, 133–140 (2002).
89. Reddy, P. H. & Beal, M. F. Amyloid beta, mitochondrial dysfunction and synaptic damage: implications for cognitive decline in aging and Alzheimer's disease. *Trends Mol. Med.* **14**, 45–53 (2008).
90. Cheignon, C. *et al.* Oxidative stress and the amyloid beta peptide in Alzheimer's disease. *Redox Biol.* **14**, 450–464 (2018).
91. Schilling, T. & Eder, C. Amyloid-β-induced reactive oxygen species production and priming are differentially regulated by ion channels in microglia. *J. Cell. Physiol.* **226**, 3295–3302 (2011).
92. De Felice, F. G. *et al.* Alzheimer's disease-type neuronal tau hyperphosphorylation induced by A beta oligomers. *Neurobiol. Aging* **29**, 1334–1347 (2008).
93. Pooler, A. M. *et al.* Amyloid accelerates tau propagation and toxicity in a model of early Alzheimer's disease. *Acta Neuropathol. Commun.* **3**, 14 (2015).
94. Bloom, G. S. Amyloid-β and tau: The trigger and bullet in Alzheimer disease pathogenesis. *JAMA Neurol.* **71**, 505–508 (2014).
95. Hauptmann, S. *et al.* Mitochondrial dysfunction: An early event in Alzheimer pathology accumulates with age in AD transgenic mice. *Neurobiol. Aging* **30**, 1574–1586 (2009).
96. Leuner, K. *et al.* Mitochondrion-derived reactive oxygen species lead to enhanced amyloid beta formation. *Antioxidants Redox Signal.* **16**, 1421–1433 (2012).
97. Kinney, J. W. *et al.* Inflammation as a central mechanism in Alzheimer's disease. *Alzheimer's Dement. Transl. Res. Clin. Interv.* **4**, 575–590 (2018).
98. Ismail, R. *et al.* The relationships between neuroinflammation, beta-amyloid and tau deposition in Alzheimer's disease: A longitudinal PET study. *J. Neuroinflammation* **17**, 1–11 (2020).

99. Lee, Y.-J., Bae Han, S., Nam, S.-Y., Oh, K.-W. & Tae Hong, J. Inflammation and Alzheimer's Disease. *Arch Pharm Res* **33**, 1539–1556 (2010).
100. Kolarova, M., García-Sierra, F., Bartos, A., Ricny, J. & Ripova, D. Structure and pathology of tau protein in Alzheimer disease. *Int. J. Alzheimers. Dis.* 731526 (2012).
101. Naseri, N. N., Wang, H., Guo, J., Sharma, M. & Luo, W. The complexity of tau in Alzheimer's disease. *Neurosci. Lett.* **705**, 183–194 (2019).
102. Muralidar, S., Ambi, S. V., Sekaran, S., Thirumalai, D. & Palaniappan, B. Role of tau protein in Alzheimer's disease: The prime pathological player. *Int. J. Biol. Macromol.* **163**, 1599–1617 (2020).
103. Stamer, K., Vogel, R., Thies, E., Mandelkow, E. & Mandelkow, E.-M. Tau blocks traffic of organelles, neurofilaments, and APP vesicles in neurons and enhances oxidative stress. *J. Cell Biol.* **156**, 1051–1063 (2002).
104. DuBoff, B., Götz, J. & Feany, M. B. Tau promotes neurodegeneration via DRP1 mislocalization in vivo. *Neuron* **75**, 618–632 (2012).
105. Li, X.-C. *et al.* Human wild-type full-length tau accumulation disrupts mitochondrial dynamics and the functions via increasing mitofusins. *Sci. Rep.* **6**, 24756 (2016).
106. Cummins, N., Tweedie, A., Zuryn, S., Bertran-Gonzalez, J. & Götz, J. Disease-associated tau impairs mitophagy by inhibiting Parkin translocation to mitochondria. *EMBO J.* **38**, 1–15 (2019).
107. Nunomura, A. *et al.* Oxidative Damage Is the Earliest Event in Alzheimer Disease. *J. Neuropathol. Exp. Neurol.* **60**, 759–767 (2001).
108. Devi, L., Prabhu, B. M., Galati, D. F., Avadhani, N. G. & Anandatheerthavarada, H. K. Accumulation of amyloid precursor protein in the mitochondrial import channels of human Alzheimer's disease brain is associated with mitochondrial dysfunction. *J. Neurosci.* **26**, 9057–9068 (2006).
109. Valla, J. *et al.* Impaired platelet mitochondrial activity in Alzheimer's disease and mild cognitive impairment. *Mitochondrion* **6**, 323–330 (2006).
110. Leuner, K. *et al.* Peripheral Mitochondrial Dysfunction in Alzheimer's Disease: Focus on Lymphocytes. *Mol. Neurobiol.* **46**, 194–204 (2012).
111. Trimmer, P. A. *et al.* Abnormal mitochondrial morphology in sporadic Parkinson's and Alzheimer's disease cybrid cell lines. *Exp. Neurol.* **162**, 37–50 (2000).
112. Trimmer, P. A. *et al.* Mitochondrial abnormalities in cybrid cell models of

sporadic Alzheimer's disease worsen with passage in culture. *Neurobiol. Dis.* **15**, 29–39 (2004).

113. Maruszak, A. & Zekanowski, C. Mitochondrial dysfunction and Alzheimer's disease. *Prog. Neuro-Psychopharmacology Biol. Psychiatry* **35**, 320–330 (2011).
114. Onyango, I. & Khan, S. Oxidative Stress, Mitochondrial Dysfunction, and Stress Signaling in Alzheimers Disease. *Curr. Alzheimer Res.* **3**, 339–349 (2006).
115. Clark, T. A. *et al.* Oxidative Stress and its Implications for Future Treatments and Management of Alzheimer Disease. *Int. J. Biomed. Sci.* **6**, 225–227 (2010).
116. Leuner, K. *et al.* Mitochondrial dysfunction: The first domino in brain aging and Alzheimer's disease? *Antioxidants and Redox Signaling* **9**, 1659–1675 (2007).
117. Mecocci, P., MacGarvey, U. & Beal, M. F. Oxidative damage to mitochondrial DNA is increased in Alzheimer's disease. *Ann. Neurol.* **36**, 747–751 (1994).
118. Hoekstra, J. G., Hipp, M. J., Montine, T. J. & Kennedy, S. R. Mitochondrial DNA mutations increase in early stage Alzheimer disease and are inconsistent with oxidative damage. *Ann. Neurol.* **80**, 301–306 (2016).
119. Kruse, S. E. *et al.* Mice with mitochondrial complex I deficiency develop a fatal encephalomyopathy. *Cell Metab.* **7**, 312–320 (2008).
120. Tamagno, E. *et al.* Beta-site APP cleaving enzyme up-regulation induced by 4-hydroxynonenal is mediated by stress-activated protein kinases pathways. *J. Neurochem.* **92**, 628–636 (2005).
121. David, D. C. *et al.* Proteomic and functional analyses reveal a mitochondrial dysfunction in P301L tau transgenic mice. *J. Biol. Chem.* **280**, 23802–23814 (2005).
122. Berridge, M. J. Calcium hypothesis of Alzheimer's disease. *Pflügers Arch. - Eur. J. Physiol.* **459**, 441–449 (2010).
123. Bezprozvanny, I. & Mattson, M. P. Neuronal calcium mishandling and the pathogenesis of Alzheimer's disease. *Trends Neurosci.* **31**, 454–463 (2008).
124. Wang, X. *et al.* Amyloid-β overproduction causes abnormal mitochondrial dynamics via differential modulation of mitochondrial fission/fusion proteins. *Proc. Natl. Acad. Sci. U. S. A.* **105**, 19318–19323 (2008).
125. Wang, W. *et al.* Inhibition of mitochondrial fragmentation protects against Alzheimer's disease in rodent model. *Hum. Mol. Genet.* **26**, 4118–4131 (2017).
126. Xu, L. L. *et al.* Mitochondrial dynamics changes with age in an APPsw/PS1dE9 mouse model of Alzheimer's disease. *Neuroreport* **28**, 222–228 (2017).
127. Wang, X. *et al.* Impaired balance of mitochondrial fission and fusion in

Alzheimer's disease. *J. Neurosci.* **29**, 9090–9103 (2009).

128. Manczak, M. & Reddy, P. H. Abnormal interaction between the mitochondrial fission protein Drp1 and hyperphosphorylated tau in Alzheimer's disease neurons: Implications for mitochondrial dysfunction and neuronal damage. *Hum. Mol. Genet.* **21**, 2538–2547 (2012).
129. Du, H. & Yan, S. S. Du. Mitochondrial permeability transition pore in Alzheimer's disease: Cyclophilin D and amyloid beta. *Biochim. Biophys. Acta - Mol. Basis Dis.* **1802**, 198–204 (2010).
130. Marucci, G. *et al.* Efficacy of acetylcholinesterase inhibitors in Alzheimer's disease. *Neuropharmacology* **190**, 108352 (2021).
131. Yang, Z., Zhou, X. & Zhang, Q. Effectiveness and safety of memantine treatment for Alzheimer's disease. *J. Alzheimer's Dis.* **36**, 445–458 (2013).
132. Müller, W. E. *et al.* Therapeutic efficacy of the Ginkgo special extract EGb761 ® within the framework of the mitochondrial cascade hypothesis of Alzheimer's disease. *World J. Biol. Psychiatry* **20**, 173–189 (2019).
133. DeFeudis, F. V. A brief history of EGb 761 and its therapeutic uses. *Pharmacopsychiatry* **36 Suppl 1**, S2-7 (2003).
134. Müller, W. E., Heiser, J. & Leuner, K. Effects of the standardized Ginkgo biloba extract EGb 761® on neuroplasticity. *Int. Psychogeriatrics* **24**, S21-4 (2012).
135. Knopman, D. S., Jones, D. T. & Greicius, M. D. Failure to demonstrate efficacy of aducanumab: An analysis of the EMERGE and ENGAGE trials as reported by Biogen, December 2019. *Alzheimer's Dement.* **17**, 696–701 (2021).
136. European Medicines Agency. Refusal of the marketing authorisation for Aduhelm (aducanumab). (2021).
137. Winblad, B. Piracetam: A review of pharmacological properties and clinical uses. *CNS Drug Rev.* **11**, 169–182 (2005).
138. Ratiopharm-GmbH. Piracetam-ratiopharm ® 1200 mg Filmtabletten. 1–8 (2019).
139. Domańska-Janik, K. & Zaleska, M. The action of piracetam on 14C-glucose metabolism in normal and posthypoxic rat cerebral cortex slices. *Pol. J. Pharmacol. Pharm.* **29**, 111–116 (1977).
140. Keil, U. *et al.* Piracetam improves mitochondrial dysfunction following oxidative stress. *Br. J. Pharmacol.* **147**, 199–208 (2006).
141. Kurz, C. *et al.* The metabolic enhancer piracetam ameliorates the impairment of mitochondrial function and neurite outgrowth induced by beta-amyloid peptide. *Br. J. Pharmacol.* **160**, 246–257 (2010).

142. Leuner, K., Kurz, C., Guidetti, G., Orgogozo, J.-M. & Müller, W. E. Improved mitochondrial function in brain aging and Alzheimer disease - the new mechanism of action of the old metabolic enhancer piracetam. *Front. Neurosci.* **4**, 44 (2010).
143. Stockburger, C. *et al.* Improvement of mitochondrial function and dynamics by the metabolic enhancer piracetam. *Biochem. Soc. Trans.* **41**, 1331–1334 (2013).
144. Stockburger, C., Miano, D., Pallas, T., Friedland, K. & Müller, W. E. Enhanced Neuroplasticity by the Metabolic Enhancer Piracetam Associated with Improved Mitochondrial Dynamics and Altered Permeability Transition Pore Function. *Neural Plast.* **2016**, 8075903 (2016).
145. Dickerson, B. C. *et al.* Increased hippocampal activation in mild cognitive impairment compared to normal aging and AD. *Neurology* **65**, 404–411 (2005).
146. Sperling, R. A. *et al.* Functional alterations in memory networks in early Alzheimer's disease. *Neuromolecular Med.* **12**, 27–43 (2010).
147. Putcha, D. *et al.* Hippocampal hyperactivation associated with cortical thinning in Alzheimer's disease signature regions in non-demented elderly adults. *J. Neurosci.* **31**, 17680–17688 (2011).
148. Sosulina, L. *et al.* Hippocampal hyperactivity in a rat model of Alzheimer's disease. *J. Neurochem.* **157**, 2128–2144 (2021).
149. Bakker, A. *et al.* Reduction of Hippocampal Hyperactivity Improves Cognition in Amnestic Mild Cognitive Impairment. *Neuron* **74**, 467–474 (2012).
150. Swerdlow, R. H. & Khan, S. M. A 'mitochondrial cascade hypothesis' for sporadic Alzheimer's disease. *Med. Hypotheses* **63**, 8–20 (2004).
151. Scheuermann, S. *et al.* Homodimerization of amyloid precursor protein and its implication in the amyloidogenic pathway of Alzheimer's disease. *J. Biol. Chem.* **276**, 33923–33929 (2001).
152. Rhein, V. *et al.* Amyloid-beta Leads to Impaired Cellular Respiration, Energy Production and Mitochondrial Electron Chain Complex Activities in Human Neuroblastoma Cells. *Cell. Mol. Neurobiol.* **29**, 1063 (2009).
153. Graham, F. L., Smiley, J., Russell, W. C. & Nairn, R. Characteristics of a human cell line transformed by DNA from human adenovirus type 5. *J. Gen. Virol.* **36**, 59–72 (1977).
154. Menten-Dedoyart, C. *et al.* Development and validation of a new mouse model to investigate the role of sv2a in epilepsy. *PLoS One* **11**, (2016).
155. Sherer, T. B. *et al.* Mechanism of toxicity in rotenone models of Parkinson's

disease. *J. Neurosci.* **23**, 10756–10764 (2003).

156. Radad, K. *et al.* Rotenone: from modelling to implication in Parkinson's disease. *Folia Neuropathol.* **57**, 317–326 (2019).
157. Park, Y. S., Choi, S. E. & Koh, H. C. PGAM5 regulates PINK1/Parkin-mediated mitophagy via DRP1 in CCCP-induced mitochondrial dysfunction. *Toxicol. Lett.* **284**, 120–128 (2018).
158. Xu, J. *et al.* Mono-2-ethylhexyl phthalate drives progression of PINK1-parkin-mediated mitophagy via increasing mitochondrial ROS to exacerbate cytotoxicity. *Redox Biol.* **38**, 101776 (2021).
159. Huang, B., Jones, S. A., Brandenburg, B. & Zhuang, X. Whole-cell 3D STORM reveals interactions between cellular structures with nanometer-scale resolution. *Nat. Methods* **5**, 1047–1052 (2008).
160. Wurm, C. A. *et al.* Nanoscale distribution of mitochondrial import receptor Tom20 is adjusted to cellular conditions and exhibits an inner-cellular gradient. *Proc. Natl. Acad. Sci.* **108**, 13546 LP – 13551 (2011).
161. Arasaki, K. *et al.* A Role for the ancient SNARE syntaxin 17 in regulating mitochondrial division. *Dev. Cell* **32**, 304–317 (2015).
162. Li, H. *et al.* A Bcl-xL–Drp1 complex regulates synaptic vesicle membrane dynamics during endocytosis. *Nat. Cell Biol.* **15**, 773–785 (2013).
163. Manczak, M., Kandimalla, R., Yin, X. & Hemachandra Reddy, P. Mitochondrial division inhibitor 1 reduces dynamin-related protein 1 and mitochondrial fission activity. *Hum. Mol. Genet.* **28**, 177–199 (2019).
164. Zhao, T. *et al.* Central role of mitofusin 2 in autophagosome-lysosome fusion in cardiomyocytes. *J. Biol. Chem.* **287**, 23615–23625 (2012).
165. Ding, Y., Gao, H., Zhao, L., Wang, X. & Zheng, M. Mitofusin 2-deficiency suppresses cell proliferation through disturbance of autophagy. *PLoS One* **10**, 1–14 (2015).
166. Moreau, K., Renna, M. & Rubinsztein, D. C. Connections between SNAREs and autophagy. *Trends Biochem. Sci.* **38**, 57–63 (2013).
167. Nair, U. *et al.* SNARE proteins are required for macroautophagy. *Cell* **146**, 290–302 (2011).
168. Moreau, K., Ravikumar, B., Renna, M., Puri, C. & Rubinsztein, D. C. Autophagosome precursor maturation requires homotypic fusion. *Cell* **146**, 303–317 (2011).
169. Herrmann, J. M. & Neupert, W. Protein transport into mitochondria. *Curr. Opin.*

Microbiol. **3**, 210–214 (2000).

170. Abe, Y. *et al.* Structural Basis of Presequence Recognition by the Mitochondrial Protein Import Receptor Tom20. *Cell* **100**, 551–560 (2000).
171. Wang, W. *et al.* Atomic structure of human TOM core complex. *Cell Discov.* **6**, 67 (2020).
172. Guan, Z. *et al.* Structural insights into assembly of human mitochondrial translocase TOM complex. *Cell Discov.* **7**, 22 (2021).
173. Ando, S. *et al.* The Protective Effects of Levetiracetam on a Human iPSCs-Derived Spinal Muscular Atrophy Model. *Neurochem. Res.* **44**, 1773–1779 (2019).
174. de Graaf, A. O. *et al.* Bcl-2 prevents loss of mitochondria in CCCP-induced apoptosis. *Exp. Cell Res.* **299**, 533–540 (2004).
175. Park, J. S., Kang, D. H. & Bae, S. H. P62 prevents carbonyl cyanide m-chlorophenyl hydrazine (CCCP)-induced apoptotic cell death by activating Nrf2. *Biochem. Biophys. Res. Commun.* **464**, 1139–1144 (2015).
176. Nowack, A. *et al.* Levetiracetam reverses synaptic deficits produced by overexpression of SV2A. *PLoS One* **6**, e29560–e29560 (2011).
177. Hong, W. & Lev, S. Tethering the assembly of SNARE complexes. *Trends Cell Biol.* **24**, 35–43 (2014).
178. Buckley, K. & Kelly, R. B. Identification of a transmembrane glycoprotein specific for secretory vesicles of neural and endocrine cells. *J. Cell Biol.* **100**, 1284–1294 (1985).
179. Sugiura, A., McLelland, G.-L., Fon, E. A. & McBride, H. M. A new pathway for mitochondrial quality control: mitochondrial-derived vesicles. *EMBO J.* **33**, 2142–2156 (2014).
180. Neuspiel, M. *et al.* Cargo-selected transport from the mitochondria to peroxisomes is mediated by vesicular carriers. *Curr. Biol.* **18**, 102–108 (2008).
181. Soubannier, V. *et al.* A vesicular transport pathway shuttles cargo from mitochondria to lysosomes. *Curr. Biol.* **22**, 135–141 (2012).
182. Soubannier, V., Rippstein, P., Kaufman, B. A., Shoubridge, E. A. & McBride, H. M. Reconstitution of mitochondria derived vesicle formation demonstrates selective enrichment of oxidized cargo. *PLoS One* **7**, e52830 (2012).
183. Liu, D. *et al.* The existence and function of mitochondrial component in extracellular vesicles. *Mitochondrion* **54**, 122–127 (2020).
184. Qu, L., Akbergenova, Y., Hu, Y. & Schikorski, T. Synapse-to-synapse variation

in mean synaptic vesicle size and its relationship with synaptic morphology and function. *J. Comp. Neurol.* **514**, 343–352 (2009).

185. Obashi, K. & Okabe, S. Regulation of mitochondrial dynamics and distribution by synapse position and neuronal activity in the axon. *Eur. J. Neurosci.* **38**, 2350–2363 (2013).
186. Griesche, N., Sanchez, G., Hermans, C. & Idevall-Hagren, O. Cortical mitochondria regulate insulin secretion by local Ca(2+) buffering in rodent beta cells. *J. Cell Sci.* **132**, (2019).
187. Isenmann, S., Khew-Goodall, Y., Gamble, J., Vadas, M. & Wattenberg, B. W. A splice-isoform of vesicle-associated membrane protein-1 (VAMP-1) contains a mitochondrial targeting signal. *Mol. Biol. Cell* **9**, 1649–1660 (1998).
188. Lan, L., Isenmann, S. & Wattenberg, B. W. Targeting and insertion of C-terminally anchored proteins to the mitochondrial outer membrane is specific and saturable but does not strictly require ATP or molecular chaperones. *Biochem. J.* **349**, 611–621 (2000).
189. Verstreken, P. *et al.* Synaptic mitochondria are critical for mobilization of reserve pool vesicles at Drosophila neuromuscular junctions. *Neuron* **47**, 365–378 (2005).
190. Ma, H., Cai, Q., Lu, W., Sheng, Z.-H. & Mochida, S. KIF5B Motor Adaptor Syntabulin Maintains Synaptic Transmission in Sympathetic Neurons. *J. Neurosci.* **29**, 13019 LP – 13029 (2009).
191. Ly, C. V & Verstreken, P. Mitochondria at the synapse. *Neurosci. a Rev. J. bringing Neurobiol. Neurol. psychiatry* **12**, 291–299 (2006).
192. Passmore, J. B., Pinho, S., Gomez-Lazaro, M. & Schrader, M. The respiratory chain inhibitor rotenone affects peroxisomal dynamics via its microtubule-destabilising activity. *Histochem. Cell Biol.* **148**, 331–341 (2017).
193. Detrait, E., Maurice, T., Hanon, E., Leclercq, K. & Lamberty, Y. Lack of synaptic vesicle protein SV2B protects against amyloid-β_{25-35}-induced oxidative stress, cholinergic deficit and cognitive impairment in mice. *Behav. Brain Res.* **271**, 277–285 (2014).
194. Chen, H. *et al.* Mitofusins Mfn1 and Mfn2 coordinately regulate mitochondrial fusion and are essential for embryonic development. *J. Cell Biol.* **160**, 189–200 (2003).
195. Mourier, A. *et al.* Mitofusin 2 is required to maintain mitochondrial coenzyme Q levels. *J. Cell Biol.* **208**, 429–442 (2015).

196. Fang, D., Yan, S., Yu, Q., Chen, D. & Yan, S. S. Mfn2 is Required for Mitochondrial Development and Synapse Formation in Human Induced Pluripotent Stem Cells/hiPSC Derived Cortical Neurons. *Sci. Rep.* **6**, 31462 (2016).
197. Chen, L., Gong, Q., Stice, J. P. & Knowlton, A. A. Mitochondrial OPA1, apoptosis, and heart failure. *Cardiovasc. Res.* **84**, 91–99 (2009).
198. Hu, C. *et al.* OPA1 and MICOS Regulate mitochondrial crista dynamics and formation. *Cell Death Dis.* **11**, 940 (2020).
199. Rahn, J. J., Stackley, K. D. & Chan, S. S. L. Opa1 is required for proper mitochondrial metabolism in early development. *PLoS One* **8**, e59218 (2013).
200. Fonseca, T. B., Sánchez-Guerrero, Á., Milosevic, I. & Raimundo, N. Mitochondrial fission requires DRP1 but not dynamins. *Nature* **570**, E34–E42 (2019).
201. Inoue-Yamauchi, A. & Oda, H. Depletion of mitochondrial fission factor DRP1 causes increased apoptosis in human colon cancer cells. *Biochem. Biophys. Res. Commun.* **421**, 81–85 (2012).
202. HUTCHISON, C. A., NEWBOLD, J. E., POTTER, S. S. & EDGELL, M. H. Maternal inheritance of mammalian mitochondrial DNA. *Nature* **251**, 536–538 (1974).
203. Ventura-Clapier, R. *et al.* Mitochondria: A central target for sex differences in pathologies. *Clin. Sci.* **131**, 803–822 (2017).
204. Serrano, M. E. *et al.* Anxiety-like features and spatial memory problems as a consequence of hippocampal SV2A expression. *PLoS One* **14**, e0217882–e0217882 (2019).
205. Biedler, J. L., Roffler-Tarlov, S., Schachner, M. & Freedman, L. S. Multiple neurotransmitter synthesis by human neuroblastoma cell lines and clones. *Cancer Res.* **38**, 3751–3757 (1978).
206. Maday, S., Wallace, K. E. & Holzbaur, E. L. F. Autophagosomes initiate distally and mature during transport toward the cell soma in primary neurons. *J. Cell Biol.* **196**, 407–417 (2012).
207. Evans, C. S. & Holzbaur, E. L. Degradation of engulfed mitochondria is rate-limiting in Optineurin-mediated mitophagy in neurons. *Elife* **9**, e50260 (2020).
208. Misgeld, T. & Schwarz, T. L. Mitostasis in Neurons: Maintaining Mitochondria in an Extended Cellular Architecture. *Neuron* **96**, 651–666 (2017).
209. Cagalinec, M. *et al.* Principles of the mitochondrial fusion and fission cycle in

neurons. *J. Cell Sci.* **126**, 2187–2197 (2013).

210. Arnold, B., Cassady, S. J., VanLaar, V. S. & Berman, S. B. Integrating multiple aspects of mitochondrial dynamics in neurons: Age-related differences and dynamic changes in a chronic rotenone model. *Neurobiol. Dis.* **41**, 189–200 (2011).
211. Morris, R. L. & Hollenbeck, P. J. Axonal transport of mitochondria along microtubules and F-actin in living vertebrate neurons. *J. Cell Biol.* **131**, 1315–1326 (1995).
212. Safiulina, D., Veksler, V., Zharkovsky, A. & Kaasik, A. Loss of mitochondrial membrane potential is associated with increase in mitochondrial volume: Physiological role in neurones. *J. Cell. Physiol.* **206**, 347–353 (2006).
213. Lin, M.-Y. & Sheng, Z.-H. Regulation of mitochondrial transport in neurons. *Exp. Cell Res.* **334**, 35–44 (2015).
214. Chang, C.-R. & Blackstone, C. Dynamic regulation of mitochondrial fission through modification of the dynamin-related protein Drp1. *Ann. N. Y. Acad. Sci.* **1201**, 34–39 (2010).
215. Santel, A. & Frank, S. Shaping mitochondria: The complex posttranslational regulation of the mitochondrial fission protein DRP1. *IUBMB Life* **60**, 448–455 (2008).
216. Cribbs, J. T. & Strack, S. Reversible phosphorylation of Drp1 by cyclic AMP-dependent protein kinase and calcineurin regulates mitochondrial fission and cell death. *EMBO Rep.* **8**, 939–944 (2007).
217. Archer, S. L. Mitochondrial dynamics--mitochondrial fission and fusion in human diseases. *N. Engl. J. Med.* **369**, 2236–2251 (2013).
218. Jin, J., Wei, X., Zhi, X., Wang, X. & Meng, D. Drp1-dependent mitochondrial fission in cardiovascular disease. *Acta Pharmacol. Sin.* **42**, 655–664 (2021).
219. Losón, O. C., Song, Z., Chen, H. & Chan, D. C. Fis1, Mff, MiD49, and MiD51 mediate Drp1 recruitment in mitochondrial fission. *Mol. Biol. Cell* **24**, 659–667 (2013).
220. Lee, Y., Jeong, S.-Y., Karbowski, M., Smith, C. L. & Youle, R. J. Roles of the mammalian mitochondrial fission and fusion mediators Fis1, Drp1, and Opa1 in apoptosis. *Mol. Biol. Cell* **15**, 5001–5011 (2004).
221. Shen, Q. *et al.* Mutations in Fis1 disrupt orderly disposal of defective mitochondria. *Mol. Biol. Cell* **25**, 145–159 (2014).
222. Peng, K. *et al.* The Interaction of Mitochondrial Biogenesis and Fission/Fusion

Mediated by PGC-1α Regulates Rotenone-Induced Dopaminergic Neurotoxicity. *Mol. Neurobiol.* **54**, 3783–3797 (2017).

223. Zhou, H. *et al.* Melatonin inhibits rotenone-induced SH-SY5Y cell death via the downregulation of Dynamin-Related Protein 1 expression. *Eur. J. Pharmacol.* **819**, 58–67 (2018).
224. Rocha, A. G. *et al.* MFN2 agonists reverse mitochondrial defects in preclinical models of Charcot-Marie-Tooth disease type 2A. *Science* **360**, 336–341 (2018).
225. Sebastián, D. *et al.* Mfn2 deficiency links age-related sarcopenia and impaired autophagy to activation of an adaptive mitophagy pathway. *EMBO J.* **35**, 1677–1693 (2016).
226. Chen, Y. *et al.* Mfn2 is involved in intervertebral disc degeneration through autophagy modulation. *Osteoarthr. Cartil.* **28**, 363–374 (2020).
227. Cai, H., Chen, L., Zhang, M., Xiang, W. & Su, P. Low expression of MFN2 is associated with early unexplained miscarriage by regulating autophagy of trophoblast cells. *Placenta* **70**, 34–40 (2018).
228. Xiong, W. *et al.* Mitofusin 2 participates in mitophagy and mitochondrial fusion against angiotensin II-induced cardiomyocyte injury. *Front. Physiol.* **10**, 1–12 (2019).
229. Chen, Y. & Dorn, G. W. PINK1-phosphorylated mitofusin 2 is a parkin receptor for culling damaged mitochondria. *Science.* **340**, 471–475 (2013).
230. Hoffmann-Conaway, S. *et al.* Parkin contributes to synaptic vesicle autophagy in bassoon-deficient mice. *Elife* **9**, 1–30 (2020).
231. Kane, M. S. *et al.* Autophagy controls the pathogenicity of OPA1 mutations in dominant optic atrophy. *J. Cell. Mol. Med.* **21**, 2284–2297 (2017).
232. White, K. E. *et al.* Opa1 deficiency associated with increased autophagy in retinal ganglion cells in a murine model of dominant optic atrophy. *Investig. Ophthalmol. Vis. Sci.* **50**, 2567–2571 (2009).
233. Twig, G. *et al.* Fission and selective fusion govern mitochondrial segregation and elimination by autophagy. *EMBO J.* **27**, 433–446 (2008).
234. Gomes, L. C. & Scorrano, L. High levels of Fis1, a pro-fission mitochondrial protein, trigger autophagy. *Biochim. Biophys. Acta* **1777**, 860–866 (2008).
235. Zhang, C.-S. & Lin, S.-C. AMPK Promotes Autophagy by Facilitating Mitochondrial Fission. *Cell Metab.* **23**, 399–401 (2016).
236. Ikeda, Y. *et al.* Endogenous Drp1 mediates mitochondrial autophagy and protects the heart against energy stress. *Circ. Res.* **116**, 264–278 (2015).

237. Vantaggiato, C. *et al.* The fine tuning of drp1-dependent mitochondrial remodeling and autophagy controls neuronal differentiation. *Front. Cell. Neurosci.* **13**, 1–20 (2019).
238. Inbal, B., Bialik, S., Sabanay, I., Shani, G. & Kimchi, A. DAP kinase and DRP-1 mediate membrane blebbing and the formation of autophagic vesicles during programmed cell death. *J. Cell Biol.* **157**, 455–468 (2002).
239. Hailey, D. W. *et al.* Mitochondria supply membranes for autophagosome biogenesis during starvation. *Cell* **141**, 656–667 (2010).
240. Wang, Y. *et al.* SNARE-mediated membrane fusion in autophagy. *Semin. Cell Dev. Biol.* **60**, 97–104 (2016).
241. Molino, D., Nascimbeni, A. C., Giordano, F., Codogno, P. & Morel, E. ER-driven membrane contact sites: Evolutionary conserved machineries for stress response and autophagy regulation? *Commun. Integr. Biol.* **10**, e1401699–e1401699 (2017).
242. Teplova, V. V, Tonshin, A. A., Grigoriev, P. A., Saris, N.-E. L. & Salkinoja-Salonen, M. S. Bafilomycin A1 is a potassium ionophore that impairs mitochondrial functions. *J. Bioenerg. Biomembr.* **39**, 321–329 (2007).
243. Zhdanov, A. V, Dmitriev, R. I. & Papkovsky, D. B. Bafilomycin A1 activates respiration of neuronal cells via uncoupling associated with flickering depolarization of mitochondria. *Cell. Mol. Life Sci.* **68**, 903–917 (2011).
244. Civiletto, G. *et al.* Rapamycin rescues mitochondrial myopathy via coordinated activation of autophagy and lysosomal biogenesis. *EMBO Mol. Med.* **10**, e8799 (2018).
245. He, J. N. *et al.* Rapamycin Removes Damaged Mitochondria and Protects Human Trabecular Meshwork (TM-1) Cells from Chronic Oxidative Stress. *Mol. Neurobiol.* **56**, 6586–6593 (2019).
246. Uemichi, K., Shirai, T., Hanakita, H. & Takemasa, T. Effect of mechanistic/mammalian target of rapamycin complex 1 on mitochondrial dynamics during skeletal muscle hypertrophy. *Physiol. Rep.* **9**, e14789–e14789 (2021).
247. Baba, M., Osumi, M., Scott, S. V, Klionsky, D. J. & Ohsumi, Y. Two distinct pathways for targeting proteins from the cytoplasm to the vacuole/lysosome. *J. Cell Biol.* **139**, 1687–1695 (1997).
248. Klionsky, D. J. & Eskelinen, E.-L. The vacuole versus the lysosome: when size matters. *Autophagy* **10**, 185–187 (2014).

249. Rambold, A. S., Kostelecky, B., Elia, N. & Lippincott-Schwartz, J. Tubular network formation protects mitochondria from autophagosomal degradation during nutrient starvation. *Proc. Natl. Acad. Sci.* **108**, 10190 LP – 10195 (2011).
250. Gomes, L. C., Benedetto, G. Di & Scorrano, L. During autophagy mitochondria elongate, are spared from degradation and sustain cell viability. *Nat. Cell Biol.* **13**, 589–598 (2011).
251. Nixon, R. A. Autophagy, amyloidogenesis and Alzheimer disease. *J. Cell Sci.* **120**, 4081–4091 (2007).
252. Li, L., Zhang, X. & Le, W. Autophagy dysfunction in Alzheimer's disease. *Neurodegener. Dis.* **7**, 265–271 (2010).
253. Zare-Shahabadi, A., Masliah, E., Johnson, G. V. W. & Rezaei, N. Autophagy in Alzheimer's disease. *Rev. Neurosci.* **26**, 385–395 (2015).
254. Pickford, F. *et al.* The autophagy-related protein beclin 1 shows reduced expression in early Alzheimer disease and regulates amyloid beta accumulation in mice. *J. Clin. Invest.* **118**, 2190–2199 (2008).
255. Spilman, P. *et al.* Inhibition of mTOR by rapamycin abolishes cognitive deficits and reduces amyloid-beta levels in a mouse model of Alzheimer's disease. *PLoS One* **5**, e9979–e9979 (2010).
256. Cai, Z. & Yan, L.-J. Rapamycin, Autophagy, and Alzheimer's Disease. *J. Biochem. Pharmacol. Res.* **1**, 84–90 (2013).
257. Carson, R. *et al.* Age and sex effects on synaptic density in healthy humans as assessed with SV2A PET. *J. Nucl. Med.* **59**, 541 LP – 541 (2018).
258. Lu, Y. *et al.* Partial volume correction analysis for (11)C-UCB-J PET studies of Alzheimer's disease. *Neuroimage* **238**, 118248 (2021).
259. Holland, N. *et al.* Synaptic Loss in Primary Tauopathies Revealed by [(11) C]UCB-J Positron Emission Tomography. *Mov. Disord.* **35**, 1834–1842 (2020).

9 FIGURES AND TABLES

9.1 List of figures

9.2 List of tables

10 ACKNOWLEDGEMENTS

11 RESUME